

Dissertation ETH No. 25942

**Towards an Improved Understanding of  
the Global Energy Balance:  
Temporal Variations of Solar Radiation in  
the Climate System**

A thesis submitted to attain the degree of  
**Doctor of sciences of ETH Zurich**  
Dr. sc. ETH Zurich

presented by  
**Matthias Schwarz**  
MSc, MSc, BSc, BSc University of Graz, Austria  
born on October 19, 1988,  
citizen of Austria

accepted on the recommendation of  
**Prof. Dr. Martin Wild**, examiner  
**Prof. Dr. Christoph Schär**, co-examiner  
**Dr. Doris Folini**, co-examiner  
**Dr. Stefan Kinne**, co-examiner

2019



# Abstract

The spatiotemporal distribution of absorbed solar radiation in the Earth's climate system is a fundamental driver of the Earth's climate. Today, the global long-term annual mean energy fluxes of the global energy balance are reasonably well known. In this thesis, we go beyond the long-term annual mean perspective and focus on temporal variations in the energy balance. Specifically, we study annual cycles and multidecadal changes of the shortwave fluxes of the energy balance in an observation-based framework.

To this end, we combine observations of top-of-the-atmosphere (TOA) radiative fluxes and surface albedo, both obtained from satellites, with surface flux observations. The latter are available from in-situ or satellite observations. In-situ observations are the most robust and accurate way to determine surface solar radiation but their spatial availability is limited. Satellite-derived surface radiation is less accurate but has greater spatial coverage. In this thesis, we use both data sources depending on whether accuracy or spatial coverage is needed.

Using in-situ data – which from a spatial perspective is point data – in combination with other gridded data products requires a thorough assessment of potential methodological uncertainties which arise when combining those two data sets. In Chapter 2 and Chapter 3 of this thesis, different aspects of spatiotemporal representativeness of monthly mean records of surface solar radiation point observations are assessed globally. Although large regional differences in the representativeness of point measurements occur, in most regions they can be considered representative of a larger surrounding. Therefore, examining temporal variations in the shortwave energy fluxes by combining in-situ and colocated gridded flux data is feasible. However, additional uncertainties must be taken into account.

Due to the Earth's celestial movement around the Sun, large seasonal cycles in the amount and geographic distribution of solar insolation occur. These variations play a key role in the distribution of energy in the climate system and ultimately drive the seasonality of Earth's general circulation systems, climate, and weather. Nevertheless, as recently shown by Hakuba et al. (2014b), the fraction of the incoming shortwave radiation at the top-of-the-atmosphere which is absorbed within the atmosphere does not substantially vary with season or latitude in Europe. An astonishing result, when considering that various climate elements which po-

tentially influence the shortwave radiative fluxes have notable annual cycles. In Chapter 4 we go beyond Europe and identify several regions with large annual cycles in fractional atmospheric absorption. We find that they are driven mainly by annual cycles of water vapor and different aerosol species. The largest annual cycles in fractional atmospheric absorption are apparent in regions with large annual cycles in aerosol loading related to seasonal biomass burning, which is a strong indication that these annual cycles are anthropogenically intensified or even entirely forced. We also show that the skill of global climate models to simulate the observed patterns in the annual cycles of atmospheric shortwave absorption is limited.

It is well known from observations that significant widespread variations in the amount of solar radiation reaching the Earth's surface occurred on decadal time scales, known as *global dimming* and *global brightening*. According to the principle of energy conservation – the foundation of the energy balance – such changes in surface solar radiation must go along with a change in surface absorption, the TOA net flux, or the atmospheric absorption. In the observation-based energy balance framework, we find that changing atmospheric shortwave absorption is a major cause for the observed trends in Europe and China. The simultaneous trend analysis for surface, atmospheric, and TOA fluxes suggests that changes in aerosols – and in particular absorbing ones – are responsible for the observed trends.

Taken together, this thesis demonstrates that an integrative approach to the shortwave energy balance, in which TOA, atmospheric and surface fluxes are simultaneously analyzed, can lead to valuable insights into key aspects of the climate system.

# Zusammenfassung

Das Klima der Erde wird wesentlich von der räumlichen und zeitlichen Verteilung von absorbiertener Sonnenstrahlung im Klimasystem der Erde bestimmt. Die global gemittelten Langzeit Jahresmittelwerte der einzelnen Energieflüsse der globalen Energiebilanz sind heute hinlänglich gut bekannt. In dieser Dissertation gehen wir über die Langzeit Jahresmittelwerte-Perspektive hinaus und fokussieren auf zeitliche Veränderungen in der Energiebilanz. Dabei erforschen wir in einem beobachtungsbasierten Rahmen jahreszeitliche Schwankungen und dekadische Änderungen der kurzweiligen Flüsse der Energiebilanz. Dazu kombinieren wir Satellitenbeobachtungen der Strahlungsflüsse am oberen Rand der Atmosphäre (engl. top-of-the-atmosphere, TOA) sowie der Bodenalbedo, mit Beobachtungen der Strahlungsflüsse an der Erdoberfläche. Letztere sind jeweils von In-situ- oder Satellitenbeobachtungen verfügbar.

In-situ-Beobachtungen sind die robusteste und genaueste Methode zur Bestimmung der Sonneneinstrahlung an der Erdoberfläche. Ihre räumliche Verfügbarkeit ist jedoch begrenzt. Von Satelliten abgeleitete Strahlungsflüsse an der Erdoberfläche sind weniger genau, haben jedoch eine grössere räumliche Abdeckung. In dieser Arbeit verwenden wir beide Datenquellen, abhängig davon, ob Genauigkeit oder räumliche Abdeckung erforderlich ist.

Die Verwendung von In-situ-Daten – die in räumlicher Hinsicht Punktdaten sind – in Kombination mit Rasterdatenprodukten erfordert eine gründliche Bewertung möglicher methodischer Unsicherheiten, die sich bei der Kombination dieser beiden Datensätze ergeben. In Kapitel 2 und Kapitel 3 dieser Dissertation werden verschiedene Aspekte der räumlichen und zeitlichen Repräsentativität solcher Punktmessungen von monatlich gemittelten Messungen der Sonneneinstrahlung an der Erdoberfläche auf globalem Massstab bewertet. Obwohl grosse regionale Unterschiede in der Repräsentativität von Punktmessungen auftreten, können diese in den meisten Regionen als repräsentativ für eine grössere Umgebung betrachtet werden. Durch die Kombination von In-Situ- und gerasterten Flussdaten ist es daher möglich, zeitliche Variationen in den kurzweiligen Energieflüssen zu untersuchen. Zusätzliche Unsicherheiten müssen jedoch berücksichtigt werden.

Aufgrund der Himmelsbewegungen der Erde um die Sonne unterliegt die Menge und geographische Verteilung der Sonneneinstrahlung grossen jahreszeitlichen Schwankungen. Die-

se Variationen spielen eine Schlüsselrolle bei der Verteilung der Energie im Klimasystem und bestimmen letztlich die Saisonalität der allgemeinen Zirkulationssysteme der Erde, des Klimas und des Wetters. Wie jedoch kürzlich von Hakuba et al. (2014b) gezeigt wurde, variiert in Europa der relative Anteil der in der Atmosphäre absorbierten Strahlung nicht wesentlich mit den Jahreszeiten oder dem Breitengrad. Bedenkt man, dass verschiedene Klimatelemente, die potenziell die kurzweiligen Strahlungsflüsse beeinflussen, beträchtlichen saisonalen Schwankungen unterliegen, ist dies ein unerwartetes Resultat. In Kapitel 4 erweitern wir diese Untersuchungen über Europa hinaus und identifizieren mehrere Regionen mit grossen jahreszeitlichen Schwankungen der relativen atmosphärischen Absorption. Wir haben gezeigt, dass diese hauptsächlich durch saisonale Zyklen von Wasserdampf und verschiedenen Aerosolarten verursacht werden. Die grössten jahreszeitlichen Schwankungen in der relativen atmosphärischen Absorption finden wir in Regionen mit grossen jahreszeitlichen Schwankungen in der Aerosolbelastung, welche wiederum mit der saisonalen Verbrennung von Biomasse in Verbindung stehen. Dies ist ein starkes Indiz dafür, dass diese jahreszeitlichen Schwankungen durch menschliches Handeln intensiviert oder sogar ganz erzwungen werden. Wir zeigen auch, dass globale Klimamodelle die beobachteten Strukturen in den jahreszeitlichen Schwankungen der atmosphärischer Kurzwellenabsorption nur bedingt simulieren können.

Aus Beobachtungen ist bekannt, dass auf dekadischen Zeitskalen beträchtliche Variationen in der Menge der Sonnenstrahlung, die die Erdoberfläche erreicht, auftraten. Diese sind als *"global dimming"* und *"global brightening"* bekannt. Nach dem Prinzip der Energieerhaltung – der Grundlage der globalen Energiebilanz – müssen diese Änderungen im Strahlungsfluss an der Erdoberfläche mit einer Änderung der Bodenabsorption, des Nettoflusses am oberen Rand der Atmosphäre oder der atmosphärischen Absorption einhergehen. Im Rahmen der beobachtungsbasierten Energiebilanz stellen wir fest, dass die Veränderung der atmosphärischen Kurzwellenabsorption eine Hauptursache für die beobachteten dekadischen Veränderungen in Europa und China ist. Die gleichzeitige Trendanalyse der Strahlungsfluss an der Erdoberfläche, innerhalb der Atmosphäre und am oberen Rand der Atmosphäre legt nahe, dass Änderungen in Aerosolen – und insbesondere der absorbierenden Aerosole – für die beobachteten Trends verantwortlich sind.

Zusammenfassend zeigt diese Arbeit, dass ein integrativer Ansatz für die kurzweilige Energiebilanz, bei die Strahlungsflüsse an der Erdoberfläche, innerhalb der Atmosphäre und am oberen Rand der Atmosphäre gleichzeitig analysiert werden, wertvolle Einblicke in wichtige Aspekte des Klimasystems liefern kann.

# Acknowledgements

After more than three years in Switzerland, and at the end of my doctoral studies, it is time to thank all those people who made this time so special and joyful.

First of all, I want to thank Martin Wild for being my main supervisor. Working with you was a great pleasure and I much appreciate your guidance and supervision, your great flexibility, and that you gave me the chance to become a part of your group and the scientific community.

A great 'thank you' goes to my co-supervisor Doris Folini. I always admired your honest and constructive feedback which contributed significantly to the success of this thesis. I cannot say how much I appreciate that you even took the time for me and my problems while you have gone through difficult times yourself.

I thank Christoph Schär for providing such an outstanding research environment and for being part of my Ph.D. committee.

Several other people supported my thesis in multiple ways and I want to thank them here: Stefan Kinne for agreeing to join my Ph.D. committee; Maria Hakuba for being the role model for this Ph.D. and for the input for the thesis; Su Yang for giving me the chance to extend my studies to China.; Uwe Pfeifroth and Jörg Trentmann for the help with the CM-SAF data; Richard Allan for the help with the DEEP-C reconstruction; Harald Rieder for encouraging me to apply for a Ph.D. position at ETH in the first place; Urs Beyerle, Hans-Heini Vogel and the rest of the IAC-IT team for providing such a great work environment; Rahel Buri for always having a solution for administrative problems.

Special thanks to all colleagues, and in particular those who became friends, for the great times. My time at the IAC would not have been so pleasant without you and I hope we will stick together in the future.

As this thesis was done (almost) exclusively with open source software, I want to express my gratitude to all the people involved in developing and offering the following software: Linux, Python, Spyder3, Latex, R, CDO, nview, Zotero, Github, Atom (and many more).

Thanks to my family – in particular my parents, Ursula and Ferdinand, and my brothers,

Christoph and Philipp – and all friends for the ongoing support during this path. It is a great feeling to know where home is.

Last but not least, my biggest thanks goes to my wife Lisa. I would not have been able to go through this adventure without you.



# Contents

<b>Abstract</b>	<b>iii</b>
<b>Zusammenfassung</b>	<b>v</b>
<b>Acknowledgements</b>	<b>vii</b>
<b>1 Introduction</b>	<b>1</b>
1.1 The global energy balance	1
1.1.1 Current best estimates of the shortwave fluxes	2
1.1.2 Regional differences	4
1.2 Temporal variations in the energy balance	5
1.2.1 Multidecadal changes in surface solar radiation: from global dimming to global brightening and beyond	5
1.2.2 Seasonal cycles in the shortwave energy balance	6
1.3 What factors determine the shortwave fluxes of the global energy balance?	7
1.3.1 External forcing: changes in incoming solar radiation	7
1.3.2 Internal forcing: potential explanatory variables within the climate system	7
1.4 An observational approach	10
1.5 Main Datasets	10
1.5.1 Top-of-the-atmosphere fluxes	11
1.5.2 Surface data	13
1.6 Objectives and outline	15
<b>2 Spatial representativeness of surface-measured variations of downward solar radiation</b>	<b>17</b>
2.1 Introduction	19
2.2 Data and Methods	20
2.2.1 Satellite-Derived SSR: The SARA Data Set	20
2.2.2 Direct Surface Observations of SSR	22
2.2.3 Methods	24
2.3 Results	27
2.3.1 Correlation Analysis	27

---

2.3.2	Spatial Sampling Errors	36
2.4	Discussion	37
2.5	Synthesis and Conclusion	41
<b>3</b>	<b>From point to area: worldwide assessment of the representativeness of monthly surface solar radiation records</b>	<b>43</b>
3.1	Introduction	45
3.2	Data and methods	47
3.2.1	High-resolution satellite-derived SSR data	47
3.2.2	Representativeness metrics	48
3.3	Representativeness: Quantitative estimates	52
3.3.1	Decorrelation length	53
3.3.2	Spatial sampling bias	55
3.3.3	Spatial sampling error	56
3.3.4	Comprehensive view on representativeness metrics	57
3.4	Robustness of representativeness metrics	58
3.4.1	Robustness across the data sets	58
3.4.2	Target grid sizes and their impact on the metrics presented	61
3.4.3	Benefits from bias correction	61
3.5	Investigating potential explanatory variables	62
3.6	BSRN case study	64
3.7	Summary and Conclusion	65
<b>4</b>	<b>The annual cycle of fractional atmospheric shortwave absorption in observations and models: spatial structure, magnitude and timing</b>	<b>69</b>
4.1	Introduction	70
4.2	Data and Method	72
4.2.1	TOA and surface fluxes from CERES	72
4.2.2	In-situ downward surface solar radiation	73
4.2.3	Albedo	74
4.2.4	Climate Model Data	75
4.2.5	Auxiliary data	76
4.2.6	Representativeness of in-situ observations	76
4.2.7	Data processing	77
4.3	Annual mean atmospheric shortwave absorption	77
4.4	Annual cycles of atmospheric shortwave absorption	79
4.5	Drivers of the annual cycle in atmospheric absorption	82
4.6	Atmospheric shortwave absorption in CMIP5 models	83
4.7	Discussion	86
4.8	Summary and Conclusion	89
<b>5</b>	<b>Changes in atmospheric shortwave absorption as major driver of dimming and brightening</b>	<b>93</b>
Introduction		94

---

Shortwave energy balance changes inferred from colocated space and surface observations.	96
Discussion and conclusions.	99
Methods	101
Surface shortwave radiation.	101
TOA shortwave radiation.	102
Albedo.	103
<b>6 Summary, conclusions, and outlook</b>	<b>107</b>
<b>Appendices</b>	<b>115</b>
<b>A Appendix for Chapter 1</b>	<b>117</b>
A.1 Spatial distribution of the shortwave energy fluxes	117
A.2 One layer model of for shortwave fluxes	119
A.3 Composite time series of total solar irradiance	121
<b>B Appendix for Chapter 2</b>	<b>123</b>
B.1 Spatial Sampling Errors	123
<b>C Appendix for Chapter 4</b>	<b>127</b>
C.1 Atmospheric shortwave absorption for individual members of the CMIP5	127
<b>Bibliography</b>	<b>127</b>
<b>Curriculum Vitae</b>	<b>157</b>



## 1.1 The global energy balance

The global energy balance describes the long term mean energy fluxes in the Earth's climate system. It is based upon the classical physics principle of energy conservation. Although the estimates for the individual components of the energy balance differ between the earlier (Abbot and Fowle, 1908; Dines, 1917) and more recent assessments (Trenberth et al., 2009; Ramanathan, 1987; Kiehl and Trenberth, 1997; Stephens et al., 2012; Wild et al., 2015; Ohmura, 2014; L'Ecuyer et al., 2015), the principle framework is well established since more than 100 years. Figure 1.1 shows the schematic representation of the global energy balance of Wild et al. (2013).

In the framework of the global energy balance, the top-of-the-atmosphere (TOA) is regarded as the system's boundary. At this boundary, radiation originating from the Sun reaches the Earth's climate system. This incoming shortwave (SW) radiation at TOA ( $I_t^\downarrow$ ) enters the climate system and penetrates the atmosphere. During its path through the atmosphere, the radiation is scattered, absorbed or transmitted by the optically thick atmosphere. Eventually, a major part of the SW radiation reaches the Earth's surface ( $I_s^\downarrow$ ), where it is partly absorbed and reflected. As a whole, SW radiation reaching the Earth's TOA is either absorbed in the atmosphere ( $A_a$ ), absorbed at the surface ( $A_s$ ), or reflected back to space ( $I_t^\uparrow$ ). The amount of radiation which is not reflected back to space and stays in the climate system – the TOA net SW radiation ( $I_t^n = I_t^\downarrow - I_t^\uparrow$ ) – and its partitioning into atmospheric and surface absorption ( $I_t^n = A_a + A_s$ ), heats the planet, and drives the Earth's climate system.

The Earth and its climate system lose energy through emission of longwave (LW) radiation to space. A substantial part of the LW radiation is, however, absorbed and reemitted in all directions in the atmosphere by various gases. The reemitted radiation results in a substantial LW downward flux at the surface that is typically referred to as the greenhouse effect. The residual between shortwave absorbed and net longwave radiation (upward minus downward LW flux) at the surface determines the amount of energy which is available for the two turbulent heat fluxes – the sensible and latent heat fluxes – which transport energy from the surface into the atmosphere.

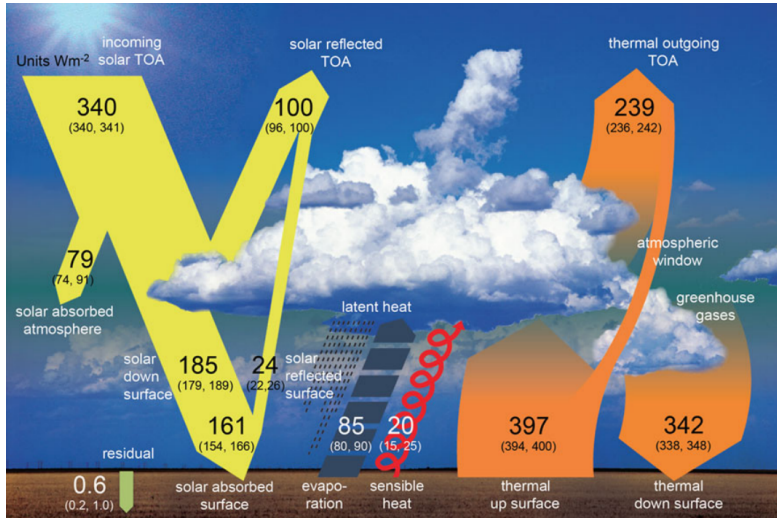


**Figure 1.1:** Schematic diagram of the global energy balance from Wild et al. (2013). Yellow arrows indicate shortwave fluxes, orange arrows indicate longwave fluxes. Units are in  $W/m^2$ .

However, due to anthropogenic emission of greenhouse gases and the associated reduction in TOA outgoing LW radiation, imbalances in the TOA and surface energy balances occur which lead to accumulation of energy in the climate system. Most of the surplus of energy is accumulated in the oceans. The remaining part is melting the cryosphere, heating soils, and the atmosphere and is leading to globally rising temperatures (IPCC, 2013).

### 1.1.1 Current best estimates of the shortwave fluxes

Over the past decades, high-quality space born top-of-the-atmosphere flux observations became available. Today, incoming solar radiation at the TOA is the most accurately known and stable flux of the energy balance (Stephens et al., 2012). Since 1978, the spatially- and spectrally integrated radiant energy coming from the Sun and reaching the Earth's TOA is continuously measured from space (Kopp, 2016). Figure 1.2 shows the spectral irradiance of the Sun at the TOA and at the surface, as well as the Planck spectrum for a blackbody with temperature  $T=5785K$ . Most recent measurements by the Total Irradiance Monitor (TIM) instrument of the Solar Radiation and Climate Experiment (SORCE) provide a value for the total solar irradiance of  $1360.8 \pm 0.5 W/m^2$  during solar minimum and normalized to one astronomical unit (Kopp and Lean, 2011). Considering that the Earth is an oblate spheroid and that its declination angle and the Earth-Sun distance have annual cycles, the value of the total solar irradiance at TOA has to be divided by the factor 4.0034 (instead of 4, when assuming that the Earth is a sphere) to obtain the global annual mean TOA incoming flux (Loeb et al.,

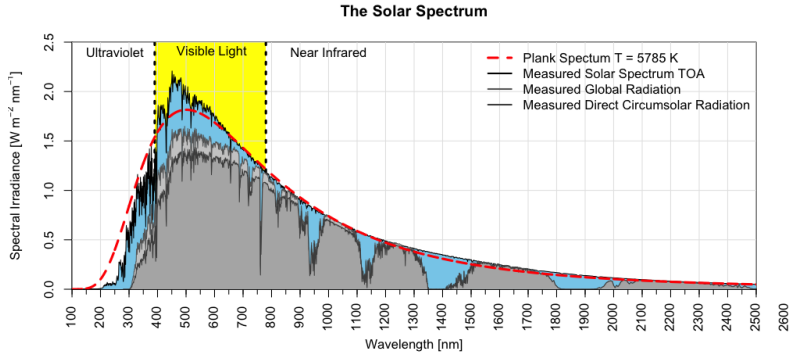


**Figure 1.2:** *The Solar Spectrum: blackbody, top of the atmosphere, global and direct-circumsolar radiation. Datasource: Gueymard (2004); Image source: Schwarz (2015)*

2009). This leads to the currently most accurate value for the global annual mean incoming TOA radiation during solar minimum of  $339.9\text{W}/\text{m}^2$  (e.g., Stephens et al., 2012).

Thanks to the Earth Radiation Budget Experiment (ERBE, Barkstrom 1984) and the Earth's Radiant Energy System (CERES, Wielicki et al. 1996) satellite missions, also the TOA reflected shortwave flux is known today with unprecedented accuracy. Section 1.5.1 provides a more detailed description of these dataset. The most recent published estimate based on the most advanced CERES data (Loeb et al., 2017) suggests a global mean TOA shortwave reflected flux of  $99.1\text{W}/\text{m}^2$ . Taking together the incoming and reflected SW TOA fluxes, the current best estimate for the planetary albedo is 0.292 (Stephens et al., 2015). Altogether, the global annual mean TOA shortwave fluxes are known today with very high accuracy. However, satellite measurements are not yet accurate enough to allow a direct estimation of the Earth Imbalance at TOA (Loeb, 2018).

At the surface, the most robust way to obtain surface downwelling shortwave radiation is by using in-situ pyranometer observations. Section 1.5.2 gives an overview of the measurements and several observational networks. In contrast to the space-born observations, in-situ observations are spatially scarce, which hampers the estimation of a global annual mean value. By combining in-situ measurements of surfaces solar radiation with state-of-the-art global climate models, Wild et al. (2013) computed the best estimate global mean value for surface downward solar radiation of  $185\text{W}/\text{m}^2$  (with a conservative uncertainty range of  $179\text{--}189\text{W}/\text{m}^2$ ). Globally averaged, about 13% of the surface solar radiation are reflected at the surface (Trenberth et al., 2009; Wild et al., 2013).

The amount of shortwave radiation absorbed in the atmosphere is typically calculated as a residual between the global annual mean SW TOA net and the surface absorbed SW flux (e.g., Wild et al., 2013). Recently Hakuba et al. (2014b) used an observation-based approach

and estimated shortwave atmospheric absorption directly from European in-situ surface solar radiation observations and colocated satellite observations of the SW TOA net flux and albedo. They found that  $23\pm 1\%$  of the TOA incoming shortwave radiation is absorbed in the atmosphere. Hakuba et al. (2016) confirmed this estimate for the *fractional* atmospheric shortwave absorption in a near-global assessment.

As this thesis' focus is on the shortwave fluxes of the energy balance, we do not review best estimates for the other fluxes of the energy balance. For this we refer to Ramanathan (1987), Kiehl and Trenberth (1997), Stephens et al. (2012), Trenberth et al. (2009), Wild et al. (2015); Ohmura (2014) and L'Ecuyer et al. (2015).

### 1.1.2 Regional differences

The global energy balance describes the climatological global and annual mean energy fluxes in the climate system. Its mean state is well known. This global and annual mean perspective is, however, only a simplified view of the Earth's energy balance as regional differences in the fluxes occur. These differences are crucial for climate and weather. They depend on how the energy entering the climate system is partitioned in space, time, and among physical processes.

Due to the Earth's shape,  $I_t^\downarrow$  depends on the cosine of the geographic latitude according to Lambert's cosine-law,  $I_t^\downarrow(\theta) = I_t^\downarrow \cos(\theta)$ . So naturally, at the equator, a lot more energy is entering the system than at higher latitudes. This latitudinal dependence is visible in all shortwave fluxes, as shown in Figure A.1 in the Appendix A.1. The figure gives an overview of the spatial differences and zonal means in the annual mean shortwave fluxes calculated from the CERES-EBAF data set (see Section 1.5.1 for the data description). These latitudinal gradients in radiative fluxes lead to temperature differences between the equator and the poles, which trigger the balancing wind systems known as the global circulation system.

Besides this prevailing latitudinal dependence, regional differences in the partitioning of radiation occur within the climate system. They, however, depend on the intrinsic optical properties of the atmosphere and the surface. These properties are determined by different climate factors, such as the surface altitude, the surface albedo, the amount and the distribution of clouds, water vapor and aerosol, as further detailed in Section 1.3.

Interestingly, Hakuba et al. (2016) showed that the fraction of incoming radiation at TOA which is absorbed in the atmosphere is to a large degree latitudinal invariant with a *fractional* atmospheric absorption of  $23\pm 2\%$ . This feature is clearly visible in the zonal averages shown in Figure A.1h. The figure shows that the (zonally averaged) latitudinal changes in TOA reflected and surface absorbed radiation are such that the fractional shortwave absorption basically stays constant.

Besides spatial differences, also temporal changes in the energy balance occur, as discussed in more detail in Section 1.2.



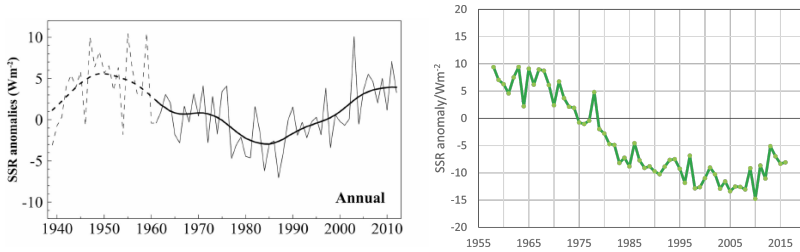


**Figure 1.3:** Long term annual mean surface solar radiation records for Europe (left) and China (right) from Sanchez-Lorenzo et al. (2015) and (adjusted) from Yang et al. (2018), respectively. Each plot shows a composite time series from multiple station records in the respective region.

## 1.2 Temporal variations in the energy balance

### 1.2.1 Multidecadal changes in surface solar radiation: from global dimming to global brightening and beyond

Several pioneering studies reported observational evidence that the amount of surface solar radiation reaching the Earth's surface was not constant over time but declined since the 1950s (Ohmura and Lang, 1989; Russak, 1990; Dutton et al., 1991; Stanhill and Moreshet, 1992a,b; Liepert et al., 1994; Stanhill and Moreshet, 1994). Soon, the reduction in surface solar radiation was confirmed by several studies as summarized in the review paper by Wild (2009a). The term *dimming* was first used in Stanhill and Moreshet (1994) in the context of a reduction of surface solar radiation. Later, the review paper of Stanhill and Cohen (2001) coined the term *global dimming* and summarized the observational evidence for a reduction in surface solar radiation. Note, that the word "*global*" refers to the reduction in *global* radiation (i.e., the sum of direct and diffuse radiation at the surface) and does not necessarily describe the spatial scale of the phenomenon (Wild, 2009a).

Using updated surface solar radiation records, Wild et al. (2005) showed that the widespread dimming leveled off and even turned to an increase in surface solar radiation since the mid 1990s. They termed this increase "*global brightening*". This brightening trend was confirmed by several studies across different regions as summarized in Wild (2009a). Only in India continued dimming was reported (Kumari et al., 2007). More recent assessments for the US (Augustine and Dutton, 2013) and Europe (Sanchez-Lorenzo et al., 2015) point to a continued brightening with a tendency to stabilization of surface solar radiation levels in the early 21st century. A recent reassessment of Chinese data showed that the dimming in China leveled off in the 1990s, but only turned into a brightening in 2005 (Yang et al., 2018). Figure 1.3 shows the surface solar radiation records from Sanchez-Lorenzo et al. (2015) and Yang et al. (2018).

Although global climate models typically are not able to reproduced the full extent of past

variations of surface solar radiation (Wild, 2009b), their projections suggest that surface solar radiation will continue to undergo decadal variations also in the future. Haywood et al. (2011) showed that in a future warmer climate surface solar radiation will decrease because of increasing water vapor and the corresponding increase in atmospheric absorption. It was also shown that although global warming is triggered by increasing greenhouse gas emissions and associated decreasing outgoing longwave emissions at TOA, increasing shortwave absorption in the climate system will – from an energy balance perspective – be the major energy source for global warming (Trenberth and Fasullo, 2009; Donohoe et al., 2014). Accountable for this are different feedback processes which alter the shortwave energy balance. Following Trenberth and Fasullo (2009) and Donohoe et al. (2014) in a warmer climate (i) fewer clouds are present and less shortwave radiation is reflected by the bright surfaces of clouds (i.e., SW cloud feedback); (ii) less of the Earth’s surface will be covered with (sea-) ice and snow which will reduce the Earth’s surface albedo and lead to more surface absorption (i.e., the ice-albedo feedback); (iii) increasing water vapor concentrations (i.e., water vapor feedback) will increase atmospheric shortwave absorption.

These decadal changes in the  $I_s^\downarrow$  have a tremendous impact on the climate system and were reported to affect surface warming rates, the hydrological cycle, the cryosphere, as well as the biosphere (Wild, 2009a, and references therein). However, the outlined changes in surface shortwave radiation have not yet been viewed in an observation-based shortwave energy balance perspective. In such a perspective – according to the principle of energy conservation which constitutes the very fundament of the energy balance as such – changes in any of the shortwave fluxes (such as the observed one in surface radiation) must go along with changes in at least one of the other shortwave fluxes. In this thesis, we aim to fill this knowledge gap and study which of the shortwave fluxes in the energy balance changed by how much during the dimming and brightening phenomenon.

### 1.2.2 Seasonal cycles in the shortwave energy balance

Besides these decadal changes in the energy balance, also large seasonal cycles occur. Due to the Earth’s shape, rotation, tilt of the rotational axis, and the eccentricity of the Earth’s orbit around the Sun, large seasonal cycles in the amount and geographic distribution of solar insolation occur. These variations play a key role in the distribution of energy in the climate system and ultimately drive the seasonality of the Earth’s general circulation systems, climate and weather.

However, Hakuba et al. (2014b) found for Europe that the fractional atmospheric shortwave absorption does also not substantially vary with season. An astonishing result, when considering that various climate elements which potentially influence the shortwave radiative fluxes (see Section 1.3) have notable annual cycles. Given the robustness of fractional shortwave absorption, Hakuba et al. (2014b) even suggest that the fractional atmospheric absorption might serve as a first-order validation of climate models.

As the focus of this thesis is on temporal variations in the climate system, we further investigate the robustness of atmospheric absorption against seasonal variations beyond Europe.

### 1.3 What factors determine the shortwave fluxes of the global energy balance?

The above-described variations naturally raise the questions which process ultimately govern the observed changes. However, the scientific community could not yet find consensus about this. Next, we will briefly review the prime candidates which have been proposed as potential causes of temporal variation in the shortwave energy balance.

#### 1.3.1 External forcing: changes in incoming solar radiation

Temporal variations in incoming shortwave radiation at TOA are induced either due to variations in the Earth's orbital parameters or by intrinsic variations of the Sun's radiative output (Kopp, 2016). Since changes in the Earth's orbital parameters, known as Milankovitch cycles (Hays et al., 1976), vary on paleoclimatological time scales of thousands of years, their impact on the climatological time scales considered here is negligible.

The most important variations in the Sun's radiative output for the time scales considered here are the daily to weekly variations in the photospheric magnetic activity and the variations due to the 11-year solar cycle. However, both only impinge changes in the total solar irradiance on the order of  $\sim 0.1\%$  (Fröhlich, 2006; Kopp, 2016). Figure 1.4 shows a composed time series for total solar irradiance of the Physikalisch-Meteorologisches Observatorium Davos (PMOD, Fröhlich 2006). In Appendix A.3 the original time series are shown.

Therefore, the incoming shortwave flux at TOA is the temporally most invariant flux in the energy balance and cannot serve as an explanation for the above described decadal variations (Wild, 2009a). Consequently, changes intrinsic to the climate system must be responsible for these variations.

#### 1.3.2 Internal forcing: potential explanatory variables within the climate system

In order to be able to describe the factors determining the shortwave flows in the simplest possible way, it has proven to be useful to apply a simple model in which the atmosphere is described as a single absorbing and transmitting layer above the Earth's surface. Following Stephens et al. (2015), and as shown in Appendix A.2, the systems absorption, reflection, and transmittance itself are governed by only three inherent variables: atmospheric reflection ( $r$ ), atmospheric transmission ( $t$ ), and the surface albedo ( $\alpha$ ). Note, that the inherent atmospheric reflection, transmission, and absorption ( $a$ ) add up to one ( $r+t+a=1$ ) so the inherent atmospheric absorption can be easily diagnosed from the reflection and transmission.

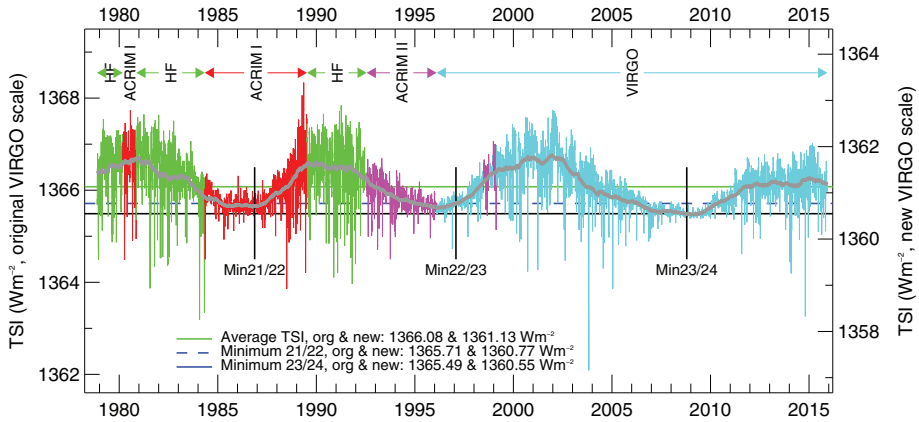


**Figure 1.4:** Total solar irradiance composite of the Physikalisch-Meteorologisches Observatorium Davos (PMOD, Fröhlich 2006) since 1978 based on different data sets (indicated by colors) from Kopp (2016). The right-hand scale indicates the currently accepted absolute value for the total solar irradiance (Kopp and Lean, 2011).

## Surface albedo

The surface albedo can impact Earth's energy balance as it controls which fraction of the surface radiation is absorbed at the surface. Bright surfaces, like snow- or ice-covered surfaces, reflect most of the incident radiation, while dark surfaces like oceans or land surfaces, absorb most of the radiation. The surface albedo, therefore, regulates the surface shortwave energy uptake. The global mean surface albedo is strongly dependent on the global mean surface temperatures (e.g., Curry et al., 1995). At higher temperature, snow and ice retreats and bright surfaces shrink on the expense of darker ones, which leads to higher surface absorption and, eventually, to higher temperatures. Wild et al. (2015) provide an estimate of 0.135 for the global mean surface albedo.

## Clouds

The presence or absence of clouds has a strong impact on the energy balance as they influence the atmosphere's reflectivity and transmissivity. A convenient concept to quantify the effect of clouds is to consider the difference between all-sky fluxes (i.e., radiative fluxes when clouds are present) and clear-sky fluxes (i.e., radiative fluxes when clouds are absent) (Harrison et al., 1990; Stephens et al., 2015). The influence of clouds on the shortwave fluxes is complex and heavily depends on the clouds structure and microphysics (e.g. Stephens and Tsay, 1990). Wild et al. (2018) provide an assessment based on a combination of observations and climate models about the influence of clouds on the whole energy balance. They quantify the effect of clouds on TOA shortwave radiation to  $-47\text{W}/\text{m}^2$ , on atmospheric absorption to  $+7\text{W}/\text{m}^2$ , and

on surface radiation to  $-54\text{W/m}^2$ . Noteworthy is the fact that the effect of clouds at the TOA and the surface is almost a magnitude larger than their effect on atmospheric absorption.

### Water vapor and aerosols

Considering a cloud-free atmosphere, the atmosphere's shortwave absorptance, transmittance, and reflectance are governed by the amount of radiatively active species such as water vapor and aerosols within the atmosphere. Radiation transfer equations can be used to describe the attenuation of radiation within the atmosphere (e.g., Liou, 2002; Seinfeld and Pandis, 2006): Following the Beer-Lambert-Bouguer law, the transmittance of the (cloud-free) atmosphere depends exponentially on the optical depth of the atmosphere. The optical depth of the atmosphere depends on the amount and optical properties of the abundant species (e.g. Takemura et al., 2000).

Water vapor is the most important gaseous absorber in the atmosphere and is responsible for most of the clear-sky atmospheric absorption (Kiehl and Trenberth, 1997; Shine et al., 2012). The water vapor absorption spectrum is a direct result of the asymmetric bent triatomic atomic structure of the water vapor molecule. Because of this, it can vibrate in three different modes and very efficiently absorbs radiation in the near infrared region (Liou, 2002). Water vapor absorption, however, does not scale linearly with its abundance in the atmosphere but follows a logarithmic relation (Yamamoto and Onishi, 1952).

The direct effect of aerosols on the energy balance depends on whether the aerosol species tends to primarily scatter or absorb radiation (e.g., Seinfeld and Pandis, 2006). While primarily absorbing species lead to a positive TOA forcing (i.e., more energy stays in the system), aerosols which mainly scatter radiation lead to a negative TOA forcing (i.e., less energy stays in the system). At the surface, the forcing is negative for all aerosol species. For the atmosphere the opposite is true. The most important aerosol species in the atmosphere are black carbon, organic carbon, sulfate aerosols, sea salt, and mineral dust (e.g., Takemura et al., 2002). While black carbon, organic carbon and sulfate are mostly related to anthropogenic sources, sea salt and mineral dust are related to natural sources. Because of their intrinsic optical properties, sea salt, dust, and sulfate aerosol mostly scatter radiation, while black carbon mostly absorbs radiation (e.g Takemura et al., 2000).

Aerosols, however, also influence the energy balance and climate indirectly by altering clouds through different pathways (Lohmann and Feichter, 2005). Aerosols in clouds lead to more and smaller cloud droplets. Due to these smaller cloud droplets, the clouds reflect solar radiation more efficiently as the cloud albedo gets higher (Twomey effect, Twomey 1959). Due to the smaller cloud droplets also the cloud's precipitation efficiency decreases which extends the cloud's lifetime (Albrecht, 1989). For the other indirect aerosol effects we refer to the review of Lohmann and Feichter (2005).

## 1.4 An observational approach

In this thesis we aim to study temporal variations of the shortwave fluxes of the energy balance. To do so, we follow up on Hakuba et al. (2016) and combine the most robust currently available high-quality observational data to derive the partitioning of shortwave radiation according to the following equations:

$$I_t^n = I_t^\downarrow - I_t^\uparrow \quad (1.1)$$

$$A_s = I_s^\downarrow \cdot (1 - \alpha) \quad (1.2)$$

$$A_a = I_t^n - A_s \quad (1.3)$$

We use long-term colocated observation of TOA radiative fluxes from satellite observations (see Section 1.5.1), in-situ surface solar radiation observations from different observation networks (see Section 1.5.2), and satellite-derived surface albedo estimates (see Section 1.5.2) to study the temporal variations in the energy balance outlined above. Since this approach requires that we combine in-situ point observations with gridded satellite data products, methodological uncertainties which arise due to this approach must be addressed. More specifically, it must be inferred whether and to which extent the point observations are representative of their larger surroundings.

This issue is of great concern across different research fields in atmospheric science (e.g., Nappo et al., 1982; Dutton et al., 2012; Schutgens et al., 2016a,b; Bulgin et al., 2016; Boersma et al., 2016; Schutgens et al., 2017) and different aspects of representativeness have already been studied for the specific case of surface radiation (Long and Ackerman, 1995; Barnett et al., 1998; Zelenka et al., 1999; Li et al., 2005; Deneke et al., 2009; Journée et al., 2012; Hakuba et al., 2013a, 2014a; Huang et al., 2016; Lohmann et al., 2016; Schutgens et al., 2016b; Madhavan et al., 2017).

However, the specific question, whether a monthly mean time series of surface solar radiation from in-situ observations is representative of the whole area covered by the CERES satellite pixels, is not yet answered. In two chapters of this thesis (Chapter 2 and Chapter 3) we will address this key issue.

## 1.5 Main Datasets

This section provides an overview of the main data sets used in this thesis. Figure 1.5 shows a schematic about the temporal coverage of the data sets over time. The individual data sets are discussed below.

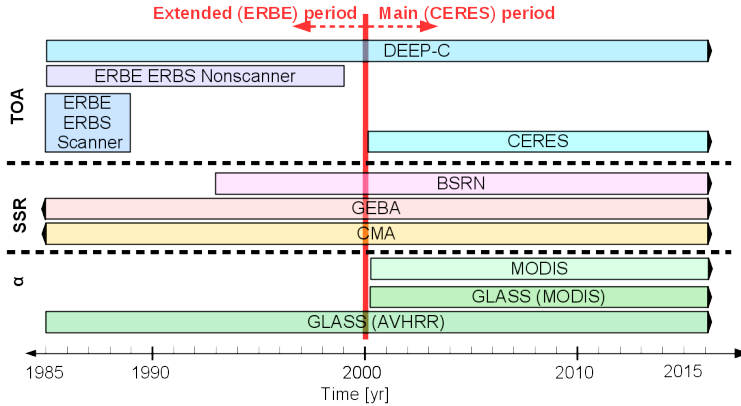


Figure 1.5: Main datasets used in this thesis and their temporal coverage.

### 1.5.1 Top-of-the-atmosphere fluxes

#### The Clouds and the Earth’s Radiant Energy System (CERES) data

The primary data set for the TOA fluxes is the Clouds and the Earth’s Radiant Energy System (CERES) data. The data set is available since 03/2000 in monthly mean temporal- and one-degree spatial resolution (Wielicki et al., 1996). The CERES data sets build on satellite observations (see Figure 1.6a) of broadband radiometer measurements measured with the CERES instrument (see Figure 1.6b,c). Currently, six in-orbit satellites carry CERES instruments (see Figure 1.6d). The CERES sensor consists of three radiometers which measure the shortwave ( $0.2\text{--}5\mu\text{m}$ ), thermal window ( $8\text{--}12\mu\text{m}$ ) and total ( $0.2\text{--}100\mu\text{m}$ ) spectral region.

Each radiometer of the sensor consists of an active and a passive thermistor bolometer detector which are both placed in a bridge current on a common heat sink. When the active detector absorbs energy, the resistance of the thermistor material decreases. This causes a voltage difference in the bridge that can be processed as a signal voltage which can be used to infer filtered radiances (Cooper et al., 1992; Wielicki et al., 1996). The imperfect spectral response of the filtered irradiance is corrected by converting it into unfiltered irradiances (Loeb et al., 2001, 2016). These instantaneous unfiltered irradiances are then further processed in several steps, as described in (Loeb et al., 2009). The resulting final CERES TOA flux product has a one-degree spatial, and monthly mean temporal resolution.

Additionally, the CERES’ energy balanced and filled (EBAF) product is gap filled and adjusted within its uncertainty range, such that the shortwave and longwave TOA fluxes are consistent with in-situ observations of Earth’s energy imbalance (Loeb et al., 2017).

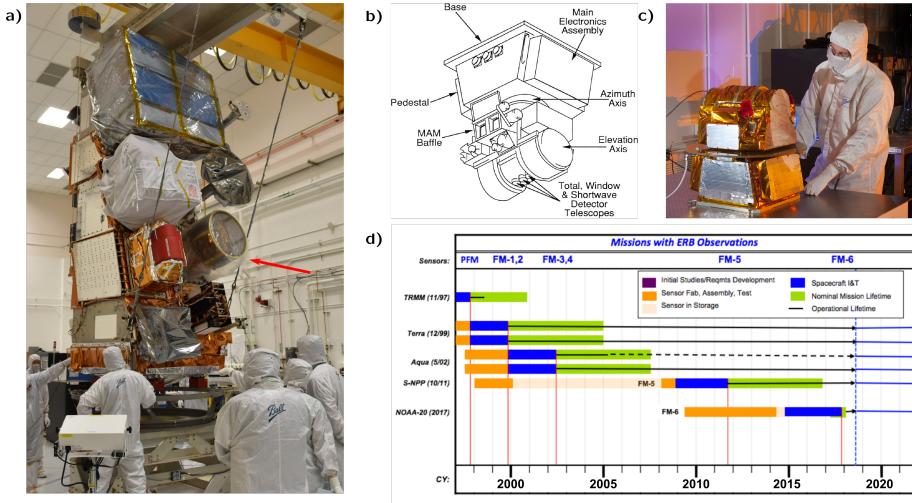


**Figure 1.6:** The CERES mission. (a) shows the Joint Polar Satellite System (JPSS)-1 with a red arrow pointing to the mounted CERES instrument (image source: NASA, [https://www.jpss.noaa.gov/satellite\\_gallery.html#gallery-23](https://www.jpss.noaa.gov/satellite_gallery.html#gallery-23), February 2019). (b) shows a schematic of the CERES instrument (Image Source: Wielicki et al. 1996). (c) shows the CERES instrument (image source:<https://ceres.larc.nasa.gov/jpss1/lrc-ceres-fm6.jpg>, February 2019). (d) shows all satellite missions which carry CERES instruments and their timeline (Loeb, 2018).

## The ERBE data and the DEEP-C reconstruction

The temporal variations we are aiming to examine appear on decadal time scales and require long and homogeneous data sets. Since the CERES observations only started in 03/2000 other satellite data sets are also taken into account.

The Earth Radiation Budget Experiment (ERBE, Barkstrom 1984) collected TOA flux data from 1985 to 1999 with the Nonscanner Wide Field of View (WFOV) instrument onboard of the Earth Radiation Budget Satellite (ERBS). Although the data has a much coarser spatial and temporal resolution than the CERES data, it provides a valuable long term record for shortwave TOA fluxes (Wong et al., 2006).

Within the Diagnosing Earth's Energy Pathways in the Climate system (DEEP-C) project, the CERES and ERBE satellite data records, atmospheric reanalysis, and climate model simulations were used to reconstruct a homogeneous TOA flux record from 1985 up to present (Allan et al., 2014; Liu et al., 2017). We will use this data set in Chapter 5 to contrast long term trends at the surface with the TOA time series.



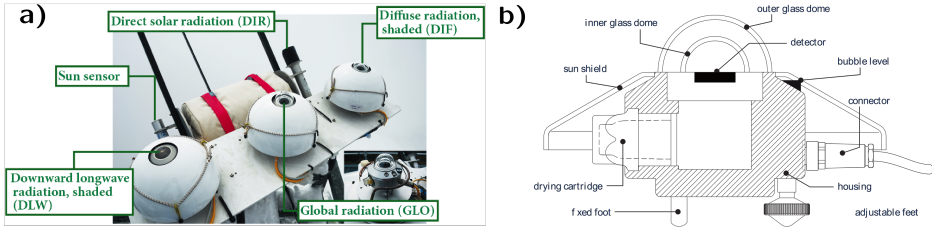


**Figure 1.7:** (a) Typical arrangement of an in-situ surface radiation measurement here shown for a typical site of the Austrian Radiation Network (ARAD; Olefs et al. 2016) and (b) a schematic of a thermopile Kipp & Zonen CM22 pyranometer (Kipp&Zonen, 2016) .

## 1.5.2 Surface data

### In-situ surface solar radiation observations

The most robust and precise way to determine surface solar radiation is by using surface in-situ observations. Such observations are typically conducted with thermopile pyranometers (see Figure 1.7). These instruments measure broadband radiation using the thermoelectric detection principle (e.g. Beaubien et al., 1998): radiation which enters the sensor is absorbed by a horizontal black surface, which is thereby heated. Comparing the temperature difference between the heated black surface (hot junction) and a reference (cold junction) allows to infer the incoming radiant energy. The sensors are protected against environmental influences by single or double glass domes. The transmissivity of the glass domes limits the spectral response of the instrument to 200nm to  $3\mu\text{m}$ . Therefore, the dome also ensures that only shortwave radiation is measured.

The surface solar radiation (among experimentalists also referred to as global radiation) is the sum of irradiance of the direct sunbeam and the diffuse irradiance (e.g. Wild, 2009a). It can either be measured with one single pyranometer or with a combined method. With a single pyranometer, direct and diffuse radiation are measured at the same time. For the combined method, the direct sunbeam and the diffuse radiation are measured separately with two different instruments. The diffuse radiation is measured with a shaded pyranometer. The shading ensures that the direct beam is not measured by the pyranometer, as the direct beam is measured separately with a pyrliometer. A suntracker ensures that the pyrliometer always points directly to the Sun and that the pyrliometer is shaded correctly. The later setup is referred to as the summation method because surface solar radiation is computed from the sum of direct and diffuse irradiance. This summation method is preferred because uncertainties related to the cosine response of pyranometers are avoided Dutton et al. (2012).

In this thesis we utilize long term surface solar radiation observations from several different data sources:

**The Baseline Surface Radiation Network (BSRN):** The BSRN was established in 1992 and currently measures and stores high quality radiation data at more than 60 stations worldwide (Driemel et al., 2018). The network was set up to serve as a benchmark for satellite radiometry and climate models, and to detect long-term variation of the surface irradiances (Ohmura et al., 1998).

**The Global Energy Balance Archive (GEBA):** The GEBA database systematically collects and stores surface radiation data from various sources, as in detail described in Wild et al. (2017), and achieved to collect data from more than 2500 locations in 2017.

**The Chinese Meteorological Administration (CMA):** The CMA compiles radiation data which is routinely measured at several Chinese sites using pyranometers. We use data from the CMA which has been homogenized by Yang et al. (2018).

**The Global Tropical Moored Buoy Array (GT MBA):** The GT MBA program of the Pacific Marine Environmental Laboratory (PMEL) of the National Oceanic and Atmospheric Administration (NOAA) in the US provides surface radiation data from three different buoy arrays located in the tropical Pacific (Tropical Atmosphere Ocean / Triangle Trans-Ocean Buoy Network in the Pacific; TOA/TRITON; McPhaden et al. 1998), the tropical Atlantic (Prediction and Research Moored Array in the Atlantic; PIRATA; Servain et al. 1998), and the tropical Indian ocean (Research Moored Array for African-Asian-Australian Monsoon Analysis and Prediction in the Indian Ocean; RAMA; McPhaden et al. 2009), respectively.

## Surface albedo

In order to calculate the surface absorbed flux, the surface albedo must be known. The currently most advanced albedo data is the albedo product from the Moderate-resolution Imaging Spectrometer (MODIS) onboard of the NASA satellites TERRA and AQUA which are available since 03/2000. The accuracy of the MODIS albedo data has proven to be well within 5% Schaaf et al. (2010). The MODIS data uses a semiempirical kernel-driven bidirectional reflectance model in combination with the observed multispectral data to derive land surface albedo (Schaaf et al., 2010). The latest MODIS product (Version 6) temporally interpolates between the 16-day observation period of the satellites to provide daily albedo values with a  $0.05^\circ$  resolution (Schaaf and Wang, 2015).

For albedo values before 2000 we rely on the Global Land Surface Satellite (GLASS) data-set (Liang et al., 2013). The GLASS data computes albedo from Advanced Very High Resolution Radiometer (AVHRR) and MODIS observation. The AVHRR based GLASS albedo is available from 1981 onwards.

## 1.6 Objectives and outline

The overarching objective of this thesis is to study the outlined aspects of temporal variations (Section 1.2) of the shortwave fluxes in the energy balance framework. From the observational perspective, the most robust way to infer the partitioning of shortwave radiant energy in the framework of the energy balance is by combining flux measurements from the top-of-the-atmosphere and the surface. A key prerequisite for such an observational approach is to infer the spatiotemporal representativeness of surface in-situ observations and to quantify potential associated uncertainties which arise due to such an approach.

The main research questions which are addressed in this thesis are:

1. Are records of monthly mean surface solar radiation from in-situ measurements representative of their larger surrounding in order to facilitate their combination with the gridded TOA fluxes within reasonable uncertainties?
2. Are there any regions where direct fractional atmospheric shortwave absorption has notable annual cycles and what are the main reasons for the presence or absence of such annual cycles?
3. Which shortwave fluxes in the energy balance change along with the observed surface flux changes that occur during the dimming and brightening phenomenon and can we learn something about the very origin of the phenomenon itself in the energy balance perspective?

These research questions are addressed in the chapters of this thesis which are organized as follows:

### **Chapter 1: Introduction**

The first chapter of this thesis provides a brief introduction into the energy balance framework and discusses regional and temporal variations in the energy balance and what might cause these variations. Further, the observational approach as well as the main data sets, which are used in this thesis, are introduced in a general way.

### **Chapter 2: Spatial representativeness of surface-measured variations of downward solar radiation**

The second chapter of this thesis infers the spatiotemporal representativeness of European surface solar radiation observations. The chapter builds upon robust in-situ observations as well as high-resolution satellite-derived surface solar radiation estimates to estimate the distance up to which a monthly surface solar radiation record can be considered to be representative.

### **Chapter 3: From point to area: worldwide assessment of the representativeness of monthly surface solar radiation records**

In this chapter, we infer, if there are regional differences in the spatiotemporal representativeness of point observation on a near-global scale using high-resolution satellite-derived surface solar radiation.

**Chapter 4: The annual cycle of fractional atmospheric shortwave absorption in observations and models: spatial structure, magnitude and timing**

This chapter infers if any region with notable annual cycles in fractional atmospheric shortwave absorption exists. The chapter is based on satellite-derived TOA and surface fluxes to achieve a near-global coverage. The results are contrasted to in-situ observations.

**Chapter 5: Changes in atmospheric shortwave absorption as major driver of dimming and brightening**

In this chapter, we ask which of the shortwave fluxes of the energy balance components change along with the observed surface trends, known as the dimming and brightening phenomenon. The chapter is based on colocated in-situ surface solar radiation observations, gridded TOA fluxes and surface albedo. We focus on two regions with, particularly dense surface solar radiation station networks.

**Chapter 6: Summary, conclusions, and outlook** In the final chapter of this thesis, we provide an extended summary of the main finding of this thesis and discuss their broader implications. We highlight some aspects which go beyond our own research objectives and might trigger future investigations.

# Spatial representativeness of surface-measured variations of downward solar radiation

M. Schwarz<sup>1</sup>, D. Folini<sup>1</sup>, M. Z. Hakuba<sup>2,3</sup>, M. Wild<sup>1</sup>

Accepted article

Journal of Geophysical Research: Atmospheres

Volume 122, Issue 24

DOI: 10.1002/2017JD027261

ISSN: 2169-8996

## Key points:

- Point observations of variations in surface-measured downward solar radiation are largely representative of their larger surroundings
- Correlations between sites decrease linearly with increasing distance
- Errors due to spatial sampling are of the same magnitude as measurement errors

1. Institute for Atmospheric and Climate Science, ETH Zurich, CH-8092 Zurich, Switzerland.
2. Department of Atmospheric Sciences, Colorado State University, Ft. Collins, CO 80523, USA
3. Jet Propulsion Laboratory, California Institute of Technology, Pasadena, CA 91109, USA

## Abstract

*When using time series of ground-based surface solar radiation (SSR) measurements in combination with gridded data, the spatial and temporal representativeness of the point observations must be considered. We use SSR data from surface observations and high-resolution (0.05°) satellite-derived data to infer the spatiotemporal representativeness of observations for monthly and longer time scales in Europe. The correlation analysis shows that the squared correlation coefficients ( $R^2$ ) between SSR times series decrease linearly with increasing distance between the surface observations. For deseasonalized monthly mean time series,  $R^2$  ranges from 0.85 for distances up to 25 km between the stations, to 0.25 at distances of 500 km. A decorrelation length (i.e., the e-folding distance of  $R^2$ ) on the order of 400 km (with spread of 100–600 km) was found.  $R^2$  from correlations between point observations and collocated grid box area means determined from satellite data were found to be 0.80 for a 1° grid. To quantify the error which arises when using a point observation as a surrogate for the area mean SSR of larger surroundings we calculated a spatial sampling error (SSE) for a 1° grid of 8(3)W/m<sup>2</sup> for monthly (annual) time series. The SSE based on a 1° grid, therefore, is of the same magnitude as the measurement uncertainty. The analysis generally reveals that monthly mean (or longer temporally aggregated) point observations of SSR capture the larger-scale variability well. This finding shows that comparing time series of SSR measurements with gridded data is feasible for those time scales.*

## 2.1 Introduction

The spatial and temporal representativeness of measured geophysical state variables is of great concern across different research fields in atmospheric science (e.g., Nappo et al., 1982; Dutton et al., 2012; Schutgens et al., 2016a,b; Bulgin et al., 2016; Boersma et al., 2016; Schutgens et al., 2017). This is also true for ground-based downward solar radiation (often referred to as surface solar radiation, SSR) measurements.

As a crucial energy flux in the global energy balance, it is of great concern to determine SSR with high accuracy on different spatial and temporal time scales. SSR can be measured directly on the Earth's surface using station-based pyranometer and pyrliometer observations. For these station-based measurements, it is a priori not clear whether and to which extent they are representative of their larger surroundings. This issue is particularly important when using station-based SSR measurements in combination with other climate data, as it is commonly done for satellite and model validation (e.g., Shuttleworth and Dickinson, 1989) and to derive radiation budgets (e.g., Hakuba et al., 2014b; Wild et al., 2015).

SSR (i.e., the sum of direct and diffuse solar radiation) varies on different scales in space and time depending on the local climatological and meteorological conditions. Cloud cover, cloud optical properties, water vapor, aerosols loading and types, topography, and surface albedo (due to multiple scattering of the reflected radiation) can alter SSR by changing the amount of direct and/or diffuse radiation (e.g., Hay, 1984; Long and Ackerman, 1995; Barnett et al., 1998; Solomon et al., 1998; Liepert and Tegen, 2002; Madhavan et al., 2017).

So far, the spatial characteristics of SSR-variability on subdaily or daily time scales (Long and Ackerman, 1995; Barnett et al., 1998; Zelenka et al., 1999; Journée et al., 2012; Madhavan et al., 2017) as well as the variability of SSR on multiannual mean (i.e., climatological) time scales (Li et al., 1995; Dutton et al., 2006; Hakuba et al., 2013a, 2014a) have been analyzed. Overall similar results have been found, which point to a general decrease of correlation between two measurements with increasing spatial distance between them. Moreover, it was noted that in complex topography representativeness seems to be lower than in more homogeneous terrain. In terms of scalability, Li et al. (2005) as well as Deneke et al. (2005) found that spatial representativeness generally increases with increasing averaging period. Additionally, a combination of SSR records from multiple colocated sites can decrease biases attributed to a lack of spatial representativeness (Barnett et al., 1998; Journée et al., 2012; Hakuba et al., 2013a). However, no general scaling relation for the representativeness of ground-based SSR observations is available.

Following up on the investigations of Hakuba et al. (2013a, 2014a) — who examined the representativeness of multiannual mean SSR values — the spatial representativeness of temporal variability of long-term surface SSR observations is investigated. This is done by analyzing monthly, seasonal and annual mean SSR time series measured during the period from 1983 to 2015 (see section 2.2).

The overall topic is addressed via the following specific questions: How does the correlation between two SSR time series change depending on the distance between the location of the SSR measurements? What other factors potentially affect the correlations? What is the correlation between a point observation and a colocated area mean time series? How does the position of the point observation within the corresponding area affect the correlation? What is a robust bias estimate when using a single surface observation as a proxy for SSR variations of a larger area?

One pending issue, which we will focus on in a future study, is to expand the climatological analysis of Hakuba et al. (2014b) and compute time series of absorption of shortwave radiation in a column of the atmosphere on monthly, seasonal and annual time scales. For that specific analysis, SSR from surface point observations has to be combined with gridded data. In terms of spatial resolution, the bottleneck for that analysis is the top of the atmosphere (TOA) net shortwave radiation data set from the Clouds and the Earth's Radiant Energy System (CERES) of the American National Aeronautics and Space Administration (NASA) with its  $1^\circ$  regular grid. We, therefore, use the CERES grid as the main reference grid of the upcoming analyses in this paper.

Section 2.2 gives an overview of the data and methods used in this paper. In section 2.3 all results are shown while the discussion of the results is given in section 2.4. The synthesis and conclusions are presented in section 2.5.

## 2.2 Data and Methods

SSR data from two origins, surface and satellite-derived observations, have been used. Since Europe has the worldwide highest SSR station density the focus of this work is on this area. An overview of the domain is given in Figure 2.1.

### 2.2.1 Satellite-Derived SSR: The SARA H Data Set

The Satellite Application Facility on Climate Monitoring (CM-SAF) is operated by the European Organisation for the Exploitation of Meteorological Satellites (EUMETSAT), which derives products from data obtained by the Meteosat satellites (Schmetz et al., 2002). The data set used in this study is provided by CM-SAF as a continuous data set of monthly mean incoming SSR covering the period from 1983 to 2015 (Surface Solar Radiation data set - Heliosat - Edition 2, hereafter called SARA H) (Müller et al., 2015a).

The SARA H data set is based on radiative transfer modeling and visible channel observations from the Meteosat Visible and the Infrared Imager (MVISIRI) on board the Meteosat first-generation satellites (Meteosat 2–7) and the Spinning Enhanced Visible and Infrared Imager (SEVIRI) onboard the Meteosat second-generation satellites (Meteosat 8–10) (Müller et al., 2015b). Due to geostationary orbit and the longitudinal position of the Meteosat satellites



around the zero meridian, the data set covers a disk region  $\pm 65^\circ$  in latitudinal and longitudinal direction with a very high spatial resolution of  $0.05^\circ$  which corresponds to a great-circle (orthodromic) distance on the Earth's surface of roughly 6 km. The footprint resolution of the raw data is 2.5 km and 3 km at the equator (around 7.5 km and 9 km at  $60^\circ\text{N}$ ) for the first- and second-generation Meteosat satellites, respectively (Schmetz et al., 2002). The final grid resolution of  $0.05^\circ$  was achieved by applying a nearest-neighbor interpolation method to the data at the end of the CM-SAF algorithm (see below). Because of the high spatial resolution, each pixel of the data set may be used as a surrogate for a surface observation. Therefore, we use the data as a proxy for the spatial variability of surface point observations.

We note that the SSR field most likely also shows some variations on distances below 6 km. However, Long and Ackerman (1995) showed that daily average SSR shows very high correlations ( $R^2 > 0.9$ ) for distances up to few tens of kilometers between the measurements sites. Moreover, Madhavan et al. (2017) showed that single SSR observations can already be considered to be representative for a surrounding of few kilometers when temporal averaging intervals are only a few hours. From that, and taking into account the finding from Li et al. (2005) and Deneke et al. (2005) that spatial representativeness generally increases with increasing averaging intervals, we argue that the spatial variability in the SSR field below 6 km is negligible for the time scales of interest in the present study.

The algorithm from CM-SAF to derive the SARA data set comprises two main segments: one segment incorporates the derivation of the normalized effective cloud albedo, which is obtained from direct satellite observations; the other segment consists of a look-up table based radiation transfer model (Posselt et al., 2012; Müller et al., 2015b). The radiation transfer modeling is used to calculate clear-sky irradiance for a variety of different atmospheric states. As input for the modeling the following data are used: (i) aerosol monthly climatologies obtained from the MACC-data set from the European Center for Medium Range Weather Forecast (ECMWF), (ii) monthly mean integrated water vapor from ERA-40 and ERA-interim reanalyses (Uppala et al., 2005; Dee et al., 2011), (iii) ozone climatological mean from the standard atmosphere and (vi) climatological surface albedo. The all-sky surface solar irradiance is estimated by multiplying the clear-sky irradiance with a clear-sky index. The latter is a function of the effective cloud albedo, which, in turn, is calculated from the visible channel observations of the Meteosat first- and second-generation satellites. The clear-sky index is defined (per individual pixel) as the fraction of reflected irradiance to a predefined maximum reflectance, whereby the clear-sky reflectance (which is estimated by a minimum approach during a time span of around one month) is subtracted from both quantities beforehand.

The monthly means are derived by averaging daily means, which themselves are computed from hourly means. The hourly means are computed by averaging over three observations per hour. The daily and monthly averages are computed only when a minimum of three hours per day and 10 days per month are available, respectively. A complete description

of the retrieval algorithm can be found in Müller et al. (2009, 2012, 2015b) and references therein. From examining the data coverage of the hourly SARA data we find that only 1% of all days have less than three hourly observations (and are therefore missing), only 1% of all days have between 3 and 10 hourly observations per day, and 3% of all days have between 10 and 15 hourly observations per day. Ultimately the procedure results in a very high data coverage and therefore a spatially and temporally continuous data set which is particularly suited to study the representatives of SSR surface observations (Müller et al., 2015b). The monthly mean SSR data used in the present study are directly provided by the CM-SAF. The uncertainty of the SARA data was assessed in the CM-SAF validation report by comparing the SARA SSR data to 15 BSRN observations. Averaged over the stations differences of  $5.5 \text{ W/m}^2$  were found (Müller et al., 2015a).

During the observational period from 1983 to 2015, 11 different satellites (Meteosat 2–10) covering two generations of Meteosat satellites were used for the retrieval of normalized effective cloud albedo. Although the same algorithm is used for the whole period, the homogeneity of the product has to be assessed. Similar to Brinckmann et al. (2013), who examined the homogeneity of the CM-SAF MVIRI data set (which only takes data from the Meteosat first-generation satellites), we assessed the homogeneity by applying Standard Normal Homogeneity Tests (SNHT) (Alexandersson, 1986) on the spatial mean of the full domain CM-SAF monthly mean time series. Since SNHTs are ideally applied on a series only in comparison with a reference data set, the ERA-Interim (Dee et al., 2011) and ERA-20C (Poli et al., 2016) surface solar radiation reanalysis data products have been used as such. Depending on which reference was used, significant inhomogeneities were found in 1990 (when using ERA-20C as reference) and in 2006 (when using ERA-I as reference). Both inhomogeneities appear when there was a satellite change. Moreover, when testing the two reference series (ERA-I and ERA-20C) against each other, a significant inhomogeneity in 1990 was found, which points to an insufficient homogeneity of the ERA reanalysis surface radiation data sets themselves. By applying the SNHT only on the regional scale (i.e., use European monthly means instead of full disk Meteosat means), no inhomogeneities were found.

Nevertheless, all results in this study were computed for the whole CM-SAF period (1983–2015) as well as a most likely homogeneous period (1993–2006), but no significant differences in the results were found. Therefore, results shown in the following relate to the whole CM-SAF observation period.

### 2.2.2 Direct Surface Observations of SSR

To evaluate the spatiotemporal representativeness of ground-based surface solar radiation observations, data from the Baseline Surface Radiation Network (BSRN, Ohmura et al. 1998) and the Global Energy Balance Archive (GEBA, Gilgen and Ohmura 1999; Wild et al. 2017) have been used. Both data sets measure SSR from direct surface measurements with pyranometers (applies to many GEBA sites), possibly in combination with pyrhemometers (for

BSRN sites and a minority of GEBA sites).

Associated, published uncertainty estimates for direct SSR observations we are aware of (see below) are absolute operational measurement uncertainty estimates incorporating effects from the measurement device and the statistical treatment (notably temporal averaging). More detailed estimates that break down the error in individual contributions would be highly desirable.

### BSRN

The BSRN was established in the late 1980s to provide high accuracy surface radiation measurements (Ohmura et al., 1998). At present, more than 50 BSRN stations are available worldwide. The data are provided with a temporal resolution of 1 min intervals for most of the sites. Due to the high standards on the data quality and homogeneity of BSRN, it is providing the most accurate SSR data currently available and therefore serves as a benchmark data set. Monthly means are calculated from the 1 min data as recommended by Roesch et al. (2011). Thereby, a monthly diurnal cycle, binned into 15 min intervals, is calculated from the 1-minute data for each month. The monthly mean diurnal cycle is then averaged to receive the monthly mean SSR. The monthly mean is only valid if all 96 fifteen-minute bins are available. A 15 min bin is valid if at least 20% of the data are available for that bin. The uncertainty for monthly (annual) mean SSR from BSRN measurements were estimated by Dutton et al. (2012) to be  $\pm 8(6) \text{ W/m}^2$  on the 95%-level. This corresponds roughly to an error of 3% (10%) during European summer (winter). In this study, we make use of nine European BSRN stations (see Figure 2.1).

### GEBA

The GEBA collects and stores worldwide radiation data at the Earth's surface from various sources (Gilgen and Ohmura, 1999; Wild et al., 2017). It incorporates more than 2,500 globally distributed stations including some of the oldest and longest SSR records available. As the monthly means in the GEBA stem from various sources, no unique averaging scheme is used. However, a substantial part of data in GEBA is provided via the World Radiation Data Center (WRDC) which is one of the recognized and sponsored World Meteorological Organization (WMO) data centers. These monthly data were computed using the averaging scheme from WRDC. There the daily values are provided in daily integrated sums of radiation if all hour intervals of a day are valid. The monthly mean of daily integrated radiation is calculated by summing all valid daily sums and dividing by the number of valid days if not more than 10 days are missing during a month. The monthly mean of daily radiation sum (given in  $\text{J/cm}^2$ ) can easily be transformed to the common units of  $\text{W/m}^2$ .

The uncertainty (random error with zero mean) of single-monthly (annual) mean values has been estimated to be 5% (2%) by Gilgen et al. (1998) based on intercomparison between dif-

ferent pyranometer measurements conducted at the same station over a period of 3 years. As the error analysis is based on the analysis of variances, the significance level of the estimate is at the one standard deviation level.

In order to ensure that only homogeneous data records are used for this study, we apply a series of absolute homogeneity tests (i.e., the Standard Normal Homogeneity Test (Alexandersson, 1986), the Pettitt test (Pettitt, 1979), the Buishand range test (Buishand, 1982) and the Von Neumann ratio test (Von Neumann, 1941)) to the GEBA SSR time series as described in Hakuba et al. (2013b) and Wijngaard et al. (2003) and only take into account data records which are homogeneous according to these tests. Moreover, only data records with a data coverage of 50% and more between 1983 and 2015 are considered in our analysis.

Our data quality criteria together with the spatial constraints from the Meteosat observational disk result in 140 GEBA stations which were included in the analysis (see Figure 2.1).

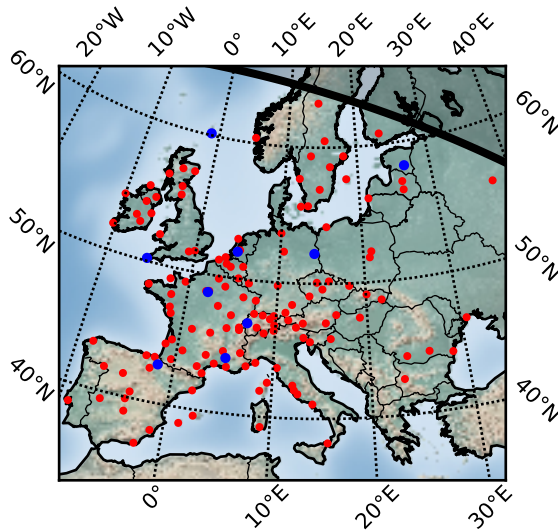


**Figure 2.1:** Spatial domain with BSRN (blue dots) and GEBA (red dots) stations used. The shaded area in the northeast indicates the Meteosat-Disk border.

### 2.2.3 Methods

In this paper, the representativeness of temporal variations of individual measured SSR time series for their larger surrounding is examined. Since different temporal and spatial scales are analyzed, it is useful to introduce the following terminology. Regarding the spatial dimension, time series from SSR observational sites (see section 2.2.2) and time series from single pixels from SARA (see section 2.2.1) are referred to as point observations while time

series which are computed from multiple, spatially aggregated, SARA pixels are referred to as gridded (single grid box) observations.

In the temporal domain, we consider annual, seasonal, monthly deseasonalized (absolute and relative), and single-month time series. Annual (seasonal) time series are computed from the raw monthly time series of the observational networks only if all 12 (3) months of an individual year (season) are available. Deseasonalized time series are used in absolute ( $W/m^2$ ) and relative (%) form as the deviation from multiannual mean monthly values. Time series which consist of observations from only one month (e.g., January) are referred to as single-month time series.

Since some of the performed analyses rely on the data being normally distributed, the SARA data set was tested in this respect using a Kolmogorov-Smirnov test for normal distribution at the 95%-significance level. It reveals that the data on annual, seasonal, and single-month time scales is mostly normally distributed. For the monthly time scale the majority of data are normally distributed southward of  $55^\circ N$ . Small radiation quantities north of  $55^\circ N$ , especially in winter, are a likely cause that the data are not normally distributed.

### Correlation Analysis

The squared Pearson product-moment correlation coefficient ( $R^2$ ) is calculated and used as a measure for the ability of a time series, measured at a certain location, to estimate a SSR time series at a distant location. To evaluate the spatial pattern of temporal SSR representativeness of an observation site, the following analyses have been carried out:

1. Point-to-Point Correlation: By calculating the squared correlation coefficient between two distant points and sorting the outcome according to the great-circle (i.e., orthodromic) distance between the point observations, a general spatial correlation pattern can be calculated. This pattern has been calculated for (1) correlation coefficients based on purely ground-based observations (i.e. BSRN and GEBA observations; hereafter called site-to-site correlation) and (2) correlation coefficients between surface observations and individual surrounding SARA pixels (which are considered to be point observations due to the high spatial resolution of the data set, see section 2.2.1, hereafter called site-to-pixel correlation).
2. Point-to-Area Correlation: To infer the representativeness of point observation for a larger surrounding, squared correlation coefficients have been calculated between point observations and the corresponding colocated area mean SSR time series. The latter are calculated from aggregating SARA pixels in order to simulate coarser grid resolutions. The squared correlation coefficients have been calculated (1) for surface observations against SARA box (hereafter referred to as site-to-box correlation) and (2) for SARA pixels against SARA box (hereafter referred to as pixel-to-box correlation). This analysis directly addresses the question whether a single surface point observation

is sufficient to describe the temporal variations in SSR for a larger area, as occurring in satellite products or in output from numerical models.

The SARAH data have been tested for the possible occurrence of temporal autocorrelations since they can significantly influence the analysis. For the deseasonalized monthly mean SARAH data, the average autocorrelation in Europe is well below 0.1 at a time lag of one 1 and essentially 0 for lag times greater than 1 month.

### Spatial Sampling Error

Below we introduce two measures to quantify spatial sampling errors (SSEs) that arise from estimating the temporal variability of SSR for a larger area from a point observation for single time steps. Both measures are similar to those used by Hakuba et al. (2013a, 2014b) with two important differences: here we also consider temporal variability, not climatological values, and we use a more strict measure by looking at the 95th percentile or interpercentile range (see below).

The SSE analysis is done for the 1° grid of the radiation data sets from the Clouds and the Earth's Radiant Energy System (CERES) of the American National Aeronautics and Space Administration (NASA) (Wielicki et al., 1996). Individual SARAH pixels are considered to be point observations, box means are computed by aggregation of SARAH pixels within the 1° grid. Differences between box means and underlying point data are quantified via percentiles (on the 95% level,  $P^{95}$ ) and interpercentile ranges (also on the 95% level, i.e.,  $IPR^{95} = P^{97.5} - P^{2.5}$ ). Subscripts indicate the dimension over which the percentile is calculated ( $x$ ,  $y$ , and  $t$  for longitude, latitude and time, respectively; e.g.,  $P_t^{95}$  is the 95th percentile in the temporal dimension). Monthly, annual, seasonal and single-month time scales are considered. For monthly and seasonal scales, SSR anomalies on the level of individual pixels and with respect to the climatological mean are used. This also automatically corrects for latitudinal SSR variations that arise on astronomical grounds, that is, the orbital configuration of the Sun and the Earth.

The first measure we introduce is  $SSE_s$ , a site-specific measure that describes the deviation of the site's collocated pixel from the box mean during the whole observation period. For each surface observation site, the 95%-percentile of the absolute difference between the SSR time series of the collocated SARAH pixel ( $SSR_s(t)$ ) and 1° box mean ( $SSR_a(t)$ ) has been calculated:

$$SSE_s = P_t^{95}(|SSR_s(t) - SSR_a(t)|). \quad (2.1)$$

If desired,  $P^{95}$  and  $IPR^{95}$  can easily be converted to any other percentile by multiplying with the appropriate  $z$  values, for example,  $P^{68} = P^{95} * z_{\sigma}/z_{95}$  (with  $z$ -values  $z_{\sigma} = 1$  and  $z_{95} = 1.96$ ) as the underlying data are mostly normally distributed (see above).

The second measure we introduce,  $SSE_a$ , is site independent and characterizes the variability of SSR within the 1° target grid. The  $SSE_a$  is calculated from the 95%-percentile (tempo-

ral dimension) of the 95%-percentile (spatial dimension) of all absolute differences between SARAH pixels  $SSR_p$  within the  $1^\circ$  box and the corresponding box mean:

$$SSE_a = P_t^{95} \left( P_{x,y}^{95} (|SSR_p(x,y,t) - SSR_a(t)|) \right). \quad (2.2)$$

Other percentiles may again be easily obtained, by multiplying with twice the corresponding  $z$  values. The factor 2 enters as percentile ranges were calculated in space and time.

Put simply,  $SSE_s$  compares the  $1^\circ$  box mean SSR to the SSR at one individual pixel (at an observation site), while  $SSE_a$  compares the box mean to the SSR of all pixels within the box. Consequently,  $SSE_a$  is typically larger than  $SSE_s$ .

## 2.3 Results

### 2.3.1 Correlation Analysis

For the correlation analysis, we discriminate between point-to-point and point-to-area correlations. The first is carried out in order to elaborate if and to which extent SSR time series from two distant points correlate. The point-to-area correlation analysis directly addresses the question whether a single surface point observation is sufficient to describe the temporal variations of SSR for a collocated larger area.

#### Point-to-Point Correlation

**Site-to-Site Correlation** The site-to-site correlation relies only on truly ground-based measurements (see section 2.2.3) and can thus be considered the most robust measure for spatial correlation of SSR time series. Altogether, observational records from more than 12,000 station pairs were analyzed with distances ranging from a few kilometers up to a distance of 4,200 km (which corresponds to roughly  $38^\circ$  on a great circle).

Overall, the squared correlation coefficient decreases with increasing distance, as expected. For the deseasonalized monthly time scale (red bold line in Figure 2.2a) a high median  $R^2$  of around 0.85 at the first bin was found. We note, however, that the statistics for the first distance bins are less robust as only few station pairs are available for very short distances (see Figure 2.2b). The squared correlation coefficients between the majority of stations which are less than  $1^\circ$  apart from each other are well above 0.5 on all time scales. Only at seasonal and single-month time scales, the winter shows slightly lower correlations. Generally,  $R^2$  decreases essentially linearly until it drops below 0.25 at distances around 500 km. As the number of available stations is limited some bins only have few stations from which the bin statistics are calculated which in turn explains some of the fluctuations of the lines shown in Figure 2.2. These fluctuations are less visible when more observations are available close to the site as can be seen for the site-to-pixel correlation in section 2.3.1 (and explicitly in

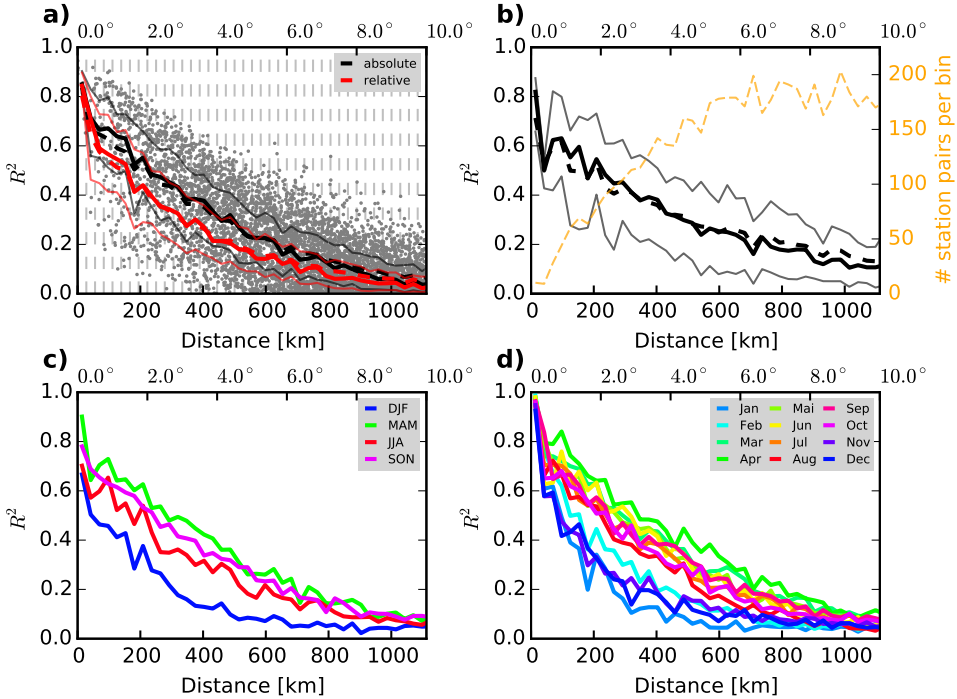


**Figure 2.2:** Site-to-site correlation as a function of orthodromic distance on (a) monthly deseasonalized (in absolute and relative deviation from monthly means), (b) annual, (c) seasonal, and (d) single-month time scale. The lines in all panels show the  $0.25^\circ$  binned statistics of the underlying site-to-site correlations. Shown are median (bold continuous), mean (bold dashed), and the 25 and 75th percentiles (thin lines) of all available station pairs in the corresponding  $0.25^\circ$  bins (gray dashed vertical lines in Figure 2.2a). The gray points in panel (a) denote individual station pairs. The orange dashed line in Figure 2.2b shows the number of available station pairs per bin.

Figures 2.4 and 2.5). For distances between  $500\text{ km}$  and  $1,000\text{ km}$  the squared correlation coefficients in Figure 2.2 asymptotically decreases until they finally are essentially 0 at distances above  $1,000\text{ km}$  (not shown). The spread in the site-to-site correlations is relatively constant with increasing distance. On average, the spread for the deseasonalized monthly (annual) time scale is 0.25 (0.33) as can be seen from the thin lines in Figures 2.2a and 2.2b, which indicate the 25th and 75th percentiles for each bin. For the seasonal and single-month time scale similar spreads were found (not shown).

The correlation patterns for the absolute and relative deseasonalized time scales (see Figure 2.2a) are almost the same. This although absolute and relative deseasonalizing give different weight to different seasons. In both cases, the difference of the monthly mean values from their climatological values are computed. However, there is a natural annual cycle not



only in mean SSR but also in the standard deviation of SSR. Monthly mean deseasonalized SSR time series show the largest variability (standard deviation) in summer if absolute units are considered. By contrast, for relative units the variability is largest in winter because the denominator (wintertime SSR) is small. Given that wintertime correlations are lower than those during summertime, as can be seen in the blue and bluish lines in the Figures 2.2c and 2.2d, putting more weight on wintertime by calculating relative deseasonalized time series lowers the correlation coefficients. However, differences in the correlation coefficients between absolute and relative deseasonalized time series are relatively small ( $\approx 0.1$ ).

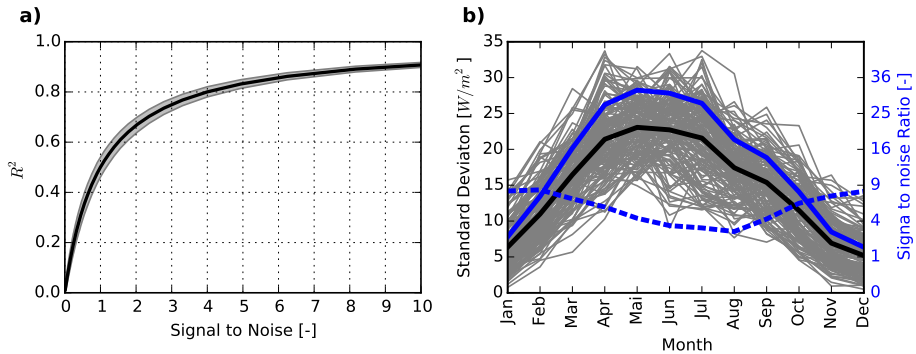


**Figure 2.3:** (a) Correlations between an artificial standard normally distributed time series and the same time series with added Gaussian random noise for different noise levels. The noise level is the square of the ratio of the standard deviation of the signal (per definition equal to 1) and the standard deviation of the added noise. The bold line shows the mean from the Monte-Carlo simulations. The gray shaded area shows 95th interpercentile range. (b) Standard deviations for monthly data of all stations (gray lines) and the mean over all stations (black bold line) as well as corresponding mean signal-to-noise ratios when using the error estimate of Dutton et al. (2012) (converted to the 1 sigma level, i.e.,  $8/1.96 \text{ W/m}^2$ ; blue line) and the error estimate of Gilgen et al. (1998) (blue dashed line).

Different potential reasons come to mind as to why correlations are lower in winter than in other seasons. One possible factor could be seasonal differences in cloud cover and synoptic scale weather patterns. A detailed analysis of this hypothesis is, however, beyond the scope of the present paper. Another, at least partial explanation may be the less favorable signal-to-noise ratio (i.e., the ratio of the typical SSR variations compared to its measurement error; more details follow below) in winter as compared to other seasons.

To investigate this idea further we performed a simple numerical experiment in which we looked at correlations between an artificial standard normally distributed time series of the same length as the investigated time series, and the same time series with added Gaussian random noise. The signal-to-noise ratio (SNR) in the experiment is defined as the square of the ratio between the standard deviation of the signal (per definition equal to one) and

the standard deviation of the added noise (varying from 0.1 to 10 which equals to SNRs of 100 to 0.01, respectively). We recall that our data are essentially normally distributed; see section 2.2.3. To obtain robust statistics, we used a Monte Carlo approach with 100 different time series and 100 different noise overlays per time series and noise level. The experiment shows that the correlation decreases with increasing noise (see Figure 2.3a). The decrease is substantial ( $R^2 < 0.5$ ) if the SNR falls below 1, while already a somewhat higher SNR of 4 yields  $R^2 > 0.8$ . Figure 2.3b gives an idea of the SNR of our actual data. Shown are the standard deviations of the monthly data of all available stations and the mean over all stations (thick black line), which we interpret as typical magnitude of the SSR signal. For the noise level of the SSR measurements we have two choices: the error estimate of monthly mean data by Gilgen and Ohmura (1999) (5% of monthly mean value) or by Dutton et al. (2012) ( $8 \text{ W/m}^2$  divided by 1.96, to convert from the 95%-level to the  $1\sigma$ -level). The latter choice (blue solid line in Figure 2.3b) yields a SNR for winter between about 1 and 2. Even closely neighboring stations thus should show correlations  $R^2$  of at most 0.5 to 0.7, which is roughly what is seen in Figure 2.2c. The former choice (blue dashed line), by contrast, has high SNR (about 3 or more) year round. Winter SNR (above 5) correspond to  $R^2 > 0.8$ , suggesting other relevant factors for the low winter correlations in Figure 2.2c. We come back to this point in section 2.4.

Overall, the correlation patterns of all analyzed time scales show remarkably similar results. Because of that good agreement, all further results will be presented only for the absolute deseasonalized monthly time scale if not indicated otherwise. We stress, however, that most analyses were performed for all time scales and show very similar results. An additional advantage of using the deseasonalized series (which we recall have negligible temporal autocorrelation, see section 2.2.3) is the higher data coverage compared to the annual time scale, since annual means can only be computed (without any gap-filling techniques) if all 12 monthly mean values of a year are available.

**Site-to-Pixel Correlations** Spatial correlation patterns were computed for all SSR monitoring sites by correlating the (absolute monthly deseasonalized) observed time series of the surface sites against the surrounding SARA pixels (termed site-to-pixel correlation as stated in Chapter 2.2.3). The resulting maps of squared correlation coefficients show local, site-specific patterns as exemplarily shown for the sites Payerne, Dublin Airport, and Lindenberg in Figure 2.4a, 2.4b and 2.4c). Again,  $R^2$  generally decreases with increasing distance from the ground observation site. Most dominating features that modulate  $R^2$  are identified to be specific topographic features, like mountain ranges (see Figure 2.4a) and coastlines (see Figure 2.4b). Stations in more homogeneous terrain, like the BSRN station Lindenberg in Germany (see Figure 2.4c), show generally smoother correlation patterns with higher  $R^2$  than sites which are situated in complex terrain.

To provide an overall statement about the spatial representativeness of SSR observations

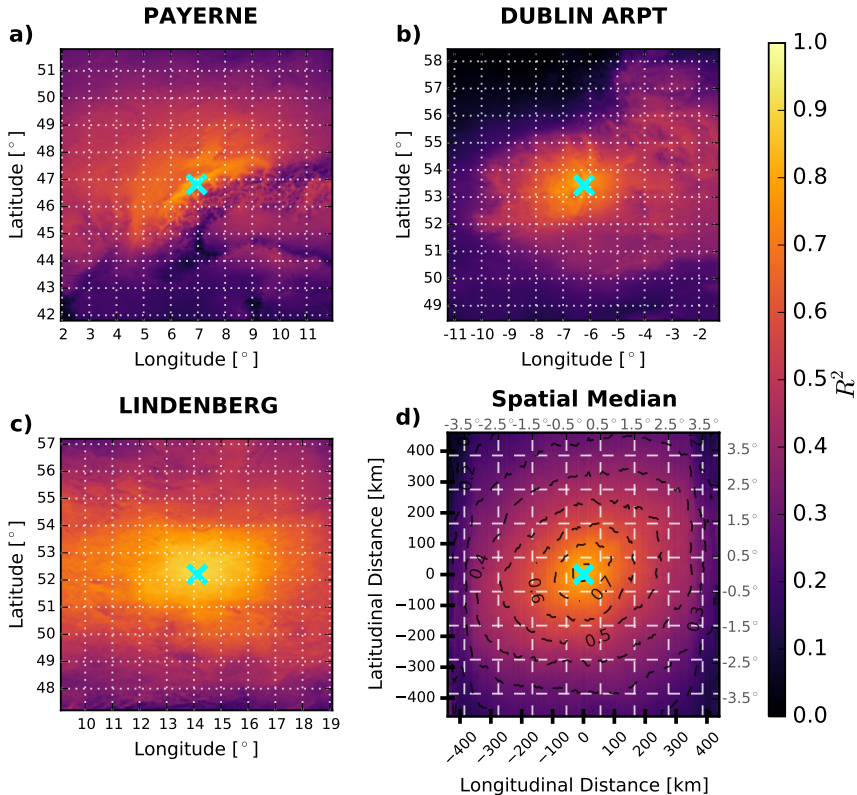


**Figure 2.4:** Site-to-pixel spatial correlation patterns derived from station observations and SARAH for (a) Payerne, (b) Dublin Airport, and (c) Lindenberg, as well as (d) the median across all sites. Bright colors indicate high point-to-point correlations between the surface observations and the SARAH pixels. The cyan crosses indicate the position of the stations. White horizontal and vertical dashed lines show the 1° CERES grid up to  $\pm 5^\circ$  around the station in Figure 2.4a–2.4c and the 1° grid centered at the station (Figure 2.4d). The black dashed lines in (d) show the  $R^2$  contour lines with spacing of 0.1.

in the European midlatitudes, a single correlation map has been derived by calculating the median correlation from the correlation maps of all sites as shown in Figure 2.4d. The figure shows generally high ( $R^2 > 0.8$ ) correlations in close proximity (around 25 km). For a  $1^\circ$  surrounding area around the station (i.e., from  $-0.5^\circ$  to  $0.5^\circ$  in latitudinal and longitudinal distance indicated by the white grid of Figure 2.4d), the squared correlation coefficients are well above 0.7. With increasing distance from the center point,  $R^2$  generally decreases as expected. However, even at distances of up to  $2.0^\circ$  (which corresponds roughly to 220 km) from the surface observation location the squared correlation coefficients are well above 0.50.

In order to validate the above correlation pattern found from site-to-pixel correlations, the outcome has been compared to the site-to-site based analysis from section 2.3.1. By binning the median site-to-pixel correlations (see Figure 2.4d) to bins of  $0.25^\circ$  and comparing them against the purely station observation based correlations (see Figure 2.2a), a very good agreement was found in terms of mean, median and 25th and 75th percentiles as shown in Figure 2.5. Generally, a remarkable consistency between purely observation based and satellite-derived correlation patterns has been found, which is a strong indication for the adequate representation of the correlation pattern from Figure 2.4d. The biggest differences (which are still relatively small) between observation and satellite-derived correlation curves were found at very short distances between the stations where only a small number of station pairs are available. Nevertheless, when a sufficient number of station pairs is available in a distance bin, the agreement between station-based and satellite-derived correlation is very high.

## Point-to-Area Correlation

**Site-to-Box Correlation** All above-mentioned patterns refer to point-to-point correlations. In the following we investigate the correlation of a site's time series and that of a larger collocated surrounding. Therefore, a multitude of the high-resolution SARA pixels were spatially aggregated to simulate coarser and coarser resolutions. The analysis should show, whether the time series of a surface observation is sufficient to describe temporal variations in SSR for a larger area and whether it is generally possible to compare the temporal variations from surface point observations with gridded data products such as satellite data and numerical model output.

Figure 2.6a shows site-to-box correlations across all sites when correlating the sites' time series against that of collocated site-centered boxes of different sizes. In comparison to the site-to-site correlation from Figure 2.2a, the site-to-box correlation generally shows a smaller decrease of  $R^2$  with increasing distance. This can be expected as the site-to-box correlations implicitly integrate all site-to-pixel correlations within a grid box. While the squared correlation coefficient for the site-to-site analysis at  $0.5^\circ$  distances already dropped below 0.70, it is still higher than 0.80 for the site-to-box analysis for the  $1^\circ$  box (note that a factor of two has to be considered when comparing distances and grid sizes). Even more pronounced

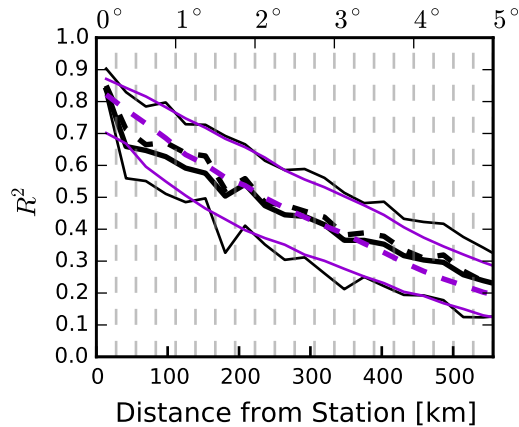


**Figure 2.5:** Site-to-pixel correlation patterns compared to the site-to-site correlation pattern for the absolute deseasonalized monthly time scale. Black lines are computed from site-to-site correlations (as shown in Figure 2.2) while violet lines are computed from site-to-pixel correlations (as shown in Figure 2.4). The lines indicate the 0.25° binned statistics of the underlying site-to-site and site-to-pixel correlations. Shown are median (bold continuous), mean (bold dashed), and the 25% and 75% percentiles (thin lines).

differences can be seen for coarser grids and larger distances.

However, the lines in Figure 2.6a refer to correlations between surface observations and the corresponding colocated, site centered grid boxes. In reality only few surface sites are exactly centered with respect to a given regular grid, as for example the 1° CERES grid (see Figure 2.6b). Therefore, the correlations between grid boxes and noncentered sites were inferred to provide a more realistic view of the correlation patterns. As a benchmark, median correlations of all available sites were evaluated for regular grids (i.e., grids starting at the zero-meridian and the equator with equidistant spacing in latitudinal and longitudinal direction) with different grid sizes (black line in Figure 2.6c). The squared correlation coefficients for individual sites are found to be 15–20% smaller if the sites' locations are sufficiently off centered with respect to the regular grid (compare Figures 2.6a and 2.6c). A similar dependence of sampling error on grid box size was found by (Schutgens et al., 2016a) for aerosol optical thickness (AOT) and surface black carbon (BC), who also point out that such a dependence required existence of spatial and temporal correlation of the underlying data on subgrid scale.

To analyze the effect of the positions of the sites with respect to the colocated box, site-to-box correlations have been calculated for less favorable configurations. Thereto, the box from which the area mean time series was calculated was shifted in all possible ways with

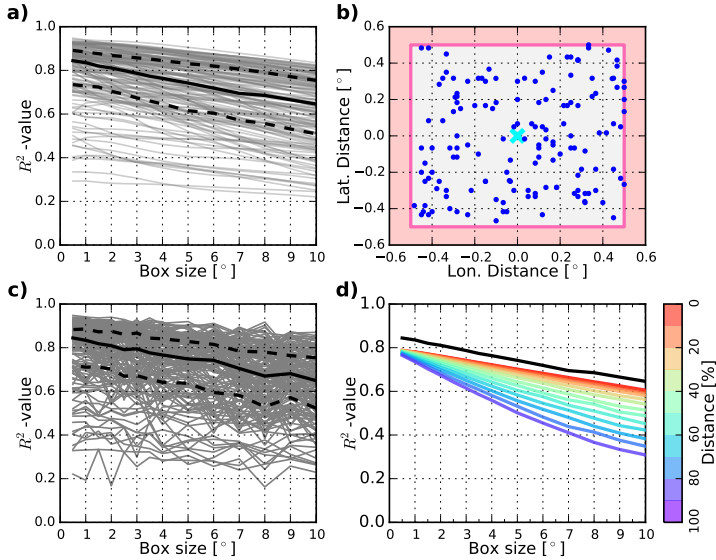


**Figure 2.6:** Site-to-box correlation patterns as derived by correlating monthly mean deseasonalized observational time series of stations and surrounding boxes calculated from the spatial aggregation of high-resolution SARA pixels. (a) The correlations of all individual sites (gray lines) as well as median (black line) and 25th and 75th percentiles (black dashed lines) across all sites for different box sizes centered with respect to the observational sites. (b) The true position of the stations with respect to their colocated  $1^\circ$  CERES grid is illustrated in. Blue dots indicate the individual positions of the stations within their corresponding colocated pixel, the cross indicates the center of the  $1^\circ$  CERES pixel. (c) The same plot as Figure 2.6a but calculated for fixed regular grids (i.e., sites are no longer in the center of the boxes; see text for explanation). (d) The median site-to-box correlation for different pixel resolutions is shown for site-centered boxes (black line; same line as in Figure 2.6a) and arbitrarily shifted grid boxes (colored lines). The coloring indicates the distance between the center point of the box and the location of the observation station in percent of the maximum possible distance (i.e., pixel size times  $\sqrt{2}/2$ ).

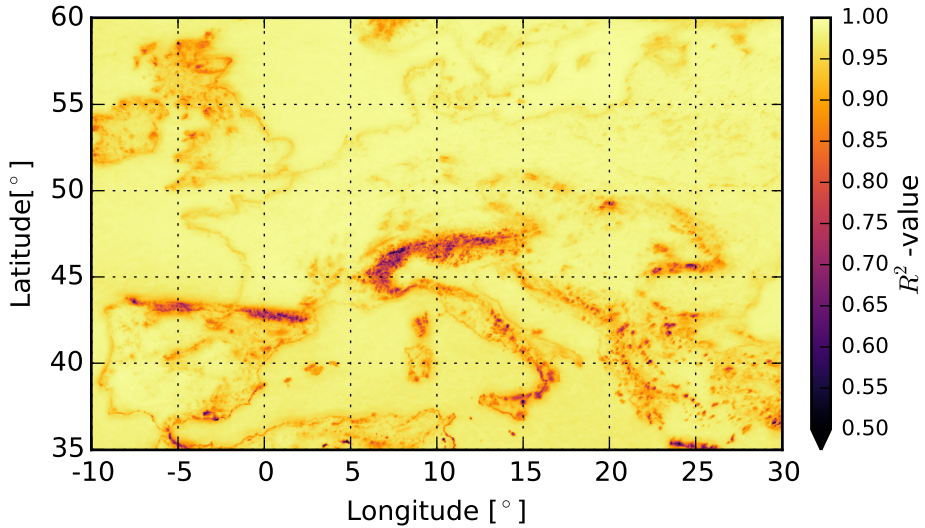


**Figure 2.7:** Squared correlation coefficients for the correlation of each SARAH pixel in Europe with its corresponding colocated aggregated and site-centered  $1^\circ$  grid box (termed pixel-to-box correlation) for the deseasonalized monthly mean time scale during the period 1983–2015.

respect to the sites. To quantify how off centered the sites are with respect to a surrounding grid box, the distances between the sites' locations and the center point of the corresponding box was calculated. To allow an easier comparison between different grid resolutions, the calculated distances have been normalized with respect to the maximum possible distance between pixel-center-point and site (i.e., pixel size times  $\sqrt{2}/2$ ). From Figure 2.6d it follows that the correlation decreases when the sites get more and more off centered with respect to the box center. However, the effect of unfavorable grid configurations is rather small for small box sizes. Specifically, the differences between the site-centered and regular  $1^\circ$  CERES grid are negligibly small as the correlations over small distances are found to be very high in any case (see Figure 2.2) and, therefore, do not substantially reduce the site-to-box correlations.

Overall, 80% of the stations show squared correlation coefficients higher than 0.75 for the site-to-box analysis at the  $1^\circ$  CERES grid. Most of the stations with lower correlations are either located in mountainous regions with complex topography or are near coastlines. This finding is a strong indication that most stations are well suited to quantify the temporal SSR variability even for a larger surrounding if they are not located in overly inhomogeneous terrain.

**Pixel-to-Box Correlation** To provide an insight for spatial correlations also for areas where no surface sites are available a so-called synthetic correlation analysis was carried out. Synthetic thereby refers to correlation analysis of single SARAH pixels against aggregated SARAH grid boxes without using any SSR station observations.

Figure 2.7 shows the synthetic correlation map of Europe. Shown are the correlations between each  $0.05^\circ$  SARAH pixel and its corresponding, colocated and pixel-centered spatially aggregated  $1^\circ$  box. Overall, most areas in Europe show very high correlations well above  $R^2 > 0.9$  due to the high correlations between points which are only a few kilometers apart as shown in Figure 2.2 and the former mentioned integration effect.

Note that, the high correlations from the synthetic correlation analysis can be regarded as ideal measurement scenario with no observational bias and are therefore relatively high. Comparing the site-to-box correlations of all surface observation sites with the corresponding pixel-to-box correlations shows that site-to-box correlations are on average lower by 0.15. However, the general pattern, with higher correlations in homogeneous and lower ones in complex terrain, is again very clearly visible.

### 2.3.2 Spatial Sampling Errors

The SSE generally quantifies the bias which arises when using a SSR point observation as a surrogate for SSR of a larger region, such as the area covered by a  $1^\circ$  CERES pixel. The  $SSE_a$  describes the difference (on the 95% level, see section 2.2.3) of individual pixels from the corresponding  $1^\circ$  box mean values and can be regarded as conservative error measure for single time steps due to spatial sampling within a  $1^\circ$  box. The error due to spatial sampling for individual stations,  $SSE_s$ , quantifies the difference (on the 95% level) between the station's colocated  $0.05^\circ$  pixel and the corresponding  $1^\circ$  box mean also for single time steps (see section 2.2.3). Typically, the  $SSE_s$  is smaller than the  $SSE_a$ .

Figures 2.8a and 2.8b show the 95% interpercentile range of the differences between individual pixels and the box mean during the observational period for two exemplary  $1^\circ$  CERES boxes colocated with the stations Dublin and Lindenberg respectively on the monthly time scale. While at the station Lindenberg a rather homogeneous pattern can be observed throughout the colocated  $1^\circ$  pixel, the SSEs of the individual pixels at Dublin show more variability. This is also visible in the difference between  $SSE_s$  and  $SSE_a$ , both of which are given on top of the corresponding figures. While the difference in  $SSE_s$  and  $SSE_a$  is only  $2.3 \text{ W/m}^2$  at Lindenberg, the difference at Dublin is  $7.3 \text{ W/m}^2$ . Note that even though the variability at Dublin is higher, the site-specific sampling errors between Dublin and Lindenberg differ by only  $0.5 \text{ W/m}^2$ .

Overall, roughly 75% of all stations show a  $SSE_s$  smaller than  $10 \text{ W/m}^2$  on the deseasonalized timescale. The median  $SSE_s$  over all stations is  $8.7 (2.8) \text{ W/m}^2$  for the monthly (annual) time scale. The individual values of  $SSE_s$  and  $SSE_a$  for different time scales can be found in



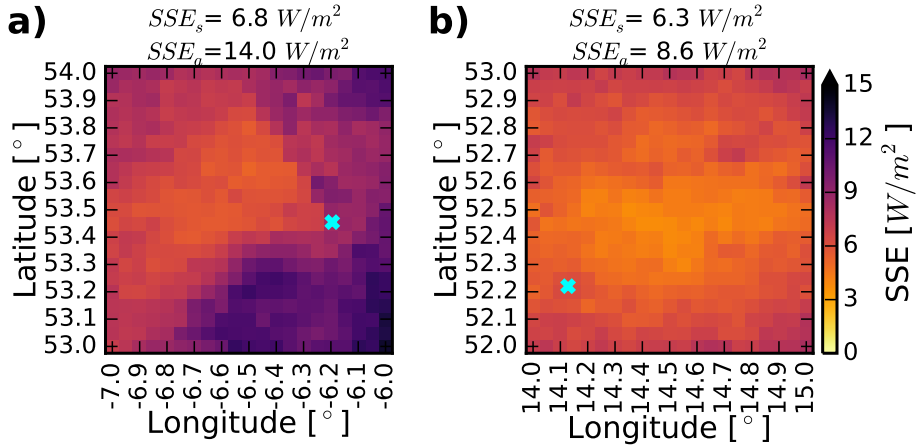


**Figure 2.8:** Spatial sampling error (a) at Dublin and (b) Lindenberg based on monthly data. Shown are differences (95% level) between the time series of the individual pixels and the corresponding 1° CERES box. The cyan crosses indicate the stations position within the CERES box. Dark colors indicate larger errors.

Table B.1 given in Appendix.

A map for the site-independent  $SSE_a$  is shown in Figure 2.9. The figure shows the sampling error (on the 95%-level) for the whole European domain based on the 1° CERES grid for the monthly deseasonalized time scale. Similar features as in the synthetic pixel-to-box correlation analysis (see Figure 2.7) can be identified. Overall, the median  $SSE_a$  across the whole domain is 10.5 (2.8)  $W/m^2$  on the monthly (annual) time scale. It should be mentioned that the  $SSE_a$  on the 95%-level is a conservative estimate and that spatial sampling errors for individual sites can be substantially smaller as has been shown above.

## 2.4 Discussion

Our overall goal was to clarify whether temporal variations in surface measured SSR time series (on monthly and longer time scales) are representative for larger surroundings and to estimate the error which arises due to spatial sampling when using time series of single surface observations as a surrogate for larger areas. These questions have to be addressed when aiming to analyze temporal variations in the radiation budget by using SSR point observations in combination with gridded data (e.g. Wild, 2009a; Allen et al., 2013).

In the following, we want to evoke consequences of our findings with regard to this overarching goal and also put the results from section 2.3 yet more into perspective with regard to

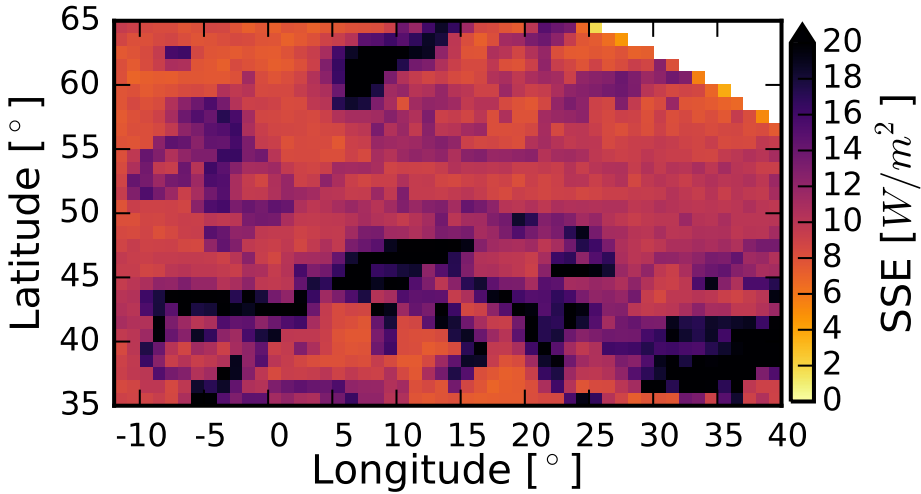


**Figure 2.9:** Site independent spatial sampling errors ( $SSE_a$ ) according to equation 2.2 for all  $1^\circ$  CERES boxes in the observational domain. It quantifies the deviation of single SARA pixels within a  $1^\circ$  box from the box mean value in  $W/m^2$  for the deseasonalized monthly time scale.

existing literature.

Before focusing on the results the underlying data should be discussed. Homogeneity tests (similar to Brinckmann et al., 2013) for the SARA data set revealed two significant inhomogeneities when tested for the Meteosat full disk mean time series (see section 2.2.1). When considering not the whole Meteosat disk but only the observational domain (i.e., Europe) no inhomogeneities were found. No differences were found when computing all results for the most-likely homogeneous period (i.e., 1991-2006) compared to the whole period (i.e., 1983-2015). To ensure high data quality for the surface observations, only data which passed the homogeneity and data coverage criteria were used (see section 2.2.2).

It was shown that correlation patterns of seasonal and single-month time series show nearly linearly decreasing squared correlation coefficients with increasing distance up to roughly 500 km. When defining the  $e$ -folding distance (i.e., the distance where the squared correlation coefficient drops below  $1/e$ ) as an estimate for the decorrelation distance, the average decorrelation distance can be estimated to be around 400 km (see Figure 2.2). Therefore, SSR measurements which are further apart than twice the average decorrelation distance can be considered as completely independent of each other. However, the spread between the 25th and 75th percentiles in Figure 2.2 shows also that the spread in the decorrelation length (e.g., for annual means) is substantial and ranges roughly between 100 and 600 km. This

spread also makes it difficult to give general recommendations on the spacing of an optimal measurement network that provides sufficient coverage yet few redundant sites.

This range of decorrelation lengths is in line with the idea that mesoscale synoptic cloud variations are a main driver of SSR variations. In fact, Parding et al. (2016) present an empirical decomposition of measured daily SSR in spring and summer in northern Europe into Grosswetterlagen (daily classifications of synoptic weather patterns). The decomposition explains between 22% and 58% of seasonally averaged observed transmittance (which is a proxy for SSR as it is computed by dividing the TOA incoming radiation through the SSR) in summer (3–42% in spring) over about four decades at 10 stations. The relative importance of synoptic scale effects varies with season, latitude and considered timescale, as does cloud cover, with typically higher cloud cover in winter and/or more northern latitudes (see, e.g., Meerkötter et al., 2004). On decadal time scales, correlations between cloud cover and large scale circulation indices have been found, for example, the North Atlantic Oscillation (Chiacchio and Wild, 2010; Li et al., 2014) or the Pacific Decadal Oscillation (Schwartz et al., 2014). Any of these effects may be reflected in the SARA data set, for which cloud observations are the dominant feature influencing the SSR on pixel level.

The investigation of the signal-to-noise ratio (i.e., squared ratio of the standard deviation of the signal to the standard deviation of the noise; SNR; see section 2.3.1) and how it affects time series correlations also allows to put into perspective the two different, published estimates for the measurement uncertainty ( $8 \text{ W/m}^2$  for monthly mean BSRN observations (Dutton et al., 2012) and 5% for monthly GEBA SSR data (Gilgen and Ohmura, 1999)). The 5% error estimate implies a comparatively high SNR in winter that should allow for correlation coefficients  $R^2 > 0.8$  for nearby sites. This is, however, not what we find when looking at site-to-site correlations. Consequently, either the 5% error estimate is too optimistic, at least for winter, or other factors exist that have a degrading effect on site-to-site correlations, even at short distances. The  $8 \text{ W/m}^2$  error estimate, by contrast, seems rather overly pessimistic, at least in winter. The associated SNR would imply correlations as low or even lower than what site-to-site correlations show. In summer, the roles are switched in that the 5% error estimate would limit correlations to below 0.8, while the  $8 \text{ W/m}^2$  error estimate corresponds to a very high SNR and little effect on correlations. From the literature it is unclear which of the two error estimates is to be preferred under what conditions. The example given here illustrates, however, the relevance of the choice.

The presented SSE provides a conservative sampling error for deviations from climatological values (i.e., anomalies) for single-monthly, annual, and seasonal means for a  $1^\circ$  grid. The magnitude of the error is similar to the reported measurement uncertainties which can be found in literature (Gilgen et al., 1998; Dutton et al., 2012). As the SSE is computed from anomalies, our approach implicitly accounts for latitudinal variations in SSR due to the astronomical configuration of the Earth and Sun and other systematic dependencies. Therefore, the presented SSE quantifies the differences between the anomalies measured at a site com-

pared to that of a grid box for single time steps. In contrast, the error estimate of Hakuba et al. (2013a) quantifies systematic differences (biases) of long-term means between sites and boxes, which can be corrected (as done in Hakuba et al., 2014b). When not working with pixel based anomalies but absolute values (and therefore not correcting the latitudinal SSR variations and other possible systematic differences) the  $SSE_s$  averaged over all sites is roughly  $4(2)W/m^2$  larger for the monthly (annual) time scale and therefore larger than the value found by Hakuba et al. (2013a) (which is around  $3W/m^2$  for monthly and annual means). This is in line with Li et al. (2005) and Deneke et al. (2005), who stated that longer averaging intervals increase the representativeness of SSR measurements.

The uncertainty (averaged across sites) which arises from estimating SSR of a  $1^\circ$  box from a single observation within the box can be estimated by adding the uncertainty from the measurement device and the sampling error using simple error propagation techniques (Bevington and Robinson, 2003; Hakuba et al., 2014b). We assume both errors are uncorrelated and random to estimate the combined error with the square root of the sum of the squared individual errors. For monthly (annual) means we find an overall error estimate of  $12(7)W/m^2$  (on the 95%-level). As the presented SSE is calculated based on individually deseasonalized time series, systematic differences in the long-term climatological mean between a site and its collocated grid box are implicitly corrected (see Hakuba et al., 2013a, 2014b). Following up on the signal-to-noise discussion from above (and again using the standard deviations of the SSR observations as the typical magnitude of the SSR signal) we want to emphasize that the standard deviation of the noise should be lower than  $10W/m^2$  to obtain SNR ratios above 2 for annual means and lower than  $11W/m^2$  for monthly means. Comparing these values to the error estimates (on the  $1\sigma$  level) reveals that the temporal variation in monthly and annual SSR measured at a site may be used as surrogate to a large surrounding.

We finally note that other errors may exist, which we did not address in this study, as we assume them to be small. This includes, for example, the error due to different spectral sensitivities of the measurement devices (Gilgen et al., 1998) or also the error due to a different temporal sampling of the raw data (Schutgens et al., 2016b). We expect the latter to be negligible for SSR as the sampling frequency and data coverage are high (see section 2.2.2).

By focusing on temporal changes of SSR on monthly and longer time scales our study bridges the gap between studies which focused on short term variations in the SSR field (Long and Ackerman, 1995; Barnett et al., 1998; Madhavan et al., 2017) and those which examined representativeness on climatological time scales (Li et al., 1995; Dutton et al., 2006; Hakuba et al., 2013a, 2014a). The presented correlations on monthly and longer time scales are considerably larger than those from studies looking at day-to-day or interday variations and remain high up to a few hundred kilometers.

We explicitly note that although some stations show lower spatial representativeness, they still provide very useful climate data. Stations with lower representativeness should, however, only be used for analyses where larger scale representativeness is not an issue. On

the other hand, it is desirable to achieve gridded data with high enough resolution so that errors due to spatial sampling are small enough to allow a valid comparison between surface observations and gridded data. Moreover, it is desirable to establish and conserve dense measurement networks of SSR all around the globe to ensure that changes in the shortwave radiation balance can be measured with high precision as station-based observations are the single most robust way to infer SSR.

## 2.5 Synthesis and Conclusion

We examined how well a SSR time series measured at a surface site describes the temporal SSR variability of a larger surrounding area and whether it is generally possible to compare temporal variations measured from surface observations with gridded data products such as satellite data and numerical model output. For this purpose, we examined monthly and longer temporally aggregated time series of ground-based and satellite-derived SSR.

We find high correlations of  $R^2 = 0.85$  between surface point observations on monthly mean scales for stations in close proximity (up to around 25 km) to each other. With increasing distance between the point observations, the squared correlation coefficients decrease linearly and fall below 0.25 at distances of roughly 500 km. The decorrelation length between point observations (i.e., the distance where the squared correlation coefficient drops below  $1/e$ ) was estimated to be 400 km with a substantial spread of 100–600 km. Correlation patterns are found to be consistent on deseasonalized monthly, seasonal, annual, and single-month time scales.

Repeating the same analysis with SSR time series from colocated satellite pixels instead of ground-based measurements, the same overall findings are obtained. Squared correlation coefficients are, however, generally higher by about 0.15, which is plausible as this purely satellite based analysis can be regarded as ideal measurement scenario with no observational biases between the pixels.

Squared correlation coefficients between ground-based SSR time series and the surrounding, satellite based area mean time series are generally high as well, about 0.8 for the 1 degree CERES grid in homogeneous terrain. The decrease of  $R^2$  with distance is weaker than for point-to-point correlations. Values are only slightly smaller for distances of two degrees (see Figure 2.6c), the typical grid cell size of a state of the art global climate model.

Turning from correlations to absolute errors, we expanded the spatial sampling error (SSE) concept by Hakuba et al. (2013a) from climatological mean data to SSEs for anomalies and single time steps. The found SSEs vary across sites with lower errors at sites in more homogeneous terrain. Averaging across all sites, we find a SSE with respect to a regular  $1^\circ$  grid of  $8.7 (2.8) \text{ W/m}^2$  for the monthly (annual) time scale.

The findings suggest that SSR variations inferred on a station basis can be considered representative of a larger surrounding. The error which arises due to spatial representativeness has

been quantified for a  $1^\circ$  grid. Overall, the SSEs are of the same magnitude as the in-situ SSR measurement uncertainty. Therefore, we conclude that it is feasible to use surface measured time series of SSR on monthly and longer temporally averaged time scales in combination with gridded data with at least  $1^\circ$  resolution.

## Acknowledgments

This study was funded by the Swiss National Science Foundation grant 20002\_159938/1 (Towards an improved understanding of the Global Energy Balance: temporal variations of solar radiation in the climate system). We thank Guido Müller for the maintenance of the GEBA (data is available at [www.geba.ethz.ch](http://www.geba.ethz.ch)) and Jörg Trendman and Uwe Pfeiffroth for their support in using the CM-SAF data (data is available under [www.cmsaf.eu](http://www.cmsaf.eu)). The authors thank BSRN for providing the data via [www.bsrn.awi.de](http://www.bsrn.awi.de). We thank WRDC for providing data via <http://wrdc.mgo.rssi.ru/>. ERA-I and ERA-20C data is available via <http://apps.ecmwf.int/data sets/data/interim-full-daily/> and <http://apps.ecmwf.int/data sets/data/era20c-daily/>. We further thank the anonymous reviewers for their constructive and helpful comments.

# From point to area: worldwide assessment of the representativeness of monthly surface solar radiation records

M. Schwarz<sup>1</sup>, D. Folini<sup>1</sup>, M. Z. Hakuba<sup>2,3</sup>, M. Wild<sup>1</sup>

Accepted article

Journal of Geophysical Research: Atmospheres

Volume 123, Issue 24

DOI: <https://doi.org/10.1029/2018JD029169>

ISSN: 2169-8996

## Key points:

- Representativeness of monthly SSR point observations is assessed near globally with three metrics
- Point and 1-degree gridded data can be combined, except near coasts, mountains, and in the tropics
- Combined uncertainties vary strongly with region and exceed measurement uncertainties by on average 40%

1. Institute for Atmospheric and Climate Science, ETH Zurich, CH-8092 Zurich, Switzerland.
2. Department of Atmospheric Sciences, Colorado State University, Ft. Collins, CO 80523, USA
3. Jet Propulsion Laboratory, California Institute of Technology, Pasadena, CA 91109, USA

## Abstract

*The representativeness of surface solar radiation (SSR) point observations is an important issue when using them in combination with gridded data. We conduct a comprehensive near-global (50°S to 55°N) analysis on the representativeness of SSR point observations on the monthly mean time scale. Thereto, we apply the existing concepts of decorrelation lengths ( $\delta$ ), spatial sampling biases ( $\beta$ ), and spatial sampling errors ( $\epsilon$ ) to three high-resolution gridded monthly mean SSR data sets (CLARA, SARAHP, and SARAH-E) provided by the Satellite Application Facility on Climate Monitoring. While  $\delta$  quantifies the area for which a point observation is representative,  $\beta$  and  $\epsilon$  are uncertainty estimates with respect to the 1-degree reference grid (G). For this grid we find a near-global average  $\delta_G = 3.4^\circ$ ,  $\beta_G = 1.4 \text{ W/m}^2$ , and  $\epsilon_G = 7.6 \text{ W/m}^2$  with substantial regional differences. Disregarding tropical, mountainous, and some coastal regions, monthly SSR point observations can largely be considered representative of a 1-degree grid. Since  $\epsilon$  is an uncorrectable error the total uncertainty when combining point with 1-degree gridded data is roughly 40% higher than the uncertainty of station-based SSR measurements alone if a rigorous bias correction is applied. Cloud cover and terrain data can at maximum explain 50% of the patterns of the representativeness metrics. We apply our methodology to the stations of the Baseline Surface Radiation Network. Overall, this study shows that representativeness is strongly dependent on local conditions and that all three metrics ( $\delta$ ,  $\beta$ , and  $\epsilon$ ) must be considered for a comprehensive assessment of representativeness.*

## Plain Language Summary

*Station-based observations are the most robust way to measure the amount of solar radiation reaching the Earth's surface (surface solar radiation [SSR]). These measurements are point observations yet are often used in combination with satellite or model data (e.g., for validation or for derivation of other quantities). The latter have a typical spatial extent up to a few hundred kilometers. Thus, it is important that the point observations are representative of this large area. In this paper, we show that the representativeness of SSR point observations varies regionally and is strongly dependent on local conditions. We find that some regions are problematic in terms of representativeness. However, in most regions SSR point observations can be considered representative for a 1-degree grid. We quantified additional uncertainties, which have to be taken into account when combining point and gridded data.*



### 3.1 Introduction

For downwelling surface solar radiation (SSR) the combination of point data with gridded data products is of interest to validate satellite-derived and modeled data products by using station-based observations as reference (e.g., Shuttleworth and Dickinson, 1989; Garratt et al., 1993; Garratt, 1994; Wild et al., 1995; Hatzianastassiou et al., 2005; Wild et al., 2006; Bodas-Salcedo et al., 2008; Freidenreich and Ramaswamy, 2011; Kato et al., 2012a,b; Zhang et al., 2013; Rutan et al., 2015; Folini and Wild, 2015; Zhang et al., 2015) or to compute derived energy fluxes in the climate system (Hakuba et al., 2014b). The combination of point and gridded data, however, generally raises the question, to what extent the point data is representative of the area covered by the colocated pixel of the gridded data and whether additional uncertainties have to be taken into consideration. Typically, the SSR point data is used without further quantifying uncertainties that arise from imperfect spatial representativeness of the SSR point data as it is cumbersome to quantify such effects. Combining point and gridded SSR data is, nevertheless, legitimate from the point of view that well maintained in-situ SSR measurements are the most accurate, precise and robust way to determine SSR. But, neglecting representativeness issues may substantially affect the outcomes and conclusions from such studies.

Different facets about the question of representativeness of SSR point observations have been addressed in previous studies, covering different spatial and temporal scales, different geographic regions, concerning different variables, and using different metrics to quantify representativeness (Long and Ackerman, 1995; Barnett et al., 1998; Zelenka et al., 1999; Li et al., 2005; Deneke et al., 2009; Journée et al., 2012; Hakuba et al., 2013a, 2014a; Huang et al., 2016; Lohmann et al., 2016; Schutgens et al., 2016b; Madhavan et al., 2017; Schwarz et al., 2017). Three popular measures, to be used also in the present study, are the decorrelation length ( $\delta$ , Schwarz et al. 2017), the climatological mean bias ( $\beta$ , Hakuba et al. 2013a, 2014a), and the nonclimatological error ( $\epsilon$ , Schwarz et al. 2017).

The climatological (or multiannual) mean time scale is advantageous in terms of representativeness as temporal variations are averaged out and the remaining miss-match between point and gridded data can in principle be corrected. Hakuba et al. (2013a, 2014a) showed (for Europe and the Meteosat disk) that SSR point observations can be biased with respect to colocated gridded data depending on the position of the point observation within the colocated grid boxes. Knowledge about systematic differences (i.e., biases) between point and gridded data can, however, be used to correct the point data to better represent the area of the colocated gridded data point. Such bias correction was applied by Hakuba et al. (2014b) in order to most accurately study climatological absorption of solar energy in the atmosphere over Europe by combining surface point observations with satellite-derived gridded top-of-the-atmosphere flux data, and surface albedo data.

For time scales where temporal variability of the records are not averaged out but serve

as the main feature, also other aspects of representativeness (besides systematic differences) have to be considered. For short time scales from minutes to days, some studies (e.g. Long and Ackerman, 1995; Barnett et al., 1998; Zelenka et al., 1999; Li et al., 2005; Deneke et al., 2009; Journée et al., 2012; Lohmann et al., 2016; Huang et al., 2016; Madhavan et al., 2017) investigated the representativeness of point data. These studies use dense station networks (Long and Ackerman, 1995; Barnett et al., 1998; Zelenka et al., 1999; Lohmann et al., 2016; Huang et al., 2016; Madhavan et al., 2017) and/or high-resolution satellite derived SSR data (Li et al., 2005; Deneke et al., 2009; Journée et al., 2012) to determine the covariability of the (often normalized) SSR records between sites as a function of the distance between the sites. Li et al. (2005), Deneke et al. (2005), Huang et al. (2016) and Madhavan et al. (2017) showed that longer temporal averaging generally increases the spatial representativeness of SSR point observations. For daily averaged SSR the representativeness was found to be several kilometers around the observational site. Unfortunately, dense SSR measurement networks are scarce which hinders conclusions in regions without such extensive measurement efforts. Also, the observational periods of those networks are often limited to a relatively short time span, which prohibits analyzing spatial representativeness for longer averaging intervals such as months and years.

To study representativeness of SSR on monthly to annual time scales Schwarz et al. (2017) utilized 149 ground-based decadal long SSR records from Europe. With a purely station based analysis, they could show that monthly mean SSR from such observations can be considered representative of an area with radius 400 km around the sites. They compared their station based results to satellite-derived representativeness estimates and found that the satellite-derived representativeness patterns match the station based ones very well. They could, therefore, utilize the satellite-derived SSR data to show that an additional error term has to be taken into account when using SSR point data in combination with 1-degree gridded data. For Europe and a 1-degree reference grid, they find that this error term is of the same magnitude as typical in-situ measurement errors.

This study aims to answer the question whether the findings of Hakuba et al. (2013a, 2014a) for climatological means over Europe and the Meteosat disk, as well as the results by Schwarz et al. (2017) for monthly mean time series in Europe, are applicable globally or whether regional differences in the representativeness of SSR point observations on these time scales occur. This main research question is addressed by applying existing concepts of representativeness on different high-resolution data sets, which altogether lead to a near-global (50°S-55°N) coverage. We build upon the results of Schwarz et al. (2017) that high-resolution SSR satellite products reproduce the spatiotemporal structure of SSR sufficiently well to allow estimates about the representativeness also in regions where surface measurements are scarce. We will argue, based on our analysis, that some regions are less suited for combining point with gridded SSR data. We, moreover, examine to what degree cloud cover and terrain features can explain the regionally different representativeness.

This study is structured as follows: section 3.2 introduces the SSR data sets and defines the metrics (i.e., the decorrelation length, the spatial sampling bias, and the spatial sampling error) by which we quantify representativeness. The results for these metrics are presented in section 3.3. In section 3.4 the robustness of results across the used data sets, the impact of different target grid sizes, and the benefit from bias corrections are shown. To which extend cloud cover and terrain data can explain the spatial patterns of the representativeness metrics is shown in section 3.5. Section 3.6 is a case study, which applies the results of this study to the specific case of the Baseline Surface Radiation Network (BSRN). Finally, section 3.7 provides a summary and conclusions.

## 3.2 Data and methods

### 3.2.1 High-resolution satellite-derived SSR data

Three SSR data sets provided by the Satellite Application Facility on Climate Monitoring (CM-SAF) of the European Organization for the Exploitation of Meteorological Satellites (EUMETSAT) are used in this study. All data sets use a retrieval which combines satellite measurements of back-scattered shortwave radiation and radiation transfer modeling to infer SSR (a detailed description of the retrieval can be found in Müller et al. 2009 and Müller et al. 2012). Beside satellite measurements of back-scattered shortwave radiation, the CM-SAF uses auxiliary data for surface albedo, aerosols, total column ozone and water vapor in their retrieval. For water vapor the CM-SAF utilizes ERA-Interim monthly reanalysis data, whereas climatological values are used in the radiation transfer modeling for surface albedo, aerosols and total column ozone (Huld et al., 2016; Pfeifroth et al., 2017; Karlsson et al., 2017a). Using climatologies for those variables might lead to some underestimation in the spatiotemporal variability of the SSR fields. We, therefore, note that our representativeness estimates might overestimate the representativeness.

The main data set we use in this study is the CM-SAF cloud, albedo and surface radiation data set (Edition 2; hereafter referred to as CLARA; Karlsson et al. 2017b). It is based on instantaneous global area coverage (GAC) retrievals from the advanced very high-resolution radiometer (AVHRR) on-board of the polar-orbiting National Oceanic and Atmospheric Administration (NOAA) satellites (Karlsson et al., 2017a,b).

The data set is available from 1983 to 2015 with monthly mean temporal resolution and a spatial resolution of  $0.25^\circ$ . We use data between  $50^\circ\text{S}$  and  $55^\circ\text{N}$  and from 2001 onward as from then on at least two satellites are available for the daily AVHRR observations, which results in a high spatial and temporal data coverage (Karlsson et al., 2013).

Moreover, two surface solar radiation data sets based on the Heliosat method (SARAH) are used in this study. Both data sets are based on observations from geostationary Meteosat satellites. The data sets have a very high spatial resolution of  $0.05^\circ$  and are provided in

hourly, daily and monthly temporal resolution. The prime SARAH data set (Edition 2; hereafter referred to as SARAH-P; Pfeifroth et al. 2017) is available from 1983 to 2015 and covers a disk region of  $\pm 65^\circ$  around the nadir point of the Meteosat prime satellites, which is at the cutting point between the zero meridian and the equator (i.e., the Meteosat disk). The SARAH-East data set (Edition 1; hereafter referred to as SARAH-E; Huld et al. 2016) is available for the period 1999-2015 with one missing year in 2006. The spatial domain covers a disk region of  $\pm 65^\circ$  around the nadir point of the satellites, which was at  $63^\circ$  E for the period from 1999 to 2006 and at  $57^\circ$  E for the period 2007-2015.

The SARAH data sets originate from observations of the geostationary Meteosat satellites with high spatial resolution and high temporal sampling rates (up to four complete disk scans per hour). The geostationary orbit limits, however, the spatial coverage of the SARAH products. As the SARAH data is only available for the two Meteosat disks we use CLARA data, which originates from AVHRR observations from sun-synchronous polar orbiting satellites, to achieve a near-global data coverage. The drawback of the polar orbiting satellites is that the temporal sampling is lower compared to the geostationary orbits (each point on the Earth surface is sampled twice a day), which potentially limits the accuracy of the data. Also, the spatial resolution of the CLARA data set is lower than the one from SARAH. We will show in section 3.3, however, that these differences do not drastically change the results for the metrics introduced in the next section.

We note, that several studies, which analyzed in-situ SSR measurements, underpin the use of satellite-derived SSR for representative estimates. More specifically, it has been shown that already hourly averaged SSR measurements are representative for an area up to a few kilometers (Long and Ackerman, 1995; Madhavan et al., 2017) and that temporal averaging generally increases the representativeness of SSR measurements (Li et al., 2005; Deneke et al., 2005; Huang et al., 2016; Madhavan et al., 2017). We, therefore, argue that the spatial resolution of  $0.05^\circ$  ( $0.25^\circ$ ), which roughly corresponds to 6 (30) km on the Earth's surface, is sufficient to capture spatiotemporal variations of monthly mean SSR at a single site. Schwarz et al. (2017) moreover showed that the spatial correlation patterns calculated from monthly mean time series of in-situ SSR observations agree very well with the patterns calculated from high-resolution satellite-derived SSR data over Europe which shows that satellite-derived SSR reasonably well reproduces the general spatiotemporal structure of the real SSR field. Based on the results of the above-mentioned studies we are confident that using pixel-based high-resolution satellite-derived monthly mean SSR as surrogate for point observations is acceptable to infer the addressed research questions.

### 3.2.2 Representativeness metrics

The metrics we use to quantify representativeness were essentially established by Hakuba et al. (2013a) and Schwarz et al. (2017) and will be explained in detail in this section. We apply their concepts of decorrelation lengths ( $\delta$ ), spatial sampling biases ( $\beta$ ), and spatial

sampling errors ( $\epsilon$ ) to quantify the representativeness of point observation on near-global scale and to identify possible regional differences. We use the 1-degree regular grid from the Clouds and the Earth's Radiant Energy System (CERES, Loeb et al. (2002)) program as the main target grid. Our goal is to quantify regional differences in the uncertainty that arises if a single point measurement (i.e., a pixel) within a 1-degree CERES grid box is used to describe the temporal variations of that 1-degree grid box.

The first metric,  $\delta$ , is of interest as it is used in the literature to quantify the area for which a measured time series is representative. Also, it is a crucial metric for the combination of point and gridded SSR data since such a combination would be inappropriate if  $\delta$  is small in comparison to the typical spatial scale of the gridded data. The other two metrics,  $\beta$  and  $\epsilon$ , are useful as they provide uncertainty estimates in  $W/m^2$ , the units of the SSR data as such.

In this study, we discriminate between pixels and grid boxes. The smallest spatial entities of a (gridded) data set are referred to as pixels (indicated by subscript P). Grid boxes (indicated by subscript G) refer to 1-degree CERES grid boxes, which are calculated by spatially aggregating all pixels within the 1-degree CERES box. In other words, a grid box refers to the mean of all pixels inside a 1-degree CERES grid box. We evaluate the above measures, for pairs of pixels (pixel-to-pixel; used for  $\delta$ ) or pairs of pixel and associated grid box (pixel-to-box; used for  $\beta$  and  $\epsilon$ ), before we aggregate them into grid box specific (uncertainty) estimates.

Wherever possible and practicable we use a rather strict significance level of 95%. We, however, lower the significance to the 68.2% level for the grid box specific metrics (i.e.,  $\beta_G$  and  $\epsilon_G$ ; see section 3.2.2 and 3.2.2) to be able to conduct a valid comparison between the different data sets.

### Decorrelation length

Similar to Schwarz et al. (2017), correlation patterns for each pixel of the data sets are calculated. For each pixel, the correlations (in terms of squared Pearson correlation coefficient,  $R^2$ ) between the monthly mean deseasonalized time series of this pixel and the time series of the surrounding pixels are calculated. This reveals how synchronous SSR variations of the considered pixel are with respect to its surrounding pixels.

Generally, as one would expect, the patterns arising from these pixel-to-pixel correlations show very high correlations ( $R^2 \approx 1$ ) in close proximity of the considered pixel with a decreasing correlation with increasing distance (see also Schwarz et al., 2017). However, the decrease is not strictly uniform in each direction for all pixels, as the correlations are substantially modulated by external factors such as local topographic features and persistent synoptic-scale weather patterns (see also Dutton et al., 2006; Schwarz et al., 2017). Here we neglect such directional differences and calculate the average distance over all directions at which  $R^2$  drops below  $1/e$  and define this distance as the decorrelation length for the considered pixel ( $\delta_P$ ). This distance can be regarded as the spatial extent up to which the temporal

variability in SSR for a larger area is captured by observations at a single point. We provide  $\delta$  in units of degrees ( $^\circ$ ) along a great circle. Any given  $\delta$  can be easily translated into a distance in kilometers by multiplying with 111 km.

Likewise, from  $\delta_P$  the correlation  $R^2$  for any distance of  $x$  can be estimated with  $R^2(x, \delta_P) = 1 - x * \frac{1-1/\epsilon}{\delta_P}$ . Here we assume that  $R^2$  decreases linearly with distance from  $R^2 = 1$  at zero distance, an assumption Schwarz et al. (2017) show to hold to a high degree in Europe for  $x < \delta_P$ .

To estimate the average decorrelation length within a 1-degree grid box ( $\delta_G$ ), we simply average all  $\delta_P$  values within that box.

### Bias and error from decomposition of SSR time series

Before we define  $\beta$  and  $\epsilon$  in a mathematically appropriate and concise manner in the sections 3.2.2 and 3.2.2, we demonstrate their physical interpretation by examining an idealized case study based on SARAH-P data.

A monthly mean SSR time series,  $SSR(t)$ , can be decomposed into a climatological contribution (i.e., low frequency contribution), consisting of the long-term mean  $\overline{SSR}$  and a climatological seasonal cycle  $\widetilde{SSR}$  (which varies around  $\overline{SSR}$  and whose long-term average is zero), and the deviation (anomaly) from this climatological value  $SSR'(t)$  (i.e., the high-frequency contribution):

$$SSR(t) = \overline{SSR} + \widetilde{SSR} + SSR'(t) \quad (3.1)$$

Consider two SSR time series  $P(t)$  and  $G(t)$  decomposed according to Equation (3.1). If subtracted from each other, their difference can be split into a contribution from the climatological signal and the difference of the high-frequency part. More specifically, if  $P(t)$  is a time series of a pixel within a 1-degree box and  $G(t)$  the time series of spatially average SSR of that grid box, we designate the difference between the climatological contributions of the two time series as bias (i.e.,  $\beta_P$ , see section 3.2.2) and the difference in the high-frequency part as error (i.e.,  $\epsilon_P$ , see section 3.2.2):

$$B(t) - G(t) = \underbrace{\overline{G} - \overline{P}}_{\Rightarrow \beta_P} + \underbrace{\widetilde{G} - \widetilde{P}}_{\Rightarrow \widetilde{\beta}_P} + \underbrace{G'(t) - P'(t)}_{\Rightarrow \epsilon_P} \quad (3.2)$$

$$\underbrace{\hspace{10em}}_{\widetilde{\beta}_P}$$

We consider the sum of climatological difference and the difference in the annual cycle between the pixel and the grid box as a systematic difference ( $\widehat{\beta}_P = \beta_P + \widetilde{\beta}_P$ ), which in principle can be corrected (Hakuba et al., 2014a). During this study, we will for simplicity not explicitly show the bias contribution  $\widetilde{\beta}_P$  from the difference in the annual cycle.  $\widetilde{\beta}_P$  should, however, be taken into account as it will increase  $\epsilon_P$  by roughly 14% if it is neglected as we will show in section 3.4.3. The difference  $\epsilon_P$  from the high-frequency contributions cannot

be corrected as its occurrence is random.

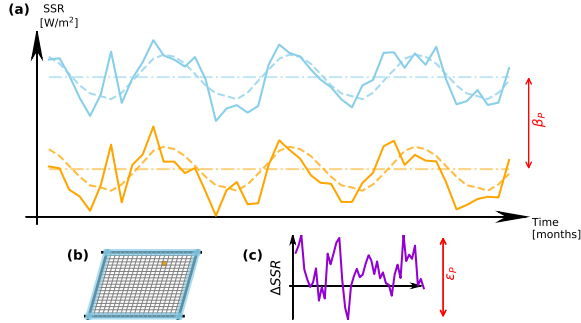


**Figure 3.1:** Illustration of  $\beta_p$  and  $\epsilon_p$  from decomposed SSR time series after Equation (3.1) from SARAHP-SSR data. Panel (a) shows the decomposed SSR time series from a pixel and a grid box. The continuous lines show the monthly time series, the dot-dashed lines show the climatological means, and the dashed lines show the monthly climatological cycle. Orange colors correspond to a SSR time series of a pixel, while the blue colors correspond to a grid box mean as indicated in (b). The violet line in (c) shows the differences of the anomalies of the two SSR time series shown (i.e.,  $G'(t) - P'(t)$  from Equation(3.2)).  $\beta_p$  and  $\epsilon_p$  are indicated by red arrows in (a) and (c), respectively. Note, that the contributions from the climatological annual cycle and the anomaly are weighted by a factor of  $1/400$  and  $1/100$  in (a) to make  $\beta_p$  and  $\epsilon_p$  better visible.

Figure 3.1 exemplarily shows the decomposition of SSR for a pixel and a grid box from SARAHP data. It illustrates that the differences in the climatological values of the two time series lead to  $\beta_p$  (Figure 3.1a) and that the differences in the anomalies of the time series lead to  $\epsilon_p$  (Figure 3.1c).

### Spatial sampling bias

The spatial sampling bias for each individual pixel ( $\beta_p$ ) with respect to the 1-degree CERES grid is defined as the deviation of the SSR climatological long-term mean of the pixel ( $\overline{SSR_p}$ ) from its collocated climatological mean of the grid box ( $\overline{SSR_G}$ ):

$$\beta_p = \overline{SSR_p} - \overline{SSR_G} \quad (3.3)$$

The box average ( $\overline{SSR_G}$ ) is thereby calculated by averaging  $\overline{SSR_p}$  of all pixels in a 1-degree box. In order to be able to provide a single bias estimate (and not twelve), we do not show possible influences of the climatological annual cycle on  $\beta$ . We come back to this point in section 3.4.3.

To quantify the magnitude of a typical  $\beta_p$  value for each 1-degree box (hereafter referred to as  $\beta_G$ ) we calculate the standard deviation of the  $\beta_p$  values of all  $N$  pixels within a 1-degree

box:

$$\beta_G = \sqrt{\frac{1}{N} \sum_{p=1}^N (\beta_p - \langle \beta_p \rangle)^2} = \sqrt{\frac{1}{N} \sum_{p=1}^N (\beta_p)^2} \quad (3.4)$$

where  $\langle \beta_p \rangle$  is the average of all  $\beta_p$  values in a grid box (which is equal to zero). The  $\beta_G$  is similar to the measure used in Hakuba et al. (2013a, 2014a) except that we use the standard deviation instead of the mean absolute deviation ( $MAD = 1/N \sum_p (|\beta_p - \overline{\beta_p}|)$ ) as measure for the subgrid variability. This choice was made as one can easily recalculate the  $\beta_G$  for any other significance level using z-values when assuming that the  $\beta_p$  values inside a grid box are normally distributed (as done e.g., in Folini et al., 2017).

### Spatial sampling error

We quantify  $\epsilon_P$  rather rigorously as the 95% percentile ( $P^{95}$ ) of the absolute differences between monthly deseasonalized SSR time series of a pixel ( $SSR'_P(t)$ ) and the corresponding monthly deseasonalized box mean time series ( $SSR'_G(t)$ ):

$$\epsilon_P = P^{95}(|SSR'_P(t) - SSR'_G(t)|) \quad (3.5)$$

Note that our data coverage (between 14 years for CLARA and 32 years for SARAHP, see section 3.2.1) is such that the 95% percentile, albeit a rather strict measure, still translates into about 8 to 20 months worth of data.

To spatially aggregate the  $\epsilon_P$  into values specific to their respective 1-degree boxes ( $\epsilon_G$ ) we use the 68.2% percentile of all  $\epsilon_P$  values in a grid box:

$$\epsilon_G = P^{68.2}(\epsilon_P). \quad (3.6)$$

$\epsilon_G$  is similar to the measure used in Schwarz et al. (2017) except that we use the 68.2% percentile instead of the 95% percentile range for the spatial aggregation. The choice ensures that enough pixels per 1-degree box are available for each data set as in particular the CLARA data set with a 0.25° resolution has only 16 pixels per 1-degree box.

### 3.3 Representativeness: Quantitative estimates

In this section, we present all results for the metrics described in section 3.2.2 based on the near-globally available CLARA data. We will especially focus on regional differences of the discussed metrics on global scale. In the last part of this section, we provide a comprehensive view by bringing together all three representativeness metrics.



## 3.3.1 Decorrelation length

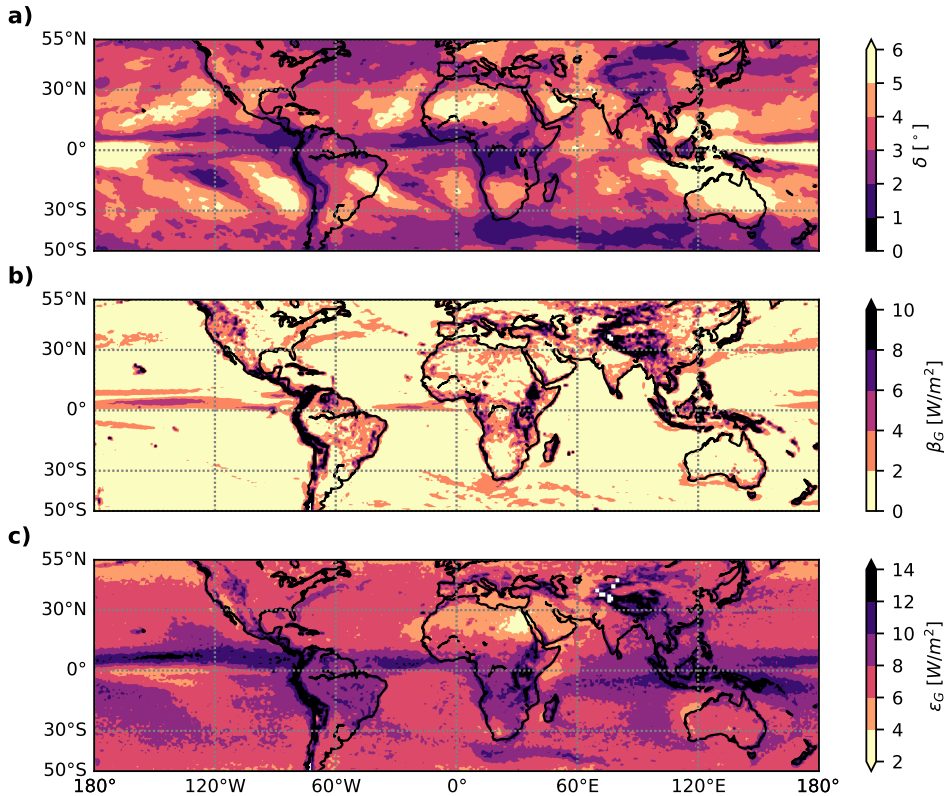


**Figure 3.2:** Estimates for the decorrelation length ( $\delta$ , panel a), the spatial sampling bias ( $\beta_G$ , panel b)), and the spatial sampling error ( $\epsilon_G$ , panel c)) with respect to the 1-degree CERES grid based on CLARA data. Bright/dark colors indicate higher/lower correlations (a) and lower/higher biases and errors (b and c). Thus, bright colors indicate good representativeness.

Figure 3.2a shows  $\delta_G$  calculated from CLARA data. The map reveals that there are quite some regional differences throughout the observational domain. The global mean  $\delta_G$  is  $3.36^\circ$  (see also Table 3.1).

Which value of  $\delta$  is deemed acceptable is certainly debatable and highly dependent on the concrete application. For the aim of combining time series of point and 1-degree gridded data, however, we argue based on the linear approximation for point-to-point correlation introduced in section 3.2.2, that  $\delta < 1^\circ$ , is insufficient and  $1^\circ \leq \delta < 2^\circ$  is problematic. In the best case, that the considered site is exactly in the center of the colocated 1-degree grid box, the squared correlation between the center pixel and the pixels at the edge of the 1-degree

**Table 3.1:** Domain Median (First Three Rows) and Median Differences of the Overlapping Area From the Corresponding Data Sets (Last Three Rows) for  $\delta_G$ ,  $\beta_G$ , and  $\epsilon_G$

Data	$\delta_G$ [°]	$\beta_G$ [W/m <sup>2</sup> ]	$\epsilon_G$ [ W/m <sup>2</sup> ]
CLARA	3.36 (2.39, 4.50)	1.39 (0.67, 3.08)	7.58 (6.32, 9.39)
SARAH-P	3.31 (2.41, 4.36)	1.33 (0.57, 2.69)	6.96 (5.56, 9.06)
SARAH-E	3.21 (2.00, 4.23)	1.43 (0.66, 3.61)	7.75 (5.82, 9.95)
CLARA - SARAH-P	-0.17 (-0.56, 0.22)	0.02 (-0.33, 0.49)	0.41 (-0.45, 1.08)
CLARA - SARAH-E	0.05 (-0.30, 0.55)	-0.02 (-0.59, 0.57)	0.23 (-1.08, 0.91)
SARAH-P - SARAH-E	0.20 (-0.16, 0.74)	-0.03 (-0.28, 0.23)	0.05 (-0.63, 0.70)

Note.  $1\sigma$  confidence intervals are given in brackets.

box ( $x = \sqrt{0.5^2 + 0.5^2}$ ) is roughly 0.55 for  $\delta = 1$  and 0.78 for  $\delta = 2$ . This means that two time series which are within the same 1-degree grid box are already substantially out of sync, and thus, the time series are hardly representative of each other. If the SSR from points within a 1-degree grid box are out of sync, time series analysis becomes problematic as there is no option to correct for this deficit.

Considering smaller  $\delta_G$  values, only 8.0% (0.3)% of the CLARA pixels show a  $\delta_G$  less than 2 degrees (1 degree). The very small  $\delta_G$  values can mainly be found in the mountainous regions of the Andes, the Himalayan region and the Malay Archipelago (i.e., the Southeast Asian islands); in the equatorial regions of Africa and South America; and in the oceanic region south of 35° S between Africa and New Zealand. Generally, however,  $\delta_G$  is significantly larger than one degree in most areas around the globe.

For Europe,  $\delta_G$  is roughly 4–5° and, therefore, very similar to the value found by Schwarz et al. (2017) who used station based SSR surface observations to infer  $\delta$ . Other regions besides Europe with remarkably high  $\delta$ s are the United States, India, and China. As SSR in all these regions is substantially affected by aerosol changes (e.g., Wild, 2009a; Yoon et al., 2014) this regions are particularly interesting in terms of SSR and energy balance research. The large  $\delta$  values found in these regions suggest that already a small number of surface observation sites in those regions is sufficient to sample SSR variations there. This fits with Sanchez-Lorenzo et al. (2015), who found that 5 stations already capture essentially the same decadal variation in Europe as a more comprehensive set of 50 stations.

Regions with very large  $\delta_G$  values ( $\delta_G > 5^\circ$ ) are the Sahara, the Arabian Peninsula, parts of Brazil, the Pacific region west of Chile, and the El Niño–Southern Oscillation (ENSO) region including Australia and parts of Indonesia. For the ENSO region, we also find teleconnections, meaning that there are high correlations with positive and negative signs throughout the region as is exemplarily shown in Figure 3.3 (note that we show correlation coefficients [r] and not squared ones [ $R^2$ ] as used for the calculation of  $\delta$ ). The finding of positive and negative correlations of SSR in the ENSO region is in line with previous studies that focused on the impact of ENSO on SSR (e.g., Pavlakakis et al., 2008; Pinker et al., 2017; Stephens et al., 2018). As these studies either used modeled SSR, satellite-derived SSR estimates with coarse resolution, or SSR from reanalysis, our finding can be counted as additional evidence

based on high-resolution satellite data for the strong influence of ENSO on SSR. Figure 3.3 also exemplarily shows that the correlation coefficients do not decrease uniformly in each direction. For the specific correlation pattern shown here, the longitudinal extension is much larger than the latitudinal, likely due to the general structure of the ENSO phenomenon.

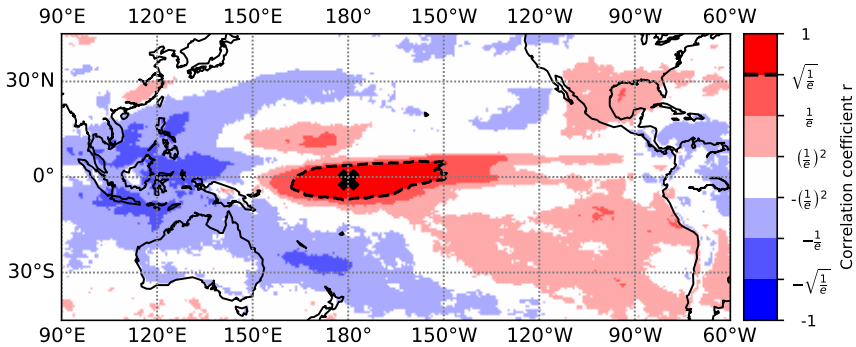


**Figure 3.3:** Correlation map for the El Niño–Southern Oscillation (ENSO) region based on CLARA data. Shown is the correlation between the deseasonalized monthly surface solar radiation at  $180^\circ$  W,  $0^\circ$  N (black cross) with its larger surrounding. Red (blue) colors indicate positive (negative) correlation coefficients. The dashed line corresponds to the  $r = \sqrt{1/e}$  line, which indicates the decorrelation distance (i.e.,  $R^2 < 1/e$ ).

### 3.3.2 Spatial sampling bias

For the Meteosat disk, and hence for the SARAH-P data set,  $\beta$  was already quantified by Hakuba et al. (2014a). Here, we extend their concepts to the CLARA (see below) and SARAH-E data (see section 3.4) and thus to near-global scales. For completeness and to be able to check the consistency between the data sets we also show  $\beta$  for SARAH-P data with the now longer available data coverage (see section 3.4).

The map for  $\beta_G$  calculated from the CLARA data is shown in Figure 3.2b. We find a median  $\beta_G$  of around  $1.4 \text{ W/m}^2$  as can be seen in Table 3.1.

Generally, mountainous regions and some coastal regions have higher  $\beta_G$  than regions in more homogeneous terrain. Over oceans  $\beta_G$  is small except in the tropical regions, where  $\beta_G$  is somewhat higher compared to the rest of the ocean basins.

Typically, the  $\beta_P$  values within a 1-degree box of the reference grid have an equator-to-pole gradient with more positive (negative)  $\beta_P$  for those pixels that are more equatorward (poleward) than the center of the 1-degree box (not shown). This gradient arises as the more equatorward (poleward) pixels generally have higher (lower) climatological SSR because of the strong latitudinal dependence of SSR. This general pattern is, however, modulated by topography, persistent cloud fields, and other features (Hakuba et al., 2013a).

### 3.3.3 Spatial sampling error

The map of  $\epsilon_G$  as calculated from the CLARA data is shown in Figure 3.2c. The domain median for  $\epsilon_G$  from the CLARA data is  $7.6 \text{ W/m}^2$  (see also Table 3.1). Concerning the upper limit of  $\epsilon_G$ , 95% of the 1-degree boxes from the CLARA data give  $\epsilon_G$  smaller than  $11.2 \text{ W/m}^2$ .

Regarding regional patterns, similar features as for  $\delta_G$  and  $\beta_G$  can be identified where mountainous regions and some coastlines have larger  $\epsilon_G$  values. Besides mountainous regions, the tropics show clearly higher  $\epsilon_G$  values compared to the CLARA domain median of  $7.6 \text{ W/m}^2$ . Particularly interesting in this context is, for instance, the ENSO region. Although the highest  $\delta$  values have been found for that region (see Figure 3.2a) also very large  $\epsilon_G$  values are found there. This example shows that  $\delta$  alone is not a sufficient measure for representativeness and that also other representativeness metrics have to be taken into account.

The subgrid structure of  $\epsilon_P$  is different than the one of  $\beta_P$ . Instead of an equator-to-pole gradient (which was found for  $\beta_P$ ) we rather find concentric patterns with smallest errors in the center of the 1-degree boxes and larger errors further away from the center (not shown). Again, there is modulation to this general behavior by topography, notably mountains and coast lines.

As  $\epsilon_P$  is not correctable it is interesting for an error budget calculation to know whether the  $\epsilon_P$  or the observational measurement uncertainty of state-of-the-art pyranometers is the dominant error term. The operational measurement uncertainty of monthly mean SSR measurements was estimated by (a) Gilgen et al. (1998) to be 5% of the monthly SSR (based on root-mean-square errors and therefore on the  $1\sigma$ -level) and by (b) Dutton et al. (2012) to be  $8 \text{ W/m}^2$  (95%-level). The median  $\epsilon_G$  of roughly  $7.6 \text{ W/m}^2$  is, therefore, similar to these literature values.

Assuming that both error terms are uncorrelated and random, a total error can be computed by calculating the root of the sum of all squared error terms. Adding up the literature values for the uncertainty of ground-based SSR measurement devices (i.e.,  $8 \text{ W/m}^2$ ; see above) and the typical sampling error estimate (i.e., the median  $\epsilon_G$ ) the overall error for monthly means becomes roughly 40% larger compared to the pure ground-based measurement device uncertainty. This estimate, however, implies that a rigorous bias correction was applied before combining gridded and point data (the benefits from applying bias corrections are shown in section 3.4.3).

We note that the given median  $\epsilon_G$  value is not uniformly applicable to any location on the Earth's surface, since substantial regional differences occur, as can clearly be seen in Figure 3.2c. Moreover, the  $\epsilon_G$  value should also not carelessly be taken as a valid error measurement for a specific location as it describes the typical error (see section 3.2.2) for all the pixels within a 1-degree box. Depending on the position of a station with respect to the 1-degree grid, the location-specific error (i.e.,  $\epsilon_P$ ) and can be substantially larger (or smaller) than the

$\epsilon_G$ . We, therefore, recommend using location-specific values whenever possible. Note, that the same argumentation is also valid for  $\beta$ .

### 3.3.4 Comprehensive view on representativeness metrics

After showing the results of the three representativeness metrics separately, we now bring the findings together. Depending on the specific application a different set of metrics has to be considered. For the specific task of combining time series of monthly SSR point data with time series of 1-degree gridded data all, shown metrics must be considered. However, when the combination of point and gridded SSR data is used to study climatological SSR,  $\beta_G$  becomes the most important metric while the other two may be neglected.

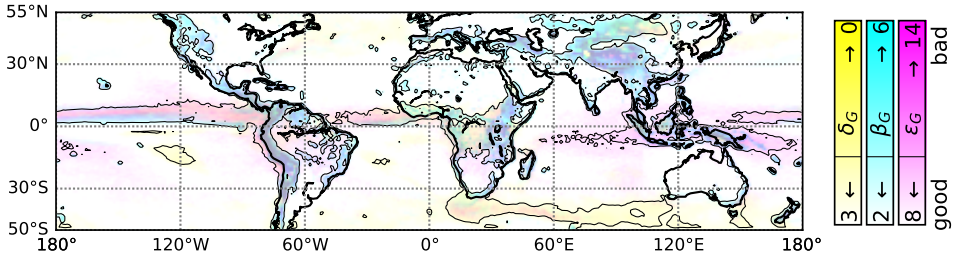
First, we note that the pattern correlations among the  $\delta_G$ ,  $\beta_G$  and  $\epsilon_G$  maps derived from CLARA data are relatively small. The pattern correlation coefficient between the one degree averaged  $\delta_G$  and  $\epsilon_G$  ( $\delta_G$  and  $\beta_G$ ) is  $r = -0.24$  ( $r = -0.25$ ). The pattern correlation between  $\beta_G$  and  $\epsilon_G$  is  $r = 0.57$ . This relatively small correlations highlight that all three metrics must be considered if a comprehensive conclusion about representativeness at a certain point should be drawn.

Figure 3.4 shows a combined map for  $\delta_G$ ,  $\beta_G$ , and  $\epsilon_G$ . For each metric, we specify a value range which classifies if the considered metric is problematic at a specific location. The choice of the value range is based on the discussions in the previous sections. As outlined in section 3.3.1,  $\delta < 1^\circ$  is insufficient and  $1^\circ \leq \delta < 2^\circ$  is problematic when aiming to combine point with 1-degree gridded data. Such low  $\delta$ s imply that a single point observation is hardly representative for the whole 1-degree box. Since this deficit cannot be corrected, regions with such low  $\delta$ s should be treated with special care. In contrast to that,  $\beta$  could in principle be corrected if it is known. We, therefore, define the value range that we consider as problematic rather generous and only consider  $\delta_G > 2 W/m^2$  as problematic. To define a value range for  $\epsilon$  we compare  $\epsilon_G$  to the uncertainty of monthly mean in-situ SSR measurements (i.e.,  $8 W/m^2$ ; Dutton et al., 2012) to determine which of the two error terms is the leading one.

Since we are addressing a very specific question, we note, that for some other questions other value ranges might be more meaningful. However, users who need different value ranges can always refer back to Figure 3.2 which shows the full range of all representativeness metrics individually.

Regions with  $\delta < 3^\circ$ ,  $\beta_G > 2W/m^2$ , and  $\epsilon > 8W/m^2$  are considered as problematic and are shown in color in Figure 3.4. The color saturation increases for worsening representativeness. For  $\delta_G = 0$ ,  $\beta_G > 8$  and  $\epsilon_G > 14$  the color saturation reaches 100%. If more than one representativeness metric is problematic the colors are mixed. Regions, where representativeness is good, are white (transparent).

The figure shows that different representativeness metrics limit the representativeness in different regions. In the tropical region, the representativeness is limited by relatively high



**Figure 3.4:** Color composite for the representativeness metrics  $\delta_G$  (yellow),  $\beta_G$  (cyan), and  $\epsilon_G$  (magenta). Colored regions are problematic with respect to the respective metric. Saturated colors indicate worse representativeness. Colors are mixed where more than one metric is considered problematic. The black contour shows if any metric is above 1/3 of its value's range.

$\epsilon_G$  and partly by low  $\delta_G$  values. Although  $\delta_G$  is highest in the ENSO region (as discussed in section 3.3.1), the high  $\epsilon_G$  limit the representativeness. In regions with complex topography,  $\delta_G$  and  $\epsilon_G$  are high.

### 3.4 Robustness of representativeness metrics

#### 3.4.1 Robustness across the data sets

In the following, we show that the results presented in section 3.3 are robust throughout all available high-resolution SSR data sets. The maps for the metrics computed based on CLARA data have already been introduced and are shown in Figure 3.2. The results based on SARAHP and SARAHE data are shown in Figure 3.5. Figure 3.5c is essentially a reproduction of Figure 2 of Hakuba et al. (2014a). The only differences are the observational periods considered and small differences in the calculation of  $\beta_G$  (we use the standard deviation while Hakuba et al. (2014a) used mean absolute deviations; see also section 3.2.2). We show it nevertheless to facilitate the comparison with the  $\beta_G$  estimates from the other data sets. The visual comparison of the different maps in Figures 3.2 and 3.5 already suggest overall good agreement of  $\delta$ ,  $\beta$  and  $\epsilon$  across all three data sets.

The panels a-c of Figure 3.6 show the cumulative distribution function for  $\delta_G$ ,  $\beta_G$ , and  $\epsilon_G$  for the whole observational domain of the CLARA, SARAHP, and SARAHE domain. Although the data sets cover different geographical regions, the cumulative distribution functions from the different data sets for the whole domain of the respective data sets and the respective domain medians and  $1\sigma$  confidence intervals (shown in Table 3.1) are very similar to each other.

For the regions where the data sets overlap, we calculate the differences in the estimates for the metrics as computed from the different data sets. Panels (d)–(f) of Figure 3.6 show

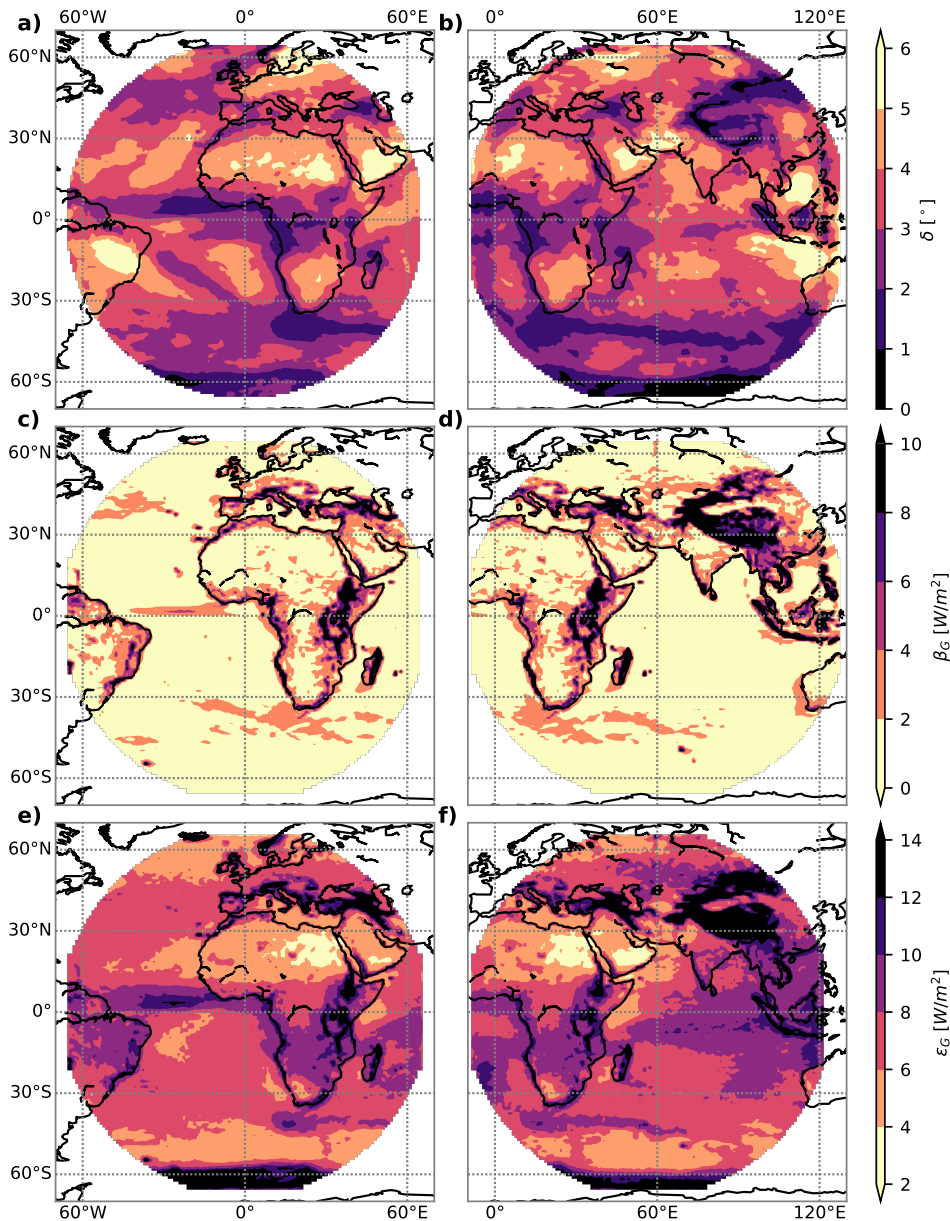


**Figure 3.5:** Estimates for the decorrelation length ( $\delta$ , panels (a) and (b)), the spatial sampling bias ( $\beta_G$ , panel c and d), and the spatial sampling error ( $\epsilon_G$ , panels (e) and (f)) with respect to the 1-degree CERES grid based on monthly SARA-P (a, c, and e) and SARA-E (b,d, and e) data. Bright/dark colors indicate higher/lower correlations (a and b) and lower/higher biases and errors (b-e).

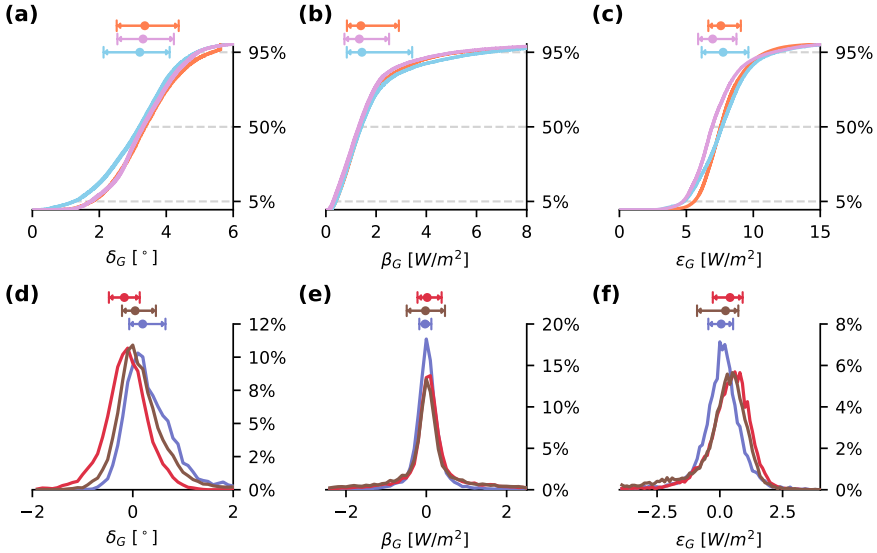


**Figure 3.6:** Cumulative distribution functions for  $\delta_G$  (a),  $\beta_G$  (b), and  $\epsilon_G$  (c) and probability density functions (PDFs) for the differences between data sets for  $\delta_G$  (d),  $\beta_G$  (e), and  $\epsilon_G$  (d). For the computation of the PDFs, only the overlapping areas of the corresponding data sets were considered. In panels (a)–(c) the cumulative distribution functions for CLARA (orange lines), SARAH-P (magenta lines), and SARAH-E (blue lines) data are shown. Panels (d)–(f) show PDFs of the differences of the overlapping area of CLARA and SARAH-P data (dark-red lines), CLARA and SARAH-E data (brown lines), and SARAH-P and SARAH-E data (dark-blue lines). The bars on top indicate the  $1\sigma$  confidence levels and the median (point) for the corresponding variable and data set. The corresponding numbers are shown in Table 3.1.

the probability density functions (PDF) for those differences. The median differences in the overlapping regions are close to zero (see also Table 3.1; the table also shows  $1\sigma$  confidence intervals).

Despite the different temporal sampling frequencies and the different spatial resolutions of the data sets used, only small differences in the representativeness metrics occur. This indicates that the data sets consistently reveal the general spatial structure of the metrics which we use to quantify spatial representativeness. We are, therefore, confident that using the CLARA data set to get a near-global perspective is acceptable although the CLARA data has a coarser spatial resolution than the SARAH data sets.

This is in line with Hakuba et al. (2014a) who showed (in their Figure 4) that  $\beta_G$  for a 1-degree grid has only a weak dependency on the resolution of the underlying data set and that only a small portion of the bias is not detected when using coarser data. They explicitly note that a data set with an even coarser spatial resolution of  $0.5^\circ$  (which is much coarser than



what we use in the global assessment) still can reproduce 75% of  $\beta_G$ . Hakuba et al. (2014a) explicitly noted that a global assessment of  $\beta$  is feasible with coarser data products than the one from SARAH data. Our findings show a similar robustness against the spatial scale of the underlying data for the nonclimatological, time series based metrics  $\delta$  and  $\epsilon$ .

### 3.4.2 Target grid sizes and their impact on the metrics presented

Although we focus on the 1-degree CERES grid, the globally high  $\delta$  would suggest that also data sets with coarser resolutions (e.g., such as those from current state of the art climate models, which range from  $1^\circ$  to  $3^\circ$ ) can be used in combination with SSR point observations. Using a coarser target grid would, however, increase the  $\epsilon$  and  $\beta$  estimates and require a reexamination of those estimates.

Using a coarser grid, such as a  $2.5 \times 2.5^\circ$  grid (which is comparable to the typical grid size of the climate models in the Coupled Model Intercomparison Project Phase 5 ensemble), for instance, would increase the domain median  $\epsilon_G$  (which is implicitly bias corrected) presented in section 3.3.3 by about 60% compared to the 1-degree grid (not shown, calculation based on CLARA data). Reducing the grid size to  $0.5 \times 0.5^\circ$  degree would, on the other hand, reduce the domain median  $\epsilon_G$  by 30% compared to the 1-degree grid (not shown, calculation based on SARAH-P data).

### 3.4.3 Benefits from bias correction

We now test the relative importance of different bias corrections (BC) to the value of  $\epsilon$ . To quantify the benefit of different BCs, we calculate  $\epsilon$  in three different ways: (i) for not bias-corrected SSR, (ii) for long-term mean (LTM-BC) bias-corrected SSR, (iii) for climatological seasonal cycle (CSC-BC) bias-corrected SSR. For the LTM-BC we use the  $\beta_P$  from section 3.3.2. For the CSC-BC, we calculate  $\beta_P$  for each month separately according to Equation (3.3). After the bias correction, we examine the difference in the domain-averaged improvement in  $\epsilon_P$  estimates for all data sets (i.e., we calculate the improvement in  $\epsilon_P$  per pixel before we calculate the domain average).

The domain-averaged improvements in the  $\epsilon_P$  estimates for all data sets are shown in Table 3.2. Using  $\epsilon_P$  from SSR data without bias correction as a starting point,  $\epsilon_P$  decreases on average by around 7% when using the LTM-BC and roughly 15% when applying the CSC-BC. Analyzing the improvements for land and sea separately shows that the bias correction improves land pixels substantially more (roughly 25% improvement) than those over sea (roughly 10% improvement).

Comparing  $\epsilon_P$  from the CSC-BC SSR data and the one calculated based on deseasonalized data (see section 3.3.3) shows that both lead to the same improvements compared to the not corrected data (not shown). Applying the CSC-BC thus comes very close to the optimal case. We, therefore, suggest using monthly bias correction when working with monthly data.

Following that argumentation, we note that  $\epsilon$  as presented in section 3.3.3 must be increased (on average) by roughly 15% (or 25% for land pixels) if no bias correction is applied.

Taking a different point of view, the above findings also show that (potentially correctable) sampling biases for a 1-degree grid tend to be smaller (about 15–25%) compared to uncorrectable sampling errors.

**Table 3.2:** Domain average absolute (in  $W/m^2$ ) and relative (in %) improvements in  $\epsilon_P$  for long-term mean bias-correction (LTM-BS) and climatological seasonal cycle bias-correction (CSC-BC) of SSR for all data sets.

Bias correction	Absolute changes [ $W/m^2$ ]			Relative changes [%]		
	CLARA	SARAH	SARAH	CLARA	SARAH	SARAH
<b>Land + Sea</b>						
LTM-BC	-0.85	-0.87	-1.22	-6.0	-7.2	-8.1
CSC-BC	-1.79	-1.57	-2.26	-14.3	-13.8	-16.5
<b>Land only</b>						
LTM-BC	-1.87	-1.67	-2.12	-10.7	-11.5	-12.2
CSC-BC	-3.85	-2.95	-3.84	-25.3	-22.0	-24.3
<b>Sea only</b>						
LTM-BC	-0.47	-0.46	-0.48	-4.3	-4.9	-4.8
CSC-BC	-1.02	-0.85	-0.98	-10.2	-9.4	-10.2

*Note.* Improvements are shown with respect to  $\epsilon_P$  from not bias-corrected SSR for land and sea, land only, and sea only.

### 3.5 Investigating potential explanatory variables

In this section, we ask the question to what degree the spatial patterns found for  $\delta$ ,  $\beta$ , and  $\epsilon$  can be explained by clouds or terrain characteristics.

As shown in section 3.3.4 the pattern correlations among the representativeness metrics are rather low. Due to the different patterns of the metrics, we also look at possible underlying causes for each metric separately. A thorough, quantitative analysis of physical causes and responses is beyond the scope of the present paper. Some interesting information can, however, already be obtained from a simple pattern correlation analysis. In particular, we quantify a variable's potential to explain an observed pattern in one of the representativeness metrics by calculating squared pattern correlations (PC2).

To facilitate a valid comparison between predictor (i.e., one of the possible explanatory variables) and predictand (i.e., one of the representativeness metrics) we calculate the metric of the considered predictand based on data from the predictor. For example, to test clear-sky SSR as predictor for  $\delta_G$  we first calculate  $\delta$  based on clear-sky SSR data only ( $\delta_G^{CS}$ ), before we calculate the PC2 between the two  $\delta$  fields. We apply the same principle to clear-sky SSR,

cloud fraction and terrain characteristics. For cloud fraction, we use monthly deseasonalized cloud fraction data for total, low, middle, and high clouds from the CLARA-A2 fractional cloud cover data (CFC-T, CFC-L, CFC-M, and CFC-H, respectively).

We use the Global 30 Arc-Second Elevation (GTOPO30) data set provided by the U.S. Geological Survey (USGS) which we downloaded with  $0.05^\circ$  resolution using NASA's Spatial Data Access Tool to quantify terrain characteristics. For each 1-degree grid box, we calculate the average height (AH) by simply averaging the elevations of the GTOPO30 pixels within the corresponding grid boxes and the relief energy (RE) by calculating the standard deviation of the elevations of all GTOPO30 pixels within a 1-degree CERES box.

**Table 3.3:** Squared pattern correlation (PC2) between the presented representativeness metrics ( $\delta_G$ ,  $\beta_G$ , and  $\epsilon_G$ ) and possible explanatory variables ( $\delta_G^i$ ,  $\beta_G^i$ ,  $\epsilon_G^i$ ).

	$\delta_G$	$\beta_G$	$\epsilon_G$
$\delta_G^{CS}$	0.20	—	—
$\beta_G^{CS}$	—	0.13	—
$\epsilon_G^{CS}$	—	—	0.05
$\delta_G^{CFC,T}$	0.54	—	—
$\beta_G^{CFC,T}$	—	0.52	—
$\epsilon_G^{CFC,T}$	—	—	0.18
$\delta_G^{CFC,L}$	0.08	—	—
$\beta_G^{CFC,L}$	—	0.18	—
$\epsilon_G^{CFC,L}$	—	—	0.04
$\delta_G^{CFC,M}$	0.05	—	—
$\beta_G^{CFC,M}$	—	0.47	—
$\epsilon_G^{CFC,M}$	—	—	0.19
$\delta_G^{CFC,H}$	0.26	—	—
$\beta_G^{CFC,H}$	—	0.19	—
$\epsilon_G^{CFC,H}$	—	—	0.23
AH	0.08	0.28	0.16
RE	0.07	0.52	0.21

Note. Explanatory variables ( $\delta_G^i$ ,  $\beta_G^i$ ,  $\epsilon_G^i$ ) are calculated based on data of clear-sky surface solar radiation data (CS); cloud fraction for total, low, middle, and high clouds (CFC-T, CFC-L, CFC-M, and CFC-H); average height (AH); or relief energy (RE).

Table 3.3 shows the PC2 values for all considered fields. A first test to examine to which extent clouds influence the spatial structure of the representativeness metrics was performed by calculating the representativeness metrics using monthly clear-sky SSR. For all three metrics, the PC2 is low. The CLARA all-sky and clear-sky products differ solely in the presence or absence of clouds. The fact that PC2 between all-sky and clear-sky SSR are not strictly zero indicates the presence of some common, noncloud SSR structuring agents. However, the generally low PC2 (0.2 at most, for  $\delta$ ) also points to the overall dominant role of clouds

for the spatiotemporal structure of the SSR field.

From examining PC2 of the representativeness metrics for all-sky SSR data with cloud data we find that roughly 50% of the spatial variability found in  $\delta_G$  and  $\beta_G$  could be explained using total cloud fraction data. Interestingly, high clouds have the highest potential to explain  $\delta_G$  and  $\epsilon_G$  while middle-level clouds have the highest correlations with  $\beta_G$ . Recalling, that the low PC2 between clear-sky SSR and all-sky SSR points to an overall dominant role of clouds as structuring agent (see above). The overall modest correlation of (total) cloud cover with all-sky SSR suggests that the optical properties of clouds may also have a relevant impact on the spatial representativeness patterns in Figure 3.2. This is in line with other studies (e.g. Matus and L'Ecuyer, 2017, and references therein) who showed that besides cloud fraction also other cloud-related parameters are important for their radiative effects. For cloud optical thickness (also from CM-SAF's CLARA-A2) for liquid clouds, ice clouds, and the sum of those two we found, however, PC2 of at maximum 50% (not shown).

Terrain characteristics are also one potential candidate to explain the pattern structure of the representativeness metrics. While the  $\delta_G$  only shows small (negative) correlations with terrain characteristics, the  $\beta_G$  and  $\epsilon_G$  show larger (positive) correlations. For  $\beta_G$  RE can reproduce roughly 50% of the observed spatial variability.

From the above analysis, we can summarize that terrain variability is a main driver for the spatial variability in  $\beta_G$ .  $\delta_G$ , and  $\epsilon_G$  are, however, largely independent of the terrain variables RE and AH. There is, however, quite some spatial covariability between RE and  $\delta_G^{CFC}$  (which is 0.23 0.08 0.45, and 0.08 for total, low, middle, and high CFC) which is not unexpected as persistent cloud features are often related to specific topographic features.

### 3.6 BSRN case study

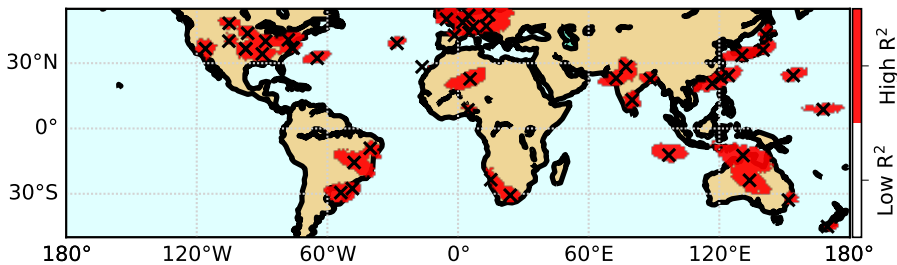


**Figure 3.7:** Spatial correlations of SSR from CLARA pixels collocated to BSRN sites between 50°S and 55°N and their surroundings. Red areas show regions where the  $R^2$  from correlations between collocated BSRN pixels and their surroundings are larger than  $1/e$ . Black crosses indicate the positions of the BSRN stations. Blue and brown colors indicate sea and land surfaces.

To illustrate the usefulness of our methodology, we present a case study, which applies the findings of this paper to the BSRN (Ohmura et al., 1998). The SSR data from the BSRN are often regarded as benchmark data as they provide high-quality SSR data with known accuracy from currently 59 global observation stations. We do not use any of the data from the BSRN except the locations of the sites to extract the  $\delta$ ,  $\beta$ , and  $\epsilon$  at the sites' locations using the CM-SAF data sets. For the extraction of the derived metrics, we prioritize SARAH-P data over SARAH-E and CLARA data. From the 59 operating BSRN stations, 47 are within 50° S and 55° N, which corresponds to the CLARA latitudinal extent. The average  $\delta_p$  of the BSRN stations is 3.5°. The average absolute  $\beta_p$  and  $\epsilon_p$  (both with respect to the 1-degree CERES grid) across the BSRN sites are 2.79 and 8.79 W/m<sup>2</sup>, respectively.

From Table 3.4 it can further be taken that 15 out of the 47 sites have  $\epsilon_p > 8\text{W/m}^2$ , i.e., larger than the pyranometer measurement accuracy. 15 sites, by contrast, have  $\epsilon_p < 6\text{W/m}^2$ , four of them below  $5\text{W/m}^2$ . Three sites have a  $\delta_p < 1^\circ$ , eleven others have  $2^\circ \leq \delta_p < 3^\circ$ . In total 26 sites have  $\delta > 3^\circ$  and  $\epsilon_p \leq 8\text{W/m}^2$  thus are representative of their larger surroundings according to different metrics.

To test for which area fraction of the observational domain the BSRN as a whole can directly measure SSR variability, we calculate the total number of pixels that have a correlation higher than  $1/e$  with one of the sites collocated pixels. We find that all stations which are within the observational domain (50° S to 55° N) can together sample 16 (7)% of CLARA's land (total) surface pixels as can be seen in Figure 3.7.

### 3.7 Summary and Conclusion

In this study, we asked the question whether the combination of monthly SSR point data with (1-degree) gridded data is feasible globally. We combined different existing concepts of representativeness — decorrelation lengths ( $\delta$ , Schwarz et al. (2017)), spatial sampling biases ( $\beta$ , Hakuba et al. (2013a, 2014a)), and spatial sampling errors ( $\epsilon$ , Schwarz et al. (2017)) — and applied them to three high-resolution SSR data sets (CLARA, SARAH-P, and SARAH-E) provided by the Satellite Application Facility on Climate Monitoring (CM-SAF). Using these data sets allows, for the first time, conclusions about the representativeness of SSR point observations near-globally (50° S to 55° N). By looking at three aspects of representativeness, we provided a comprehensive view, which shows that substantial regional differences occur and that all three metrics ( $\delta$ ,  $\beta$ , and  $\epsilon$ ) must be considered for a profound characterization of representativeness.

From analyzing the spatial structure in the three representativeness metrics we found that some regions — namely the tropics, mountainous regions, and some coastlines — are problematic in terms of representativeness due to lacking correlation with the surrounding regions (low decorrelation lengths), large spatial sampling biases, large spatial sampling errors, or a combination of those aspects. In most regions, however, SSR point observations can be

considered representative of a 1-degree surrounding. For the (near-global) domain average we found  $\delta_G = 3.4^\circ$ ,  $\delta_G = 1.4W/m^2$ , and  $\epsilon_G = 7.6W/m^2$ . We stress that these numbers are not uniformly applicable, as large regional differences exist. For the combination of point and 1-degree gridded data, the uncorrectable  $\epsilon$  has to be taken into account in the error budget calculations. This leads to a combined uncertainty which is roughly 40% larger than the measurement uncertainty of pyranometers alone. These  $\epsilon_G$  estimates are based on bias corrected SSR. Without such corrections  $\epsilon_G$  increases roughly 25% over land and 10% over oceans leading to a higher combined uncertainty.

Exploring the role of the target grid resolution, we showed that reducing the resolution to  $2.5^\circ$  increases the global mean  $\epsilon_G$  by roughly 60% while increasing the grid resolution to  $0.5^\circ$  decreases  $\epsilon_G$  by 30% compared to the 1-degree (bias corrected) estimates. We explored to which extent terrain characteristics and cloud fraction correlate with the spatial patterns of the representativeness metrics (see section 3.5). The patterns of the metrics are largely complementary (low spatial correlations among each other) and, accordingly, no single variable can explain the patterns of all metrics equally well. The analyzed variables can, at maximum, explain roughly 50% of the spatial variability of the metrics. Total cloud fraction shows highest correlations. We, therefore, speculate that optical properties of clouds may have an impact on the representativeness patterns.

A case study based on the BSRN applies the findings of the study to a real station network. Based on our decorrelation analysis we showed that 47 sites, which are within the area covered by the CLARA data set, together sample 16% of the domain's total land area (see Figure 3.7). We provide a table with our representativeness estimates for each individual station (see Table 3.4).

With this study, we showed that the spatial representativeness of monthly mean point-based SSR observations is strongly dependent on local conditions. Therefore, special care should be taken when using estimates of representativeness from studies with limited spatial extent for global conclusions.

## Acknowledgments

This study was funded by the Swiss National Science Foundation grant 20002\_159938/1 (Towards an improved understanding of the Global Energy Balance: temporal variations of solar radiation in the climate system). We thank the CM-SAF, the BSRN, and the USGS for providing the data sets. Additionally, the authors thank Jörg Trentmann and Uwe Pfeifroth for the support with the CM-SAF data. We also thank the two anonymous reviewers for their comments and suggestions.

All surface solar radiation data sets are available online under [www.cmsaf.eu](http://www.cmsaf.eu). More specifically, the SARAH-P (version 2) data are available via [https://doi.org/10.5676/EUM\\_SAF\\_CM/SARAH/V002](https://doi.org/10.5676/EUM_SAF_CM/SARAH/V002), the SARAH-E (version 1) are available via [https://doi.org/10.5676/DWD/JECD/SARAH\\_E/V001](https://doi.org/10.5676/DWD/JECD/SARAH_E/V001), and the CLARA (edition 2) are available via [https://doi.org/10.5676/EUM\\_SAF\\_CM/CLARA\\_AVHRR/V002](https://doi.org/10.5676/EUM_SAF_CM/CLARA_AVHRR/V002). The positions of the BSRN stations are available via [bsrn.awi.de](http://bsrn.awi.de). The GTOPO30 from the United States Geological Survey (USGS) is available via NASA's Spatial Data Access Tool (<https://webmap.ornl.gov/>). The CM-SAF cloud fraction data are available via [https://doi.org/10.5676/EUM\\_SAF\\_CM/CLARA\\_AVHRR/V002](https://doi.org/10.5676/EUM_SAF_CM/CLARA_AVHRR/V002). The Global 30 Arc-Second Elevation (GTOPO30) data set provided by the U.S. Geological Survey (USGS) are available via NASA's Spatial Data Access Tool (<https://webmap.ornl.gov/>).

**Table 3.4:**  $\delta_p$ ,  $\beta_G$ ,  $\epsilon_G$ ,  $\beta_P$ , and  $\epsilon_P$  derived from CM-SAF data for all currently operating BSRN stations between 50°S and 55°N.

Station	Latitude	Longitude	$\delta$	$\beta_G$	$\epsilon_G$	$\beta_P$	$\epsilon_P$
Alice Springs	-23.798	133.888	5.6	1.2	7.5	-0.8	7.3
Bermuda	32.267	-64.667	3.4	1.7	7.2	-0.1	5.5
Billings	36.605	-97.516	3.6	1.6	6.7	-1.2	4.6
Bondville	40.067	-88.367	3.4	1.2	6.5	0.9	6.0
Boulder	40.125	-105.237	2.9	7.3	11.9	10.8	13.3
Brasilia	-15.601	-47.713	5.9	2.5	8.9	-3.2	7.5
Cabauw	51.971	4.927	5.1	1.5	6.9	-0.4	7.8
Camborne	50.217	-5.317	3.6	1.5	7.9	-3.8	11.1
Carpentras	44.083	5.059	3.2	10.5	12.9	14.5	13.4
Cener	42.816	-1.601	2.4	11.1	11.5	-10.7	11.8
Chesapeake Light	36.905	-75.713	2.9	1.0	7.1	-0.9	6.8
Cocos Island	-12.193	96.835	4.5	0.4	8.7	-0.6	8.9
Darwin Met Office	-12.424	130.893	5.6	1.8	9.4	-0.1	6.6
De Aar	-30.667	23.993	4.1	1.1	5.5	-1.5	5.2
Desert Rock	36.626	-116.018	3.6	3.1	5.0	-2.6	4.3
Dongsha Atoll	20.700	116.730	3.9	3.1	8.6	-0.2	6.5
Eastern North Atlantic	39.091	-28.029	3.0	1.7	6.5	-1.1	9.6
Florianopolis	-27.605	-48.523	3.4	4.9	10.8	1.8	5.9
Fort Peck	48.317	-105.100	2.9	2.3	8.2	1.7	6.0
Fukuoka	33.582	130.376	3.9	3.0	8.3	-0.0	5.2
Gandhinagar	23.110	72.628	3.9	0.7	6.3	-0.2	7.0
Gobabeb	-23.561	15.042	2.5	3.3	6.9	1.6	8.7
Goodwin Creek	34.255	-89.873	3.9	2.0	7.2	1.8	5.4
Gurgaon	28.425	77.156	3.8	1.3	6.5	1.0	6.0
Howrah	22.553	88.306	2.8	2.4	7.8	-1.2	7.3
Ilorin	8.533	4.567	2.8	5.8	7.6	0.6	5.0
Ishigakijima	24.337	124.164	3.3	3.2	8.3	-2.6	6.5
Izana	28.309	-16.499	0.2	12.9	21.2	-6.6	50.4
Kwajalein	8.720	167.731	3.1	2.1	8.2	-0.3	7.1
Langley Research Center	37.104	-76.387	3.1	2.3	6.7	4.0	6.7
Lauder	-45.045	169.689	1.6	8.0	9.4	6.5	8.6
Lindenbergl	52.210	14.122	4.9	1.2	6.2	2.3	6.4
Lulin	23.469	120.874	2.3	12.9	12.9	-15.9	14.4
Minamitorishima	24.288	153.983	3.6	1.1	8.3	0.8	8.4
Newcastle	-32.884	151.729	2.4	5.3	10.6	3.6	10.2
Palaiseau, SIRTAS	48.713	2.208	4.9	2.2	6.3	-0.5	5.3
Payerne	46.815	6.944	4.6	6.4	11.8	1.6	9.7
Petrolina	-9.068	-40.319	3.9	4.2	9.0	3.1	8.7
Rock Springs	40.720	-77.933	3.4	2.7	7.4	-3.2	6.6
Sapporo	43.060	141.329	2.6	4.9	8.4	5.6	7.1
Sioux Falls	43.730	-96.620	3.1	1.3	6.8	-0.8	4.5
Sonnblick	47.054	12.958	1.2	6.9	14.6	-4.5	29.4
Southern Great Plains	36.605	-97.485	3.6	1.6	6.7	-1.5	4.1
Sao Martinho da Serra	-29.443	-53.823	4.4	2.5	7.2	0.6	5.2
Tamanrasset	22.790	5.529	4.8	3.1	6.6	-3.1	6.6
Tateno	36.058	140.126	3.4	3.4	8.2	0.7	8.0
Tiruvallur	13.092	79.974	3.7	3.2	8.6	0.1	6.7

Note.  $\delta$  is given in degrees while  $\beta_G$ ,  $\epsilon_G$ ,  $\beta_P$ , and  $\epsilon_P$  are proved in  $W/m^2$ .



4

# The annual cycle of fractional atmospheric shortwave absorption in observations and models: spatial structure, magnitude and timing

M. Schwarz<sup>1,\*</sup>, D. Folini<sup>1</sup>, S. Yang<sup>1,2</sup>, & M. Wild<sup>1</sup>

**Resubmitted to Journal of Climate after minor revisions**

1. Institute for Atmospheric and Climate Science, ETH Zurich, CH-8092 Zurich, Switzerland.
2. National Meteorological Information Center, China Meteorological Administration, Beijing, China

## Abstract

We use the best currently available in-situ and satellite-derived surface and top-of-the-atmosphere (TOA) shortwave radiation observations to explore climatological annual cycles of fractional (i.e. normalized by incoming radiation at the TOA) atmospheric shortwave absorption ( $\bar{a}$ ) on a global scale. The analysis reveals that  $\bar{a}$  is a rather regional feature where the reported non-existing  $\bar{a}$  in Europe is an exception rather than the rule. In several regions, large and distinctively different  $\bar{a}$  are apparent. The magnitudes of  $\bar{a}$  reach values up to 10% in some regions, which is substantial given that the long term global mean atmospheric shortwave absorption is roughly 23%. Water vapor and aerosols are identified as major drivers for  $\bar{a}$  while clouds seem to play only a minor role for  $\bar{a}$ . Regions with large annual cycles in aerosol emissions from biomass burning also show the largest  $\bar{a}$ . As biomass burning is generally related to human activities,  $\bar{a}$  is likely also anthropogenically intensified or forced in the respective regions. We also test if climate models are able to simulate the observed pattern of  $\bar{a}$ . In regions where  $\bar{a}$  is driven by the annual cycle of natural aerosols or water vapor, the models perform well. In regions with large  $\bar{a}$  induced by biomass burning aerosols, the models' performance is very limited.

## 4.1 Introduction

The principal energy fluxes in the climate system are known for more than 100 years (Abbot and Fowle, 1908, and many after that). In the shortwave (SW) part of the Earth's energy balance, incoming radiation (I) at the top-of-the-atmosphere (TOA), is either absorbed at the surface (S), absorbed in the atmosphere (A), or reflected back to space (R):

$$I = S + A + R \quad (4.1)$$

with  $S = SSR \cdot (1 - \alpha)$ , where SSR is the surface downward radiation and  $\alpha$  is the surface albedo. Today, long term global mean fluxes of the Earth's shortwave energy balance are well known from global observations as well as from investigations of climate model outputs and combinations of those data sources (e.g. Kiehl and Trenberth, 1997; Trenberth et al., 2009; Stephens et al., 2012; Wild, 2012; L'Ecuyer et al., 2015; Wild et al., 2015).

From the observational perspective, the availability of surface radiation data from different data sources like the Global Energy Balance Archive (GEBA; Wild et al. 2017) or the Baseline Surface Radiation Network (BSRN; Ohmura et al. 1998), as well as the development of accurate satellite-based measurements of surface albedo (e.g., from Moderate-resolution Imaging Spectrometer, or MODIS; Schaaf et al. 2002), incoming solar radiation at the TOA (from the Solar Radiation and Climate Experiment, or SORCE; Kopp et al. 2005), and measurements of SW reflected radiation at the TOA (from the Clouds and the Earth's Radiant Energy System, or CERES; Wielicki et al. 1996) lead to improved estimates of the SW radiative fluxes in the

climate system. Taken together, the long term mean SW fluxes of the Earth's global energy balance are known today with unprecedented accuracy.

However, considerably less is known about the temporal variations in the energy balance. Although several studies inferred different aspects of the temporal variability of the energy balance (e.g., Trenberth and Stepaniak, 2004; Fasullo and Trenberth, 2008a,b; Kato, 2009; Mlynczak et al., 2011; Trenberth et al., 2015), only a few studies focused on annual cycles of atmospheric shortwave absorption – the variable of interest in this study.

Donohoe and Battisti (2013) demonstrated the importance of the annual cycle of atmospheric shortwave absorption for the seasonal heating of the troposphere. They show that the seasonal heating of the troposphere is largely driven by direct absorption of radiation in the atmosphere rather than by heating from the ground. Recently, Santer et al. (2018) showed in a fingerprint study, that changes in the annual cycles of tropospheric temperatures can already be attributed to human activities with very high significance. A better understanding of the main seasonal heating source of the atmosphere is, therefore, crucial to predict future changes (Donohoe and Battisti, 2013). Especially in summer, increased water vapor in the atmosphere will lead to increased shortwave atmospheric absorption in a warmer climate (e.g. Dwyer et al., 2012; Donohoe et al., 2014). A substantial annual cycle in atmospheric absorption, peaking in local summer, might lead to a more pronounced annual cycle in tropospheric temperatures and generally impact the local meteorology and climate.

Depending on where radiant energy is deposited in the climate system, different impacts on local meteorology can be expected. While direct heating of the atmosphere by atmospheric absorption tends to stabilize air masses (e.g. Hansen et al., 1997; Koren et al., 2004; Yang et al., 2016), absorption of shortwave radiation at the surface rather triggers convection by transferring radiant energy into latent heat. Increased atmospheric absorption, therefore, also tends to dampen the hydrological cycle, as less energy is available at the surface for evaporation (Ramanathan et al., 2001, 2005).

By using high-quality observations, Hakuba et al. (2014b) were able to calculate a station based multi-annual mean best estimate for absorption of SW radiation in the atmosphere in Europe by combing surface radiation data with the TOA net fluxes from CERES and MODIS albedo at more than 150 stations in Europe. They found that, independent of latitude and season,  $23\pm 1\%$  of the incoming shortwave radiation at the TOA is absorbed in the atmosphere. In a global assessment, Hakuba et al. (2016) showed that this *fractional* atmospheric SW absorption only has a weak latitudinal dependence with nearly zonally constant values of  $23\pm 2\%$ .

That an annual cycle in fractional atmospheric shortwave absorption may exist and may vary with region and time, is plausible given that the main drivers of atmospheric absorption – water vapor, clouds, and aerosols – are known to have annual cycles that may even depend on region (e.g., Gaffen et al., 1992; Rossow and Lacis, 1990; Carslaw et al., 2010). Thus there is ample motivation to further study the annual cycle of shortwave atmospheric absorption.

Here we extend the investigations of Hakuba et al. (2014b) and Hakuba et al. (2016) and assess regional annual cycles of fractional atmospheric shortwave absorption at global scale by using the best currently available observations. Thereto, we mostly rely on satellite-derived data but also anchor the analysis on in-situ observations wherever possible.

Moreover, we will investigate if global climate models from the fifth coupled model inter-comparison program (CMIP5) are capable of simulating atmospheric absorption accurately. It has been shown that substantial biases in the energy balance between observations and global climate models prevail, such as an underestimation of atmospheric shortwave absorption often found in climate models (Wild, 2008; Wild et al., 2015). Further studying the representation of the annual cycles of atmospheric shortwave absorption in the models could potentially provide insight into which processes are responsible for this mismatch.

In this study we aim to answer the following questions: Are there any regions where fractional atmospheric shortwave absorption has an annual cycle? If so, what are potential causes for the seasonal variations? And, are the CMIP5 models able to simulate the patterns found? To answer these questions we organize this paper as follows: In Section 4.2 we introduce the data and methods applied. In Section 4.3 we briefly revisit the global pattern of annual mean atmospheric absorption based on observations. In Section 4.4 we analyze annual cycles of atmospheric absorption from observations. In Section 4.5 we examine which processes are the most likely causes for the patterns found in the previous section. We infer the ability of CMIP5 models to simulate the annual cycles of atmospheric absorption by comparing the model output to the observational data in Section 4.6. Finally, we discuss several aspect of the results in Section 4.7, before we provide our summary and conclusions in Section 4.8.

## 4.2 Data and Method

In absolute units, the annual cycle of any radiative flux in the climate system is largely governed by the astronomically induced seasonal cycle. This is also true for atmospheric absorption, which – in absolute units – is largest in the respective summer seasons. Here, we normalized the shortwave atmospheric absorption with the incoming TOA radiation, similarly as Hakuba et al. (2014b), to get a better insight into the changes in the atmosphere. Since the attenuation of radiation can be described with the Beer-Lambert-Bouguer law, looking at annual cycles of *fractional* atmospheric absorption gives direct insights into the annual cycles of the optical properties of the atmosphere as a whole. Therefore, we present all quantities in fractions of incoming radiation at the TOA ( $I$ ). We indicate this by lowercase variables (e.g.,  $a=A/I$ ).

### 4.2.1 TOA and surface fluxes from CERES

We utilize monthly SW fluxes from the Energy Balanced and Filled (EBAF) data of the Clouds and Earth's Radiant Energy System (CERES) Ed. 4.0 (Wielicki et al., 1996; Loeb et al., 2017)

from 2000 to 2016. The data set is based on measurements of the CERES instruments, which fly on the Terra, Aqua, Suomi National Polar-Orbiting Partnership (SNPP), and NOAA-20 satellites. The instruments measure upward fluxes for the shortwave (i.e. the  $0.3 - 5\mu m$ ), total ( $0.3 - 200\mu m$ ) and window ( $8 - 12\mu m$ ) spectral regions with global coverage each day. The processing from the raw instantaneous measurements to TOA radiative fluxes requires several processing steps as described in Loeb et al. (2017). The EBAF data additionally has been objectively constrained within its uncertainty range, such that the global annual net TOA fluxes are consistent with measured heat storage estimates from different data sources (see Loeb et al., 2012, 2017, and references therein). The uncertainty of the regional one-degree monthly TOA SW reflected irradiance is estimated to be  $\pm 3 Wm^{-2}$  from 03/2000 to 06/2002 and  $\pm 2.5 Wm^{-2}$  after that period ( $1\sigma$ -level; Loeb et al. 2017). For TOA incoming SW fluxes, CERES uses data from the Total Irradiance Monitor (TIM) of the Solar Radiation and Climate Experiment (SORCE; Kopp et al. 2005; Loeb et al. 2012). The uncertainty of SORCE TIM is estimated to be 0.035% for absolute and  $0.001\%yr^{-1}$  for relative changes in total solar irradiance which allows determining possible long-term variations with very high precision (Kopp et al., 2005). The net shortwave TOA radiative fluxes are calculated by combining the TIM and the CERES EBAF measurements.

Besides the TOA flux data, we also use monthly SW surface up- and downward fluxes from the CERES EBAF surface product Ed. 4.0 (Kato et al., 2012a, 2018) from 2000 to 2016. Surface fluxes are computed by the Fu-Liou radiative transfer model (hourly computing interval) with input data for cloud properties (from MODIS and geostationary satellites), temperature, specific humidity, and ozone profiles (from the Goddard Earth Observing System reanalysis), aerosol types and optical thickness (from a model that assimilated MODIS aerosol optical thickness), and surface albedo (from clear-sky CERES footprints). The monthly averaged data product resulting from that radiative transfer modeling is then adjusted such that the computed TOA fluxes match the CERES EBAF TOA Ed.4 fluxes. For a more complete description of the CERES EBAF surface data, we refer to Kato et al. (2018) and references therein. The uncertainty of the CERES EBAF surface product was estimated to be  $\pm 3 Wm^{-2}$  ( $1\sigma$  for the surface downward SW fluxes; Kato et al. 2018).

### 4.2.2 In-situ downward surface solar radiation

Downward surface solar radiation can only be measured directly on the Earth's surface using in-situ pyranometer observations and can be considered as "ground truth". We use monthly mean time series of SSR from four different data sources in the time period from 2000 to 2016, mainly for validation of the CERES-based estimates.

The Baseline Surface Radiation Network (BSRN, Ohmura et al. 1998) provides flux data since the 1990s at currently more than 60 sites distributed around the globe. Most data is available in one (some in three or five) minute averages from one-second sampling intervals. Monthly means are calculated as recommended by Roesch et al. (2011). Dutton et al. (2012)

estimated the monthly and annual mean uncertainty (95%-level) for BSRN shortwave data to be  $\pm 8 \text{ W m}^{-2}$  and  $\pm 6 \text{ W m}^{-2}$ , respectively. We incorporate data from 33 BSRN stations. Because of the very high data quality requirements of the BSRN, the data serves as a benchmark for SSR.

The Global Energy Balance Archive (GEBA, Wild et al. 2017) collects and stores data for surface energy flux components from more than 2500 stations. The database provides monthly data which are collected from various different sources as described in Wild et al. (2017). Gilgen et al. (1998) estimated the uncertainty for monthly and annually averaged SSR to  $\pm 5\%$  and  $\pm 2\%$ , respectively, of the corresponding monthly and annual mean values base on root-mean-squared differences. We use 358 GEBA stations distributed over all continents (except Antarctica).

The Chinese Meteorological Administration (CMA) routinely collects SSR data using pyranometers. We use 87 stations from the homogenized dataset described in Yang et al. (2018). Shi et al. (2008) point out that the error of the CMA pyranometer measurements likely does not exceed 5%. The data is therefore likely of comparable quality to the GEBA data.

The Global Tropical Moored Buoy Array (GT MBA) program of the Pacific Marine Environmental Laboratory (PMEL) of the National Oceanic and Atmospheric Administration (NOAA) in the USA provides data from the Tropical Atmosphere Ocean / Triangle Trans-Ocean Buoy Network in the Pacific (TOA/TRITON; McPhaden et al. 1998), the Prediction and Research Moored Array in the Atlantic (PIRATA; Servain et al. 1998), and the Research Moored Array for African-Asian-Australian Monsoon Analysis and Prediction in the Indian Ocean (RAMA; McPhaden et al. 2009). All three ocean buoy networks measure downward surface solar radiation routinely with mounted pyranometers that are replaced annually. A more detailed description of the sensor and an estimate of the total error for annual means of  $\pm 5 \text{ W/m}^2$  can be found in Colbo and Weller (2009). It was reported that some buoys in the tropical north Atlantic Ocean ( $8^\circ\text{N}$ - $21^\circ\text{N}$ ) significantly underestimate surface downward radiation because of dust accumulation on the sensor (Foltz et al., 2013).

### 4.2.3 Albedo

We use processed bihemispherical reflectance data (i.e., white-sky albedo) for the broad-band shortwave spectral region ( $0.3$ – $5.0 \mu\text{m}$ ) of the MCD43C3 Climate Modeling Grid (CMG) Albedo Product from the MODIS version 6 data (Schaaf and Wang, 2015). The data is available since 03/2000 with daily temporal resolution and  $0.05^\circ$  spatial resolution.

The MODIS albedo is derived from global coverage observations from the MODIS instruments onboard the Terra and Aqua satellites. Both satellites are in a sun-synchronous orbit (10:30am and 1:30pm equator crossing time) with a repeat cycle of 16 days. Because of the large swath width of the MODIS sensor (i.e., 2330km), each point of the Earth is sampled every 1-2 days (Wanner et al., 1997). From the directional observations the bidirectional

reflectance distribution functions (BRDF) are derived using a semiempirical kernel-driven bidirectional reflectance model (Schaaf et al., 2002). In the MODIS v006 data, the BDRF is retrieved daily from cloud-free observations and represent the best BRDF possible based on 16 days worth of inputs (corresponding to about 15 to 20 multiangular observations Wanner et al. 1997) with the day of interest emphasized ([https://www.umb.edu/spectralmass/terra\\_aqua\\_modis/v006/mcd43c3](https://www.umb.edu/spectralmass/terra_aqua_modis/v006/mcd43c3)). From the BDRF, instantaneous black-sky and white-sky albedo are derived and provided for local solar noon conditions (Schaaf et al., 2002). The albedo for ambient sky conditions (blue-sky) can be estimated by weighing the black- and white-sky albedo via the diffuse ratio (i.e. the fraction of direct to total surface downward radiation; Schaepman-Strub et al. 2006).

The MODIS albedo product has been extensively validated with in-situ observations, airborne measurements and other albedo products (e.g. Liang et al., 2002; Jin et al., 2003; Salomon et al., 2006; Román et al., 2009; Cescatti et al., 2012; Wang et al., 2012b; Roman et al., 2013; Hakuba et al., 2014b; Wang et al., 2014). The accuracy of the MODIS operational albedos has proven to be well within 5% (Schaaf et al., 2010).

Since the TOA flux data is available at one-degree spatial and monthly temporal resolution, we average the daily MODIS  $0.05^\circ$  data temporally and spatially to meet the CERES resolutions. In order to estimate monthly mean albedo, we use instantaneous white-sky albedo as a surrogate for daily mean albedo values. This is a pragmatic approach, as white-sky albedo is independent of the solar zenith angle (SZA) and, therefore, has no diurnal cycle. Using instantaneous black-sky albedo at local solar noon as a surrogate for daily means leads to biases of around -9% because of the SZA dependence (i.e., smallest values are reached at local noon) of the black-sky albedo (Grant et al., 2000; Wang et al., 2015a). White-sky albedo, however, does not show diurnal variation as it is independent of SZA. It is larger/smaller than black-sky albedo at low/high SZAs (Schaepman-Strub et al., 2006; Liu et al., 2009) and therefore a more practical estimate for daily mean albedo. Calculating blue-sky daily mean albedo would require records for direct and total solar radiation with very high temporal resolution which are only available for a limited number of stations.

In a detailed analysis for Europe, (Hakuba et al., 2014b) showed that the associated error in atmospheric surface absorption from spatial averaging is for the most part smaller than  $0.1\text{W}/\text{m}^2$ , thus small enough to be safely neglected.

#### 4.2.4 Climate Model Data

We compare the observation based findings to model output from the CMIP5 models. We use data from the historic (1993-2005) and preindustrial control simulations (piControl). For piControl we utilize the whole integration period (which varies from model to model). A more complete description of the models and the experiments can be found in Taylor et al. (2011).

All calculations are conducted on the models' native grids. To be able to compare the model data to the observational data the final output fields are regridded onto the CERES one-degree grid using bilinear interpolation.

#### 4.2.5 Auxiliary data

Several auxiliary data sets are used to attribute the features found in the observations to key atmospheric variables. We use the information on cloud properties and water vapor (based on MODIS and geostationary imager) as well as data on aerosol optical depth at 550nm (based on MODIS) from the monthly CERES SYN1deg v4 data (Rutan et al., 2015). Further, we utilize data for different aerosol species from the Modern-Era Retrospective Analysis for Research and Applications, version 2 (MERRA-2; Gelaro et al. 2017).

#### 4.2.6 Representativeness of in-situ observations

In the analysis, we combine in-situ point observations with colocated satellite-derived and modeled gridded data sets. For a valid combination within reasonable uncertainties, the point observations must be representative of the whole area covered by the smallest entity of the gridded data sets. In this work, this smallest entity is the CERES  $1^\circ \times 1^\circ$  grid, where a single grid box roughly corresponds to a surface area of  $(100 \times 100) \text{ km}^2$ .

This combination of point and gridded data can cause additional uncertainties because of potential representativeness issues. In a long-term (climatological) mean perspective, point observations can be biased with respect to a one-degree grid box (i.e. they measure systematically higher or lower values compared to the area mean). This spatial sampling bias ( $\beta$ ) was first examined by Hakuba et al. (2013a) for Europe and was extended by Hakuba et al. (2014a) and Schwarz et al. (2018) to the Meteosat-disc (i.e.  $\pm 60^\circ$  around the cutting point between the equator and the zero-meridian) and to a near-global analysis (i.e.  $50^\circ\text{S}$ - $55^\circ\text{N}$ ), respectively.  $\beta$  has to be calculated for each station and grid individually but can be corrected once it is known (see Hakuba et al., 2014a). The  $\beta$ s can have values up to several  $\text{W/m}^2$  depending on the position of the station with respect to its colocated grid box. We use estimates for  $\beta$  similarly as described in Schwarz et al. (2018) to correct the in-situ data. We use a bias correction for each month of the year separately as suggested by Schwarz et al. (2018).

For time series analysis, not only systematic differences but also the spatiotemporal structure of the SSR field must be taken into account. First, SSR from an in-situ point observation should sufficiently well correlate with the surroundings. Schwarz et al. (2017) defined the decorrelation length of a site ( $\delta$ ) as the average distance at which the correlation of the monthly SSR time series between a site and the surrounding drops below  $1/e$ . For Europe, they find decorrelation lengths ( $\delta$ ) on the order of 400 km around the sites. This value is, however, not uniformly applicable as shown in the near-global analysis by Schwarz et al. (2018).



Secondly, an additional spatial sampling error ( $\epsilon$ ), which originates due to the in-situ observations' imperfect representation of the area-mean time series, must be taken into account. This additional error was quantified by Schwarz et al. (2017) and Schwarz et al. (2018) for Europe and near-globally, respectively. We use (site based) estimates of  $\delta$  and  $\epsilon$  as described in Schwarz et al. (2018) to exclude stations with small correlation with their surrounding ( $\delta < 2^\circ$ ) and excessively large spatial sampling errors ( $\epsilon > 16W/m^2$ ).

#### 4.2.7 Data processing

To calculate  $A$  based on CERES data we simply subtract the surface absorbed flux – calculated from the difference of up- and downward surface shortwave fluxes – from the TOA net flux.

For the calculation of  $A$  based on in-situ data, we calculate the surface absorbed flux by  $S=(1-\alpha)SSR$ , where we use  $\alpha$  from MODIS. If the MODIS albedo is missing (e.g., over oceans), we use albedo calculated from the CERES EBAF surface product.

All data is available at, or is averaged to, monthly mean temporal resolution. We first calculate monthly time series of  $A$ . To calculate annual cycles, we average over all available monthly mean values of a month (e.g., January) if at least two monthly observations are available. To calculate annual means, we average the mean annual cycle if all twelve months of the annual cycle are available.

We follow this approach so that we are able to analyze as many in-situ observations as possible without extensive gap filling techniques. A shortcoming of this approach is the issue of not precise temporal co-location of all data as described in Schutgens et al. (2016b) when comparing the in-situ and CERES data.

### 4.3 Annual mean atmospheric shortwave absorption

Before we analyze annual cycles in the shortwave energy balance, we reexamine the spatial variability in the multiannual mean atmospheric shortwave absorption ( $\bar{a}$ ). We explore the spatial patterns using the CERES TOA and surface data. We anchor the analysis using surface observations.

Figure 4.1 shows  $\bar{a}$  from the CERES EBAF data as well as from station data. Hakuba et al. (2016) thoroughly discussed the weak latitudinal gradients of zonally averaged  $\bar{a}$ . Some significant regional differences can, however, clearly be identified.

High altitude regions, such as the mountain ranges on the west side of the North American continent, the Andes, the Himalayan and the adjacent Hindukusch mountains as well as the Iranian mountains, and the Tibetan plateau show clearly smaller  $\bar{a}$ . This is not surprising given the smaller atmospheric optical path length in those regions. From analyzing the (500m binned) altitude dependence of  $\bar{a}$  from all in-situ observations, we find a decreasing  $\bar{a}$  with increasing altitude of  $\frac{\delta\bar{a}}{\delta h} = -2.2(\pm 0.5) \% \text{ per } 1000 \text{ m}$  (not shown).

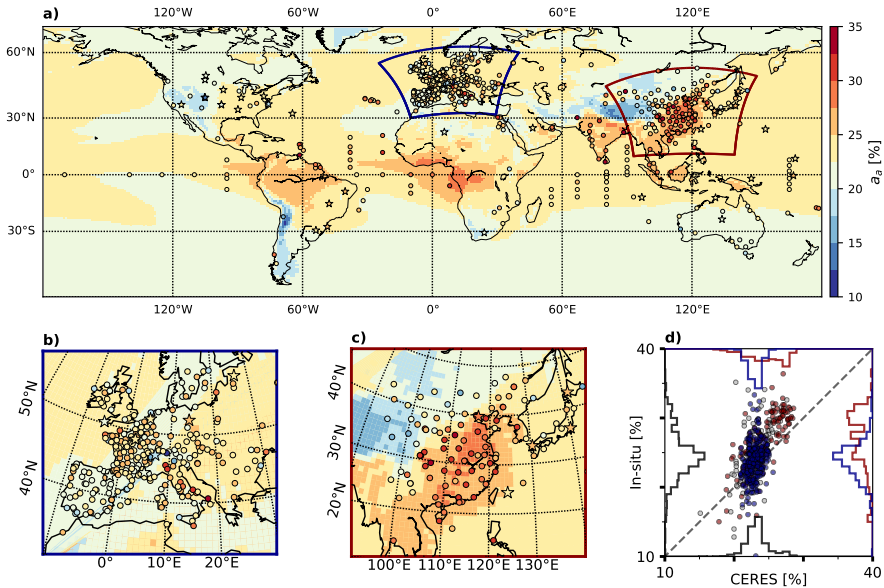


**Figure 4.1:** Multiannual mean (2000-2016) fractional absorption of shortwave radiation in the atmosphere. Colored regions indicate  $\bar{a}$  from CERES data only. Stars (points) represent BSRN (GEBA and CMA ) in-situ observations. Blue/red coloring indicates lower/higher absorption. Panels (a), (b), and (c) show  $\bar{a}$  globally, for Europe, and for Asia respectively. (d) shows the scatter-plot for colocated CERES-only and in-situ  $\bar{a}$ . The black, red and blue lines show the normalized probability density functions for all, Chinese, and European stations, respectively, for CERES-only estimates (bottom and top) and in-situ estimates (left and right).

Distinct positive anomalies in  $\bar{a}$  can be identified in the tropical African and South American regions as well as over the Indian Subcontinent and the Chinese lowlands. While the positive anomalies in the tropics are likely related to high water vapor concentrations, and in the case of Africa high black carbon concentrations, the high  $\bar{a}$  in India and China are likely due to high aerosol burdens in those regions (see also Sections 4.4 and 4.5). Figures 4.1b and 4.1c show  $\bar{a}$  in Europe and Asia in more detail. The station mean absorption (and standard deviation) in Europe is  $\bar{a}^{\text{EUR}} = 23.9 \pm 2.7\%$  which is in good good agreement with the value found by Hakuba et al. (2014b). For China, the station mean absorption is, however,  $\bar{a}^{\text{CH}} = 27.1 \pm 4.1\%$  and some Chinese stations even show  $\bar{a} > 30\%$ . This substantially higher  $\bar{a}$  compared to other parts of the world is presumably related to high anthropogenic aerosol burdens in China.

Figure 4.1c shows a scatterplot which compares the in-situ  $\bar{a}$  to the colocated CERES only estimates. The correlation between them is  $r=0.62$  which indicates that CERES misses some of the spatial variability. However, the root mean square error of  $\text{RMSE}=2.42\%$  is comparably

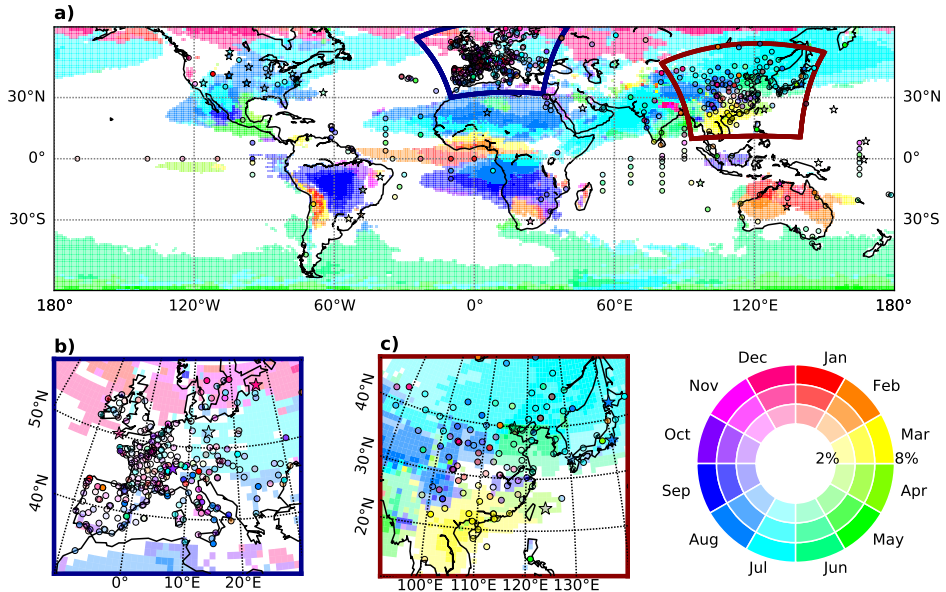


**Figure 4.2:** The annual cycle of fractional atmospheric shortwave absorption globally (a), in Europe (b), and in Asia (c). The magnitude of the annual cycle ( $|\bar{a}|_m$ ) is indicated by the opacity of the coloring. The month during which the maximum absorption occurs ( $|\bar{a}|_p$ ) is indicated by different colors. In transparent regions, the magnitude of the annual cycle of  $|\bar{a}|_m$  is less than 2%. A higher opacity of the colors indicates higher amplitudes. Stars (points) represent BSRN (GEBA, CMA and buoy) in-situ observations.

small and the main spatial features are clearly visible in both data sets. Averaged over all stations / European stations only / Chinese stations only, CERES underestimates  $\bar{a}$  compared to in-situ observations by about  $-1.4(\pm 2.8)\%$  /  $-0.8(\pm 2.6)\%$  /  $-2.4(\pm 2.7)\%$  (standard deviation in brackets).

#### 4.4 Annual cycles of atmospheric shortwave absorption

In this section, we put the focus on the climatological annual cycle of fractional shortwave absorption in the atmosphere ( $\bar{a}$ ). For European in-situ observations, Hakuba et al. (2014b) found that the fractional atmospheric absorption has no notable annual cycle. The present analysis goes beyond Europe to infer  $\bar{a}$  globally.

To this aim, we analyse the magnitude  $|\bar{a}|_m$  and phase  $|\bar{a}|_p$  of the climatological annual cycle of fractional atmospheric shortwave absorption over the whole domain. We define  $|\bar{a}|_m$  as the difference between their maximum and the minimum absorption in the climatological annual cycle and  $|\bar{a}|_p$  as month where the climatological absorption reaches its maximum.

Figure 4.2 shows both, the magnitude and the phase of  $\bar{a}$  in a combined chart. The coloring and opacity in the Figure indicate the month of maximum absorption and the magnitude of the annual cycle, respectively.

Comparing the overall spatial pattern of  $\bar{a}$  (Figure 4.1a) and  $\bar{a}$  (Figure 4.2a) reveals that the two fields are distinctively different with a spatial correlation of basically zero.

In Europe, only small variations are occurring during the year as shown in Figure 4.2b. This is in agreement with Hakuba et al. (2014b) who found no significant annual cycle in an European analysis. Interestingly, station observations (points and stars in Figure 4.2) generally show somewhat larger annual cycles than the CERES data. Averaged over Europe, the mean annual cycle across all stations has a magnitude of around 4.1%, while the CERES-only estimates for collocated pixels show a magnitude of only 1.7%.

Beyond Europe, regions with notable  $\bar{a}$  can be identified (see Figure 4.2). Figure 4.3 shows  $\bar{a}$  for several regions which show large  $|\bar{a}|_m$  according to Figure 4.2. In Figure 4.3,  $\bar{a}$  based on CERES data as well as  $\bar{a}$  from in-situ observations within the respective regions (Figures 4.3a-j), boxplots for the differences in  $|\bar{a}|_m$  from in-situ and collocated CERES pixels (Figure 4.3i), and an overview of the spatial extent of the regions (Figure 4.3l) are shown.

Central Africa (CAF) and South America (SAM) are the regions with the largest  $|\bar{a}|_m$  which, for some pixels, reach more than 10%. The  $|\bar{a}|_p$  for those regions is in August (CAF) and September (SAM). Unfortunately, no in-situ observations are available in SAM. In CAF, two land sites and four ocean buoys are available. They show the same general structure of  $\bar{a}$  as shown in Figure 4.3c. The ocean buoy located at 6°S / 8°E (i.e., dark green line Figure 4.3c) shows an even larger annual cycle than the CERES data. Note that the dust accumulation bias reported by Foltz et al. (2013) only affects stations in the northern tropical Atlantic. Therefore, the in-situ buoy data can be considered trustworthy in CAF.

The region around the Atlantic Equator (EQA) shows a less pronounced maximum  $|\bar{a}|_m \approx 5\%$  and a small double peak in  $\bar{a}$  with  $|\bar{a}|_p$  in February.

In the Sahara (SAH) and Australia (AUS),  $\bar{a}$  peaks in their respective summer months. For SAH, the BSRN station Tamanrasset (purple line in Figure 4.3f) and an ocean buoy (21°N/23°W, red line in Figure 4.3) show a slightly more pronounced  $\bar{a}$  than the CERES data. The buoy data in this region might, however, be affected by the dust accumulation bias (Foltz et al., 2013). We expect that the station Tamanrasset is not affected by such biases as it is a BSRN station which is (according to the BSRN data quality requirements; McArthur 2005) frequently maintained. In AUS the station data also show slightly higher  $|\bar{a}|_m$  than the CERES data, as can be seen in Figure 4.3b.

In the Arabian Sea (ARS) in-situ observations and CERES show some differences (Figure 4.3a). While the CERES data suggest a pronounced peak in July, the stations from India, Pakistan, and the United Arab Emirates do not show a clear common  $\bar{a}$ .

In South East Asia (SEA) the in-situ and CERES data agree that  $|\bar{a}|_p$  is in March, as shown in Figure 4.3h. Again, the in-situ data show larger  $|\bar{a}|_m$ .

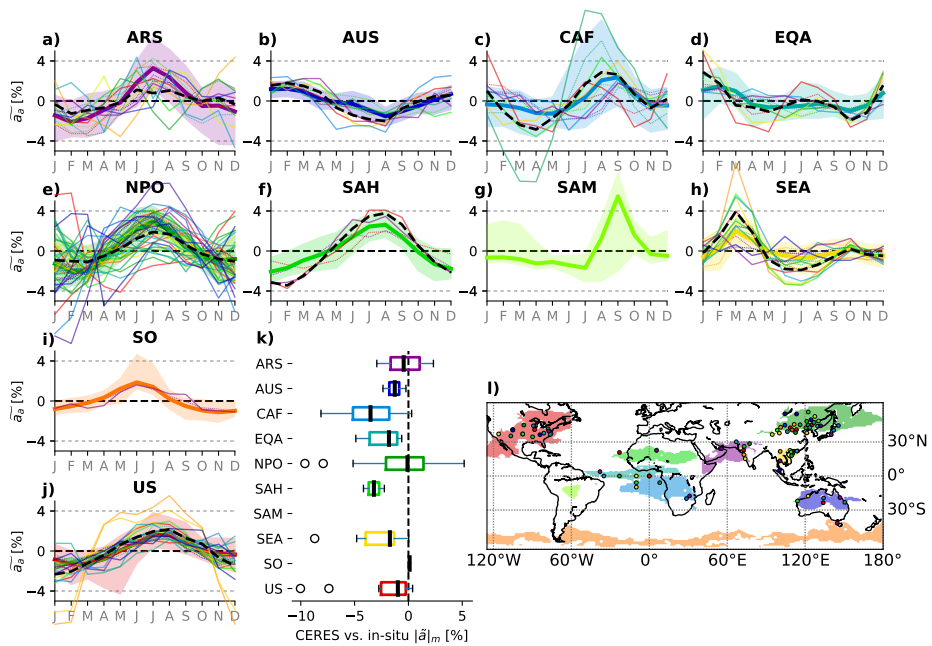


**Figure 4.3:** The annual cycle of fractional atmospheric shortwave absorption for selected regions based on CERES and in-situ data. Panels a-j show  $\bar{a}$  from CERES (colored shading) and in-situ data (thin colored lines). Continuous thin lines correspond to individual in-situ observations while the dashed lines correspond to the respective co-located CERES pixels. The colored shading shows the range of the annual cycles of all CERES pixels of the respective region. The thick colored line indicates the CERES regional mean  $\bar{a}$ . The thick black dashed lines indicates the average over all in-situ observations. Panel k shows boxplots of the differences in  $|\bar{a}|_m$  for in-situ and colocated CERES estimates for all regions. The coloring of the shadings in panels a-j correspond to the coloring of the different regions (i.e., (a) Arabian Sea (ARS), (b) Australia (AUS), (c) Western Central Africa (CAF), (d) Equatorial Africa (EQA), (e) Northern Pacific Ocean (NPO), (f) Sahel (SAH), (g) South America (SAM), (h) South East Asia (SEA), (i) Southern Ocean (SO), and (j) United States (US)) shown in panel (l). The coloring of the thin lines in a-j corresponds to the points in the respective regions (l) and indicates the position of the in-situ data.

In the United States (US), most stations are in agreement with CERES with  $|\bar{a}|_p$  in July. Interestingly, the two BSRN stations located in Boulder suggest a larger  $|\bar{a}|_m$ .

In the Southern Ocean (SO), we find a pronounced  $\bar{a}$  which can be confirmed with an in-situ observation in southern Australia. In the region around the northern Pacific Ocean, western Russia, Northern China, and Mongolia (altogether referred to as NPO) CERES shows  $|\bar{a}|_m > 4\%$  with a pronounced summer peak. While most in-situ observations agree on this, some stations suggest  $|\bar{a}|_p$  in Winter.

Throughout the different regions we find that CERES generally underestimates  $|\bar{a}|_m$  when comparing in-situ and colocated CERES derived  $|\bar{a}|_m$  (Figure 4.3k). Largest median differences between CERES and in-situ occur in CAF and SAH. Pronounced outliers exist in NPO, SEA, and the US (see also above and the respective panels of Figure 4.3).

Overall, this analysis reveals that  $\bar{a}$  is a rather regional feature. The non-existing  $\bar{a}$  in Europe is an exception rather than the rule. In several regions, large and distinctively different  $\bar{a}$  are apparent. These signals are apparent to the same extent in in-situ observations and the CERES data. We are therefore confident that the regions with larger  $\bar{a}$  were identified correctly.

## 4.5 Drivers of the annual cycle in atmospheric absorption

In this section, we investigate potential drivers of the the annual cycles in atmospheric absorption in different regions. We do that with a simple correlation analysis. We note, however, that correlation is not necessarily causation and that the analysis can not unambiguously identify the relative importance of the potential driving variables.

First, we want to emphasize that the patterns found in  $\bar{a}$  apparently are relatively insensitive to clouds. Based on the clear-sky CERES-EBAF TOA and surface data, we calculated  $\bar{a}$  during clear-sky conditions (i.e. radiative fluxes when no clouds are present) and basically find the same pattern as in the all-sky case (Figure 4.4a). The average squared correlation coefficient ( $R^2$ ) in the region  $60^\circ S - 60^\circ N$  between the clear- and all-sky  $\bar{a}$  is  $R^2=0.77$ . This behavior – similar  $\bar{a}$  during clear- and all-sky conditions – is also found at BSRN stations where in-situ clear-sky  $\bar{a}$  based on the clear-sky identification scheme from Long and Ackerman (2000) was calculated (not shown). The largest influence of clouds (i.e. the smallest correlations between  $\bar{a}$  during clear- and all-skies) is found in the northern Pacific, west of the coast of northern South America, and in the northern Atlantic where  $\bar{a}$  is small anyway.

Consequently, the CERES SYN1deg cloud properties (i.e. cloud area fraction, cloud optical depth, liquid and ice water path, and cloud effective temperature; all for low, middle and high and total clouds) show only small correlations with  $\bar{a}$  as exemplary shown in Figure 4.4b for total cloud area fraction. Only in Australia and the Arabian Sea, clouds show some correlation with  $\bar{a}$ . Since in those regions, the clear-sky correlations are also particularly large, we speculate that clouds simply have the same annual cycle but do not influence  $\bar{a}$  critically.

Next, we test the annual cycle from aerosol optical depth (AOD) at 550nm and the total precipitable water (PW) as a proxy for total water vapor column, both from the CERES SYN1deg, as explanatory variables for  $\bar{a}$ . AOD shows high correlations in Central Africa, Equatorial Africa, South America, the Arabian Sea, and Southeast Asia, while PW shows high correlations in the Sahara, North America, Australia, the Northern Pacific region, and the United States.

Thus far only data (clouds, AOD, PW) which is effectively used in the CERES radiative transfer calculations (see also Section 4.2 Loeb et al., 2017; Kato et al., 2018) has been considered as explanatory variable for  $\bar{a}$ . To further disentangle which aerosol species are the most important drivers of  $\bar{a}$ , we correlate the mean annual cycle of different aerosol species from the MERRA-2 reanalysis with  $\bar{a}$  as shown in Figure 4.4e-j (note that CERES and MERRA-2 are largely independent of each other). Additionally, Figure 4.5 shows the extinction aerosol optical depth at 550nm for different aerosol species from MERRA-2 and PW from CERES SYN1deg for each region.

In regions which are known for excessive seasonal biomass burning – i.e., Central Africa, South America, and Southeast Asia — the aerosol species  $\text{SO}_4$ , organic carbon, and black carbon show highest correlations with  $\bar{a}$ . In all those regions, organic carbon contributes particularly strongly to the annual cycle in aerosol optical depth (see Figure 4.5) and, therefore, also to  $\bar{a}$ . In the United States, also aerosol species related to human activities seem to contribute to the aerosol induced  $\bar{a}$ . In the US, however, PW also plays a major role.

In Australia, aerosol extinction as well as PW peak in the austral winter. Although the annual cycle of dust correlates with  $\bar{a}$  (Figure 4.4f) it seems to play only a minor role as its abundance and scattering and absorption efficiencies are too small (Figure 4.5b).

In the Arabian Sea and the Southern Ocean,  $\bar{a}$  correlates with the annual cycle of sea salt. In the Arabian Sea, the relative contribution of sea salt to total AOD is, however, also small (Figure 4.5a).

Overall, from this section we conclude that in each region,  $\bar{a}$  is driven by different variables. Water vapor and aerosols are identified as major drivers for  $\bar{a}$ . Clouds seem to only play a minor role for  $\bar{a}$ . The regions with large annual cycles in aerosols from seasonal biomass burning also show the largest  $|\bar{a}|_m$ .

## 4.6 Atmospheric shortwave absorption in CMIP5 models

Here, we infer whether CMIP5 models can reproduce the patterns found for  $\bar{a}$  and  $\bar{a}$ . The spatial patterns of  $\bar{a}$  from individual models are shown in Figure C.1 in the Appendix C.1. The ensemble mean  $\bar{a}$  is shown in Figure 4.6a. Figure 4.7a shows the skill of individual models and the ensemble mean to simulate  $\bar{a}$  in a Taylor diagram (Taylor, 2001). We use the CERES derived  $\bar{a}$  (Figure 4.1a) as reference and consider all pixels from 60°S to 60°N. The spatial correlations with  $\bar{a}$  from CERES data range from  $r=0.49$  (CMCC-CMS) to  $r=0.89$

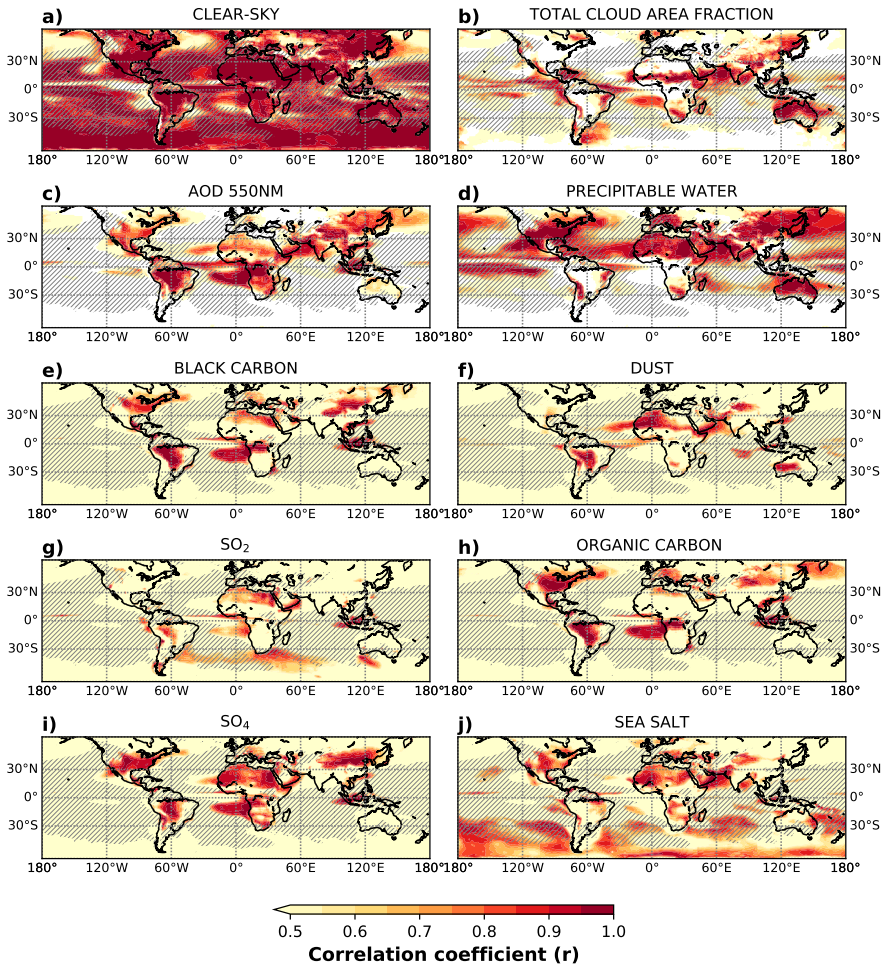


**Figure 4.4:** Correlation ( $R^2$ ) between the CERES-based  $\bar{a}$  and the annual cycles of (a) Clear-sky  $\bar{a}$ , (b) Total cloud area fraction, and (c) AOD 550nm from CERES SYN1deg and (d) Precipitable Water, (e) Black Carbon, (f) Dust, (g) SO<sub>2</sub>, (h) Organic Carbon, (i) SO<sub>4</sub>, and (j) Sea Salt from MERRA-2. Darker red colors indicate higher correlation. The hatching indicates regions with  $|\bar{a}|_m < 2\%$ .



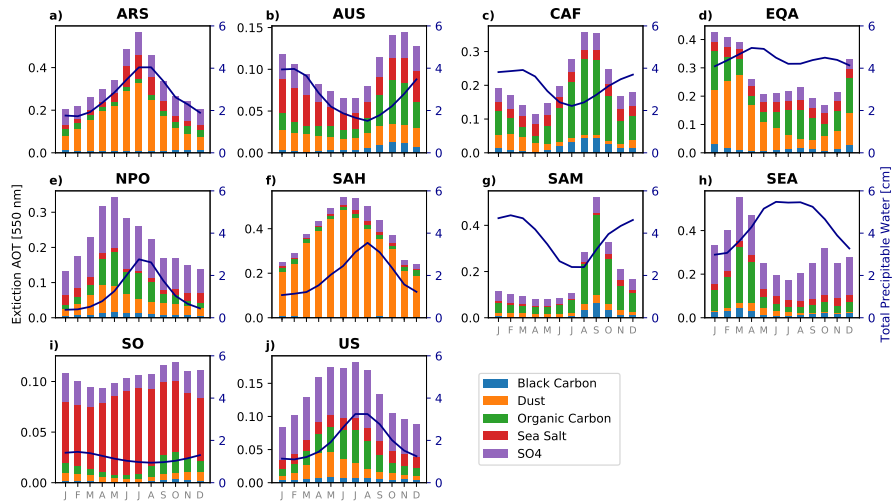


**Figure 4.5:** Annual cycles of different aerosol species and precipitable water for different regions. The regions refer to the ones in Figure 4.3k. Shown are extinction aerosol optical depth at 550nm from MERRA-2 (bars; note the different y-axis ranges) and total precipitable water from CERES SYN1deg (blue line).

(GFDL-CM3). Interestingly, the ensemble mean outperforms most individual models. This behavior – that the ensemble mean outperforms the individual models – was reported also for other variables and earlier model intercomparisons (e.g., Lambert and Boer 2001) and triggered several theoretical articles which tried to explain this feature (e.g., Gleckler et al. 2008; Rougier 2016; Christiansen 2017)

Although the models' ability to simulate  $\bar{a}$  is only moderate, we continue to infer the models' skill to reproduce  $\bar{a}$  as the two are largely independent of each other (see section 4.4). Figure A2 in the appendix depicts  $\bar{a}$  for all models, similarly as shown for the observations (in Figure 4.2). The ensemble mean  $\bar{a}$  is shown in Figure 4.6b. Taylor diagrams, where we compare  $|\bar{a}|_m$  and  $|\bar{a}|_p$  from the CMIP5 models and CERES data (Figure 4.2a), are shown in Figure 4.7b and Figure 4.7c, respectively. The Figures reveal that the models can not perfectly reproduce the patterns of the magnitudes and timing of the  $\bar{a}$ . Again, the ensemble mean outperforms most of the individual models.

To get an overview, which regions are most problematic for the models, Figure 4.8 shows Taylor diagrams that show the skill of the models to reproduce  $\bar{a}$  with respect to CERES throughout the different regions. Overall the models perform best in regions where PW or natural aerosol dominate the  $\bar{a}$  (i.e., ARS, AUS, NPO, SAH, SO and the US). In the regions where biomass aerosol species are major drivers for  $\bar{a}$  – i.e., CAF, SAM, and SEA – the model performance is limited. Further noteworthy is that the models seem to agree that there is

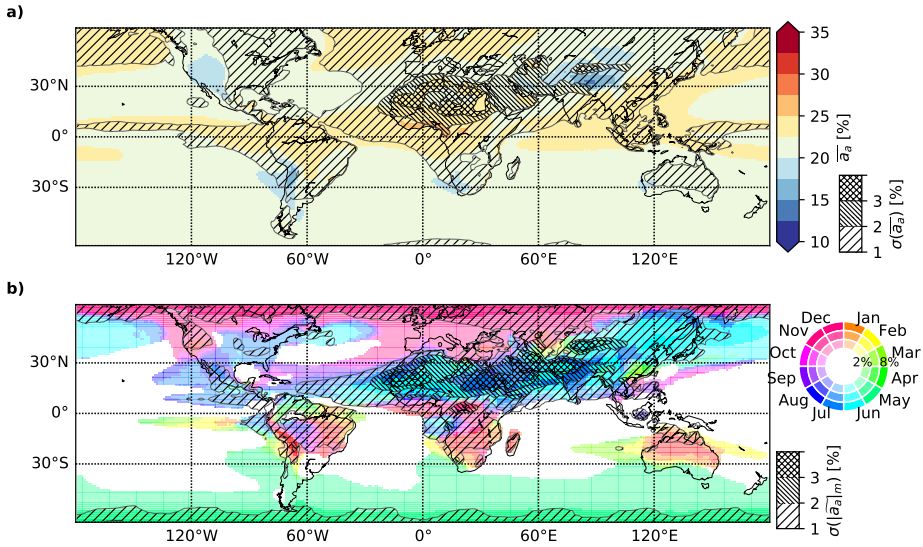


**Figure 4.6:** CMIP5 ensemble mean of (a) the annual mean and (b) the annual cycle of fractional atmospheric shortwave absorption from historic simulations (1993-2005). The hatching indicates the ensemble standard deviation of  $\bar{a}$  in (a) and the ensemble standard deviation of  $|\bar{a}|_m$  in (b).

quite a substantial  $\bar{a}$  in Europe, which is much less prominent in the observations. Noteworthy is also that the models agree among each other (Figure 4.6b) and with the observations (Figure 4.8i) about  $\bar{a}$  in the southern ocean region although it is known that the models have substantial biases in the shortwave fluxes in that region (e.g., Trenberth and Fasullo, 2010; Bodas-Salcedo et al., 2013; Meijers, 2014; Hyder et al., 2018).

The model results are based on historical simulations with the averaging period 1993 to 2005. To deduce the robustness of the models' simulated  $\bar{a}$  we compared  $\bar{a}$  from the historical simulations to the pre-industrial control simulations. Differences between the simulations were negligibly small for all models (not shown). This indicates also that – in the models – the anthropogenic influence on  $\bar{a}$  is small.

## 4.7 Discussion

In this study, we use the best observational data available for the assessment of the annual cycle of the atmospheric shortwave absorption. The albedo and TOA data sets are based on satellite observations. For surface solar radiation we largely rely on the CERES EBAF surface data set. Since surface solar radiation can not be directly measured from space, its derivation relies on sophisticated radiative transfer modeling which is also based upon several auxiliary data sets as described in detail in Kato et al. (2018). Nevertheless, the data has proven to agree

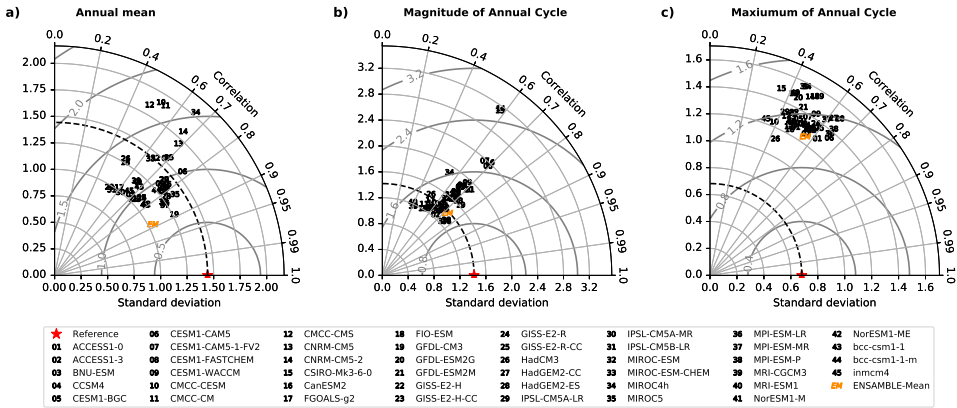


**Figure 4.7:** Taylor diagrams (Taylor, 2001) showing the skill of the CMIP5 models to simulate the spatial pattern of (a)  $\bar{a}$ , (b)  $|\bar{a}|_m$ , and (c)  $|\bar{a}|_p$  with respect to the CERES derived quantities (as shown in Figure 4.1 and 4.2). Numbers indicate the different models. The polar angle indicates the spatial correlation coefficient between the models and CERES. The polar axis indicates the spatial standard deviations of the respective fields as simulated by the models (given in %). The root mean square errors are indicated with gray contour lines. Correlations in (c) are calculated using circular correlation coefficients.

reasonably well with ground based measurements and estimated uncertainties are within a few  $\text{W/m}^2$ . (Kato et al., 2018). Moreover, we use station based SSR observations to anchor the analysis to surface observations. In most regions where in-situ data is available, they show the same basic annual cycles as the CERES data, where CERES rather tends to under- than overestimate annual cycles. This, altogether, illustrates the high quality and usefulness of the CERES surface date.

To put the magnitude of the annual cycles in general more into perspective, we want to emphasize that although the magnitudes of  $\bar{a}$  with values for  $|\bar{a}|_m$  of up to 10% seem to be relatively small in terms of fraction of incoming solar radiation at the TOA, they are fairly large when comparing them to the long term global mean atmospheric absorption of around 23% (see Figure 4.1). This means that the seasonal variation of fractional atmospheric absorption can reach values up to around 40% of the long term annual mean absorption, or, put differently, the minimum and maximum fractional atmospheric absorption differ by up to a factor of 1.5, which is quite substantial.

Considering that Hakuba et al. (2016) found that clouds play a crucial role for the near zonal constancy of annual mean fractional absorption, it is astonishing that clouds do not significantly impact the annual cycle of fractional shortwave absorption. This dichotomy

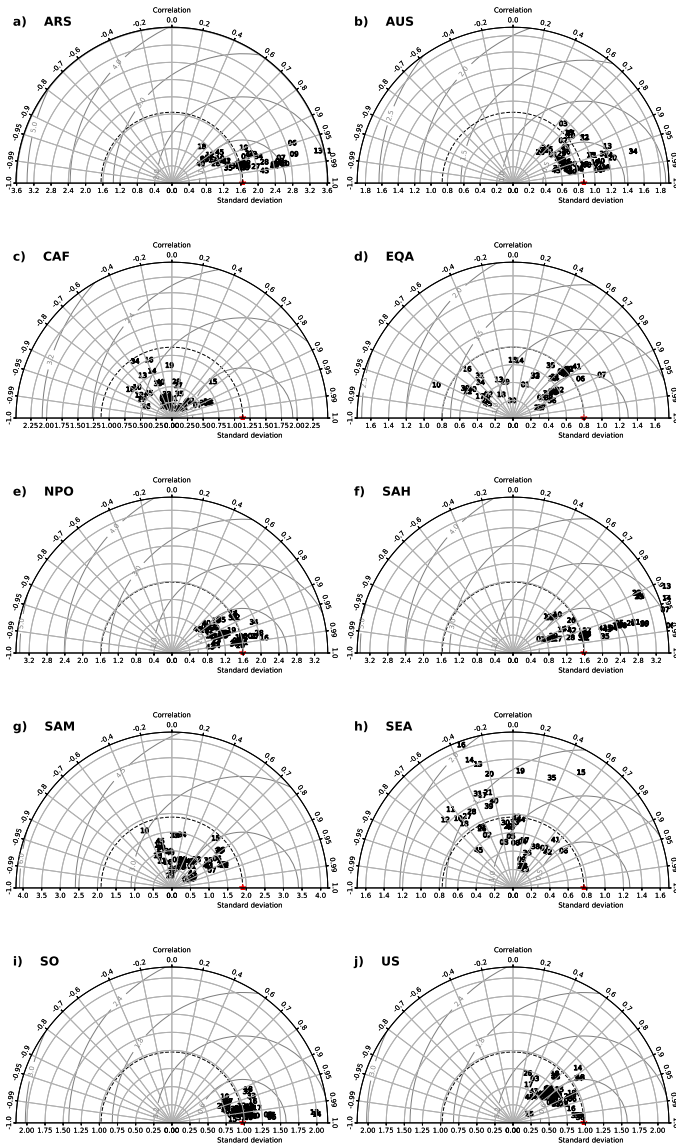


**Figure 4.8:** Taylor diagrams (Taylor, 2001) showing the skill of the CMIP5 models to simulate the  $\bar{a}$  in the different regions shown in Figure 4.3l with respect to the CERES derived quantities. Compared are the regional average  $\bar{a}$  from CERES and individual CMIP5 models. Numbers indicate the different models (see legend in Figure 4.7). The polar angle indicates the correlation coefficient between the models and CERES. The radial axis indicates the standard deviations (given in %). The root mean square errors are indicated with gray contour lines.

deserves further evaluation in future studies.

Our analysis shows that regions with extensive seasonal biomass burning have the largest annual cycles in atmospheric absorption. As biomass burning is generally related to human activities,  $\bar{a}$  is likely also anthropogenically intensified/forced. A large body of literature exists, which highlights the impact of biomass burning on local climate in these regions (e.g. Simoneit, 2002; Andreae et al., 2004; Zhang et al., 2008; Thornhill et al., 2018). Also, it was shown that so called atmospheric brown clouds – i.e. thick persistent aerosol layers above highly polluted regions – affect local climate and the hydrological cycle (Ramanathan et al., 2005). Therefore, simulating biomass burning and the corresponding  $\bar{a}$  is indispensable to be able to predict changes in local climate.

Although the CMIP5 models show limited skill in reproducing the pattern of long term mean fractional atmospheric absorption, analyzing the model's ability to simulate the annual cycle of fractional absorption was rewarding. In regions where  $\bar{a}$  is driven by natural aerosols or PW, the models show good agreement with the observations, indicating that the annual cycle of natural aerosol background as well as the PW are well captured in the models. In the regions where biomass burning aerosols are dominant, the models show generally a worse performance. This suggests that biomass burning, or at least its seasonal dependence, is not captured adequately by the models. This issue was already raised by Wild (1999) and still seems to be prevalent in the CMIP5 models.

From an energy balance perspective, global warming is initiated by increasing greenhouse gases and an associated increasing greenhouse effect. However, several studies (e.g. Trenberth and Fasullo, 2009; Donohoe et al., 2014) suggest that the main energy accumulation will happen in the shortwave part of the spectrum due to increasing absorption at the surface as a result of reduced snow and sea ice cover (snow/ice- albedo feedback) and enhanced shortwave absorption in the atmosphere caused by the well known water vapor feedback. Therefore, future studies should investigate to what extent the projected changes in atmospheric shortwave absorption influence the seasonality of the annual cycle of atmospheric absorption.

## 4.8 Summary and Conclusion

In this study, we focused on the annual cycle of atmospheric shortwave absorption, which we normalize by the incoming TOA radiation ("fractional atmospheric absorption") to suppress the large astronomically induced seasonal variations. Therefore, we were able to study purely atmospheric processes of relevance for the atmospheric absorption. We used the CERES EBAF surface and TOA data sets to calculate atmospheric absorption globally. The analysis was anchored to in-situ surface solar radiation observations from four different observational networks (BSRN, GEBA, CMA, and GTMBA). At the in-situ surface observations we used collocated MODIS albedo and CERES TOA net radiation observations to calculate

atmospheric absorption.

We showed that substantial regional differences in multi-annual mean atmospheric absorption are apparent in the observations. We found the highest fractional atmospheric absorption values in tropical Africa and South American, in the Indian subcontinent, and the Chinese lowlands. Not surprisingly, fractional atmospheric absorption is smaller in elevated regions due to the reduced atmospheric path length. The in-situ and CERES estimates agree reasonably well although the dynamical range of the CERES data is smaller than that of the in-situ data. CERES, however, tends to miss some of the spatial variability in atmospheric absorption.

Turning to annual cycles, we found several regions with pronounced annual cycles in fractional atmospheric shortwave absorption. In some of these regions, the magnitudes of the annual cycles exceed 10% of the incoming TOA radiation. The timing of the annual cycle differs substantially among the regions, suggesting that different driving factors are accountable for the annual cycles. This shows that in a global perspective the non-existing annual cycle in fractional atmospheric absorption in Europe found by Hakuba et al. (2014a), is rather an exception than the rule. The in-situ data generally confirm the CERES-based findings. In some regions the in-situ data suggest even more pronounced annual cycles.

A simple correlation analysis based on the CERES data indicated that clouds play only a minor role in explaining the annual cycles in fractional atmospheric absorption while aerosols and water vapor show the strongest correlations with the annual cycles in fractional atmospheric absorption. Depending on the region, different aerosol species correlate with the CERES-based annual cycles in atmospheric absorption. In the regions with the largest annual cycles in atmospheric absorption, biomass burning aerosols show highest correlations. Apart from the biomass burning regions the annual cycles in water vapor and natural aerosol species, such as dust and sea salt, are suggested as drivers for the annual cycle in atmospheric absorption.

Finally, we tested the ability of CMIP5 models to simulate the observed pattern of atmospheric absorption. Overall the models' skill is only moderate. In regions where the annual cycle of atmospheric absorption is driven by natural aerosols and precipitable water the models perform well. In contrast, in regions with large annual cycles in atmospheric absorption induced by biomass burning aerosols, the model performance is very limited.

Taken together, we have shown that fractional atmospheric absorption has substantial annual cycles in several regions. The drivers for these annual cycles vary through the region.

## Acknowledgments

This study was funded by the Swiss National Science Foundation grant 20002\_159938/1 (Towards an improved understanding of the Global Energy Balance: temporal variations of solar radiation in the climate system). GEBA is supported by the Federal Office of Meteorology and Climatology MeteoSwiss, in the framework of GCOS Switzerland. We thank Maria Hakuba for processing the BSRN data. We thank all people involved in collecting and storing the in-situ surface radiation data. We thank the CERES and MODIS teams for processing and providing data. Thanks to all modeling groups and people involved in the CMIP5.





# Changes in atmospheric shortwave absorption as major driver of dimming and brightening

M. Schwarz<sup>1,\*</sup>, D.Folini<sup>1</sup>, S. Yang<sup>1,2</sup>, R. P. Allan<sup>3</sup> & M. Wild<sup>1</sup>

**In revision**

1. Institute for Atmospheric and Climate Science, ETH Zurich, CH-8092 Zurich, Switzerland.
2. National Meteorological Information Center, China Meteorological Administration, Beijing, China
3. Department of Meteorology, National Centre for Earth Observation, Whiteknights, University of Reading, Earley Gate, PO Box 243, Reading RG6 6BB, UK

It is well documented that the amount of solar (shortwave) radiation reaching the Earth's surface underwent substantial decadal variations commonly known as "*global dimming and brightening*". From an energy balance perspective, it is apparent that these changes in surface radiation imply that at least one other variable of the shortwave energy balance, namely the surface absorption, the top-of-the-atmosphere (TOA) net flux, or the atmospheric absorption must change as well. Here we bring together colocated long-term observational data from the surface and space to study the decadal changes of the shortwave energy balance in Europe and China from 1985-2015. Within this observation-based framework, we show that increasing net shortwave radiation at the TOA and decreasing atmospheric absorption contribute each half to the observed "brightening" trends in Europe. Although the "dimming" in China levels off in the 1980s and 1990s, the absorption of SW radiation in the atmosphere increases, compensating the increasing TOA net radiation. After 2005, the Chinese surface trends turn into a "brightening" determined by decreasing atmospheric absorption, although TOA net radiation decreases in that period. This shows that changes in atmospheric shortwave absorption, arguably driven by changes in absorbing aerosols, are a major driver of European brightening and the dominant cause for the Chinese surface trends.

Solar (shortwave, SW) irradiance reaching the Earth's top-of-the-atmosphere ( $I_{toa}^{\downarrow}$ ) is partly absorbed in the atmosphere ( $A_{atm}$ ), partly absorbed at the surface ( $A_{sfc}$ ) and partly reflected back to space ( $I_{toa}^{\uparrow}$ ) (Abbot and Fowle, 1908; Trenberth et al., 2009; Stephens et al., 2012; Wild et al., 2013).  $A_{sfc}$  is thereby determined by the amount of shortwave radiation reaching the Earth's surface ( $I_{sfc}^{\downarrow}$ ) and the surface albedo ( $\alpha$ ). The total amount of SW radiation absorbed by the climate system as a whole is equivalent to the TOA net SW radiation  $I_{toa}^{net}$ , which is the residual between  $I_{toa}^{\downarrow}$  and  $I_{toa}^{\uparrow}$ . Altogether, the shortwave energy balance (SWEB) at the TOA, at the surface, and within the atmosphere can be written as:

$$I_{toa}^{net} = I_{toa}^{\downarrow} - I_{toa}^{\uparrow} \quad (5.1)$$

$$A_{sfc} = I_{sfc}^{\downarrow} * (1 - \alpha) \quad (5.2)$$

$$A_{atm} = I_{toa}^{net} - A_{sfc}. \quad (5.3)$$

While the TOA (Eq. 5.1) and surface (Eq. 5.2) components of the energy balance can be determined by (combining) direct observations,  $A_{atm}$  has to be inferred as a residual flux (Eq. 5.3).

It is well documented that  $I_{sfc}^{\downarrow}$  underwent substantial decadal variations since measurements became available in the first half of the 20<sup>th</sup> century (Wild, 2009a). Since the 1950s,  $I_{sfc}^{\downarrow}$  gradually decreased until the late 1980 (Ohmura and Lang, 1989; Russak, 1990; Stanhill and Moreshet, 1992a,b, 1994; Gilgen et al., 1998; Liepert, 2002). In Europe and other parts of the world this "dimming" phase was followed by a "brightening" period in which

$I_{sfc}^{\downarrow}$  started to increase again (Wild et al., 2005; Ohmura, 2006; Gilgen et al., 2009; Ohmura, 2009; Wang et al., 2012a; Sanchez-Lorenzo et al., 2015). In China, the dimming leveled off in the 1980s but did not turn into brightening until 2005 (Yang et al., 2018). From combining equations 5.1 - 5.3 it becomes apparent that a change in  $I_{sfc}^{\downarrow}$  implies that at least one other variable of the shortwave energy balance must change as well.

The dimming and brightening phenomenon was reported to affect surface temperatures, the hydrological cycle, the cryosphere, as well as the biosphere (Wild, 2009a, and references therein). Because of the widespread consequences, it is important to identify the governing processes behind dimming and brightening. An impressive, corresponding body of literature exists, which investigated potential causes behind the phenomenon. The radiative impact of fluctuations in the brightness of the sun that affect  $I_{toa}^{\downarrow}$ , changes in radiatively active gaseous compounds (notably  $O_3$ ,  $N_2O$ ,  $CH_4$ , and  $CO_2$ ) in the atmosphere, and changes in water vapor have been shown to be too small to explain the observed variations of  $I_{sfc}^{\downarrow}$  (Gray et al., 2010; Kvalevåg and Myhre, 2007; Mateos et al., 2013; Trenberth et al., 2005; Kvalevåg and Myhre, 2007; Posselt et al., 2011; Mateos et al., 2013; Wang et al., 2016; Wild, 2009a). This leaves changes in clouds and aerosols (and their interaction) as the potential causes of the observed variations (Stanhill and Moreshet, 1992b; Stanhill and Cohen, 2001; Lohmann and Feichter, 2005; Qian et al., 2006; Norris and Wild, 2007; Qian et al., 2007; Wild, 2009a; Long et al., 2009; Chiacchio and Wild, 2010; Wild, 2016).

Clouds have a large and negative effect on both,  $I_{toa}^{net}$  and  $I_{sfc}^{\downarrow}$ , meaning less SW radiation is entering the climate system and propagating to the ground due to increased TOA reflection when more clouds are present (Ramanathan et al., 1989; Loeb et al., 2009). For  $A_{atm}$  the effect of clouds is smaller than at the surface and at the TOA (Wild, 2000; Hakuba et al., 2016, 2017; Wild et al., 2018) and depends on the clouds' structure and microphysics. The presence of low clouds was reported to cause an increase  $A_{atm}$  while the presence of high clouds decreases  $A_{atm}$  (Hakuba et al., 2016).

Natural and anthropogenic aerosols can change the SWEB (Ramanathan et al., 2001) directly by altering the clear-sky atmospheric transmittance (Yu et al., 2006) or indirectly through altering cloud characteristics (Lohmann and Feichter, 2005). The sign and magnitude of the aerosol effects strongly depend on aerosol species, their properties, and their abundance (Myhre et al., 2013). While some species (like sulfate, nitrate, and mineral aerosols) tend to be primarily reflective, others (like black carbon) substantially absorb SW radiation (Boucher et al., 2013). An increase in primarily scattering aerosols, therefore, leads to a decrease in both  $I_{toa}^{net}$  (due to higher  $I_{toa}^{\uparrow}$ ) and  $I_{sfc}^{\downarrow}$  with little effect on  $A_{atm}$ . Absorbing aerosols on the other hand lead to an increase in  $A_{atm}$ , a decrease in  $I_{sfc}^{\downarrow}$ , but little change in  $I_{toa}^{net}$ .

Consensus on the relative importance of clouds, cloud-aerosol interactions, and aerosols has not yet been reached. From the above it follows that further insight can be gained by joint quantification of trends in  $I_{toa}^{net}$ ,  $I_{sfc}^{\downarrow}$ , and  $A_{atm}$ , as done in this study.

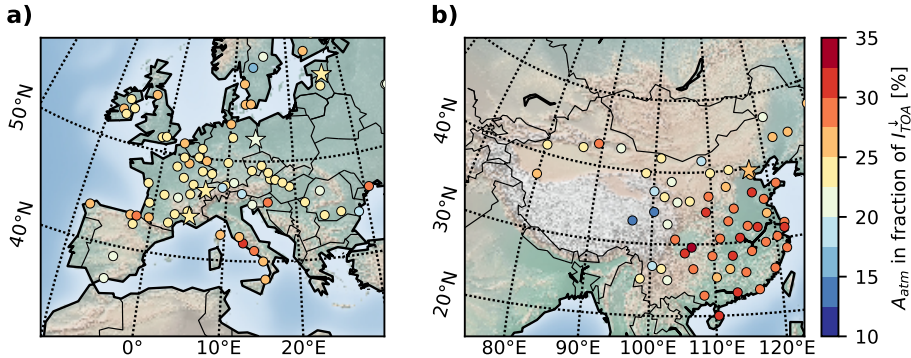


**Figure 5.1:** Fractional shortwave absorption: Long term mean (2000-2015)  $A_{atm}$  as a fraction of  $I_{toa}^{\downarrow}$  for Europe (a) and China (b). Points show GEBA and CMA stations. Stars show BSRN stations.

## Shortwave energy balance changes inferred from collocated space and surface observations.

To better understand the causes of declining surface solar radiation (dimming) and subsequent recovery (brightening) we compiled the best available observational data sets from surface and space to be able to contrast top-of-the-atmosphere, in atmosphere, and surface energy fluxes.

We use  $I_{sfc}^{\downarrow}$  data from the Baseline Surface Radiation Network (BSRN; Driemel et al. 2018), the Global Energy Balance Archive (GEBA; Wild et al. 2017), and the Chinese Meteorological Administration (CMA; Yang et al. 2018) and combine them with surface albedo estimates from the Global Land Surface Satellite (GLASS; Liang et al. 2013), and  $I_{toa}^{net}$  estimates from the DEEP-C reconstruction (Allan et al., 2014; Liu et al., 2017). We compute regionally averaged annual mean anomaly time series of all components of the SWEB based on collocated observations at 79 stations in Europe and 62 stations in China (Fig. 5.2). The methods section provides descriptions of the data sets and the data processing.

This approach goes beyond the often used surface-only perspective and allows a simultaneous observation based quantification of changes in the partitioning of  $I_{toa}^{net}$ ,  $A_{sfc}$ , and  $A_{atm}$  during brightening and dimming and, therefore, a more detailed insight about the governing processes.

Figure 5.1 shows the long term (2000-2015) annual mean  $A_{atm}$  for all European and Chinese stations in terms of fraction of  $I_{toa}^{\downarrow}$ . Globally averaged, roughly  $23 \pm 2\%$  of  $I_{toa}^{\downarrow}$  is absorbed in the atmosphere (Trenberth et al., 2009; Stephens et al., 2012; Wild et al., 2013; Hakuba et al., 2016). For Europe, our study confirms this estimate in line with Hakuba et al. (2014b). For

China, however, we find that  $A_{atm}$  exceeds 30% of  $I_{toa}^\downarrow$  and even exceeds 31% at some sites in highly developed regions.

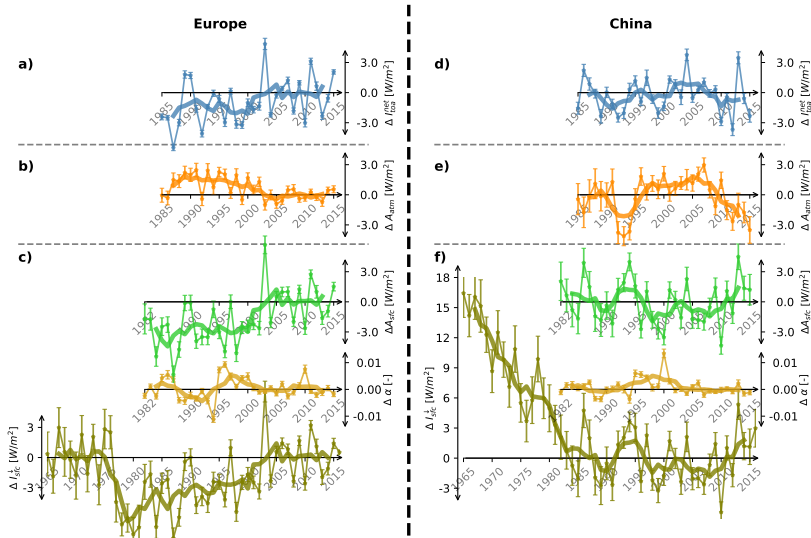


**Figure 5.2:** SWEB time series: Station mean time series of 79 stations in Europe (a-c) and 62 stations in China (d-f) for  $I_{toa}^{net}$  (a,d),  $A_{atm}$  (b, e), and  $I_{sfc}^\downarrow$ ,  $\alpha$ , and  $A_{sfc}$  (c,f). The time series are shown as deviations ( $\Delta$ ) from long term means of the reference period 2000-2015. Thin lines show station average annual means with standard errors (i.e.  $\frac{\sigma}{\sqrt{N}}$  with  $N$  the number of stations). Thick lines show centered five year running means.

Figure 5.2 shows the regionally averaged annual anomaly time series for  $I_{sfc}^\downarrow$ ,  $\alpha$ ,  $A_{sfc}$ ,  $A_{atm}$ , and  $I_{toa}^{net}$ . For the period where data of all components of the SWEB are available (i.e. 1985-2015) we compute linear trends for different sub-periods as shown in Figure 5.3.

For Europe, the well-documented decrease in  $I_{sfc}^\downarrow$  until roughly 1980 (Wild et al., 2005) and the following gradual increase of  $I_{sfc}^\downarrow$  (Wild, 2009a; Sanchez-Lorenzo et al., 2015) is clearly visible in the lowest panel of Figure 5.2c. In China,  $I_{sfc}^\downarrow$  shows a strong decrease prior to 1980 (see Fig. 5.2f). This "dimming" leveled off in China during the 1980s and 1990s and  $I_{sfc}^\downarrow$  only started to recover to some degree during the end of the observational period (Tang et al., 2011; Yang et al., 2018). This trend reversal is likely related to the implementation of more and more rigorous air quality plans in China after 2000, and thus to a reduction in air pollution (Lu et al., 2010; Jin et al., 2016; Li et al., 2018).

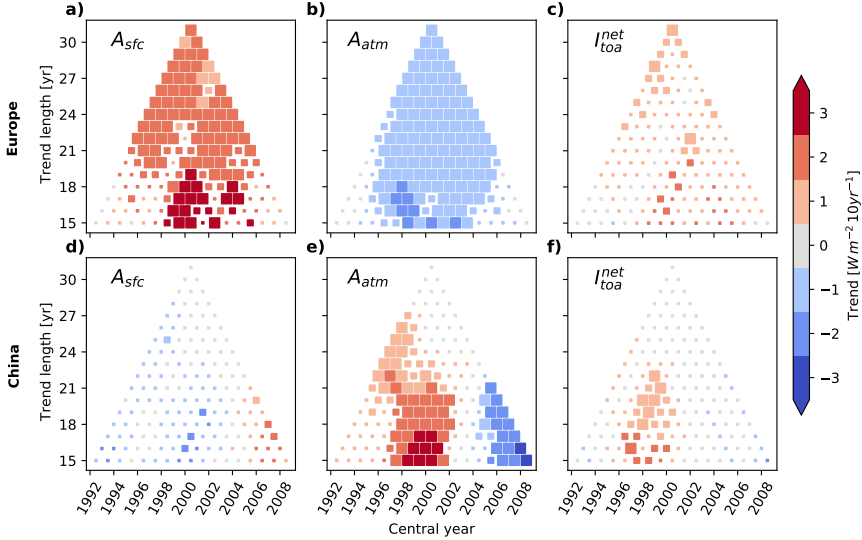


**Figure 5.3:** Trend matrices: Linear trends for  $A_{sfc}$ ,  $A_{atm}$  and  $I_{toa}^{net}$  for Europe (top row) and China (bottom row) for different periods. On the x-axis the central year of the trend window is given while on the y-axis the length of the trend is shown. The statistical significance of the trends is indicated by the size of the marker in the plots (small:  $p > 0.1$ , medium:  $0.1 \geq p > 0.05$ , large:  $p < 0.05$ ).

By combining the colocated observations of  $I_{sfc}^{\downarrow}$  and  $\alpha$  from GLASS-AVHRR (see middle panel in Fig. 5.2c & 5.2f) according to equation 5.2 we can estimate  $A_{sfc}$  for the period 1982–2015. Since  $\alpha$  shows only little variability and no trends,  $A_{sfc}$  is closely following the variability of  $I_{sfc}^{\downarrow}$  in both regions. Consequently, the brightening in Europe is accompanied by an increase in  $A_{sfc}$  (see Fig. 5.3a). In China, on the other hand, a small decrease in  $A_{sfc}$  with low statistical significance is found until 2005 which was followed by an increase thereafter (see Fig. 5.3d).

The temporal evolution of  $A_{sfc}$  is now contrasted to the  $I_{toa}^{net}$  fluxes (shown in Fig. 5.2a & 5.2d) during the period where DEEP-C is available (i.e. 1985–2015). Most of the year-to-year variability observed at the TOA is also visible at the surface (e.g., the exceptionally sunny, hot, and dry year 2003 in Europe associated with a very strong positive anomalies at the surface and at the TOA; see Fig. 5.3c & 5.2a).

In Europe,  $I_{toa}^{net}$  tends to gradually increase throughout the whole period. The observed trends in  $I_{toa}^{net}$  for all periods are considerably smaller and less significant than those observed at the surface (see Fig. 5.3a & 5.3c).

For China,  $I_{toa}^{net}$  tends to increase until the year 2004 (see Fig. 5.2d). Thereafter, a not significant decrease in  $I_{toa}^{net}$  is observed as can be seen in Figure 5.3f. In contrast to Europe, the

Chinese  $I_{toa}^{net}$  trends have opposite signs compared to the  $A_{sfc}$  trends.

Comparing changes in  $I_{toa}^{net}$  and  $A_{sfc}$  allows insight into changes in  $A_{atm}$ . In both regions, the year-to-year variability of  $A_{atm}$  is smaller than for  $A_{sfc}$  and  $I_{toa}^{net}$  as the TOA and surface flux changes compensate each other to a large degree (see Fig. 5.2b,e). Turing to trends, a small statistically nonsignificant increase in  $A_{atm}$  on the order of  $+1 \text{ W m}^{-2} \text{ decade}^{-1}$  is found in Europe from 1985-1995, followed by a significant decrease in  $A_{atm}$ , (Figure 5.2b and 5.3b). Trends starting from around 1993 show a significant decrease in  $A_{atm}$  between  $-0.6 \pm 0.2$  to  $-1.5 \pm 0.6 \text{ W m}^{-2} \text{ decade}^{-1}$  depending on the trend length and exact starting year.

In China, by contrast,  $A_{atm}$  shows rather large decadal trends (Fig 5.2e and 5.3e). Starting around the 1990s, rather large positive trends (up to around  $+3 \text{ W m}^{-2} \text{ decade}^{-1}$ ) are observed for  $A_{atm}$ . These positive trends in  $A_{atm}$  last until roughly 2005. After 2005, a sharp decrease in  $A_{atm}$  can be noted, which goes along with the above-mentioned strong increase in  $A_{sfc}$  and  $I_{sfc}^{\downarrow}$ , while  $I_{toa}^{net}$  does not show this abrupt change.

We can summarize the results as follows: In Europe, the increase in the amount of net incoming radiation at the TOA and the decrease in atmospheric absorption each contributed roughly half to the increase in surface absorption and therefore to the European brightening. In China, a transition from dimming to brightening is found around the year 2005. Before that year, an increase in the TOA net radiation was observed. This increase was overcompensated by large positive trends in atmospheric absorption, which together led to the observed dimming at the surface in China. After 2005, all trends reversed in China. At the TOA, the decrease of incoming radiation was again overcompensated by a large reduction in atmospheric absorption, which together led to a surface brightening. This shows that changes in atmospheric absorption are central to the brightening and dimming phenomenon.

## Discussion and conclusions.

For the study region of China, the analysis indicates that the redistribution of absorbed SW energy from the surface to the atmosphere, rather than changes at the TOA are associated with the dimming and brightening phenomenon during the observational period, while in Europe both effects are roughly equally relevant.

Further insight into the physical cause of the changes in  $A_{atm}$  can be obtained from the following line of argument. Taking into account that  $\alpha$  does not change substantially, an increase in  $I_{toa}^{net}$  (as observed in Europe over the whole period and in China until 2005) either goes along with decreasing clouds (reduced reflection) or a decrease in reflecting aerosols, since changes of other atmospheric constituents are shown to be incapable of explaining the changes of the SWEB. Considering that changes in clouds affect  $A_{atm}$  less than  $I_{toa}^{net}$  (Wild, 2000; Loeb et al., 2009; Hakuba et al., 2016, 2017) and that the observed changes in  $A_{atm}$  are larger than the change in  $I_{toa}^{net}$ , it is unlikely that changes in clouds alone account for the observed variations in the SWEB. An analogue argumentation holds for changes in scattering

aerosols. This suggests that changes in absorbing aerosols must be a major contributor to the dimming and brightening phenomenon. This is especially evident in China where the trends at the TOA and the surface even have opposite signs.

It is plausible that absorbing aerosols are also the main cause for the Chinese dimming in the pre-satellite era and that the high  $A_{atm}$  (Fig. 5.1b) is a remnant of this strong dimming. However, since direct continuous observations are not available, this remains speculative.

Ultimately, this study demonstrates that using combined colocated surface and TOA observations allows valuable insight into the physical processes which govern the changes in the shortwave energy balance.



## Methods

In this study we combine colocated measurements of  $I_{sfc}^{\downarrow}$ ,  $\alpha$ , and  $I_{toa}^{net}$  to compute regionally averaged annual mean time series for  $A_{sfc}$ ,  $A_{atm}$ , and  $I_{toa}^{net}$  according to equations 5.1 - 5.3 (Hakuba et al., 2014b). Below, we first introduce all data sets before we describe our data processing strategy.

### Surface shortwave radiation.

For  $I_{sfc}^{\downarrow}$  we utilize data from the Baseline Surface Radiation Network (BSRN; Driemel et al. 2018), the Global Energy Balance Archive (GEBA; Wild et al. 2017), and data from the Chinese Meteorological Administration (CMA; Yang et al. 2018).

The GEBA and CMA data is available as monthly mean time series. For BSRN stations, monthly mean times series from the raw two- and one-minute data are calculated according to the recommended procedure of Roesch et al. (2011).

Only stations which are representative for a larger surrounding are included in the analysis, to match with the scale of the TOA data. We consider two aspects of representativeness (Schwarz et al., 2017, 2018): (1) the spatial distance up to which the temporal variability of a  $I_{sfc}^{\downarrow}$  time series measured at a site can be considered representative (expressed in terms of decorrelation length,  $\delta$ ), and (2) spatial sampling errors ( $\epsilon$ ) which arise due to imperfect representativeness of the stations. In the terminology of Schwarz et al. (2018), stations which do not adequately represent the temporal variations of  $I_{sfc}^{\downarrow}$  (i.e.  $\delta < 2^\circ$ ) or have large (monthly) spatial sampling errors ( $\epsilon > 16 W/m^2$ , 95% confidence level) are excluded from the analysis.

Different uncertainty estimates for the surface observations exist. For the BSRN data, uncertainties of  $\pm 8 W m^{-2}$  and  $\pm 5 W m^{-2}$  (95% level) for monthly and annual means were reported, respectively (Dutton et al., 2012). For the GEBA data, uncertainties for monthly and annual means of  $\pm 5\%$  and  $\pm 2\%$  (root mean square error) were reported (Gilgen et al., 1998). The error of the CMA data likely does not exceed  $\pm 5\%$  and  $\pm 3\%$  for monthly and annual data (Shi et al., 2008).

The long-term stability of the  $I_{sfc}^{\downarrow}$  observations is achieved by a regular calibration of the sensors against a reference with known stability which are traceable to a known reference. BSRN measurements are calibrated annually and traceable to the world radiometric reference (WRR) from the World Radiation Center at the Physikalisch-Meteorologisches Observatorium in Davos, Switzerland (PMOD/WRC) (McArthur, 1998). The CMA data is calibrated using a multistep approach which is traceable to a national references which itself is calibrated to the WRR every five years (Wang et al., 2015b).

Within 38 years the WRR had a suggested total drift of less than 0.02% (Dutton et al., 2012). A quantitative assessment about how that translates into the stability of long term  $I_{sfc}^{\downarrow}$  measurements is lacking. However, for well calibrated instruments, we expect sufficient

stability which does not substantially influence the observed trends.

Moreover, to avoid step-changes in the surface data which might occur due to change in the instrumentation and/or relocation of the station, we assess the homogeneity of the monthly  $I_{sfc}^{\downarrow}$  time series. The GEBA time series are tested regarding their homogeneity using four different homogeneity tests as described in Hakuba et al. (2013b). The CMA data has been analyzed and homogenized using sunshine duration data as described in Yang et al. (2018). BSRN data is expected to be homogeneous because of the rigorous measurement standards of the BSRN (McArthur, 1998).

After excluding stations with insufficient spatial representativeness, stations with lacking homogeneity, or stations with less than 15 years of data for all SWEB components, we use in total four BSRN and 75 GEBA stations for Europe and one BSRN and 62 CMA stations for China.

### **TOA shortwave radiation.**

For the TOA net irradiance, we use the DEEP-C version 3 reconstruction, which is available with a spatial resolution of  $0.7^{\circ}$  and monthly temporal resolution (Allan et al., 2014; Liu et al., 2017). The reconstruction merges satellite SW TOA irradiances from the Clouds and Earth's Radiant Energy System (CERES) Energy Balanced and Filled Ed2.8 data set (available since 02/2000; Wielicki et al. 1996; Loeb et al. 2009) and the Wide Field of View (WFOV) Ed.3 Rev1 data set from the non-scanning instrument onboard of the Earth Radiation Budget Experiment (ERBE; available 1985-1999; Barkstrom 1984; Wong et al. 2006) satellites. For the reconstruction, the ERA-Interim atmospheric reanalysis (Dee et al., 2011) and a 25km resolution global atmospheric model (HadGEM3-A-GA3) with five ensemble simulations from the UPSCALE project (Mizielinski et al., 2014) were used to homogenize the satellite data sets (Allan et al., 2014; Liu et al., 2017). For the period after March 2000, CERES data is used. Before that, the reconstruction is based on an annual cycle calculated from the first five complete years of the CERES data (2001-2005) to which ERA-I deseasonalized radiative flux anomalies are added. The data is then adjusted such that the hemispheric ( $60^{\circ}S - 0^{\circ}$  and  $0^{\circ} - 60^{\circ}N$ ) mean deseasonalized anomalies match the corresponding hemispheric ERBE time series. With this approach, the DEEP-C data "combines the quality of the CERES data, stability of the ERBE data, and the realistic circulation changes depicted by ERA-I" (Allan et al., 2014).

We provide a comparison between the DEEP-C reconstruction and the directly measured data in Figure 5.4. There, all regional averages of the raw data for Europe and China from CERES EBAF v.4 (03/2000 to present; Loeb et al. 2017), the ERBE Scanner data (1985-1989) (Barkstrom, 1984), and the ERBE WFOV Nonscanner data Ed. 3 Rev.1 (Wong et al., 2006) and ERBE WFOV Nonscanner data Ed. 4 (Shrestha et al., 2017) (both WFOV Nonscanner data available from 1985 to 1999) are shown. The figure shows, that the DEEP-C data follows the

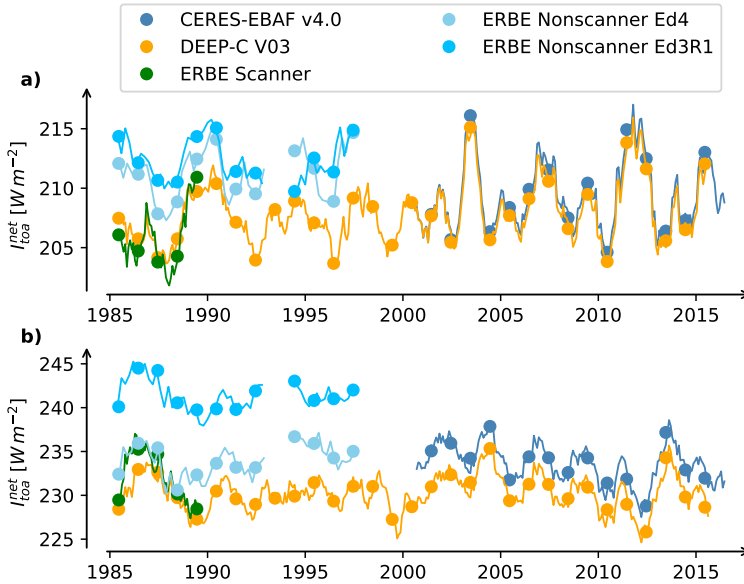


**Figure 5.4:**  $I_{toa}^{net}$  data comparison: regional average  $I_{toa}^{net}$  time series of the CERES-EBAF v.4.0, DEEP-C V03, ERBE Sanner, and ERBE Nonscanner (Ed3R1 and Ed4) data sets for (a) Europe ( $40^{\circ}\text{N}$ - $50^{\circ}\text{N}$ ;  $10^{\circ}\text{W}$ - $20^{\circ}\text{E}$ ) and (b) China ( $20^{\circ}\text{N}$ - $40^{\circ}\text{N}$ ;  $100^{\circ}\text{E}$ - $120^{\circ}\text{E}$ ). Points show annual means while the thin lines show 12-month running means.

same temporal evolution as the directly measured data and that no spurious inhomogeneities or trends are visible in the data record.

The uncertainty for annual means of  $I_{toa}^{net}$  from the DEEP-C reconstruction is  $\pm 0.31 \text{ W m}^{-2}$  (one standard-deviation confidence level) for the CERES period and  $\pm 0.67 \text{ W m}^{-1}$  (90%-confidence level) prior to the CERES period (Allan et al., 2014). The stability of the the CERES instrument is of the order of  $\pm 0.2 \text{ W m}^{-2} \text{ decade}^{-1}$  (Liu et al., 2017) while the stability of the ERBE WFOV Nonscanner instrument is of the order of  $\pm 0.35 \text{ W m}^{-2}$  during the period 1985-1999 (Wong et al., 2006).

## Albedo.

We use the Global Land Surface Satellite (GLASS) white sky albedo as the main albedo dataset. It is based on advanced very high resolution radiometer (GLASS-AVHRR; 1982 - 2015) and Moderate-resolution Imaging Spectrometer (GLASS-MODIS; 2000-2015) observations (Liang et al., 2013). The dataset provides a high-quality gap-free, long-term, self-consistent albedo record since 1982 with similar quality as the Moderate Resolution Imaging Spectroradiometer (MODIS) albedo data (Liu et al., 2013; Liang et al., 2013). The data is

available in 8-day temporal resolution with  $0.05^\circ$ . We aggregate the observations temporally to monthly means and spatially to the DEEP-C  $0.7^\circ$  grid.

For the period after 2000, we also use the MODIS white sky surface albedo from Schaaf and Wang (2015). The MODIS data currently provides one of the most reliable albedo estimates and is, therefore, used as reference data.

## Data processing.

To calculate the surface absorbed flux, we multiply the monthly  $I_{sfc}^\downarrow$  with monthly mean  $\alpha$  estimates from GLASS-AVHRR. A step inhomogeneity in the GLASS-AVHRR data around the year 2000 was corrected by subtracting the differences between the GLASS-AVHRR long-term mean before and after the year 2000. Since the MODIS albedo is currently the most reliable albedo estimate, we bias correct the GLASS-AVHRR data by subtracting the differences between the MODIS and GLASS-AVHRR data.

To test the albedo's influence on  $A_{sfc}$  and  $A_{atm}$  we computed all fluxes by assuming a constant  $\alpha$  which we calculated from the MODIS data. The comparison of the SWEB fluxes as calculated using GLASS-AVHRR and constant albedo reveals that the albedo variability only has a minor influence on the  $A_{sfc}$  and  $A_{atm}$  (now shown).

Finally, we calculate  $A_{atm}$  by subtracting  $A_{sfc}$  from  $I_{toa}^{net}$  from co-located DEEP-C data. These time series are then deseasonalized before we calculate annual mean anomalies for each station (if at least nine of twelve months are available per year). We only consider time series which have at least 15 annual mean values during the period 1985-2015. Finally, we average the annual anomaly time series of all stations in Europe and China.

## Code availability

All code used in this study to perform the analyses and to create the figures can be made available upon request from the corresponding author.

## Data availability

The DEEP-C data is available via <http://dx.doi.org/10.17864/1947.111>. The GLASS data is available via <http://g1cf.umd.edu/data/abd/>. The BSRN data is available via <https://bsrn.awi.de/>. The GEBA data is available via <http://www.geba.ethz.ch/>. The CMA data can be accessed from the Chinese Meteorological Administration <http://www.cma.gov.cn/>.

## Addendum

**Acknowledgements** This study was funded by the Swiss National Science Foundation grant 20002\_159938/1 (Towards an improved understanding of the Global Energy Balance: temporal variations of solar radiation in the climate system). Richard P. Allan was funded by the Natural Environment Research Council (NERC) SMURPHS Grant NE/N006054/1. We thank all people who were involved in collecting, processing and storing the surface radiation data for the radiation networks BSRN, GEBA and CMA. We thank the CERES, ERBE and DEEP-C teams, and the AVHRR, MODIS and GLASS teams for collecting, creating and offering the data sets.

**Competing Interests** The authors declare that they have no competing financial interests.

**Author contributions** M.S., D.F., and M.W. designed the study. Y.S. provided and homogeneous CMA data. R.A. provided the DEEP-C data and helped interpreting it. M.S. did the coding and data analysis with help of all coauthors. M.S., D.F., M.W. wrote the paper with contributions from all coauthors.

**Correspondence** Correspondence and requests for materials should be addressed to Matthias Schwarz (email: matthias.schwarz@envi...)



In this last chapter, we provide an extended summary of the main finding of this thesis. At the same time, we discuss their broader implications and highlight some aspects which go beyond our own research objectives and might trigger future investigations.

The overarching goal of this thesis was to study temporal variations in the shortwave energy balance on different time scales by using the most reliable and advanced currently available observational data sets. To that end, data on surface radiation, surface albedo, and top of the atmosphere (TOA) fluxes must be combined. Surface albedo and TOA fluxes are available as gridded data products derived from satellite observations. Surface radiation can either be obtained by direct ground-based in-situ observations or from satellites by using sophisticated radiation transfer modeling. The clear advantage of in-situ observations is that they measure surface radiation directly and, therefore, in the most robust and reliable way. However, the spatial coverage of in-situ observations is constrained and global coverage can hardly be achieved, as the number of high-quality, long-term, homogeneous in-situ observations is limited. On the other hand, satellite-derived solar radiation data offers better spatial coverage, but their retrieval relies heavily on modeling assumptions as well as on information about the state of the atmosphere, which both lead to uncertainties in the estimates. So, the dilemma is that the accurate in-situ data is spatially scarce while the satellite data achieves better spatial coverage but is more uncertain.

In this thesis, we utilize all available radiation data depending on what is most suitable for the specific question. This includes in-situ data, high-resolution satellite-derived data from geostationary satellites, as well as satellite-derived data with global coverage from polar orbiting satellites.

Using in-situ data – which from a spatial perspective is point data – in combination with gridded data products requires a thorough assessment of potential methodological uncertainties, as formulated in a research question and addressed in two chapters of this thesis (Chapter 2 and Chapter 3).

Specifically, it is a necessary criterion that the in-situ records are representative of the whole area covered by the colocated, gridded TOA flux data from CERES which, in our case, has a one-degree spatial resolution. A particular challenge of this thesis was to develop criteria

and methods to quantify the representativeness of in-situ observations. Although different aspects of the representativeness of point measurements have been covered in the literature, it has been unclear whether monthly mean surface solar radiation records are representative of their one-degree surroundings.

Three different aspects of representativeness – quantified via corresponding metrics – should be considered when aiming to combine in-situ records with gridded data. The first metric – the spatial sampling bias – quantifies systematic, potentially correctable, differences between the in-situ observation and the colocated satellite pixel and was introduced by Hakuba et al. (2013a). The other two aspects, which address the spatiotemporal representativeness, were introduced in Chapter 2 of this thesis. More specifically, one – the decorrelation length – quantifies the distance up to which an in-situ observation can reliably measure monthly temporal variations of its surroundings, while the other – the spatial sampling error – quantifies noncorrectable uncertainties which arise due to the imperfect spatial representativeness of point observations.

In Chapter 2 we focused on Europe because of the high station density in this region. For the computation of the decorrelation length, we used both in-situ and high-resolution satellite-derived data. From analyzing in-situ data only, we find that, on average, the European sites show large correlations ( $R^2 > 1/e$ ) up to 400 km around the sites. A comparison of the station-based estimates with those from the high-resolution satellite-derived data shows that the estimates from the different data sources agree very well. Given that climatological information for some atmospheric constituents (e.g., aerosols) is used in the retrievals of the high-resolution satellite data, one might expect that the satellite-derived data underestimates the spatiotemporal variability of the solar radiation field. An underestimated variability in the solar radiation field would imply, that the representativeness estimates based on this data might be somewhat too optimistic. The above-mentioned comparison shows, however, that the high-resolution satellite-derived data can capture the spatiotemporal structure of the surface solar radiation field on monthly time scales sufficiently well to study representativeness.

For the computation of the spatial sampling error, we rely on the high-resolution satellite-derived surface solar radiation data. Although Europe has a particularly high station density for surface solar radiation observations, too few stations are available to estimate this representativeness metric using only in-situ observations. We find that the spatial sampling error for a one-degree reference grid is typically of the same magnitude as the measurement uncertainty of the in-situ observations for European sites.

After focusing on Europe, we extended the analysis in Chapter 3 to a near-global scale (50°S to 55°N) using satellite-derived surface radiation data sets. Within the near-global assessment, we found large regional differences in the three metrics. This shows that all three aspects of representativeness must be evaluated for each location (and each reference grid) individually. Nevertheless, in most regions monthly surface solar radiation records from point observations can be considered representative of a one-degree reference grid. How-



ever, on top of the measurement uncertainty of the instrument, additional uncertainties have to be taken into account when a point observation is supposed to represent its one-degree surrounding.

With the information about the representativeness of the in-situ observations, we were able to exclude stations which are (according to the above-mentioned metrics) not representative for their larger surroundings. Stations which have sufficiently long time series and which are representative for their larger surroundings were then used to finally study temporal variations in the shortwave fluxes of the energy balance.

In the representativeness assessment, we focused on the monthly mean time scale. An assessment across all time scales, ranging from minutes to climatological means, as well as for different reference grids might provide further insights about the general structure of the solar radiation field. Direct validation of the representativeness metrics using dense in-situ observations would also be beneficial. This could, for example, be achieved by focusing on shorter timescales and by using dense in-situ observation networks as, for instance, presented in Madhavan et al. (2017).

The representativeness assessment could also be considered for the design of future satellite-derived data products. If a satellite-derived data product should meet a predetermined uncertainty level, it must be ensured that additional uncertainties from validation with in-situ data (i.e., spatial sampling errors) are small enough to be able to really test the products' uncertainties. As we have shown that the spatial sampling errors decrease with smaller grid sizes, the optimal spatial resolution of a satellite-derived data product could be inferred. It is also conceivable to utilize synergies between in-situ and satellite data to compile a next-generation surface radiation data product. Such a product could be anchored to the accurate in-situ observations (which might be weighed according to their representativeness) while satellite data could be used to achieve broad spatial coverage.

Although global warming is driven by decreasing longwave radiation at TOA, several studies (e.g. Trenberth and Fasullo, 2009; Donohoe et al., 2014) suggest that – from an energy balance perspective – the energy uptake by the climate system will largely be driven by increasing absorption of shortwave radiation. According to these studies, this shortwave energy uptake is a consequence of a reduced planetary albedo (i.e., a reduced shortwave reflection at TOA) due to feedbacks which increase the shortwave absorption of the climate system (e.g., the ice-albedo feedback, the water vapor feedback, and cloud feedbacks). To accurately detect such changes in the the energy balance it is necessary to employ a high-quality global observation system (Trenberth, 2009; von Schuckmann et al., 2016). In Chapter 3 we have shown that the Baseline Surface Radiation Network as a whole can only sample a small fraction of the total surface area between 50°S and 50°N. A more complete surface flux measurement network is, therefore, needed. The representativeness assessment could help to design such a direct surface observation system which avoids under- as well as oversampling. Additionally, the analysis presented here can identify ideal measurement locations. For instance,

additional in-situ observations should be installed in sensitive regions which are currently not well equipped.

With respect to the annual cycle of fractional shortwave atmospheric absorption addressed in Chapter 4, we exploit synergies between different data products to achieve global coverage and robustness. We aimed to answer the question, whether the nonexistent annual cycle in fractional atmospheric shortwave absorption in Europe found by Hakuba et al. (2014b) is a global feature or whether there are any regions with notable annual cycles. In our analysis, we identified several regions, which show large annual cycles in fractional atmospheric absorption. This shows that the nonexistent annual cycle in Europe found by Hakuba et al. (2014b) is rather an exception than the rule.

To the authors' knowledge little was known about the annual cycles of fractional shortwave atmospheric absorption. Therefore, this chapter provides first evidence of the existence of significant annual cycles of fractional atmospheric shortwave absorption in various regions.

To get a handle on the validity of the results obtained from the satellite-derived data, we compare them to estimates based on in-situ observations. Only sites which have proven to be representative according to the above-mentioned criteria were used. The comparison between the satellite-derived and in-situ based estimates showed that the dominant spatial patterns of the annual cycles are apparent in both data sources. The satellite-derived estimates, however, tend to underestimate the magnitude of the annual cycles to some degree.

A more detailed site-by-site evaluation to further explore why some sites show different behavior than the CERES estimates is pending. Such an investigation could reveal whether our representativeness metrics potentially misjudged the reliability of those sites, or if a physical process, which is not well captured by CERES, is the reason for this mismatch.

We further examined potential reasons for the regional differences in the annual cycles using a simple correlation analysis. This analysis suggests that clouds play a minor role for the annual cycle in fractional atmospheric absorption. This result is puzzling, given that Hakuba et al. (2016) found that clouds are important for the near zonal constancy of long term annual mean fractional shortwave atmospheric absorption. The correlation analysis further suggests that annual cycles in water vapor and different aerosol species dominate the annual cycles. The largest annual cycles in fractional absorption are apparent in regions with large annual cycles in aerosol loading that are related to biomass burning. As biomass burning can be attributed to human activities, this suggests that the annual cycle of fractional shortwave atmospheric absorption in those regions is intensified or even entirely forced by human activity.

We have shown that the skill of global climate models from the fifth phase of the coupled model intercomparison project (CMIP5) in simulating the pattern of long term mean and annual cycles of fractional atmospheric shortwave absorption is limited. Further research on the annual cycle of fractional atmospheric shortwave absorption and its representation in climate models is, therefore, needed.

From the model development, tuning, and validation perspective it is an open question whether the more accessible satellite-derived data can be used for validation of global climate models or if only in-situ data is useful in this respect. Similarly to other observational data, using direct in-situ observations is cumbersome as their representativeness must be assessed and the data often needs extensive postprocessing such as gap-filling or homogenization. From our own investigations, we found that CERES data generally show good agreement with the in-situ estimates for the long term means as well as for the annual cycles of atmospheric shortwave absorption. Therefore, we argue that it is reasonable to use the more accessible satellite-derived data for a first-order validation of long term means and annual cycles. Whether this is true also for the annual or monthly CERES (surface) records should be further tested. A more detailed direct validation of the CERES monthly mean surface radiation records using representative in-situ data is, therefore, pending.

When using CERES for first-order validation, we recommend to validate the models' skill in simulating fractional atmospheric shortwave absorption in several steps. A first test might be, whether the models reproduce the relatively robust near-global (60°S-60°N) long-term mean fractional atmospheric shortwave absorption of  $23 \pm 2\%$  as determined by Hakuba et al. (2014b) and Hakuba et al. (2016). A refined first-order validation could check whether the models are able to simulate the global pattern of long-term mean fractional shortwave absorption and the annual-cycle of fractional shortwave absorption, which were both shown in Chapter 4. Especially, the latter might provide some insight into how models represent the impact of seasonally varying aerosols as our analysis suggests that the annual cycle is mainly governed by aerosols and water vapor. However, whether the annual cycle of fractional atmospheric shortwave absorption can reliably be used for validation of a model's representation of aerosols must be further tested as this cannot be concluded directly from our simple correlation analysis. For this, more in-situ data is needed especially in the region with large annual cycles but poor in-situ coverage. Also, dedicated modeling studies might help to resolve this issue.

When the models agree reasonably well with CERES, they should be tested against the robust and accurate in-situ data. Using in-situ observations is, for various reasons, the most robust and reliable way to determine surface solar radiation. However, when in-situ data is used in combination with gridded data, grid specific bias corrections must be applied as outlined above. By applying such corrections, methodological uncertainties are minimized and thus uncertainties uncovered during the validation can be more directly attributed to the data product under review. Otherwise, it cannot be determined whether differences between the data product considered and the reference in-situ data arise from shortcomings of the data retrieval or due to methodological uncertainties.

This thesis also contributed significantly to understanding the *global dimming* and *global brightening* phenomenon. With respect to these multidecadal trends in the shortwave energy balance, we used the observation-based framework to examine changes in the shortwave

fluxes during dimming and brightening. So far, the dimming and brightening phenomenon was primarily studied from a surface perspective. Consensus on which processes ultimately govern the observed multidecadal trends has not yet been reached in the scientific community. In this thesis, we went beyond the surface perspective and analyzed the dimming and brightening phenomenon in an energy balance perspective, in which TOA, atmospheric, and surface shortwave fluxes were simultaneously analyzed. According to the principle of energy conservation, it is apparent that a change in surface radiation implies that at least one other variable of the shortwave energy balance, namely the surface absorption, the TOA net flux, or the atmospheric absorption must change as well. With the observation-based energy balance framework, this thesis provided further insights into the causes of the dimming and brightening phenomenon.

The most robust available long-term observations of surface radiation, surface albedo, and TOA fluxes were used. For surface solar radiation we solely relied on robust representative and homogeneous long-term in-situ observations. We focused on Europe and China because of the high density of representative and homogeneous in-situ observations in these regions. For the TOA fluxes, we used the DEEP-C reconstruction to be able to study the longest possible observation period ranging from 1985 to 2015. For surface albedo, we used the MODIS and the GLASS albedo products. For both regions, we first combined the surface and TOA data at each site individually before we averaged over all sites to achieve regional time series for the shortwave fluxes. A trend analysis based on these regional averaged time series was conducted. Since the magnitude and significance of the trends strongly depend on the trend length and the period considered, we investigated all possible periods longer than 15 years in the trend analysis.

In Europe, surface solar radiation increased since around 1980 (e.g., Wild, 2009a; Sanchez-Lorenzo et al., 2015). Since the surface albedo did basically not change throughout the observational period, the increasing surface radiation led to increasing surface absorption. At the TOA, the net incoming TOA shortwave radiation slightly increased. However, the increase in TOA net radiation was found to be smaller than the increase in surface absorption. Consequently, atmospheric shortwave absorption decreased in Europe.

In China, the pronounced dimming prior to 1980 levelled off during the 1980s and 1990s. Only in 2005, surface solar radiation started to increase again (Yang et al., 2018). Since the surface albedo shows no large variability or trends in China, the surface absorption decreased until 2005 and increased thereafter. The TOA net shortwave flux in China increased slightly until 2004 and tended to decrease thereafter. Taken together, the decreasing surface radiation and the increasing TOA net radiation observed roughly until 2005 can only go along with a rather pronounced increase in shortwave atmospheric absorption. After 2005, the surface and TOA trends reversed and the increased surface absorption and decreasing TOA net shortwave radiation went along with a pronounced decrease in atmospheric absorption.

In summary, we found that changing atmospheric absorption is a major driver of the Eu-

ropean brightening and the dominant cause for the Chinese surface trends. Based on the simultaneous trend analysis for surface, atmospheric, and TOA fluxes, we argue that changes in clouds are rather unlikely (solely) responsible for the observed trends. We rather argue that changes in aerosols – particularly the absorbing ones – play a major role for the found European and Chinese trends.

A limitation of the analysis is that only two regions are considered. Expanding the analysis beyond the two regions is, therefore, necessary in order to get a more global perspective. This, however, remains challenging as reliable, homogeneous, long-term, representative in-situ observations are scarce.

A particular problem when studying dimming and brightening in an energy balance framework is the lack of long TOA data records. The highly accurate CERES data is only available since 03/2000. Before that, we utilized a TOA flux reconstruction which goes back to 1985 and is based on reanalysis, modeling, and ERBE satellite data. As the largest changes in surface solar radiation occurred before the 1990s it would be really interesting to further expand the analysis back in time. The methodological details of such a reconstruction, however, are far from trivial and further research is needed. From the currently available data, we can only speculate that the anomalously high long term mean (2000-2010) fractional absorption found at Chinese stations is a remnant of the intense dimming phase in the region which happened prior to our observational period.

Changes in surface solar radiation have strong impacts on the climate system (Wild, 2009a, and references therein). A particularly interesting aspect is that decreasing and increasing surface radiation may counteract and enhance global warming, respectively (Wild et al., 2007). If changing atmospheric absorption is the main driver of the dimming and brightening, the phenomenon could indeed counteract the surface warming, as the amount of energy available for surface heating changed. However, in that case the surface radiation changes would have been caused by a redistribution of energy from the surface to the atmosphere. If this is, in fact, the case, the dimming and brightening did not interfere with global warming in the sense that the total amount of radiation absorbed by the climate system was changed. So, if changing atmospheric absorption is the driver for dimming and brightening, the phenomenon could have affected surface warming but not the total shortwave energy uptake in the climate system. From the currently available data, it is, however, not possible to finally conclude that changes of atmospheric shortwave absorption are indeed the main reason for dimming and brightening on a global scale (see above). Further research is, therefore, needed.

Climate models still fail to reproduce the full magnitude of the observed surface solar radiation changes (Wild, 2009b). An examination of their shortwave energy balance, in a similar manner as done in this thesis, might provide further valuable insight into the origins of the prevailing discrepancy between models and observations.

Overall, this thesis has shown that an integrative approach to the shortwave energy balance, in which TOA and surface fluxes are simultaneously analyzed, leads to valuable insights into

the climate system, thereby justifying the extra effort needed to quantify methodological uncertainties. In summary, this thesis contributes to a better understanding of the energy balance and will stimulate further investigations in the field. We hope that the ideas and concepts developed in this thesis will be used in future research and help the scientific community to better understand our climate system.

# Appendices





# A | Appendix for Chapter 1

## A.1 Spatial distribution of the shortwave energy fluxes

Global spatial pattern of climatological mean fluxes of shortwave energy as calculated from the CERES-EBAF data during all-sky conditions.

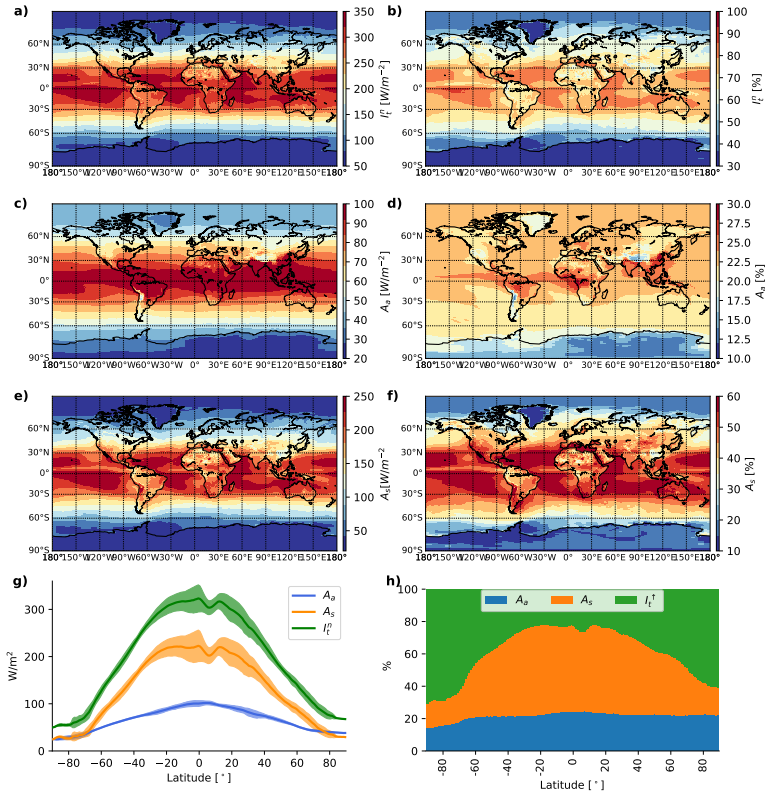


**Figure A.1:** Global spatial pattern of climatological mean shortwave fluxes as calculated from the CERES-EBAF data. The left column fluxes in  $W/m^2$  while the right column shows the fluxes in terms of fraction of incoming shortwave radiation at TOA. Panels g and h show the zonal mean shortwave fluxes in absolute units and fraction of  $I_T^\downarrow$ , respectively. The shading in panel g shows the standard deviation of the respective fluxes.

## A.2 One layer model of for shortwave fluxes

Here, we present a simple model for shortwave radiation following Taylor et al. (2007) and Stephens et al. (2015). In such a model, the atmosphere consists of a single scattering and reflecting layer above a reflective surface with albedo  $\alpha$  (see Figure A.2). The systems' total absorption ( $A = A_s + A_a$ ) describes the amount of shortwave radiation entering the climate system. It is governed by the fraction between incoming and reflected shortwave radiation at the TOA and is often referred to as *planetary albedo* ( $a_p = I_t^\uparrow/I_t^\downarrow$ ) (Stephens et al., 2015). The systems' reflection describes the amount of shortwave radiation which does not enter the climate system ( $R = I_n^\uparrow$ ), while the systems' transmittance describes the fraction of incoming radiation which reaches the surface ( $T = I_s^\downarrow/I_t^\downarrow$ ).

The fluxes at the boundaries of the atmosphere can be described using the atmospheres' inherent reflection ( $r$ ) and transmission ( $t$ ). Flatau and Stephens (1988); Stephens et al. (2015):

$$I_t^\uparrow = rI_t^\downarrow + tI_s^\uparrow \quad (\text{A.1})$$

$$I_s^\downarrow = tI_t^\downarrow + rI_s^\uparrow \quad (\text{A.2})$$

with the assumption that the intrinsic properties are identical for upward and downward fluxes. The inherent absorption is given by:  $a = 1 - t - r$ . Combining the above equations one can show:

$$T = \frac{I_s^\uparrow}{I_t^\downarrow} = \frac{t}{1 - r\alpha} \quad (\text{A.3})$$

$$R = r + \frac{t\alpha t}{1 - r\alpha} \quad (\text{A.4})$$

According to the equations, the systems' reflectance and transmittance are determined by only three parameters: the intrinsic absorption and reflection and surface albedo.

The equations can be inferred to yield the intrinsic atmospheric properties:

$$t = \frac{1 - \alpha R}{1 - \alpha^2 T^2} \quad (\text{A.5})$$

$$r = R - t\alpha T. \quad (\text{A.6})$$

From an observational perspective  $R$ ,  $T$  and  $\alpha$  can be observed and, therefore, be used to determine the systems' intrinsic properties.

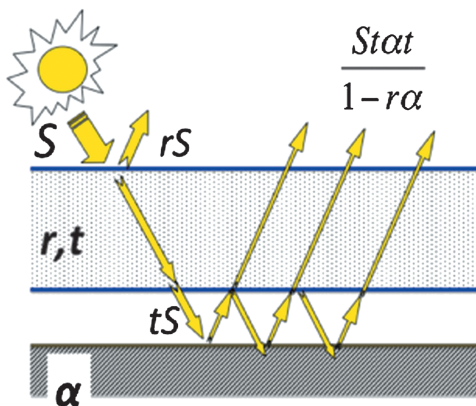


**Figure A.2:** A simple model for shortwave radiation from Stephens et al. (2015) with a single scattering and absorbing layer for the atmosphere over a reflective surface.

### A.3 Composite time series of total solar irradiance

Total solar irradiance is measured by different satellites since 1978 from Kopp (2016). Because of the temporal overlap of the different data sets, it was possible to create a homogeneous composite data record for total solar irradiance. Probably the most famous composite is the one of the Physikalisch-Meteorologisches Observatorium Davos (PMOD, Fröhlich 2006) shown in Figure 1.4. Recently, the scale of the total solar irradiance was adjusted because of some measurement biases as detailed in (Kopp and Lean, 2011).

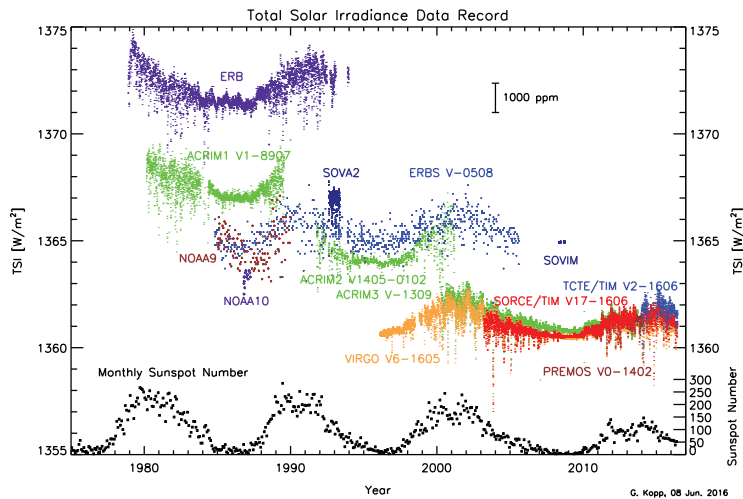


**Figure A.3:** Time series of total solar irradiance as measured by different instruments in the instrument's native scale as well as the total sunspot number from (Kopp, 2016).



## B | Appendix for Chapter 2

### B.1 Spatial Sampling Errors

Table B.1 shows the  $SSE_s$  for all used SSR stations (and the mean across all stations in the last row of the table) with respect to the  $1^\circ$  CERES grid for the different considered time scales

**Table B.1:** Site-Specific Spatial Sampling Error (SSEs, see equation 2.1) for the CERES 1° reference grid for annual, monthly, seasonal, and single month time series. Values are given in  $W/m^2$  except for the monthly relative column which is given in %.

Station	Annual	Monthly abs	Monthly rel	DJF	Seasonal			JAN	FEB	MAR	APR	MAY	Single Months			AUG	SEP	OCT	NOV	DEC
					JJA	SON	JJA						JUN	JUL	AUG					
ABERDEEN/DYCE ARPT	2.3	8.3	7.3	1.7	5.3	6.2	2.1	2.8	4.2	6.1	6.0	9.3	13.1	12.2	11.7	6.5	5.7	5.1	3.0	1.5
ABERROETH	3.1	8.9	7.5	1.9	5.0	7.2	2.5	1.6	4.2	4.8	8.4	9.9	16.5	18.1	11.8	11.8	6.7	4.2	2.9	1.8
AGEN	1.6	4.6	2.9	2.3	4.0	3.2	2.6	3.7	5.0	4.7	8.5	8.9	6.8	6.7	6.2	5.1	4.9	3.5	3.5	5.2
ACCIO	5.2	13.9	9.4	5.0	12.3	6.7	5.7	7.6	13.3	16.1	18.3	19.4	12.2	11.2	9.7	6.7	7.6	9.1	7.6	7.9
ALVERIA ARPT	3.2	10.4	4.7	4.8	10.0	4.9	3.7	5.8	8.8	10.9	13.1	11.9	13.1	11.9	6.6	9.1	13.1	7.0	8.4	6.0
AUDERRE-PERRIGNY	1.6	5.7	5.3	2.6	3.7	3.1	2.9	3.4	5.1	5.4	5.9	5.8	6.6	5.3	5.0	5.3	5.7	3.3	1.8	1.8
AVENORE	5.7	13.1	20.4	3.7	10.0	5.5	5.2	3.4	5.9	3.5	6.1	16.0	14.9	13.5	8.7	10.4	11.8	9.8	9.7	4.1
BARCELONA	2.1	7.1	3.7	2.7	5.5	5.2	3.4	3.2	6.1	7.0	7.6	6.9	7.6	6.7	8.6	5.7	7.0	5.0	5.0	3.4
BASEL	2.0	5.8	6.9	2.4	4.8	4.4	3.1	4.4	5.8	4.4	7.8	6.9	7.5	6.7	7.5	6.7	5.0	5.0	3.4	3.1
BASTIA	2.9	7.8	4.6	2.4	6.4	3.9	4.1	3.7	4.4	4.6	6.6	10.1	10.7	7.0	10.1	7.2	7.2	5.1	7.2	2.5
BELFAST/ALDERGROVE ARPT	1.7	6.4	6.3	1.3	4.8	3.5	4.0	3.0	5.4	4.4	8.5	12.4	18.5	13.4	12.4	6.4	4.1	3.2	1.9	1.4
BELMULLET	2.7	10.6	9.1	2.4	5.9	9.5	4.0	3.0	5.4	4.6	6.6	8.2	9.2	8.2	6.7	6.0	4.8	3.2	1.9	1.4
BELSK	1.4	6.2	6.9	2.3	4.4	4.4	2.1	2.7	4.5	4.5	6.1	6.8	6.2	6.2	9.2	8.0	6.4	4.1	3.2	2.9
BERGEN	1.7	5.6	1.25	1.6	4.6	4.1	1.4	3.3	3.6	6.0	5.3	8.2	7.0	5.3	5.3	5.4	3.0	3.1	3.2	2.9
BILBAO/SONDICA	3.3	9.8	5.9	2.7	7.0	7.9	5.2	1.9	3.5	5.7	7.1	8.6	5.2	8.8	7.9	7.7	9.4	9.8	6.1	4.1
BIRR	2.1	7.1	6.6	1.6	4.5	4.0	2.9	1.9	3.5	5.6	6.8	5.2	6.8	8.7	5.4	6.4	4.9	5.1	4.1	1.7
BISCARROSSE	2.1	6.6	4.1	2.5	4.2	4.3	3.6	2.7	4.6	5.1	5.7	9.6	8.7	5.4	6.4	4.9	5.6	5.6	4.7	4.4
BORDAUX-MERIGNAC	2.0	5.8	4.1	2.3	4.5	4.0	2.5	3.9	4.1	5.4	7.4	7.7	7.7	7.6	6.4	4.1	3.8	3.0	2.1	1.1
BORLANGE	1.2	4.3	10.3	1.2	2.1	2.8	1.4	1.0	1.9	4.1	6.2	6.5	5.0	3.5	6.1	3.8	3.0	2.1	1.1	0.8
BRACKNELL	2.4	5.3	4.4	1.2	4.7	3.8	1.8	1.8	2.3	3.6	5.3	6.7	6.8	6.8	8.0	5.4	4.7	4.4	3.0	4.2
BRAUNSCHEIG	1.9	6.9	4.7	3.0	4.6	3.0	2.7	4.0	5.5	6.0	8.5	8.2	6.6	6.6	6.6	4.1	4.7	4.4	6.6	6.9
BREGENZ	1.6	4.7	5.2	1.6	3.2	3.7	1.9	2.1	3.3	4.3	4.7	6.6	6.6	6.6	6.6	4.1	4.7	4.4	3.0	2.2
BREST-GUINAVAS	2.9	8.7	10.5	4.6	5.1	4.4	4.3	3.5	1.2	9.4	8.1	7.7	9.5	10.5	10.5	6.5	6.4	7.0	4.8	4.6
BUDAPEST	1.5	5.9	6.0	3.4	3.5	3.7	2.2	2.5	5.0	5.5	10.2	9.5	10.6	13.1	10.7	6.3	3.7	3.3	3.0	3.3
BUCHAREST	1.5	5.3	4.5	1.6	4.1	3.3	2.0	2.2	3.7	6.3	5.2	7.9	6.2	5.5	4.5	4.5	4.7	4.4	3.0	2.3
CACERES	1.4	3.9	7.2	2.1	2.8	1.8	1.9	2.1	4.2	3.7	8.4	8.1	3.0	4.3	2.4	2.1	2.9	3.8	3.8	2.4
CABER-CRPOUET	2.4	9.1	2.7	2.1	5.2	5.9	3.1	8.4	4.6	5.7	8.8	1.0	13.2	9.2	6.4	1.4	2.9	3.8	2.5	2.4
CAILLAN/ELMAS	3.5	8.9	6.0	5.2	5.2	4.8	4.9	8.0	8.2	10.9	10.6	9.3	7.5	7.7	9.4	9.5	7.6	7.4	7.2	4.6
CAMBONNE	3.2	10.9	8.3	2.2	5.3	5.4	3.6	2.6	6.1	8.6	11.6	11.4	13.1	16.6	9.3	11.8	5.4	4.4	2.9	2.9
CANGAS-DE-OURO	3.4	10.3	10.5	4.8	7.4	6.3	3.7	6.5	6.1	11.4	12.5	11.7	10.4	13.4	8.6	9.3	7.0	6.6	6.4	3.8
CHARENAY	3.1	13.9	10.5	5.9	9.4	6.8	6.7	8.9	13.0	11.3	16.5	18.8	16.4	15.4	13.4	9.8	12.5	11.9	10.2	7.0
CHERBOURG	3.4	12.0	13.0	4.3	7.9	7.3	6.6	8.2	12.8	13.0	8.1	12.5	14.2	14.3	11.0	11.0	8.1	11.7	11.7	9.2
CILDUD REAL	3.4	8.8	6.3	7.0	5.4	5.8	4.2	10.2	9.0	7.9	9.3	7.2	9.0	3.7	3.7	6.0	9.1	7.2	6.5	8.0
CLERMONT-FERRAND	1.9	8.6	7.1	3.1	5.1	5.1	4.4	5.0	6.8	7.9	10.9	9.0	7.6	11.5	9.2	9.8	5.0	3.8	3.8	5.0
CLONES	1.3	5.7	3.8	1.3	3.3	3.3	2.6	1.6	2.9	3.6	3.5	7.9	7.9	6.1	8.0	6.7	3.0	2.9	1.9	1.2
CONSTANTA	1.9	7.8	7.0	4.8	3.3	5.0	1.6	7.0	14.5	8.6	9.7	9.0	5.6	10.1	8.1	5.6	3.5	3.9	4.4	4.4
COPENHAGEN	1.6	6.6	6.4	1.3	3.3	4.6	2.1	1.4	3.5	3.8	3.7	7.0	7.0	2.6	2.6	6.6	4.1	3.8	2.1	1.3
CORHAYGH	8.9	19.0	28.1	17.0	9.8	14.9	9.6	18.4	22.7	17.5	20.6	16.1	20.6	22.4	13.8	13.8	4.2	4.9	1.8	1.3
CRATOVA	1.9	6.5	6.4	2.8	4.5	3.7	2.5	3.8	7.4	8.2	6.0	6.8	5.4	8.9	6.9	4.2	4.6	2.8	2.8	2.9
DAVOS	7.9	23.6	30.1	10.1	23.7	10.3	11.6	11.3	19.6	36.0	41.4	32.5	21.4	19.6	17.0	17.0	22.6	21.0	17.4	8.0
DE BILT	2.9	7.9	6.4	2.0	3.5	3.5	3.2	2.7	3.8	7.8	6.0	6.3	11.1	12.2	8.3	6.6	5.3	2.7	2.3	1.7
DE KOON	2.8	8.3	7.1	2.3	6.6	6.9	3.1	2.2	3.9	7.7	10.2	10.8	9.1	12.2	8.3	6.6	5.3	2.7	2.3	1.7
DIJON	1.9	5.8	8.3	3.1	3.6	4.2	2.0	5.7	7.1	5.5	4.7	5.4	7.9	6.6	8.4	3.9	5.8	4.1	3.8	3.8
DOBBAICO	5.2	13.5	10.6	6.9	10.8	10.5	6.0	9.6	12.1	16.8	11.8	17.3	11.6	20.4	14.9	9.0	7.7	7.1	7.7	7.7
DOUBLIN ARPT	2.6	6.8	7.1	2.1	5.3	5.1	3.4	2.6	5.5	4.6	6.6	6.2	6.2	8.8	8.5	7.2	7.6	5.2	3.1	1.6
DUNSTAPFARGE	1.9	6.1	7.5	1.6	3.9	4.5	2.2	1.3	3.6	3.3	5.7	6.2	6.9	7.8	7.2	5.3	2.9	1.5	1.3	1.6
EDINBURGH	3.2	12.3	12.7	3.1	6.1	7.8	3.6	2.6	7.2	8.6	6.1	11.5	17.0	15.4	15.6	12.1	10.4	6.7	3.4	2.0
EMBRUN	6.8	14.7	18.1	13.7	14.7	13.4	6.0	14.6	20.9	18.4	7.0	19.0	19.0	13.4	13.4	8.7	8.2	8.2	11.4	13.9
ESKDALMUIR	2.3	8.0	8.3	1.7	4.9	6.3	2.2	1.6	4.6	6.5	7.0	10.0	14.1	9.9	6.1	5.3	3.4	3.4	2.0	1.4



Table B.1 (continued)

Station	Annual	Monthly				Seasonal												Single Months											
		abs	rel	DJF	MAM	JJA	JJA	SON	JAN	FEB	MAR	APR	MAY	JUN	JUL	AUG	SEP	OCT	NOV	DEC									
GENÈVE	3.7	10.9	13.1	6.9	4.6	7.4	5.8	10.9	10.9	8.0	9.6	10.1	11.7	12.8	10.7	11.3	8.6	8.3	10.5	8.4									
GOTEBORG	3.0	9.7	12.8	3.2	4.8	6.8	2.9	1.8	7.4	7.4	8.5	8.6	12.2	10.0	13.5	11.9	8.6	5.2	3.1	1.4									
GRAZ UNIV.	3.5	14.1	14.6	6.1	8.4	8.3	5.6	13.2	12.5	16.7	13.2	12.4	11.8	13.4	12.7	11.0	8.6	10.8	10.7	9.5									
GRAZANISE	4.2	14.7	11.7	7.3	9.3	8.4	5.5	10.7	19.8	19.3	16.5	10.4	15.3	12.9	10.5	12.6	9.0	10.9	10.9	11.5									
HAMBURG - FUHLSBUETTEL	1.9	6.1	6.6	1.9	3.4	4.7	2.4	2.4	4.6	5.8	6.6	6.8	8.2	7.6	6.1	3.9	3.8	2.2	1.4										
HOFENPEISSENBERG	2.8	11.2	12.3	5.7	8.6	6.3	5.2	7.3	10.5	13.5	15.6	12.7	8.7	8.6	8.3	11.5	8.1	7.6	5.2										
HRADEC KRALOVE	2.0	7.7	3.9	2.7	5.0	5.7	2.5	3.8	4.9	7.4	7.6	8.7	7.8	8.7	7.1	8.8	4.3	4.1	3.1										
IBIZA	2.4	7.4	3.9	3.1	4.9	4.9	4.5	4.4	7.3	6.1	7.1	12.2	9.7	7.1	5.7	12.0	5.5	3.8	2.9										
INNSBRUCK ARPT	7.8	14.3	10.9	6.2	12.1	11.4	4.3	9.2	10.5	13.5	14.6	17.3	18.4	15.6	13.3	11.0	7.2	7.6	5.9										
JERSEY ARPT	2.5	8.2	6.4	2.1	4.3	6.4	3.2	2.3	5.3	9.0	9.1	10.7	9.0	8.6	8.5	7.4	4.9	3.2	2.5										
JOIKOINEN	1.2	4.8	11.2	1.1	2.8	3.0	1.4	1.0	2.7	4.4	6.1	5.1	7.9	5.6	4.5	3.7	2.4	1.0	0.8										
JUNGRAUJOCH	11.9	29.4	34.7	11.6	19.3	25.3	19.3	13.4	20.1	25.5	35.9	29.8	31.8	35.8	25.6	24.2	26.0	15.1	11.6										
KARLSBAD	6.8	6.6	11.2	3.1	6.5	5.2	1.8	1.6	8.5	5.5	8.8	6.2	8.1	8.5	7.9	4.6	2.5	1.7	1.1										
KILKENNY	1.6	4.9	4.9	1.8	3.4	3.9	1.5	1.6	3.2	3.2	5.1	5.7	5.3	7.3	6.8	3.3	2.9	1.8	1.6										
KOLOBRZEG	2.3	8.5	9.9	2.1	5.5	5.7	2.0	3.3	5.3	8.8	8.9	11.1	15.3	11.0	7.4	5.1	4.5	2.5	1.9										
KOSSETICE	1.4	5.3	7.7	3.6	3.0	3.9	1.7	3.1	8.3	5.5	5.3	5.8	6.4	5.4	5.5	4.6	3.8	3.6	3.2										
LA CORUNA	2.2	9.6	5.5	2.1	6.9	6.4	3.7	3.7	4.8	5.8	11.2	13.7	11.1	12.9	11.8	6.1	6.3	2.9	2.9										
LA DOLE	4.5	14.1	9.7	4.8	11.0	12.2	4.5	6.7	9.1	10.6	13.3	16.1	16.2	18.6	13.7	8.3	7.2	7.7	4.8										
LA ROCHE-SUR-YON	1.5	6.8	3.9	1.8	3.6	4.6	2.5	2.0	4.6	4.3	6.6	7.8	8.4	7.8	7.0	4.9	3.8	2.7	2.2										
LERWICK	2.1	8.8	10.5	0.9	5.4	5.6	1.7	1.3	2.9	5.6	7.3	12.0	12.0	10.8	10.8	7.9	4.9	3.3	1.8										
LIMOGES - BELLEGARDE	1.5	7.4	5.2	2.8	3.9	4.3	2.5	4.6	4.3	6.1	8.8	7.1	8.2	10.8	7.2	6.1	5.2	4.0	2.4										
LISBOA / INST.GEOFIS.	3.8	11.8	5.6	3.7	7.8	8.1	3.4	4.7	6.1	9.3	12.6	18.6	13.7	13.5	9.8	7.3	5.7	6.2	5.6										
LOCARNO - MONTI	22.0	19.4	10.4	18.8	15.4	10.0	13.4	10.0	13.4	21.1	23.8	25.4	22.8	20.7	19.1	16.6	20.9	15.7	12.0										
LOGRONO / AGONCILLO	2.6	8.5	8.0	5.1	6.4	5.0	3.5	6.6	4.2	5.7	7.0	9.3	9.4	8.9	8.0	7.0	7.4	5.7	6.0										
LONDONWEATHER CENTRE	2.4	7.1	5.7	1.8	4.2	5.7	2.2	2.5	4.6	4.6	4.6	5.9	9.8	8.3	9.0	6.6	4.8	2.7	2.5										
LUND	1.7	6.7	8.0	1.7	4.0	4.1	1.9	2.0	5.0	6.1	3.9	8.3	8.5	8.1	7.7	4.0	3.8	2.1	1.6										
MAASTRICHT	2.5	7.4	8.0	2.6	4.0	5.1	2.9	4.0	6.9	5.2	6.6	10.1	8.5	10.2	9.8	6.9	4.7	2.3	2.4										
MACON	2.3	7.0	7.7	2.9	4.3	4.4	4.9	4.4	7.2	4.8	5.5	9.1	8.9	6.3	7.7	6.9	5.9	5.3	3.9										
MADRID UNIV.	1.4	4.9	3.2	3.2	2.8	3.3	2.4	3.8	4.1	4.5	5.6	6.5	4.8	3.7	4.5	4.6	4.3	2.8	4.1										
MALIN HEAD C.	2.8	7.4	6.9	1.3	4.3	6.3	2.9	1.6	3.5	4.7	7.4	8.6	11.0	8.1	8.7	5.0	3.6	2.2	1.5										
MARGINEANE	1.8	7.1	4.6	2.8	5.0	3.9	2.9	4.2	6.1	6.2	9.4	9.1	8.8	6.4	5.5	4.8	5.7	5.3	4.1										
MELE C.	4.0	10.5	7.9	5.4	7.0	7.2	4.7	6.8	11.1	6.8	13.3	11.0	14.6	11.1	9.4	6.5	7.5	7.1	4.7										
MELLE	1.5	7.7	6.2	2.3	4.4	4.1	3.4	2.6	6.4	5.4	5.4	10.3	11.5	7.7	9.0	8.1	4.6	2.8	2.1										
MESSINA	3.0	8.9	6.2	4.2	6.0	4.4	6.2	5.9	9.4	9.6	8.0	10.0	9.3	4.2	7.0	8.8	9.1	6.6	7.6										
MILHUSTOV / TREBISOV	3.3	10.9	8.9	4.0	6.7	6.5	6.0	6.3	9.1	11.4	14.9	16.5	8.8	9.0	10.9	10.4	8.7	7.6	5.9										
MILLAU	2.0	6.0	4.2	2.5	5.0	4.1	2.1	3.1	4.8	4.7	7.4	7.1	7.3	5.2	5.2	4.6	4.6	2.7	3.0										
MONTPELLIER	1.7	6.0	4.3	2.2	5.5	4.7	3.4	3.3	5.9	6.9	7.1	16.2	10.2	10.2	6.8	5.8	3.7	2.4	1.8										
MOSCOW UNIV.	1.6	4.6	6.6	1.4	2.1	4.5	1.5	1.7	2.8	5.4	4.9	3.5	6.8	5.8	4.9	6.9	5.5	4.8	4.2										
MURCIA	1.6	7.2	4.1	3.2	4.8	4.1	3.6	5.3	4.1	7.5	10.2	9.6	10.2	4.9	6.9	5.5	4.8	6.2	4.2										
NANCY - ESSEY	1.6	6.3	8.0	3.2	2.4	3.8	3.2	5.6	6.0	5.4	5.0	5.8	7.0	7.5	6.8	5.3	5.6	4.7	3.3										
NANTES-ROUGUENAIS	2.1	5.9	4.3	2.8	3.7	4.5	2.3	2.9	6.8	5.6	6.0	6.4	6.4	9.2	6.9	5.2	3.2	2.5	2.2										
NICE	1.9	5.2	4.4	2.6	4.1	2.6	2.4	1.9	3.5	7.8	5.0	4.7	6.4	7.7	4.8	4.0	2.3	1.7	0.8										
NORRKPING	1.5	5.5	7.9	1.4	2.8	3.6	1.7	1.4	3.5	7.8	5.0	4.7	6.4	7.7	4.8	4.0	2.3	1.7	0.8										
ODESSA	2.2	5.8	5.6	3.6	4.1	4.1	2.6	4.8	6.7	4.6	6.6	6.3	7.4	6.1	4.9	5.7	5.0	3.1	2.3										
OOSTENDE ARPT	3.1	9.0	8.1	2.8	8.5	5.4	3.1	4.5	6.2	7.2	11.5	15.2	11.6	11.9	7.5	6.8	5.4	3.2	2.8										
OSTERSUND	1.3	5.8	20.6	0.9	4.0	3.1	1.8	5.9	3.0	5.7	7.4	5.7	8.4	6.2	5.6	3.8	2.6	0.8	0.6										
OSTRAVA / PORUBA	3.6	9.4	12.4	4.7	7.8	5.0	3.9	5.9	9.4	11.3	8.4	15.4	11.3	6.7	8.7	8.7	7.6	4.3	4.2										
PALMA DEMALLORCA	2.6	7.1	4.0	2.8	6.2	5.7	4.1	4.3	4.7	7.7	7.3	13.6	6.4	6.6	6.6	9.0	4.0	5.0	3.3										
PARIS-MONTSOURIS	1.9	6.2	4.4	1.3	4.6	5.0	1.8	2.1	3.2	4.9	6.3	6.4	8.3	8.8	5.2	3.8	4.8	4.8	2.3										

Table B.1 (continued)

Station	Annual	Monthly rel	DJF	Seasonal		JAN	FEB	MAR	APR	MAY	Single Months		AUG	SEP	OCT	NOV	DEC
				JJA	SON						JUN	JUL					
PAU-UZUN	1.7	6.6	3.9	4.2	2.7	3.1	3.9	4.4	5.9	8.7	8.8	7.9	6.9	6.3	3.4	3.5	2.5
PATVENE	2.7	9.9	11.5	4.8	5.6	8.5	9.8	11.1	7.4	11.8	11.2	9.6	7.0	8.2	6.8	6.7	6.3
PENGINAN	3.4	13.9	6.8	4.7	7.8	5.9	8.8	8.6	13.3	18.9	13.7	13.4	13.9	10.0	6.5	6.3	4.9
PISA / S. GIUSTO	3.5	7.3	4.7	3.1	4.6	3.2	6.2	7.0	12.7	9.4	7.4	6.9	6.6	6.0	5.9	5.3	3.4
PRAHA / RABDOV	2.3	6.3	7.9	3.2	4.2	3.9	6.1	5.2	4.5	7.6	7.7	8.0	5.5	4.3	4.5	2.7	2.7
PUNTIARKA	2.1	10.7	8.9	3.8	6.2	5.4	7.9	11.4	13.1	11.3	11.3	10.8	8.6	9.7	8.3	5.6	5.3
REIMS-COURCY	2.1	7.2	8.0	3.5	4.9	3.5	6.3	6.7	5.9	6.6	7.8	8.3	7.4	6.7	4.7	3.5	3.1
RENNES-ST JACQUES	2.0	6.6	5.3	2.4	5.6	2.9	5.5	5.6	7.9	8.2	7.3	8.6	6.8	5.5	4.6	3.1	2.7
ROMA / CIAMPINO	3.0	8.5	9.0	4.1	7.5	5.9	8.9	8.1	11.6	10.8	8.4	7.5	8.9	8.3	4.6	4.7	3.8
ROMA / CIAMPINO	1.6	6.6	9.6	2.0	3.6	2.2	5.6	6.1	6.0	7.5	8.4	9.6	7.9	5.5	3.0	1.7	1.4
SAENHIS	3.2	13.2	15.6	7.7	13.5	8.9	13.6	19.4	13.5	18.2	12.9	11.5	9.2	9.9	8.2	6.9	6.9
SAN SEBASTIAN	5.2	13.2	15.6	2.8	6.5	4.5	6.1	6.0	12.2	12.2	12.2	12.2	12.2	12.2	8.4	4.3	3.3
SOHIA ORS.	3.3	12.2	7.1	2.8	5.0	4.5	8.0	6.6	7.5	13.3	10.4	6.8	7.1	11.1	8.5	6.5	3.8
SONNBLICK	3.0	9.1	7.4	5.0	7.6	6.1	3.4	3.4	10.4	6.8	7.1	11.1	8.5	5.6	3.8	6.4	6.4
SONNBLICK	1.23	28.4	36.2	16.1	20.1	20.8	14.8	28.1	31.7	33.1	36.2	27.3	30.9	25.1	18.9	23.5	18.2
SOPRON	1.7	6.5	9.7	2.5	3.9	4.2	3.1	4.5	7.2	6.0	9.3	6.0	3.9	5.9	3.7	3.7	2.7
ST-HUBERT	2.8	8.5	9.7	3.9	5.4	4.8	5.0	3.3	9.3	8.3	9.2	10.2	12.6	8.1	8.4	7.3	6.5
ST-HUBERT	1.9	7.0	5.3	1.9	4.7	4.2	3.1	2.3	3.1	2.3	3.4	3.4	5.9	5.6	7.3	8.2	6.0
STOCKHOLM	1.6	6.1	8.7	1.6	3.8	5.0	1.6	1.3	3.4	3.4	3.4	3.4	5.9	5.6	6.3	6.9	10.3
STRASBOURG-ENTZHEIM	1.6	5.3	7.4	3.0	4.2	3.1	3.7	5.6	7.3	8.7	8.8	8.8	8.2	6.0	4.0	2.6	1.8
STRASBSKE PLESO	8.4	20.8	15.8	5.8	14.8	20.4	7.5	7.0	12.7	17.2	23.0	21.5	25.4	22.7	23.3	15.9	12.5
TARTU / TORAVERE	1.4	4.9	8.3	0.9	2.7	2.9	3.0	6.8	5.1	4.8	5.6	7.0	4.9	3.7	1.8	1.8	1.1
TOLEDO	2.2	8.0	6.0	5.3	4.7	3.7	4.1	8.1	8.0	9.3	5.8	5.9	8.0	7.6	7.2	6.2	7.5
TRAPES	1.8	5.9	7.0	2.1	3.4	4.2	2.5	2.7	5.5	5.8	5.8	7.1	5.0	7.2	4.8	5.6	3.9
TRIER	1.8	5.9	7.0	2.3	3.6	3.9	2.8	3.0	4.8	4.4	5.4	7.1	6.7	4.2	4.8	5.6	3.9
TRIESTE	2.1	7.1	6.1	3.3	4.6	4.2	4.2	4.8	7.1	9.5	6.7	7.6	5.7	7.7	8.4	5.9	5.3
UCCLE	1.6	5.9	5.1	1.1	3.5	4.6	2.3	3.8	4.2	8.1	8.3	7.4	7.7	4.9	4.4	2.1	1.6
UDINE / RIVOLTO	2.3	11.3	7.1	2.8	6.0	5.5	3.8	5.4	10.3	15.6	17.7	18.4	8.8	11.1	6.8	5.2	4.8
VALENTIA ORS.	3.6	11.3	11.2	2.7	7.2	9.0	5.4	4.2	7.9	8.2	6.8	5.7	4.6	4.9	3.5	6.2	4.2
VALLADOLID	1.9	6.2	10.0	2.0	3.2	4.7	2.5	1.7	5.2	5.4	4.2	7.9	5.0	5.5	4.1	2.3	1.3
VAXO / KRONBERG	3.5	9.2	6.0	3.6	7.6	4.9	5.1	9.6	6.1	10.8	13.2	12.0	7.6	5.6	7.8	5.1	5.2
VIGNA DI VALLE	2.1	7.1	9.7	2.0	4.7	5.1	1.6	1.8	4.4	4.4	9.3	5.1	9.1	7.5	8.0	8.3	4.2
VISBAEROLOG-STN	2.2	6.5	5.2	3.0	3.8	4.1	3.3	4.3	6.3	6.3	10.9	8.3	10.1	6.8	5.6	6.0	3.8
VITTRBO	2.6	6.0	4.3	1.2	4.2	2.4	2.4	4.2	5.3	7.4	6.8	9.2	7.2	7.1	4.4	3.3	1.9
VUSSINGEN	2.1	5.3	8.6	3.2	5.1	3.9	2.0	3.0	6.7	9.0	7.4	7.4	6.2	4.9	3.2	3.2	2.7
WARSAWA	1.5	6.3	6.4	2.9	2.6	4.0	1.8	4.3	10.0	4.8	4.8	3.7	5.0	3.7	3.1	2.3	3.2
WEIHENSTEPHAN	2.4	6.7	7.4	4.0	5.1	5.5	3.4	3.6	11.2	7.0	6.5	6.2	9.3	6.0	5.3	4.9	4.8
WUEZZBURG	1.5	4.5	7.2	1.5	1.9	4.1	1.2	1.6	3.4	3.4	5.6	4.6	4.0	6.0	6.1	3.5	3.4
ZILANI	1.6	6.3	8.2	3.4	4.5	4.0	2.0	1.8	2.1	6.2	7.2	8.5	7.4	7.4	6.9	5.6	6.2
ZUERICH / KILOTEN	1.6	6.3	8.3	3.0	2.9	5.1	3.0	6.0	6.0	4.2	4.9	6.4	10.4	5.7	5.9	5.6	3.7
Carbone (BSRN)	3.3	10.9	8.3	2.2	5.5	9.2	1.6	2.6	6.1	8.6	11.6	11.4	13.1	16.6	9.5	11.8	12.8
Carpiates (BSRN)	3.7	12.8	10.4	6.3	8.0	8.1	6.7	8.5	12.5	11.4	15.5	15.4	12.7	15.0	9.8	12.8	14.4
Center (BSRN)	3.6	12.3	9.6	6.2	7.4	8.4	4.4	9.4	14.4	10.0	14.6	15.2	14.9	13.9	9.1	8.5	5.6
Genec (BSRN)	2.1	8.8	10.5	5.4	5.4	5.6	1.7	1.3	2.9	5.6	7.3	12.0	10.8	7.9	4.9	3.3	1.8
Landenberg (BSRN)	1.9	6.3	7.3	2.1	3.7	4.7	1.7	2.6	5.6	7.2	6.3	6.5	7.8	4.8	5.6	3.3	2.4
Landenberg (BSRN)	1.2	5.5	4.2	1.3	4.0	4.7	1.7	2.9	2.7	5.0	6.4	6.5	6.9	6.5	3.9	3.4	2.0
Payenne (BSRN)	1.4	4.9	11.5	0.9	6.2	5.6	4.7	7.4	11.1	6.8	4.8	11.2	9.6	6.8	6.7	6.3	6.3
Torrevec (BSRN)	2.7	9.9	8.3	4.8	6.2	3.0	3.0	6.1	7.4	4.8	4.8	5.6	7.0	4.9	1.8	1.8	1.1
Mean	2.8	8.7	8.4	3.4	5.8	5.9	3.6	4.6	7.1	8.2	9.3	10.4	10.3	9.6	8.1	7.0	5.6

## C | Appendix for Chapter 4

### C.1 Atmospheric shortwave absorption for individual members of the CMIP5

Here we show  $\bar{a}$  and  $\tilde{a}$  for the historic simulations (1993-2005) of the CMIP5 models. Figure A.1 shows  $\bar{a}$  for all individual models similarly as shown for the observations in Figure 4.1. Figure A.2 shows  $\tilde{a}$  for all individual models similarly as shown for the observations in Figure 4.2.

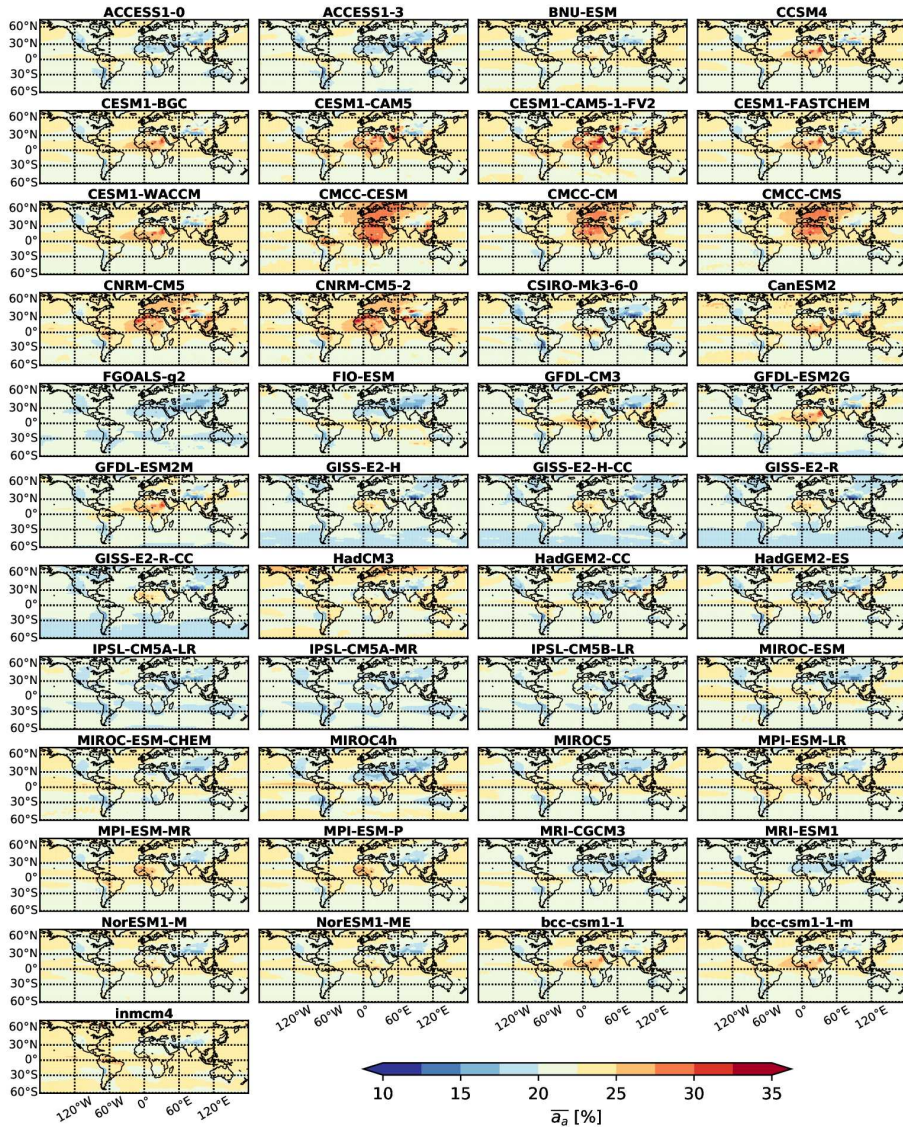


**Figure C.1:** Multiannual mean fractional absorption of shortwave radiation in the atmosphere in historic simulations (1993-2005) of the CMIP5 models. Blue/red coloring indicates lower/higher absorption.

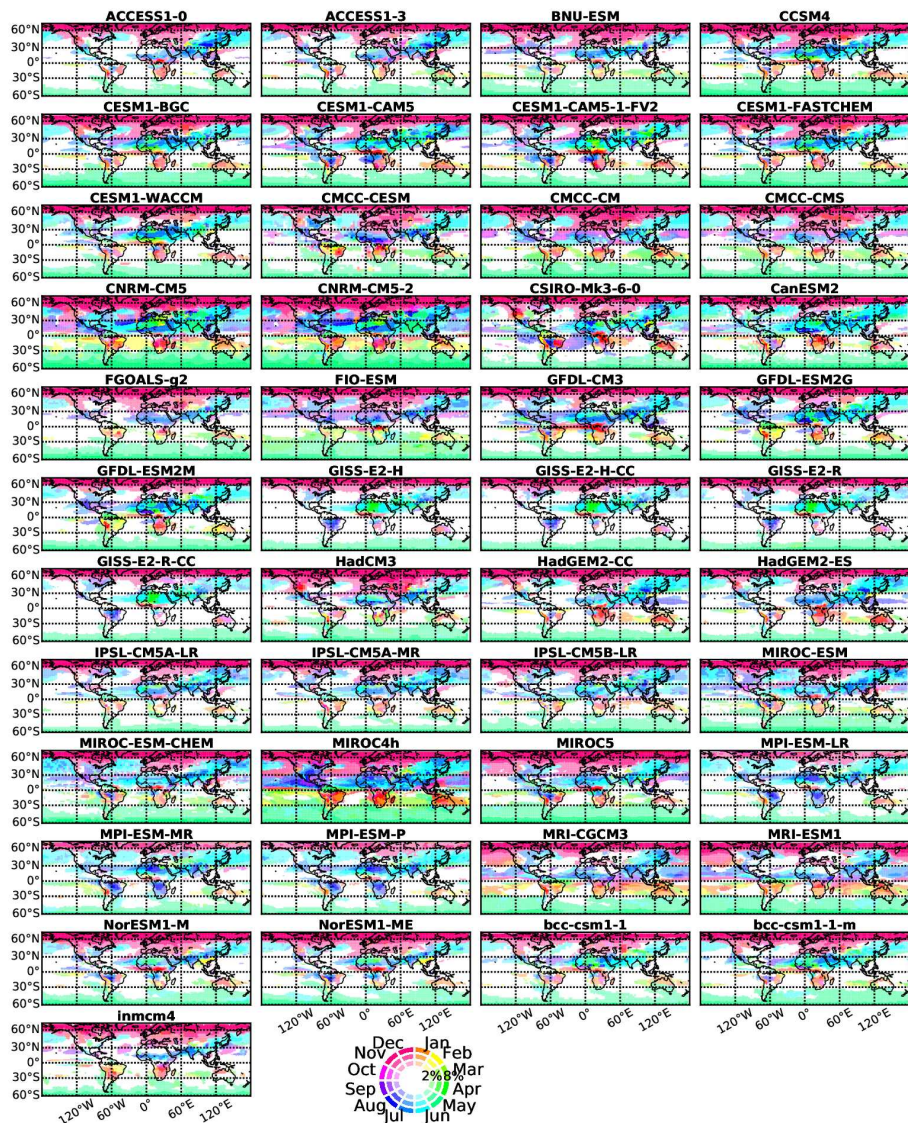


**Figure C.2:** The annual cycle in fractional shortwave atmospheric absorption in historic simulations (1993–2005) of the CMIP5 models. The magnitude of the annual cycle ( $|\bar{a}|_m$ ) is indicated by the opacity of the coloring. The month during which the maximum absorption occurs ( $|\bar{a}|_p$ ) is indicated by different colors. In transparent regions, the magnitude of the annual cycle of  $|\bar{a}|_m < 2\%$ . A higher opacity of the colors indicates higher amplitudes.



# Bibliography

- Abbot, C. G. and F. E. Fowle, 1908: Radiation and terrestrial temperature. *Annals of the Astrophysical Observatory of the Smithsonian Institution*, **2**, 125–224, 00000 ZSCC: 0000039.
- Albrecht, B. A., 1989: Aerosols, Cloud Microphysics, and Fractional Cloudiness. *Science*, **245 (4923)**, 1227–1230, doi:10.1126/science.245.4923.1227, zSCC: 0003472.
- Alexandersson, H., 1986: A homogeneity test applied to precipitation data. *Journal of Climatology*, **6 (6)**, 661–675, doi:10.1002/joc.3370060607, zSCC: 0001468.
- Allan, R. P., C. Liu, L. Norman G., P. Matthew D., R. Malcolm, S. Doug, and V. Pier-Luigi, 2014: Changes in global net radiative imbalance 1985–2012. *Geophysical Research Letters*, **41 (15)**, 5588–5597, doi:10.1002/2014GL060962, zSCC: 0000102.
- Allen, R. J., J. R. Norris, and M. Wild, 2013: Evaluation of multidecadal variability in CMIP5 surface solar radiation and inferred underestimation of aerosol direct effects over Europe, China, Japan, and India. *Journal of Geophysical Research: Atmospheres*, **118 (12)**, 6311–6336, doi:10.1002/jgrd.50426, 00000 ZSCC: 0000059.
- Andreae, M. O., D. Rosenfeld, P. Artaxo, A. A. Costa, G. P. Frank, K. M. Longo, and M. a. F. Silva-Dias, 2004: Smoking Rain Clouds over the Amazon. *Science*, **303 (5662)**, 1337–1342, doi:10.1126/science.1092779, zSCC: NoCitationData[s0].
- Augustine, J. A. and E. G. Dutton, 2013: Variability of the surface radiation budget over the United States from 1996 through 2011 from high-quality measurements. *Journal of Geophysical Research: Atmospheres*, **118 (1)**, 43–53, doi:10.1029/2012JD018551, 00000 ZSCC: 0000044.
- Barkstrom, B. R., 1984: The Earth Radiation Budget Experiment (ERBE). *Bulletin of the American Meteorological Society*, **65 (11)**, 1170–1185, doi:10.1175/1520-0477(1984)065<1170:TERBE>2.0.CO;2, zSCC: 0000719.

- Barnett, T. P., J. Ritchie, J. Foat, and G. Stokes, 1998: On the Space–Time Scales of the Surface Solar Radiation Field. *Journal of Climate*, **11** (1), 88–96, doi:10.1175/1520-0442(1998)011<0088:OTSTSO>2.0.CO;2, 00000 ZSCC: 0000046.
- Beaubien, D. J., A. Bisberg, and A. F. Beaubien, 1998: Investigations in Pyranometer Design. *Journal of Atmospheric and Oceanic Technology*, **15** (3), 677–686, doi:10.1175/1520-0426(1998)015<0677:IIPD>2.0.CO;2, 00000 ZSCC: 0000020.
- Bevington, P. R. and D. K. Robinson, 2003: *Data Reduction and Error Analysis for the Physical Sciences*. McGraw-Hill, New York, 00000 ZSCC: 0000003.
- Bodas-Salcedo, A., M. A. Ringer, and A. Jones, 2008: Evaluation of the Surface Radiation Budget in the Atmospheric Component of the Hadley Centre Global Environmental Model (HadGEM1). *Journal of Climate*, **21** (18), 4723–4748, doi:10.1175/2008JCLI2097.1, 00000 ZSCC: 0000039.
- Bodas-Salcedo, A., et al., 2013: Origins of the Solar Radiation Biases over the Southern Ocean in CFMIP2 Models. *Journal of Climate*, **27** (1), 41–56, doi:10.1175/JCLI-D-13-00169.1, zSCC: NoCitationData[s0].
- Boersma, K. F., G. C. M. Vinken, and H. J. Eskes, 2016: Representativeness errors in comparing chemistry transport and chemistry climate models with satellite UV–Vis tropospheric column retrievals. *Geosci. Model Dev.*, **9** (2), 875–898, doi:10.5194/gmd-9-875-2016, 00000 ZSCC: 0000023.
- Boucher, O., et al., 2013: Clouds and Aerosols. *Climate Change 2013: The Physical Science Basis. Contribution of Working Group I to the Fifth Assessment Report of the Intergovernmental Panel on Climate Change*, T. Stocker, D. Qin, G.-K. Plattner, M. Tignor, S. Allen, J. Boschung, A. Nauels, Y. Xia, V. Bex, and P. Midgley, Eds., Cambridge University Press, Cambridge, United Kingdom and New York, NY, USA, book section 7, 571–658, doi: 10.1017/CBO9781107415324.016, zSCC: NoCitationData[s0].
- Brinckmann, S., J. Trentmann, and B. Ahrens, 2013: Homogeneity Analysis of the CM SAF Surface Solar Irradiance Dataset Derived from Geostationary Satellite Observations. *Remote Sensing*, **6** (1), 352–378, doi:10.3390/rs6010352, zSCC: NoCitationData[s0].
- Buishand, T. A., 1982: Some methods for testing the homogeneity of rainfall records. *Journal of Hydrology*, **58** (1), 11–27, doi:10.1016/0022-1694(82)90066-X, zSCC: 0000898.
- Bulgin, C. E., O. Embury, and C. J. Merchant, 2016: Sampling uncertainty in gridded sea surface temperature products and Advanced Very High Resolution Radiometer (AVHRR) Global Area Coverage (GAC) data. *Remote Sensing of Environment*, **177**, 287–294, doi:10.1016/j.rse.2016.02.021, 00000 ZSCC: 0000014.



- Carslaw, K. S., O. Boucher, D. V. Spracklen, G. W. Mann, J. G. L. Rae, S. Woodward, and M. Kulmala, 2010: A review of natural aerosol interactions and feedbacks within the Earth system. *Atmospheric Chemistry and Physics*, **10** (4), 1701–1737, doi:<https://doi.org/10.5194/acp-10-1701-2010>, zSCC: 0000350.
- Cescatti, A., et al., 2012: Intercomparison of MODIS albedo retrievals and in situ measurements across the global FLUXNET network. *Remote Sensing of Environment*, **121**, 323–334, doi:<https://doi.org/10.1016/j.rse.2012.02.019>, zSCC: NoCitationData[s0].
- Chiacchio, M. and M. Wild, 2010: Influence of NAO and clouds on long-term seasonal variations of surface solar radiation in Europe. *Journal of Geophysical Research*, **115**, doi:[10.1029/2009JD012182](https://doi.org/10.1029/2009JD012182), zSCC: 0000073.
- Christiansen, B., 2017: Ensemble Averaging and the Curse of Dimensionality. *Journal of Climate*, **31** (4), 1587–1596, doi:[10.1175/JCLI-D-17-0197.1](https://doi.org/10.1175/JCLI-D-17-0197.1), zSCC: NoCitationData[s0].
- Colbo, K. and R. A. Weller, 2009: Accuracy of the IMET Sensor Package in the Subtropics. *Journal of Atmospheric and Oceanic Technology*, **26** (9), 1867–1890, doi:[10.1175/2009JTECHO667.1](https://doi.org/10.1175/2009JTECHO667.1), zSCC: 0000075.
- Cooper, J., B. Barkstrom, and L. Kopia, 1992: Clouds and the Earth's Radiant Energy System (CERES) experiment. *30th Aerospace Sciences Meeting and Exhibit*, American Institute of Aeronautics and Astronautics, doi:[10.2514/6.1992-724](https://doi.org/10.2514/6.1992-724), 00000 ZSCC: 0000010.
- Curry, J. A., J. L. Schramm, and E. E. Ebert, 1995: Sea Ice-Albedo Climate Feedback Mechanism. *Journal of Climate*, **8** (2), 240–247, doi:[10.1175/1520-0442\(1995\)008<0240:SIACFM>2.0.CO;2](https://doi.org/10.1175/1520-0442(1995)008<0240:SIACFM>2.0.CO;2), zSCC: 0000540.
- Dee, D. P., et al., 2011: The ERA-Interim reanalysis: Configuration and performance of the data assimilation system. *Quarterly Journal of the Royal Meteorological Society*, **137** (656), 553–597, doi:[10.1002/qj.828](https://doi.org/10.1002/qj.828), zSCC: NoCitationData[s0].
- Deneke, H., A. Feijt, A. van Lammeren, and C. Simmer, 2005: Validation of a Physical Retrieval Scheme of Solar Surface Irradiances from Narrowband Satellite Radiances. *Journal of Applied Meteorology*, **44** (9), 1453–1466, doi:[10.1175/JAM2290.1](https://doi.org/10.1175/JAM2290.1), 00000 ZSCC: 0000027.
- Deneke, H. M., W. H. Knap, and C. Simmer, 2009: Multiresolution analysis of the temporal variance and correlation of transmittance and reflectance of an atmospheric column. *Journal of Geophysical Research: Atmospheres*, **114** (D17), D17 206, doi:[10.1029/2008JD011680](https://doi.org/10.1029/2008JD011680), 00000 ZSCC: 0000027.
- Dines, W. H., 1917: The heat balance of the atmosphere. *Quarterly Journal of the Royal Meteorological Society*, **43** (182), 151–158, doi:[10.1002/qj.49704318203](https://doi.org/10.1002/qj.49704318203), zSCC: 0000076.

- Donohoe, A., K. C. Armour, A. G. Pendergrass, and D. S. Battisti, 2014: Shortwave and long-wave radiative contributions to global warming under increasing CO<sub>2</sub>. *Proceedings of the National Academy of Sciences of the United States of America*, **111** (47), 16 700–16 705, doi:10.1073/pnas.1412190111, 00000 ZSCC: 0000038.
- Donohoe, A. and D. S. Battisti, 2013: The Seasonal Cycle of Atmospheric Heating and Temperature. *Journal of Climate*, **26** (14), 4962–4980, doi:10.1175/JCLI-D-12-00713.1, 00000 ZSCC: 0000029.
- Driemel, A., et al., 2018: Baseline Surface Radiation Network (BSRN): Structure and data description (1992–2017). *Earth System Science Data*, **10** (3), 1491–1501, doi:https://doi.org/10.5194/essd-10-1491-2018, zSCC: NoCitationData[s0].
- Dutton, E., C. Long, M. Wild, A. Ohmura, J. Groebner, and A. Roesch, 2012: Long-Term In-Situ Surface Flux Data Products. *WCRP Report No. 19/2012: GEWEX Radiative Flux Assessment (RFA)*, **Volume 1: Assessment**, 135 – 158, zSCC: NoCitationData[s0].
- Dutton, E. G., D. W. Nelson, R. S. Stone, D. Longenecker, G. Carbaugh, J. M. Harris, and J. Wendell, 2006: Decadal variations in surface solar irradiance as observed in a globally remote network. *Journal of Geophysical Research: Atmospheres*, **111** (D19), D19 101, doi:10.1029/2005JD006901, zSCC: 0000076.
- Dutton, E. G., R. S. Stone, D. W. Nelson, and B. G. Mendonca, 1991: Recent Interannual Variations in Solar Radiation, Cloudiness, and Surface Temperature at the South Pole. *Journal of Climate*, **4** (8), 848–858, doi:10.1175/1520-0442(1991)004<0848:RIVISR>2.0.CO;2, zSCC: 0000080.
- Dwyer, J. G., M. Biasutti, and A. H. Sobel, 2012: Projected Changes in the Seasonal Cycle of Surface Temperature. *Journal of Climate*, **25** (18), 6359–6374, doi:10.1175/JCLI-D-11-00741.1, 00000 ZSCC: 0000057.
- Fasullo, J. T. and K. E. Trenberth, 2008a: The Annual Cycle of the Energy Budget. Part I: Global Mean and Land–Ocean Exchanges. *Journal of Climate*, **21** (10), 2297–2312, doi:10.1175/2007JCLI1935.1, zSCC: 0000112.
- Fasullo, J. T. and K. E. Trenberth, 2008b: The Annual Cycle of the Energy Budget. Part II: Meridional Structures and Poleward Transports. *Journal of Climate*, **21** (10), 2313–2325, doi:10.1175/2007JCLI1936.1, 00153 ZSCC: 0000153.
- Flatau, P. J. and G. L. Stephens, 1988: On the fundamental solution of the radiative transfer equation. *Journal of Geophysical Research: Atmospheres*, **93** (D9), 11 037–11 050, doi:10.1029/JD093iD09p11037, zSCC: NoCitationData[s0].

- Folini, D., T. N. Dall'Amor, M. Z. Hakuba, and M. Wild, 2017: Trends of surface solar radiation in unforced CMIP5 simulations. *Journal of Geophysical Research: Atmospheres*, **122** (1), 2016JD025869, doi:10.1002/2016JD025869, 00000 ZSCC: 0000003.
- Folini, D. and M. Wild, 2015: The effect of aerosols and sea surface temperature on China's climate in the late twentieth century from ensembles of global climate simulations. *Journal of Geophysical Research: Atmospheres*, **120** (6), 2261–2279, doi:10.1002/2014JD022851, 00000 ZSCC: 0000012.
- Foltz, G. R., A. T. Evan, H. P. Freitag, S. Brown, and M. J. McPhaden, 2013: Dust Accumulation Biases in PIRATA Shortwave Radiation Records. *Journal of Atmospheric and Oceanic Technology*, **30** (7), 1414–1432, doi:10.1175/JTECH-D-12-00169.1, 00000 ZSCC: 0000013.
- Freidenreich, S. M. and V. Ramaswamy, 2011: Analysis of the biases in the downward shortwave surface flux in the GFDL CM2.1 general circulation model. *Journal of Geophysical Research: Atmospheres*, **116** (D8), D08208, doi:10.1029/2010JD014930, 00000 ZSCC: 0000016.
- Fröhlich, C., 2006: Solar Irradiance Variability Since 1978. *Space Science Reviews*, **125** (1), 53–65, doi:10.1007/s11214-006-9046-5, zSCC: 0000285.
- Gaffen, D. J., A. Robock, and W. P. Elliott, 1992: Annual cycles of tropospheric water vapor. *Journal of Geophysical Research: Atmospheres*, **97** (D16), 18185–18193, doi:10.1029/92JD01999, 00000 ZSCC: 0000048.
- Garratt, J. R., 1994: Incoming Shortwave Fluxes at the Surface—A Comparison of GCM Results with Observations. *Journal of Climate*, **7** (1), 72–80, doi:10.1175/1520-0442(1994)007<0072:ISFATS>2.0.CO;2, zSCC: 0000096.
- Garratt, J. R., P. B. Krummel, and E. A. Kowalczyk, 1993: The Surface Energy Balance at Local and Regional Scales—A Comparison of General Circulation Model Results with Observations. *Journal of Climate*, **6** (6), 1090–1109, doi:10.1175/1520-0442(1993)006<1090:TSEBAL>2.0.CO;2, 00000 ZSCC: 0000065.
- Gelaro, R., et al., 2017: The Modern-Era Retrospective Analysis for Research and Applications, Version 2 (MERRA-2). *Journal of Climate*, **30** (14), 5419–5454, doi:10.1175/JCLI-D-16-0758.1, zSCC: NoCitationData[s1].
- Gilgen, H. and A. Ohmura, 1999: The Global Energy Balance Archive. *Bulletin of the American Meteorological Society*, **80** (5), 831–850, doi:10.1175/1520-0477(1999)080<0831:TGEBA>2.0.CO;2, zSCC: 0000156.

- Gilgen, H., A. Roesch, M. Wild, and A. Ohmura, 2009: Decadal changes in shortwave irradiance at the surface in the period from 1960 to 2000 estimated from Global Energy Balance Archive Data. *Journal of Geophysical Research*, **114**, doi:10.1029/2008JD011383, 00000 ZSCC: 0000046.
- Gilgen, H., M. Wild, and A. Ohmura, 1998: Means and Trends of Shortwave Irradiance at the Surface Estimated from Global Energy Balance Archive Data. *Journal of Climate*, **11** (8), 2042–2061, doi:10.1175/1520-0442-11.8.2042, zSCC: 0000348.
- Gleckler, P. J., K. E. Taylor, and C. Doutriaux, 2008: Performance metrics for climate models. *Journal of Geophysical Research: Atmospheres*, **113** (D6), doi:10.1029/2007JD008972, zSCC: NoCitationData[s0].
- Grant, I. F., A. J. Prata, and R. P. Cechet, 2000: The impact of the diurnal variation of albedo on the remote sensing of the daily mean albedo of grassland. *Journal of Applied Meteorology*, **39** (2), 231–244, doi:10.1175/1520-0450(2000)039<0231:TIOTDV>2.0.CO;2, zSCC: 0000063 WOS:000086348700008.
- Gray, L. J., et al., 2010: Solar Influences on Climate. *Reviews of Geophysics*, **48** (4), doi:10.1029/2009RG000282, zSCC: 0000881.
- Gueymard, C. A., 2004: The sun's total and spectral irradiance for solar energy applications and solar radiation models. *Solar Energy*, **76** (4), 423–453, doi:10.1016/j.solener.2003.08.039, zSCC: 0000729.
- Hakuba, M. Z., D. Folini, A. Sanchez-Lorenzo, and M. Wild, 2013a: Spatial representativeness of ground-based solar radiation measurements. *Journal of Geophysical Research: Atmospheres*, **118** (15), 8585–8597, doi:10.1002/jgrd.50673, 00000 ZSCC: 0000061.
- Hakuba, M. Z., D. Folini, A. Sanchez-Lorenzo, and M. Wild, 2014a: Spatial representativeness of ground-based solar radiation measurements-Extension to the full Meteosat disk. *Journal of Geophysical Research: Atmospheres*, **119** (20), 11,760–11,771, doi:10.1002/2014JD021946, 00000 ZSCC: 0000016.
- Hakuba, M. Z., D. Folini, G. Schaepman-Strub, and M. Wild, 2014b: Solar absorption over Europe from collocated surface and satellite observations. *Journal of Geophysical Research: Atmospheres*, **119** (6), 3420–3437, doi:10.1002/2013JD021421, 00000 ZSCC: 0000014.
- Hakuba, M. Z., D. Folini, and M. Wild, 2016: On the Zonal Near-Constancy of Fractional Solar Absorption in the Atmosphere. *Journal of Climate*, **29** (9), 3423–3440, doi:10.1175/JCLI-D-15-0277.1, 00000 ZSCC: 0000007.

- Hakuba, M. Z., D. Folini, M. Wild, C. N. Long, G. Schaepman-Strub, and G. L. Stephens, 2017: Cloud effects on atmospheric solar absorption in light of most recent surface and satellite measurements. *AIP Conference Proceedings*, **1810** (1), 090 003, doi:10.1063/1.4975543, 00000 ZSCC: 0000002.
- Hakuba, M. Z., A. Sanchez-Lorenzo, D. Folini, and M. Wild, 2013b: Testing the homogeneity of short-term surface solar radiation series in Europe. *AIP Conference Proceedings*, AIP Publishing, Vol. 1531, 700–703, doi:10.1063/1.4804866, 00000 ZSCC: 0000016.
- Hansen, J., M. Sato, and R. Ruedy, 1997: Radiative forcing and climate response. *Journal of Geophysical Research: Atmospheres*, **102** (D6), 6831–6864, doi:10.1029/96JD03436, zSCC: 0001939.
- Harrison, E. F., P. Minnis, B. R. Barkstrom, V. Ramanathan, R. D. Cess, and G. G. Gibson, 1990: Seasonal variation of cloud radiative forcing derived from the Earth Radiation Budget Experiment. *Journal of Geophysical Research: Atmospheres*, **95** (D11), 18 687–18 703, doi:10.1029/JD095iD11p18687, zSCC: 0000769.
- Hatzianastassiou, N., C. Matsoukas, A. Fotiadi, K. G. Pavlakis, E. Drakakis, D. Hatzidimitriou, and I. Vardavas, 2005: Global distribution of Earth's surface shortwave radiation budget. *Atmos. Chem. Phys.*, **5** (10), 2847–2867, doi:10.5194/acp-5-2847-2005, zSCC: 0000125.
- Hay, J. E., 1984: An assessment of the mesoscale variability of solar radiation at the earth's surface. *Solar Energy*, **32** (3), 425–434, doi:10.1016/0038-092X(84)90287-1, 00000 ZSCC: 0000059.
- Hays, J. D., J. Imbrie, and N. J. Shackleton, 1976: Variations in the Earth's Orbit: Pacemaker of the Ice Ages. *Science*, **194** (4270), 1121–1132, doi:10.1126/science.194.4270.1121, zSCC: 0003951.
- Haywood, J. M., N. Bellouin, A. Jones, O. Boucher, M. Wild, and K. P. Shine, 2011: The roles of aerosol, water vapor and cloud in future global dimming/brightening. *Journal of Geophysical Research*, **116** (D20), doi:10.1029/2011JD016000, 00000 ZSCC: 0000041.
- Huang, G., X. Li, C. Huang, S. Liu, Y. Ma, and H. Chen, 2016: Representativeness errors of point-scale ground-based solar radiation measurements in the validation of remote sensing products. *Remote Sensing of Environment*, **181**, 198–206, doi:https://doi.org/10.1016/j.rse.2016.04.001, 00000 ZSCC: 0000019.
- Huld, T., R. Müller, A. Gracia Amillo, U. Pfeifroth, and J. Trentmann, 2016: Surface Solar Radiation Data Set - Heliosat, Meteosat-East (SARAH-E) - Edition 1. Satellite Application Facility on Climate Monitoring (CM SAF), zSCC: NoCitationData[s0], zSCC: NoCitation-Data[s0].

- Hyder, P., et al., 2018: Critical Southern Ocean climate model biases traced to atmospheric model cloud errors. *Nature Communications*, **9** (1), 3625, doi:10.1038/s41467-018-05634-2, 00000 ZSCC: 0000002.
- IPCC, 2013: *Climate Change 2013: The Physical Science Basis. Contribution of Working Group I to the Fifth Assessment Report of the Intergovernmental Panel on Climate Change*. 00000 ZSCC: 0000004.
- Jin, Y., H. Andersson, and S. Zhang, 2016: Air Pollution Control Policies in China: A Retrospective and Prospects. *International Journal of Environmental Research and Public Health*, **13** (12), doi:10.3390/ijerph13121219, zSCC: 0000065.
- Jin, Y., C. B. Schaaf, F. Gao, X. Li, A. H. Strahler, W. Lucht, and S. Liang, 2003: Consistency of MODIS surface bidirectional reflectance distribution function and albedo retrievals: 1. Algorithm performance. *Journal of Geophysical Research: Atmospheres*, **108** (D5), doi:10.1029/2002JD002803, zSCC: 0000153.
- Journée, M., R. Stöckli, and C. Bertrand, 2012: Sensitivity to spatio-temporal resolution of satellite-derived daily surface solar irradiation. *Remote Sensing Letters*, **3** (4), 315–324, doi:10.1080/01431161.2011.593579, 00000 ZSCC: 0000012.
- Karlsson, K.-G., et al., 2013: CLARA-A1: The CM SAF cloud, albedo and radiation dataset from 28 yr of global AVHRR data. *Atmospheric Chemistry and Physics Discussions*, **13** (1), 935–982, doi:10.5194/acpd-13-935-2013, zSCC: NoCitationData[s0].
- Karlsson, K.-G., et al., 2017a: CLARA-A2: CM SAF cLoud, Albedo and surface RAdiation dataset from AVHRR data - Edition 2. Tech. rep., Satellite Application Facility on Climate Monitoring (CM SAF). 00000 ZSCC: 0000003 \$DOI: 10.5676/EUM\_SAF\_CM/CLARA\_AVHRR/V002\$.
- Karlsson, K.-G., et al., 2017b: CLARA-A2: The second edition of the CM SAF cloud and radiation data record from 34 years of global AVHRR data. *Atmospheric Chemistry and Physics*, **17** (9), 5809–5828, doi:10.5194/acp-17-5809-2017\$, 00000 ZSCC: 0000062.
- Kato, S., 2009: Interannual Variability of the Global Radiation Budget. *Journal of Climate*, **22** (18), 4893–4907, doi:10.1175/2009JCLI2795.1, 00000 ZSCC: 0000029.
- Kato, S., N. G. Loeb, F. G. Rose, D. R. Doelling, D. A. Rutan, T. E. Caldwell, L. Yu, and R. A. Weller, 2012a: Surface Irradiances Consistent with CERES-Derived Top-of-Atmosphere Shortwave and Longwave Irradiances. *Journal of Climate*, **26** (9), 2719–2740, doi:10.1175/JCLI-D-12-00436.1, zSCC: NoCitationData[s0].
- Kato, S., N. G. Loeb, D. A. Rutan, F. G. Rose, S. Sun-Mack, W. F. Miller, and Y. Chen, 2012b: Uncertainty Estimate of Surface Irradiances Computed with MODIS-, CALIPSO-, and

- CloudSat-Derived Cloud and Aerosol Properties. *Surveys in Geophysics*, **33** (3-4), 395–412, doi:10.1007/s10712-012-9179-x, 00000 ZSCC: 0000055.
- Kato, S., et al., 2018: Surface Irradiances of Edition 4.0 Clouds and the Earth's Radiant Energy System (CERES) Energy Balanced and Filled (EBAF) Data Product. *Journal of Climate*, **31** (11), 4501–4527, doi:10.1175/JCLI-D-17-0523.1, zSCC: NoCitationData[s0].
- Kiehl, J. T. and K. E. Trenberth, 1997: Earth's Annual Global Mean Energy Budget. *Bulletin of the American Meteorological Society*, **78** (2), 197–208, doi:10.1175/1520-0477(1997)078<0197:EAGMEB>2.0.CO;2, zSCC: 0001592.
- Kipp&Zonen, 2016: CMP series - Pyranometer; CMA series - Albedometer. Instruction Manual V1610, Delftechpark 36, 2628 XH Delft, Netherlands. ZSCC: NoCitationData[s0].
- Kopp, G., 2016: Magnitudes and timescales of total solar irradiance variability. *Journal of Space Weather and Space Climate*, **6**, A30, doi:10.1051/swsc/2016025, 00000 ZSCC: 0000031.
- Kopp, G., G. Lawrence, and G. Rottman, 2005: The Total Irradiance Monitor (TIM): Science Results. *The Solar Radiation and Climate Experiment (SORCE): Mission Description and Early Results*, G. Rottman, T. Woods, and V. George, Eds., Springer New York, New York, NY, 129–139, doi:10.1007/0-387-37625-9\_8, zSCC: NoCitationData[s0].
- Kopp, G. and J. L. Lean, 2011: A new, lower value of total solar irradiance: Evidence and climate significance. *Geophysical Research Letters*, **38** (1), doi:10.1029/2010GL045777, zSCC: 0000678.
- Koren, I., Y. J. Kaufman, L. A. Remer, and J. V. Martins, 2004: Measurement of the Effect of Amazon Smoke on Inhibition of Cloud Formation. *Science*, **303** (5662), 1342–1345, doi:10.1126/science.1089424, zSCC: 0000632.
- Kumari, B. P., A. L. Londhe, S. Daniel, and D. B. Jadhav, 2007: Observational evidence of solar dimming: Offsetting surface warming over India. *Geophysical Research Letters*, **34** (21), doi:10.1029/2007GL031133, zSCC: 0000123.
- Kvalevåg, M. M. and G. Myhre, 2007: Human Impact on Direct and Diffuse Solar Radiation during the Industrial Era. *Journal of Climate*, **20** (19), 4874–4883, doi:10.1175/JCLI4277.1.
- Lambert, S. J. and G. J. Boer, 2001: CMIP1 evaluation and intercomparison of coupled climate models. *Climate Dynamics*, **17** (2), 83–106, doi:10.1007/PL00013736, zSCC: 0000366.
- L'Ecuyer, T. S., et al., 2015: The Observed State of the Energy Budget in the Early Twenty-First Century. *Journal of Climate*, **28** (21), 8319–8346, doi:10.1175/JCLI-D-14-00556.1, zSCC: NoCitationData[s0].

- Li, J., Y. Jiang, X. Xia, and Y. Hu, 2018: Increase of surface solar irradiance across East China related to changes in aerosol properties during the past decade. *Environmental Research Letters*, **13** (3), 034006, doi:10.1088/1748-9326/aaa35a, 00000 ZSCC: 0000002.
- Li, Y., D. W. J. Thompson, Y. Huang, and M. Zhang, 2014: Observed linkages between the northern annular mode/North Atlantic Oscillation, cloud incidence, and cloud radiative forcing. *Geophysical Research Letters*, **41** (5), 1681–1688, doi:10.1002/2013GL059113, 00000 ZSCC: 0000024.
- Li, Z., M. C. Cribb, F.-L. Chang, A. Trishchenko, and Y. Luo, 2005: Natural variability and sampling errors in solar radiation measurements for model validation over the Atmospheric Radiation Measurement Southern Great Plains region. *Journal of Geophysical Research: Atmospheres*, **110** (D15), D15S19, doi:10.1029/2004JD005028, 00000 ZSCC: 0000054.
- Li, Z., C. H. Whitlock, and T. P. Charlock, 1995: Assessment of the Global Monthly Mean Surface Insolation Estimated from Satellite Measurements Using Global Energy Balance Archive Data. *Journal of Climate*, **8** (2), 315–328, doi:10.1175/1520-0442(1995)008<0315:AOTGMM>2.0.CO;2, zSCC: 0000095.
- Liang, S., et al., 2002: Validating MODIS land surface reflectance and albedo products: Methods and preliminary results. *Remote Sensing of Environment*, **83** (1), 149–162, doi:10.1016/S0034-4257(02)00092-5, zSCC: 0000352.
- Liang, S., et al., 2013: A long-term Global LAnd Surface Satellite (GLASS) data-set for environmental studies. *International Journal of Digital Earth*, **6** (sup1), 5–33, doi:10.1080/17538947.2013.805262, zSCC: NoCitationData[s0].
- Liepert, B., P. Fabian, and H. Grassl, 1994: Solar radiation in Germany - observed trends and an assessment of their causes. Pt. 1. *Contributions to Atmospheric Physics*, **67** (1), 15–29, 00000 ZSCC: 0000064.
- Liepert, B. and I. Tegen, 2002: Multidecadal solar radiation trends in the United States and Germany and direct tropospheric aerosol forcing. *Journal of Geophysical Research: Atmospheres*, **107** (D12), AAC 7–1, doi:10.1029/2001JD000760, zSCC: 0000073.
- Liepert, B. G., 2002: Observed reductions of surface solar radiation at sites in the United States and worldwide from 1961 to 1990. *Geophysical Research Letters*, **29** (10), 61–1, doi:10.1029/2002GL014910, zSCC: 0000455.
- Liou, K., 2002: *An Introduction to Atmospheric Radiation*. International Geophysics, Elsevier Science, zSCC: 0003129.



- Liu, C., et al., 2017: Evaluation of satellite and reanalysis-based global net surface energy flux and uncertainty estimates. *Journal of Geophysical Research: Atmospheres*, **122** (12), 6250–6272, doi:10.1002/2017JD026616, 00000 ZSCC: 0000009.
- Liu, J., et al., 2009: Validation of Moderate Resolution Imaging Spectroradiometer (MODIS) albedo retrieval algorithm: Dependence of albedo on solar zenith angle. *Journal of Geophysical Research: Atmospheres*, **114** (D1), doi:10.1029/2008JD009969, zSCC: NoCitation-Data[s1].
- Liu, Q., L. Wang, Y. Qu, N. Liu, S. Liu, H. Tang, and S. Liang, 2013: Preliminary evaluation of the long-term GLASS albedo product. *International Journal of Digital Earth*, **6** (sup1), 69–95, doi:10.1080/17538947.2013.804601, zSCC: 0000074.
- Loeb, N., 2018: Presentation on "State of CERES" at 30th CERES-II Science Team Meeting - September 2018 at NCAR Mesa Lab, Boulder, CO; [https://ceres.larc.nasa.gov/documents/STM/2018-09/Loeb\\_State\\_of\\_CERES-Fall2018.pdf](https://ceres.larc.nasa.gov/documents/STM/2018-09/Loeb_State_of_CERES-Fall2018.pdf). ZSCC: NoCitationData[s0], zSCC: NoCitationData[s0].
- Loeb, N. G., S. Kato, and B. A. Wielicki, 2002: Defining Top-of-the-Atmosphere Flux Reference Level for Earth Radiation Budget Studies. *Journal of Climate*, **15** (22), 3301–3309, doi:10.1175/1520-0442(2002)015<3301:DTOTAF>2.0.CO;2, 00000 ZSCC: 0000038.
- Loeb, N. G., J. M. Lyman, G. C. Johnson, R. P. Allan, D. R. Doelling, T. Wong, B. J. Soden, and G. L. Stephens, 2012: Observed changes in top-of-the-atmosphere radiation and upper-ocean heating consistent within uncertainty. *Nature Geoscience*, **5** (2), 110–113, doi: 10.1038/ngeo1375, zSCC: 0000240.
- Loeb, N. G., N. Manalo-Smith, W. Su, M. Shankar, and S. Thomas, 2016: CERES Top-of-Atmosphere Earth Radiation Budget Climate Data Record: Accounting for in-Orbit Changes in Instrument Calibration. *Remote Sensing; Basel*, **8** (3), 182, doi:http://dx.doi.org/10.3390/rs8030182, 00000 ZSCC: 0000021.
- Loeb, N. G., K. J. Priestley, D. P. Kratz, E. B. Geier, R. N. Green, B. A. Wielicki, P. O. Hinton, and S. K. Nolan, 2001: Determination of Unfiltered Radiances from the Clouds and the Earth's Radiant Energy System Instrument. *Journal of Applied Meteorology*, **40** (4), 822–835, doi:10.1175/1520-0450(2001)040<0822:DOURFT>2.0.CO;2, zSCC: 0000108.
- Loeb, N. G., B. A. Wielicki, D. R. Doelling, G. L. Smith, D. F. Keyes, S. Kato, N. Manalo-Smith, and T. Wong, 2009: Toward Optimal Closure of the Earth's Top-of-Atmosphere Radiation Budget. *Journal of Climate*, **22** (3), 748–766, doi:10.1175/2008JCLI2637.1, zSCC: 0000681.
- Loeb, N. G., et al., 2017: Clouds and the Earth's Radiant Energy System (CERES) Energy Balanced and Filled (EBAF) Top-of-Atmosphere (TOA) Edition-4.0 Data Product. *Journal of Climate*, **31** (2), 895–918, doi:10.1175/JCLI-D-17-0208.1, zSCC: NoCitationData[s0].

- Lohmann, G. M., A. H. Monahan, and D. Heinemann, 2016: Local short-term variability in solar irradiance. *Atmos. Chem. Phys.*, **16** (10), 6365–6379, doi:10.5194/acp-16-6365-2016, 00000 ZSCC: 0000022.
- Lohmann, U. and J. Feichter, 2005: Global indirect aerosol effects: A review. *Atmospheric Chemistry and Physics*, **5** (3), 715–737, doi:https://doi.org/10.5194/acp-5-715-2005, zSCC: 0002006.
- Long, C. N. and T. P. Ackerman, 1995: Surface Measurements of Solar Irradiance: A Study of the Spatial Correlation between Simultaneous Measurements at Separated Sites. *Journal of Applied Meteorology*, **34** (5), 1039–1046, doi:10.1175/1520-0450(1995)034<1039:SMOSIA>2.0.CO;2, 00000 ZSCC: 0000060.
- Long, C. N. and T. P. Ackerman, 2000: Identification of clear skies from broadband pyranometer measurements and calculation of downwelling shortwave cloud effects. *Journal of Geophysical Research: Atmospheres*, **105** (D12), 15 609–15 626, doi:10.1029/2000JD900077, zSCC: 0000443.
- Long, C. N., E. G. Dutton, J. A. Augustine, W. Wiscombe, M. Wild, S. A. McFarlane, and C. J. Flynn, 2009: Significant decadal brightening of downwelling shortwave in the continental United States. *Journal of Geophysical Research*, **114**, doi:10.1029/2008JD011263, zSCC: 0000094.
- Lu, Z., et al., 2010: Sulfur dioxide emissions in China and sulfur trends in East Asia since 2000. *Atmospheric Chemistry and Physics*, **10** (13), 6311–6331, doi:https://doi.org/10.5194/acp-10-6311-2010, zSCC: 0000483.
- Madhavan, B. L., H. Deneke, J. Witthuhn, and A. Macke, 2017: Multiresolution analysis of the spatiotemporal variability in global radiation observed by a dense network of 99 pyranometers. *Atmos. Chem. Phys.*, **17** (5), 3317–3338, doi:10.5194/acp-17-3317-2017, 00000 ZSCC: 0000009.
- Mateos, D., M. Antón, A. Sanchez-Lorenzo, J. Calbó, and M. Wild, 2013: Long-term changes in the radiative effects of aerosols and clouds in a mid-latitude region (1985–2010). *Global and Planetary Change*, **111**, 288–295, doi:10.1016/j.gloplacha.2013.10.004, 00000 ZSCC: 0000032.
- Matus, A. V. and T. S. L'Ecuyer, 2017: The role of cloud phase in Earth's radiation budget. *Journal of Geophysical Research: Atmospheres*, **122** (5), 2559–2578, doi:10.1002/2016JD025951, 00000 ZSCC: 0000044.
- McArthur, L., 2005: Baseline Surface Radiation Network (BSRN). Operations Manual, Version 2.1. WMO/TD-No. 1274, World Climate Research Programme. *World Meteorological Organization, Geneva, Switzerland, WCRP/WMO*, zSCC: NoCitationData[s0].

- McArthur, L. J. B., 1998: *Baseline Surface Radiation Network (BSRN). Operations Manual, Version 21*. WMO/TD-No. 1274, WCRP/WMO, zSCC: NoCitationData[s0].
- McPhaden, M. J., et al., 1998: The Tropical Ocean-Global Atmosphere observing system: A decade of progress. *Journal of Geophysical Research: Oceans*, **103 (C7)**, 14 169–14 240, doi: 10.1029/97JC02906, zSCC: 0001001.
- McPhaden, M. J., et al., 2009: RAMA: The Research Moored Array for African–Asian–Australian Monsoon Analysis and Prediction\*. *Bulletin of the American Meteorological Society*, **90 (4)**, 459–480, doi:10.1175/2008BAMS2608.1, zSCC: 0000396.
- Meerkötter, R., C. König, P. Bissolli, G. Gesell, and H. Mannstein, 2004: A 14-year European Cloud Climatology from NOAA/AVHRR data in comparison to surface observations. *Geophysical Research Letters*, **31 (15)**, L15 103, doi:10.1029/2004GL020098, 00000 ZSCC: 0000053.
- Meijers, S. A. J., 2014: The Southern Ocean in the Coupled Model Intercomparison Project phase 5. *Philosophical Transactions of the Royal Society A: Mathematical, Physical and Engineering Sciences*, **372 (2019)**, 20130 296, doi:10.1098/rsta.2013.0296, 00000 ZSCC: 0000050.
- Mizielinski, M. S., et al., 2014: High-resolution global climate modelling: The UPSCALE project, a large-simulation campaign. *Geoscientific Model Development*, **7 (4)**, 1629–1640, doi:https://doi.org/10.5194/gmd-7-1629-2014, zSCC: NoCitationData[s0].
- Mlynczak, P. E., G. L. Smith, and D. R. Doelling, 2011: The Annual Cycle of Earth Radiation Budget from Clouds and the Earth’s Radiant Energy System (CERES) Data. *Journal of Applied Meteorology and Climatology*, **50 (12)**, 2490–2503, doi:10.1175/JAMC-D-11-050.1, 00000 ZSCC: 0000013.
- Müller, R., T. Behrendt, A. Hammer, and A. Kemper, 2012: A New Algorithm for the Satellite-Based Retrieval of Solar Surface Irradiance in Spectral Bands. *Remote Sensing*, **4 (3)**, 622–647, doi:10.3390/rs4030622, zSCC: NoCitationData[s0].
- Müller, R., U. Pfeifroth, C. Träger-Chatterjee, R. Cremer, J. Trentmann, and R. Hollmann, 2015a: Surface Solar Radiation Data Set - Heliosat (SARAH) - Edition 1. EUMETSAT Satellite Application Facility on Climate Monitoring (CM SAF), 00000 ZSCC: 0000006, 00000 ZSCC: 0000006.
- Müller, R., U. Pfeifroth, C. Träger-Chatterjee, J. Trentmann, and R. Cremer, 2015b: Digging the METEOSAT Treasure—3 Decades of Solar Surface Radiation. *Remote Sensing*, **7 (6)**, 8067–8101, doi:10.3390/rs70608067, zSCC: 0000066.

- Müller, R. W., C. Matsoukas, A. Gratzki, H. D. Behr, and R. Hollmann, 2009: The CM-SAF operational scheme for the satellite based retrieval of solar surface irradiance — A LUT based eigenvector hybrid approach. *Remote Sensing of Environment*, **113** (5), 1012–1024, doi:10.1016/j.rse.2009.01.012, zSCC: NoCitationData[s0].
- Myhre, G., et al., 2013: Radiative forcing of the direct aerosol effect from AeroCom Phase II simulations. *Atmospheric Chemistry and Physics*, **13** (4), 1853–1877, doi:https://doi.org/10.5194/acp-13-1853-2013, zSCC: NoCitationData[s0].
- Nappo, C. J., et al., 1982: Workshop on the Representativeness of Meteorological Observations, June 1981, Boulder, Colo. *Bull. Am. Meteorol. Soc.; (United States)*, **63**:7, zSCC: NoCitationData[s0].
- Norris, J. R. and M. Wild, 2007: Trends in aerosol radiative effects over Europe inferred from observed cloud cover, solar “dimming,” and solar “brightening”. *Journal of Geophysical Research*, **112** (D8), doi:10.1029/2006JD007794, zSCC: 0000230.
- Ohmura, A., 2006: Observed long-term variations of solar irradiance at the earth’s surface. *Space Science Reviews*, **125** (1-4), 111–128, doi:10.1007/s11214-006-9050-9, zSCC: 0000077 WOS:000244449400010.
- Ohmura, A., 2009: Observed decadal variations in surface solar radiation and their causes. *Journal of Geophysical Research-Atmospheres*, **114**, D00D05, doi:10.1029/2008JD011290, zSCC: 0000142 WOS:000265102000005.
- Ohmura, A., 2014: The Development and the Present Status of Energy Balance Climatology. *Journal of the Meteorological Society of Japan. Ser. II*, **92** (4), 245–285, doi:10.2151/jmsj.2014-401, 00000 ZSCC: 0000008.
- Ohmura, A. and H. Lang, 1989: Secular variation of global radiation in Europe. *Current Problems in Atmospheric Radiation*, Deepak, Hampton, Virginia., j. lenoble and j. f. geleyn ed., zSCC: NoCitationData[s0].
- Ohmura, A., et al., 1998: Baseline Surface Radiation Network (BSRN/WCRP): New Precision Radiometry for Climate Research. *Bulletin of the American Meteorological Society*, **79** (10), 2115–2136, doi:10.1175/1520-0477(1998)079<2115:BSRNBW>2.0.CO;2, zSCC: NoCitationData[s0].
- Olefs, M., et al., 2016: The Austrian radiation monitoring network ARAD – best practice and added value. *Atmos. Meas. Tech.*, **9** (4), 1513–1531, doi:10.5194/amt-9-1513-2016, zSCC: NoCitationData[s0].
- Parding, K. M., B. G. Liepert, L. M. Hinkelman, T. P. Ackerman, K.-F. Dagestad, and J. A. Olseth, 2016: Influence of Synoptic Weather Patterns on Solar Irradiance Variability in

- Northern Europe. *Journal of Climate*, **29** (11), 4229–4250, doi:10.1175/JCLI-D-15-0476.1, 00000 ZSCC: 0000010.
- Pavlaklis, K. G., N. Hatzianastassiou, C. Matsoukas, A. Fotiadi, and I. Vardavas, 2008: ENSO surface shortwave radiation forcing over the tropical Pacific. *Atmos. Chem. Phys.*, **8** (18), 5565–5577, doi:10.5194/acp-8-5565-2008, 00000 ZSCC: 0000012.
- Pettitt, A. N., 1979: A Non-Parametric Approach to the Change-Point Problem. *Journal of the Royal Statistical Society. Series C (Applied Statistics)*, **28** (2), 126–135, doi:10.2307/2346729, zSCC: 0002144.
- Pfieferth, U., S. Kothe, R. Müller, J. Trentmann, R. Hollmann, P. Fuchs, and M. Werscheck, 2017: Surface Radiation Data Set - Heliosat (SARAH) - Edition 2. Satellite Application Facility on Climate Monitoring (CM SAF), 00000 ZSCC: 0000008.
- Pinker, R. T., S. A. Grodsky, B. Zhang, A. Busalacchi, and W. Chen, 2017: ENSO impact on surface radiative fluxes as observed from space. *Journal of Geophysical Research: Oceans*, **122** (10), 7880–7896, doi:10.1002/2017JC012900, 00000 ZSCC: 0000006.
- Poli, P., et al., 2016: ERA-20C: An Atmospheric Reanalysis of the Twentieth Century. *Journal of Climate*, **29** (11), 4083–4097, doi:10.1175/JCLI-D-15-0556.1, zSCC: NoCitation-Data[s0].
- Posselt, R., R. Mueller, R. Stöckli, and J. Trentmann, 2011: Spatial and Temporal Homogeneity of Solar Surface Irradiance across Satellite Generations. *Remote Sensing*, **3** (5), 1029–1046, doi:10.3390/rs3051029, 00000 ZSCC: 0000035.
- Posselt, R., R. W. Müller, R. Stöckli, and J. Trentmann, 2012: Remote sensing of solar surface radiation for climate monitoring — the CM-SAF retrieval in international comparison. *Remote Sensing of Environment*, **118**, 186–198, doi:10.1016/j.rse.2011.11.016, zSCC: NoCitationData[s0].
- Qian, Y., D. P. Kaiser, L. R. Leung, and M. Xu, 2006: More frequent cloud-free sky and less surface solar radiation in China from 1955 to 2000. *Geophysical Research Letters*, **33** (1), doi:10.1029/2005GL024586, zSCC: 0000276.
- Qian, Y., W. Wang, L. R. Leung, and D. P. Kaiser, 2007: Variability of solar radiation under cloud-free skies in China: The role of aerosols. *Geophysical Research Letters*, **34** (12), L12 804, doi:10.1029/2006GL028800, zSCC: 0000143.
- Ramanathan, V., 1987: The role of earth radiation budget studies in climate and general circulation research. *Journal of Geophysical Research: Atmospheres*, **92** (D4), 4075–4095, doi:10.1029/JD092iD04p04075, zSCC: 0000395.

- Ramanathan, V., R. D. Cess, E. F. Harrison, P. Minnis, B. R. Barkstrom, E. Ahmad, and D. Hartmann, 1989: Cloud-Radiative Forcing and Climate: Results from the Earth Radiation Budget Experiment. *Science*, **243** (4887), 57–63, doi:10.1126/science.243.4887.57, zSCC: 0001697.
- Ramanathan, V., P. J. Crutzen, J. T. Kiehl, and D. Rosenfeld, 2001: Aerosols, Climate, and the Hydrological Cycle. *Science*, **294** (5549), 2119–2124, doi:10.1126/science.1064034, 03183 ZSCC: 0003183.
- Ramanathan, V., et al., 2005: Atmospheric brown clouds: Impacts on South Asian climate and hydrological cycle. *Proceedings of the National Academy of Sciences of the United States of America*, **102** (15), 5326–5333, doi:10.1073/pnas.0500656102, zSCC: 0001096.
- Roesch, A., M. Wild, A. Ohmura, E. G. Dutton, C. N. Long, and T. Zhang, 2011: Assessment of BSRN radiation records for the computation of monthly means. *Atmospheric Measurement Techniques*, **4** (2), 339–354, doi:10.5194/amt-4-339-2011, zSCC: 0000113.
- Román, M. O., et al., 2009: The MODIS (Collection V005) BRDF/albedo product: Assessment of spatial representativeness over forested landscapes. *Remote Sensing of Environment*, **113** (11), 2476–2498, doi:10.1016/j.rse.2009.07.009, zSCC: 0000197.
- Roman, M. O., et al., 2013: Use of In Situ and Airborne Multiangle Data to Assess MODIS- and Landsat-Based Estimates of Directional Reflectance and Albedo. *IEEE Transactions on Geoscience and Remote Sensing*, **51** (3), 1393–1404, doi:10.1109/TGRS.2013.2243457, zSCC: 0000074.
- Rossow, W. B. and A. A. Lacis, 1990: Global, Seasonal Cloud Variations from Satellite Radiance Measurements. Part II. Cloud Properties and Radiative Effects. *Journal of Climate*, **3** (11), 1204–1253, doi:10.1175/1520-0442(1990)003<1204:GSCVFS>2.0.CO;2, zSCC: 0000170.
- Rougier, J., 2016: Ensemble Averaging and Mean Squared Error. *Journal of Climate*, **29** (24), 8865–8870, doi:10.1175/JCLI-D-16-0012.1, 00000 ZSCC: 0000017.
- Russak, V., 1990: Trends of solar radiation, cloudiness and atmospheric transparency during recent decades in Estonia. *Tellus B: Chemical and Physical Meteorology*, **42** (2), 206–210, doi:10.3402/tellusb.v42i2.15205, zSCC: 0000109.
- Rutan, D. A., S. Kato, D. R. Doelling, F. G. Rose, L. T. Nguyen, T. E. Caldwell, and N. G. Loeb, 2015: CERES Synoptic Product: Methodology and Validation of Surface Radiant Flux. *Journal of Atmospheric and Oceanic Technology*, **32** (6), 1121–1143, doi:10.1175/JTECH-D-14-00165.1, 00000 ZSCC: 0000049.

- Salomon, J., C. Schaaf, A. Strahler, Feng Gao, and Yufang Jin, 2006: Validation of the MODIS bidirectional reflectance distribution function and albedo retrievals using combined observations from the aqua and terra platforms. *IEEE Transactions on Geoscience and Remote Sensing*, **44** (6), 1555–1565, doi:10.1109/TGRS.2006.871564, zSCC: NoCitationData[s0].
- Sanchez-Lorenzo, A., M. Wild, M. Brunetti, J. A. Guijarro, M. Z. Hakuba, J. Calbó, S. Mysatakidis, and B. Bartok, 2015: Reassessment and update of long-term trends in downward surface shortwave radiation over Europe (1939-2012). *Journal of Geophysical Research: Atmospheres*, **120** (18), 9555–9569, doi:10.1002/2015JD023321, 00000 ZSCC: 0000045.
- Santer, B. D., et al., 2018: Human influence on the seasonal cycle of tropospheric temperature. *Science*, **361** (6399), eaas8806, doi:10.1126/science.aas8806, zSCC: NoCitationData[s0].
- Schaaf, C. B., J. Liu, F. Gao, and A. H. Strahler, 2010: Aqua and Terra MODIS Albedo and Reflectance Anisotropy Products. *Land Remote Sensing and Global Environmental Change: NASA's Earth Observing System and the Science of ASTER and MODIS*, B. Ramachandran, C. O. Justice, and M. J. Abrams, Eds., Springer New York, New York, NY, Remote Sensing and Digital Image Processing, 549–561, doi:10.1007/978-1-4419-6749-7\_24, zSCC: NoCitationData[s1].
- Schaaf, C. B. and Z. Wang, 2015: MCD43A1 MODIS/Terra+Aqua BRDF/Albedo Model Parameters Daily L3 Global - 500m V006. NASA EOSDIS Land Processes DAAC, zSCC: NoCitationData[s0], doi:10.5067/MODIS/MCD43A1.006, zSCC: NoCitationData[s0].
- Schaaf, C. B., et al., 2002: First operational BRDF, albedo nadir reflectance products from MODIS. *Remote Sensing of Environment*, **83** (1–2), 135–148, doi:10.1016/S0034-4257(02)00091-3, zSCC: 0001773.
- Schaepman-Strub, G., M. E. Schaepman, T. H. Painter, S. Dangel, and J. V. Martonchik, 2006: Reflectance quantities in optical remote sensing—definitions and case studies. *Remote Sensing of Environment*, **103** (1), 27–42, doi:10.1016/j.rse.2006.03.002, zSCC: 0000802.
- Schmetz, J., P. Pili, S. Tjemkes, D. Just, J. Kerkmann, S. Rota, and A. Ratier, 2002: An Introduction to Meteosat Second Generation (MSG). *Bulletin of the American Meteorological Society*, **83** (7), 977–992, doi:10.1175/1520-0477(2002)083<0977:AITMSG>2.3.CO;2, zSCC: 0000811.
- Schutgens, N., S. Tsyro, E. Gryspeerdt, D. Goto, N. Weigum, M. Schulz, and P. Stier, 2017: On the spatio-temporal representativeness of observations. *Atmos. Chem. Phys.*, **17** (16), 9761–9780, doi:10.5194/acp-17-9761-2017, 00000 ZSCC: 0000016.

- Schutgens, N. A. J., E. Gryspeerdt, N. Weigum, S. Tsyro, D. Goto, M. Schulz, and P. Stier, 2016a: Will a perfect model agree with perfect observations? The impact of spatial sampling. *Atmos. Chem. Phys.*, **16** (10), 6335–6353, doi:10.5194/acp-16-6335-2016, 00000 ZSCC: 0000050.
- Schutgens, N. A. J., D. G. Partridge, and P. Stier, 2016b: The importance of temporal collocation for the evaluation of aerosol models with observations. *Atmos. Chem. Phys.*, **16** (2), 1065–1079, doi:10.5194/acp-16-1065-2016, 00000 ZSCC: 0000033.
- Schwartz, R. E., A. Gershunov, S. F. Iacobellis, and D. R. Cayan, 2014: North American west coast summer low cloudiness: Broad-scale variability associated with sea surface temperature. *Geophysical Research Letters*, **41** (9), 2014GL059825, doi:10.1002/2014GL059825, 00000 ZSCC: 0000024.
- Schwarz, M., 2015: Influence of Low Ozone Episodes on Erythral UV Radiation in Austria. Master Thesis, University of Graz, Graz, Austria, zSCC: NoCitationData[s0].
- Schwarz, M., D. Folini, M. Z. Hakuba, and M. Wild, 2017: Spatial Representativeness of Surface-Measured Variations of Downward Solar Radiation. *Journal of Geophysical Research: Atmospheres*, **122** (24), 2017JD027261, doi:10.1002/2017JD027261, zSCC: 0000005 ZSCC: 0000005.
- Schwarz, M., D. Folini, M. Z. Hakuba, and M. Wild, 2018: From Point to Area: Worldwide Assessment of the Representativeness of Monthly Surface Solar Radiation Records. *Journal of Geophysical Research: Atmospheres*, **123** (24), 13,857–13,874, doi:10.1029/2018JD029169, zSCC: 0000002 ZSCC: 0000002.
- Seinfeld, J. H. and S. N. Pandis, 2006: *Atmospheric Chemistry and Physics: From Air Pollution to Climate Change*. 2d ed., Wiley, Hoboken, N.J, zSCC: 0000076.
- Servain, J., A. J. Busalacchi, M. J. McPhaden, A. D. Moura, G. Reverdin, M. Vianna, and S. E. Zebiak, 1998: A Pilot Research Moored Array in the Tropical Atlantic (PIRATA). *Bulletin of the American Meteorological Society*, **79** (10), 2019–2032, doi:10.1175/1520-0477(1998)079<2019:APRMAI>2.0.CO;2, zSCC: 0000251.
- Shi, G.-Y., T. Hayasaka, A. Ohmura, Z.-H. Chen, B. Wang, J.-Q. Zhao, H.-Z. Che, and L. Xu, 2008: Data Quality Assessment and the Long-Term Trend of Ground Solar Radiation in China. *Journal of Applied Meteorology and Climatology*, **47** (4), 1006–1016, doi:10.1175/2007JAMC1493.1, zSCC: 0000186.
- Shine, K. P., I. V. Ptashnik, and G. Rädcl, 2012: The Water Vapour Continuum: Brief History and Recent Developments. *Surveys in Geophysics*, **33** (3-4), 535–555, doi:10.1007/s10712-011-9170-y, zSCC: 0000099.



- Shrestha, A. K., et al., 2017: Spectral unfiltering of ERBE WFOV nonscanner shortwave observations and revisiting its radiation dataset from 1985 to 1998. *AIP Conference Proceedings*, **1810 (1)**, 090 008, doi:10.1063/1.4975548, zSCC: NoCitationData[s0].
- Shuttleworth, W. J. and R. E. Dickinson, 1989: Comments on 'Modelling tropical deforestation: A study of GCM land-surface parametrizations' by R. E. Dickinson and A. Henderson-Sellers (January B 1988, 114, 439–462). *Quarterly Journal of the Royal Meteorological Society*, **115 (489)**, 1177–1179, doi:10.1002/qj.49711548910, 00000 ZSCC: 0000061.
- Simoneit, B. R. T., 2002: Biomass burning — a review of organic tracers for smoke from incomplete combustion. *Applied Geochemistry*, **17 (3)**, 129–162, doi:10.1016/S0883-2927(01)00061-0, zSCC: 0001116.
- Solomon, S., R. W. Portmann, R. W. Sanders, and J. S. Daniel, 1998: Absorption of solar radiation by water vapor, oxygen, and related collision pairs in the Earth's atmosphere. *Journal of Geophysical Research: Atmospheres*, **103 (D4)**, 3847–3858, doi:10.1029/97JD03285, zSCC: 0000089.
- Stanhill, G. and S. Cohen, 2001: Global dimming: A review of the evidence for a widespread and significant reduction in global radiation with discussion of its probable causes and possible agricultural consequences. *Agricultural and Forest Meteorology*, **107 (4)**, 255–278, doi:10.1016/S0168-1923(00)00241-0, zSCC: 0000996.
- Stanhill, G. and S. Moreshet, 1992a: Global radiation climate changes in Israel. *Climatic Change*, **22 (2)**, 121–138, doi:10.1007/BF00142962, 00000 ZSCC: 0000032.
- Stanhill, G. and S. Moreshet, 1992b: Global radiation climate changes: The world network. *Climatic Change*, **21 (1)**, 57–75, doi:10.1007/BF00143253, zSCC: 0000097.
- Stanhill, G. and S. Moreshet, 1994: Global radiation climate change at seven sites remote from surface sources of pollution. *Climatic Change*, **26 (1)**, 89–103, doi:10.1007/BF01094010, 00000 ZSCC: 0000036.
- Stephens, G. L., D. O'Brien, P. J. Webster, P. Pilewski, S. Kato, and J.-I. Li, 2015: The albedo of Earth. *Reviews of Geophysics*, **53 (1)**, 141–163, doi:10.1002/2014RG000449, zSCC: 0000070.
- Stephens, G. L. and S.-C. Tsay, 1990: On the cloud absorption anomaly. *Quarterly Journal of the Royal Meteorological Society*, **116 (493)**, 671–704, doi:10.1002/qj.49711649308, zSCC: 0000315.
- Stephens, G. L., et al., 2012: An update on Earth's energy balance in light of the latest global observations. *Nature Geoscience*, **5 (10)**, 691–696, doi:10.1038/ngeo1580, zSCC: 0000354.

- Stephens, G. L., et al., 2018: Regional Intensification of the Tropical Hydrological Cycle During ENSO. *Geophysical Research Letters*, **45** (9), 4361–4370, doi:10.1029/2018GL077598, 00000 ZSCC: 0000004.
- Takemura, T., T. Nakajima, O. Dubovik, B. N. Holben, and S. Kinne, 2002: Single-Scattering Albedo and Radiative Forcing of Various Aerosol Species with a Global Three-Dimensional Model. *Journal of Climate*, **15** (4), 333–352, doi:10.1175/1520-0442(2002)015<0333:SSAARF>2.0.CO;2, zSCC: 0000418.
- Takemura, T., H. Okamoto, Y. Maruyama, A. Numaguti, A. Higurashi, and T. Nakajima, 2000: Global three-dimensional simulation of aerosol optical thickness distribution of various origins. *Journal of Geophysical Research: Atmospheres*, **105** (D14), 17 853–17 873, doi:10.1029/2000JD900265, zSCC: 0000375.
- Tang, W.-J., K. Yang, J. Qin, C. C. K. Cheng, and J. He, 2011: Solar radiation trend across China in recent decades: A revisit with quality-controlled data. *Atmospheric Chemistry and Physics*, **11** (1), 393–406, doi:https://doi.org/10.5194/acp-11-393-2011, zSCC: 0000125.
- Taylor, K. E., 2001: Summarizing multiple aspects of model performance in a single diagram. *Journal of Geophysical Research: Atmospheres*, **106** (D7), 7183–7192, doi:10.1029/2000JD900719, zSCC: 0003224.
- Taylor, K. E., M. Crucifix, P. Braconnot, C. D. Hewitt, C. Doutriaux, A. J. Broccoli, J. F. B. Mitchell, and M. J. Webb, 2007: Estimating Shortwave Radiative Forcing and Response in Climate Models. *Journal of Climate*, **20** (11), 2530–2543, doi:10.1175/JCLI4143.1, zSCC: 0000097.
- Taylor, K. E., R. J. Stouffer, and G. A. Meehl, 2011: An Overview of CMIP5 and the Experiment Design. *Bulletin of the American Meteorological Society*, **93** (4), 485–498, doi:10.1175/BAMS-D-11-00094.1, 00000 ZSCC: 0000002.
- Thornhill, G. D., C. L. Ryder, E. J. Highwood, L. C. Shaffrey, and B. T. Johnson, 2018: The effect of South American biomass burning aerosol emissions on the regional climate. *Atmospheric Chemistry and Physics*, **18** (8), 5321–5342, doi:https://doi.org/10.5194/acp-18-5321-2018, 00000 ZSCC: 0000007.
- Trenberth, K. E., 2009: An imperative for climate change planning: Tracking Earth's global energy. *Current Opinion in Environmental Sustainability*, **1** (1), 19–27, doi:10.1016/j.cosust.2009.06.001, zSCC: 0000097.
- Trenberth, K. E., J. Fasullo, and L. Smith, 2005: Trends and variability in column-integrated atmospheric water vapor. *Climate Dynamics*, **24** (7-8), 741–758, doi:10.1007/s00382-005-0017-4, zSCC: NoCitationData[s1].

- Trenberth, K. E. and J. T. Fasullo, 2009: Global warming due to increasing absorbed solar radiation. *Geophysical Research Letters*, **36** (7), L07706, doi:10.1029/2009GL037527, zSCC: 0000108.
- Trenberth, K. E. and J. T. Fasullo, 2010: Simulation of Present-Day and Twenty-First-Century Energy Budgets of the Southern Oceans. *Journal of Climate*, **23** (2), 440–454, doi:10.1175/2009JCLI3152.1, zSCC: 0000252.
- Trenberth, K. E., J. T. Fasullo, and J. Kiehl, 2009: Earth's Global Energy Budget. *Bulletin of the American Meteorological Society*, **90** (3), 311–324, doi:10.1175/2008BAMS2634.1, zSCC: 0001230.
- Trenberth, K. E. and D. P. Stepaniak, 2004: The flow of energy through the earth's climate system. *Quarterly Journal of the Royal Meteorological Society*, **130** (603), 2677–2701, doi:10.1256/qj.04.83, zSCC: 0000102.
- Trenberth, K. E., Y. Zhang, J. T. Fasullo, and S. Taguchi, 2015: Climate variability and relationships between top-of-atmosphere radiation and temperatures on Earth. *Journal of Geophysical Research: Atmospheres*, **120** (9), 2014JD022887, doi:10.1002/2014JD022887, 00000 ZSCC: 0000040.
- Twomey, S., 1959: The nuclei of natural cloud formation part II: The supersaturation in natural clouds and the variation of cloud droplet concentration. *Geofisica pura e applicata*, **43** (1), 243–249, doi:10.1007/BF01993560, zSCC: 0000534.
- Uppala, S. M., et al., 2005: The ERA-40 re-analysis. *Quarterly Journal of the Royal Meteorological Society*, **131** (612), 2961–3012, doi:10.1256/qj.04.176, zSCC: NoCitationData[s0].
- Von Neumann, J., 1941: Distribution of the Ratio of the Mean Square Successive Difference to the Variance. *The Annals of Mathematical Statistics*, **12** (4), 367–395, doi:10.1214/aoms/1177731677, zSCC: 0000841.
- von Schuckmann, K., et al., 2016: An imperative to monitor Earth's energy imbalance. *Nature Climate Change*, **6** (2), 138–144, doi:10.1038/nclimate2876, zSCC: 0000097.
- Wang, D., S. Liang, T. He, Y. Yu, C. Schaaf, and Z. Wang, 2015a: Estimating daily mean land surface albedo from MODIS data. *Journal of Geophysical Research: Atmospheres*, **120** (10), 4825–4841, doi:10.1002/2015JD023178, zSCC: 0000015.
- Wang, J., A. Dai, and C. Mears, 2016: Global Water Vapor Trend from 1988 to 2011 and Its Diurnal Asymmetry Based on GPS, Radiosonde, and Microwave Satellite Measurements. *Journal of Climate*, **29** (14), 5205–5222, doi:10.1175/JCLI-D-15-0485.1, 00000 ZSCC: 0000022.

- Wang, K., Q. Ma, Z. Li, and J. Wang, 2015b: Decadal variability of surface incident solar radiation over China: Observations, satellite retrievals, and reanalyses. *Journal of Geophysical Research: Atmospheres*, **120** (13), 6500–6514, doi:10.1002/2015JD023420, 00000 ZSCC: 0000036.
- Wang, K. C., R. E. Dickinson, M. Wild, and S. Liang, 2012a: Atmospheric impacts on climatic variability of surface incident solar radiation. *Atmospheric Chemistry and Physics*, **12** (20), 9581–9592, doi:10.5194/acp-12-9581-2012, zSCC: 0000073.
- Wang, Z., et al., 2012b: Evaluation of Moderate-resolution Imaging Spectroradiometer (MODIS) snow albedo product (MCD43A) over tundra. *Remote Sensing of Environment*, **117**, 264–280, doi:https://doi.org/10.1016/j.rse.2011.10.002, zSCC: 0000094 Remote Sensing of Urban Environments.
- Wang, Z., et al., 2014: Evaluation of MODIS albedo product (MCD43A) over grassland, agriculture and forest surface types during dormant and snow-covered periods. *Remote Sensing of Environment*. 140: 60-77., **140**, 60–77, doi:10.1016/j.rse.2013.08.025, zSCC: NoCitation-Data[s0].
- Wanner, W., A. H. Strahler, B. Hu, P. Lewis, J.-P. Muller, X. Li, C. L. B. Schaaf, and M. J. Barnsley, 1997: Global retrieval of bidirectional reflectance and albedo over land from EOS MODIS and MISR data: Theory and algorithm. *Journal of Geophysical Research: Atmospheres*, **102** (D14), 17 143–17 161, doi:10.1029/96JD03295, zSCC: 0000353.
- Wielicki, B. A., B. R. Barkstrom, E. F. Harrison, R. B. Lee, G. Louis Smith, and J. E. Cooper, 1996: Clouds and the Earth's Radiant Energy System (CERES): An Earth Observing System Experiment. *Bulletin of the American Meteorological Society*, **77** (5), 853–868, doi:10.1175/1520-0477(1996)077<0853:CATERE>2.0.CO;2, zSCC: 0001504.
- Wijngaard, J. B., A. M. G. Klein Tank, and G. P. Können, 2003: Homogeneity of 20th century European daily temperature and precipitation series. *International Journal of Climatology*, **23** (6), 679–692, doi:10.1002/joc.906, zSCC: 0000615.
- Wild, M., 1999: Discrepancies between model-calculated and observed shortwave atmospheric absorption in areas with high aerosol loadings. *Journal of Geophysical Research: Atmospheres*, **104** (D22), 27 361–27 371, doi:10.1029/1999JD900925, 00000 ZSCC: 0000057.
- Wild, M., 2000: Absorption of solar energy in cloudless and cloudy atmospheres over Germany and in GCMs. *Geophysical Research Letters*, **27** (7), 959–962, doi:10.1029/1999GL011144, 00000 ZSCC: 0000026.
- Wild, M., 2008: Short-wave and long-wave surface radiation budgets in GCMs: A review based on the IPCC-AR4/CMIP3 models. *Tellus A*, **60** (5), 932–945, doi:10.1111/j.1600-0870.2008.00342.x, zSCC: 0000081.

- Wild, M., 2009a: Global dimming and brightening: A review. *Journal of Geophysical Research*, **114**, doi:10.1029/2008JD011470, zSCC: 0000728.
- Wild, M., 2009b: How well do IPCC-AR4/CMIP3 climate models simulate global dimming/brightening and twentieth-century daytime and nighttime warming? *Journal of Geophysical Research*, **114**, doi:10.1029/2008JD011372, 00000 ZSCC: 0000046.
- Wild, M., 2012: New Directions: A facelift for the picture of the global energy balance. *Atmospheric Environment*, **55**, 366–367, doi:10.1016/j.atmosenv.2012.03.022, 00000 ZSCC: 0000020.
- Wild, M., 2016: Decadal changes in radiative fluxes at land and ocean surfaces and their relevance for global warming. *Wiley Interdisciplinary Reviews: Climate Change*, **7 (1)**, 91–107, doi:10.1002/wcc.372, 00000 ZSCC: 0000054.
- Wild, M., D. Folini, C. Schär, N. Loeb, E. G. Dutton, and G. König-Langlo, 2013: The global energy balance from a surface perspective. *Climate Dynamics*, **40 (11-12)**, 3107–3134, doi: 10.1007/s00382-012-1569-8, zSCC: 0000250.
- Wild, M., M. Z. Hakuba, D. Folini, P. Dörig-Ott, C. Schär, S. Kato, and C. N. Long, 2018: The cloud-free global energy balance and inferred cloud radiative effects: An assessment based on direct observations and climate models. *Climate Dynamics*, doi:10.1007/s00382-018-4413-y, zSCC: NoCitationData[s0].
- Wild, M., C. N. Long, and A. Ohmura, 2006: Evaluation of clear-sky solar fluxes in GCMs participating in AMIP and IPCC-AR4 from a surface perspective. *Journal of Geophysical Research*, **111 (D1)**, doi:10.1029/2005JD006118, zSCC: 0000071.
- Wild, M., A. Ohmura, H. Gilgen, and E. Roeckner, 1995: Validation of General Circulation Model Radiative Fluxes Using Surface Observations. *Journal of Climate*, **8 (5)**, 1309–1324, doi:10.1175/1520-0442(1995)008<1309:VOGCMR>2.0.CO;2, zSCC: 0000221.
- Wild, M., A. Ohmura, and K. Makowski, 2007: Impact of global dimming and brightening on global warming. *Geophysical Research Letters*, **34 (4)**, doi:10.1029/2006GL028031, zSCC: 0000294.
- Wild, M., A. Ohmura, C. Schär, G. Müller, D. Folini, M. Schwarz, M. Z. Hakuba, and A. Sanchez-Lorenzo, 2017: The Global Energy Balance Archive (GEBA) version 2017: A database for worldwide measured surface energy fluxes. *Earth System Science Data*, **9 (2)**, 601–613, doi:https://doi.org/10.5194/essd-9-601-2017, zSCC: NoCitationData[s2].
- Wild, M., et al., 2005: From Dimming to Brightening: Decadal Changes in Solar Radiation at Earth's Surface. *Science*, **308 (5723)**, 847–850, doi:10.1126/science.1103215, zSCC: 0001089.

- Wild, M., et al., 2015: The energy balance over land and oceans: An assessment based on direct observations and CMIP5 climate models. *Climate Dynamics*, **44** (11-12), 3393–3429, doi:10.1007/s00382-014-2430-z, zSCC: NoCitationData[s0].
- Wong, T., B. A. Wielicki, R. B. Lee, G. L. Smith, K. A. Bush, and J. K. Willis, 2006: Reexamination of the Observed Decadal Variability of the Earth Radiation Budget Using Altitude-Corrected ERBE/ERBS Nonscanner WFOV Data. *Journal of Climate*, **19** (16), 4028–4040, doi:10.1175/JCLI3838.1, zSCC: 0000164.
- Yamamoto, G. and G. Onishi, 1952: Absorption of solar radiation by water vapor in the atmosphere. *Journal of Meteorology*, **9** (6), 415–421, doi:10.1175/1520-0469(1952)009<0415:AOSRBW>2.0.CO;2, 00000 ZSCC: 0000025.
- Yang, S., X. L. Wang, and M. Wild, 2018: Homogenization and Trend Analysis of the 1958–2016 In Situ Surface Solar Radiation Records in China. *Journal of Climate*, **31** (11), 4529–4541, doi:10.1175/JCLI-D-17-0891.1, 00000 ZSCC: 0000003.
- Yang, X., C. Zhao, J. Guo, and Y. Wang, 2016: Intensification of aerosol pollution associated with its feedback with surface solar radiation and winds in Beijing. *Journal of Geophysical Research: Atmospheres*, **121** (8), 4093–4099, doi:10.1002/2015JD024645, zSCC: 0000034.
- Yoon, J., J. P. Burrows, M. Vountas, W. von Hoyningen-Huene, D. Y. Chang, A. Richter, and A. Hilboll, 2014: Changes in atmospheric aerosol loading retrieved from space-based measurements during the past decade. *Atmos. Chem. Phys.*, **14** (13), 6881–6902, doi:10.5194/acp-14-6881-2014, zSCC: NoCitationData[s0].
- Yu, H., et al., 2006: A review of measurement-based assessments of the aerosol direct radiative effect and forcing. *Atmospheric Chemistry and Physics*, **6** (3), 613–666, doi:https://doi.org/10.5194/acp-6-613-2006, zSCC: NoCitationData[s0].
- Zelenka, A., R. Perez, R. Seals, and D. Renné, 1999: Effective Accuracy of Satellite-Derived Hourly Irradiances. *Theoretical and Applied Climatology*, **62** (3-4), 199–207, doi:10.1007/s007040050084, zSCC: 0000282.
- Zhang, T., P. W. Stackhouse, S. K. Gupta, S. J. Cox, J. Colleen Mikovitz, and L. M. Hinkelman, 2013: The validation of the GEWEX SRB surface shortwave flux data products using BSRN measurements: A systematic quality control, production and application approach. *Journal of Quantitative Spectroscopy and Radiative Transfer*, **122**, 127–140, doi:10.1016/j.jqsrt.2012.10.004, 00000 ZSCC: 0000052.
- Zhang, X., S. Liang, M. Wild, and B. Jiang, 2015: Analysis of surface incident shortwave radiation from four satellite products. *Remote Sensing of Environment*, **165**, 186–202, doi:10.1016/j.rse.2015.05.015, 00000 ZSCC: 0000041.

Zhang, Y., R. Fu, H. Yu, R. E. Dickinson, R. N. Juarez, M. Chin, and H. Wang, 2008: A regional climate model study of how biomass burning aerosol impacts land-atmosphere interactions over the Amazon. *Journal of Geophysical Research: Atmospheres*, **113** (D14), doi:10.1029/2007JD009449, 00000 ZSCC: 0000049.





# Curriculum Vitae

## Personal information

Surname / First name **SCHWARZ Matthias, MSc MSc BSc BSc**  
Nationality Austria  
Date of birth 19.10.1988

## Education

since 01/2016 PhD Position in Climate Science  
ETH Zurich  
Department of Environmental Systems Science, Institute for Atmospheric and Climate Science  
Topic: Towards an improved understanding of the global energy balance: temporal variation of solar radiation in the climate system

04/2013 – 03/2016 Master of Sciences (MSc) in Environmental Systems Sciences: Geography  
University of Graz  
Focus on High Mountain and Climate Geography  
Master's thesis: Validation of an Open-source Computational Fluid Dynamics Snowdrift Model with Terrestrial Laserscans, supervised by Prof. Gerhard Lieb

02/2014 – 10/2015 Master of Sciences (MSc) in Physics  
University of Graz  
Focus on Geophysics – Physics of the Atmosphere and Climate  
passed with distinction  
Master's thesis: The Influence of Low Ozone Episodes on UV-Radiation Doses in Austria; Supervised by Prof. Harald Rieder

03/2011 – 02/2014 Bachelor of Science (BSc) in Environmental Systems Sciences: Physics  
University of Graz

09/2009 – 03/2013 Bachelor of Science (BSc) in Environmental Systems Sciences: Geography  
University of Graz

05/2009 Paramedic training  
during civilian service at Red Cross Austria

2003 – 2008 Higher Technical Institute (HTL) Ortwein Graz Andritz  
finished with Matura (general qualification for university entrance)

## Work

since 01/2016 PhD Candidate ETH Zurich

03/2015 – 09/2015 Teaching Assistant  
at University of Graz for the lecture *Mathematical Methods: Statistical Methods*

05/2014 – 12/2015 Research Assistant  
at University of Graz for Prof. Harald Rieder, Climate Processes and Environmental Meteorology

10/2010 – 12/2015 Technical Assistant for the Institute of Water Analysis IWA, Graz-Umgebung  
*Laboratory management: Chemical analysis in the field of municipal wastewater disposal*

04/2015 Project Assistant  
Central Agency for Meteorology and Geodynamics (ger: Zentralanstalt für Meteorologie und Geodynamik ZAMG) Graz

06/2009 – 07/2009 Engineer at HTL Bau, Leibnitz

05/2009 – 04/2009 Civil service  
Working as certified paramedic during compulsory civilian service at Red Cross, Leoben

